DEVELOPMENT OF A LINE-FIELD MAGNETO-MOTIVE OPTICAL COHERENCE TOMOGRAPHY SYSTEM

Jessica Barnett Barrick

A dissertation submitted to the faculty at the University of North Carolina at Chapel Hill in partial fulfillment of the requirements for the degree of Doctor of Philosophy in the Department of Physics and Astronomy.

Chapel Hill
2020

Approved by:

Amy L. Oldenburg

Laurie E. McNeil

Tamara Branca

Richard Superfine

Laura Mersini-Houghton

ABSTRACT

Jessica Barnett Barrick: Development of a line-field magneto-motive optical coherence tomography system
(Under the direction of Amy L. Oldenburg)

The mechanism by which certain species of animals are able to detect the Earth's magnetic field has remained a mystery for as long as we have known that they exhibit geomagnetic navigation. Certain species of bacteria are known to contain single chains of magnetite crystals, each with a diameter of ~50 nm, that are used to orient the bacteria. Searching for similar magnetoreceptors in larger animals requires a high-speed, high-resolution imaging system with the ability to detect single magnetic nanoparticles. Optical coherence tomography (OCT) is a biomedical imaging modality that produces 2D, cross-sectional images of optically turbid media with a resolution on the order of 1-10 μm. Magneto-motive OCT (MMOCT) is a functional form of OCT that can detect the sub-resolution displacement of magnetic nano- or micro-particles embedded in weakly diamagnetic, optically scattering, elastic media (such as human and animal tissues) subject to a sinusoidally-varying magnetic gradient force. This dissertation describes the design and implementation of an MMOCT system composed of a novel combination of a line-field configuration with a supercontinuum light source and a faster MMOCT imaging scheme. The combination of the line illumination with a high-speed 2D camera and the low-noise, high-power supercontinuum light source produces the best combination of axial resolution, optical SNR, and imaging speed of any line-field-OCT (LFOCT) system to date. The performance of the LF-OCT system combined with the faster

magnet modulation scheme results in a LF-MMOCT system with a volumetric imaging speed comparable to that of the highest speed MMOCT system to date. High volumetric imaging speed is essential for the problem of endogenous magnetite detection, as is high magnetic sensitivity. The LF-MMOCT system is optimized to produce the best possible magnetic SNR at kilohertz framerates. We then demonstrate the detection of single magnetic point particles, measure the vibration amplitude produced by an external magnetic gradient force on each point particle, and compare that vibration amplitude to a theoretical value. The ability to image a single magnetic point particle with a high-resolution, high-sensitivity, and high-speed LF-MMOCT system provides a key proof of concept that this system may be used for endogenous magnetite detection.

Dedicated to my mom and dad

ACKNOWLEDGEMENTS

I would first like to thank my dad. This PhD project is the culmination of 20 years of hard work, good fortune, and a lot of support from my friends, family and teachers. None of it would have been possible without the help and support of my dad who worked hard to ensure I could get the best possible education. I would also like to thank my patient partner, Nirmaan, who has supported me throughout this entire PhD by doing everything from bringing me food when I was working late in lab to helping me print conference posters at the last minute. His unwavering confidence in me carried me through dark times when it seemed like my project would never be completed.

I also owe a huge debt of gratitude to Ana Doblas, my mentor and friend. Her help and advice has been as invaluable as her constant encouragement and whole-hearted support. I would never have gotten over the first hurdle in my project without Ana's help and the countless hours we spent aligning and re-aligning the LF-OCT system. I also could not have finished my project without the network of wonderful, smart women in my graduate program. Allison Hartman provided helpful insight into actually getting to the finish line and applying for jobs, and, just as importantly, made sure I took occasional breaks from lab. Allison began the tradition of women in physics gatherings and provided invaluable assistance in my graduate coursework via her website AlPaltheScienceGal. Casey Berger hosted women in physics gatherings that provided us a group of friends who understood the unique challenges and frustrations of being a woman in physics. She was also always ready with a great book recommendation or a new coffee house to try when I needed inspiration. Joule Othman and

Bethany Lanham Hill helped me through the first year of graduate course work by working through problem sets with me and making the first year fun in spite of the stress. I am so proud of and grateful to all of them.

I would also like to thank my friends Tyler Wilson, Laura Chuckray, and Sarah Eliza Berro. Tyler has shared in every high and low of this project with me from day one. She knows every silly mistake I have made in lab and every triumph. Without her commiseration and laughter, I probably would not have finished grad school. For the past ten years, Tyler, Laura, and Sarah Eliza have supported me throughout my entire physics education, and they have shared in and encouraged my love of physics. I feel very lucky to have friends like these.

Finally, I would like to thank my lab mates, past and present: Justin Sierchio who helped me understand optical aberrations and helped me apply for jobs, Lin Yang who helped me with LabVIEW coding and geometrical optics, Ruofei Bu who helped me with dissertation formatting, Ben Levy who helped me with numerous questions about hardware design and magnetic contrast, and Santosh Balakrishnan, Kelsey Oeler, and Hillel Price who were always available for OCT discussions. Of course, none of this would have been possible without the support of our lab head, Dr. Amy L. Oldenburg.

TABLE OF CONTENTS

LIST OF TABLES

LIST OF FIGURES

LIST OF ABBREVIATIONS

ALI	Air/liquid interface
AR	Anti-reflective
CBF	Ciliary beat frequency
CCD	Charge-coupled device
CMOS	Complimentary metal-oxide semiconductor
COPD	Chronic obstructive pulmonary disease
DFT	Discrete Fourier transform
FF-OCT	Full-field optical coherence tomography
FPN	Fixed pattern noise
FOV	Field of view
FWHM	Full-width half-maximum
GUI	Graphical user interface
hBE	Human bronchial epithelial
IFT	Inverse Fourier transform
IR	Infrared
LF-OCT	Line-field optical coherence tomography
MCOCT	Molecular contrast optical coherence tomography
MMOCT	Magneto-motive optical coherence tomography
MNP	Magnetic nano-particle
MRI	Magnetic resonance imaging
NA	Numerical aperture
NIR	Near Infrared

OCT	Optical coherence tomography
OPD	Optical path delay
OPL	Optical path length
PCL	Periciliary layer
PDMS	Polydimethylsiloxane
PSF	Point spread function
RIN	Relative intensity noise
SD-OCT	Spectral-domain optical coherence tomography
SNR	Signal-to-noise ratio
SPIO	Superparamagnetic iron oxides
STD	Standard deviation
TEM	Transmission electron microscopy

CHAPTER 1 - MOTIVATION

Optical Coherence Tomography (OCT) is a biological imaging modality developed in 1991 [1] as a way to perform "optical biopsies" [2] which could potentially replace the need for tissue excision or could help guide surgical biopsies. OCT produces cross-sectional images of biological tissue with a penetration depth of a few millimeters and a resolution of a few microns, placing it between microscopy and ultrasound on a size scale. Where microscopy can image at the cellular level, and ultrasound, among other biomedical imaging modalities, can image whole organs, OCT is uniquely suited for imaging at the size-scale between individual cells and organs: at the tissue scale. OCT performs cross-sectional imaging by detecting the magnitude and echo time delay of light backscattered from optically turbid media. Optically turbid means that the index of refraction of the material is spatially varying on the size-scale of the imaging wavelength. OCT can directly image various biological tissues such as skin, airways, and eyes. OCT can also be used for distinguishing features which have similar optical properties as their surroundings (*e.g.* index of refraction and scattering coefficient) if a contrast agent is used. The field of molecular contrast OCT (MCOCT) consists of the various methods of contrasting molecules or molecular processes that are otherwise indistinguishable from their surroundings. MCOCT methods include both direct methods wherein the contrast agent augments or attenuates the backscattered light and indirect methods wherein the contrast agent indirectly modulates the OCT signal [3].

One such contrast agent developed to be used with OCT is magnetic nanoparticles (MNP). By embedding sub-resolution, magnetic nanoparticles in the tissue being imaged, and

then applying a sinusoidally varying magnetic field, OCT can detect the resultant periodic phase shift produced by the deformation of the elastic, optically scattering medium mechanically coupled to the magnetic nanoparticles. This technique, known as Magneto-Motive OCT (MMOCT) was developed by Amy L. Oldenburg in 2005 initially as a form of MCOCT capable of imaging magnetically-labeled macrophage cells [4], and was later demonstrated *in vivo* to detect the uptake of magnetite nanoparticles in tadpole livers after the tadpoles had been immersed in a tank containing magnetic nanoparticles [5]. The first MMOCT imaging tracked the periodic change in the amplitude of the light back-scattered by the scattering medium, caused by the induced motion of magnetic nanoparticles mechanically coupled to it. The technique was improved upon by tracking the periodic change in the optical phase of the OCT signal, a much more sensitive measurement than merely tracking the amplitude [6–8]. After the initial period of development, that same MMOCT technique was used to image a wide variety of biological samples without significantly changing the imaging setup or the processing algorithm: rat mammary tumors *ex vivo* [7], *in vivo* mouse eye [9,10], blood clots in *ex vivo* porcine arteries with magnetically-labeled platelets [11,12], blood clots in *ex vivo* rabbit arteries with magnetic micro-spheres [13,14], and *in vivo* detection of targeted magnetic nano-particles in rat breast-cancer tumors [15].

In recent years, some attempts have been made to improve upon the basic MMOCT system design. These advances are composed of: a pulsed MMOCT system which enables imaging from a distance of 30 mm from the magnetic field source [16–18], adding a second magnetic field source to enable imaging in liquids [19], and finally the introduction of volumetric MMOCT imaging of tissue phantoms [20]. The original motivation for MMOCT was to use exogenous magnetic nanoparticles as contrast agents to image non-magnetic

properties of biological tissues (*e.g.* contrasting magnetically labeled platelets in blood clots). This dissertation investigates a novel MMOCT application: to image naturally occurring magnetic particles in biological tissues.

The ability to detect and spatially locate magnetic nanoparticles is of increasing interest to biologists who study geomagnetic navigation. Many species of animals (spanning multiple classes of animals including mammals, fish, birds, and reptiles) are known to sense the Earth's magnetic field and to use this information to navigate. One particularly puzzling example is studied by our collaborator in the Biology Department, Kenneth J. Lohmann: loggerhead turtles are able to navigate from their nesting grounds to the ocean upon first hatching, and they then travel thousands of miles through dark, seemingly featureless water in order to return years later to their original nesting grounds [21–23]. Their navigation is well correlated with perception of the Earth's magnetic field; however, the mechanism by which turtles sense the Earth's magnetic field remains a mystery.

There are three hypotheses currently established for potentially explaining sea turtles' magnetic perception: 1) electromagnetic induction, 2) chemical magnetoreception, and 3) magnetite [24,25]. For electromagnetic induction, the animal must have electroreceptors (known to occur in sharks) and must live in an electrically-conductive environment [26]. The chemical magnetoreception hypothesis rests on the idea that during the brief time that the spin of the unpaired electron of a free radical is precessing, external magnetic fields may affect the resultant spin state of the electron once transferred back to its donor molecule. It is unknown whether this process occurs in animals, but many of the best known radical-pair reactions begin with the absorption of light [27,28]. Because sea turtles travel deep underwater in the absence of light for much of their migration, this does not seem like a likely hypothesis for sea turtles'

magnetoreception. The third hypothesis is that biomineralized magnetite crystals (Fe_3O_4) are naturally occurring in some animals. These magnetic particles could physically rotate as the animal passes through a changing magnetic field. This hypothesis is supported by certain species of anaerobic bacteria that are known to contain chains of Fe_3O_4 crystals and to use these chains of paramagnetic crystals to orient themselves in the absence of light [29]. Because sea turtles also spend some of their time during migration deep under water (in the absence of light) like the magnetotactic bacteria and because they are not known to contain electroreceptors, the magnetite is the most promising theory to explain how animals like sea turtles are able to sense the Earth's magnetic field. To test this hypothesis, we need the ability to detect and spatially locate potential magnetoreceptors embedded somewhere within the body of a sea turtle. Because sea turtles are endangered, the search would only be conducted on excised tissue taken from naturally deceased animals.

Endogenous magnetite detection poses several unique challenges. For one, the magnetoreceptors are potentially isolated, single magnetite crystals. The size of the magnetite crystals found in the bacteria is ~50 nm in diameter, and they form single chains with lengths of ~ 1 μm [29]. The small amount of Fe contained in such potentially small magnetite crystals which may be present in a sparse distribution requires high magnetic sensitivity to be able to detect the induced periodic phase shift above the phase noise of the light coherently backscattered from one resolution volume. All previous MMOCT work has involved imaging exogenous magnetic nanoparticles. Significantly, because a known concentration of magnetic particles is added, that concentration can be adjusted to produce a deformation in the surrounding tissue that is sufficiently large to produce a detectable phase shift in the backscattered light. Additionally, the size of the exogenous magnetic contrast agents can be adjusted to some degree

(depending on the constraints of the application and commercial availability). In contrast, the concentration and size of endogenous magnetite is fixed so we have to design an MMOCT system that is sensitive to single magnetic particles with diameters at or below the OCT system resolution.

In addition to the requirement of high magnetic sensitivity, we require a high volumetric throughput so that large quantities of tissue can be imaged in a reasonable amount of time because the location of the magnetoreceptors is not known *a priori* and because sea turtles are large compared to the size of animals and samples previously imaged with MMOCT. MMOCT has been used to image whole, small animals (tadpoles and small fish) or small regions of larger animals. Although microscopy is able to resolve nanoparticles with a diameter of 50 nm, it may require staining to contrast the Fe and microscopy has such limited throughput that it is not a practical technique to use for this "needle in a haystack" problem. Conversely, Magnetic Resonance Imaging (MRI) can image large bodies relatively quickly and is very sensitive to small amounts of Fe, but the spatial resolution is too coarse to allow the detection of single magnetic nanoparticles with diameters of ~50 nm when averaged together with the non-magnetic tissue in the rest of the relatively large resolution volume. MMOCT is an imaging modality uniquely suited for addressing the challenges of endogenous magnetite detection in large animals because the spatial resolution of the OCT system is on the order of ~1 μm but with a much higher throughput compared to microscopy.

The figures of merit of a system capable of endogenous magnetite detection are: 1) ability to detect and spatially locate a single magnetic particle and 2) high volumetric throughput. In addition to these two requirements, the ability of an MMOCT system to detect single magnetic nanoparticles is also dependent on the sample properties, such as the Young's modulus, the

optical scattering properties (which in turn affect the SNR of the recorded images), and any phase-noise contributed by the sample (*e.g.* due to sample motion during imaging). In this dissertation, we focus only on the imaging system's properties as these are more readily controlled. The sensitivity of an MMOCT system to single magnetic particles is determined by the OCT system resolution, the optical signal-to-noise ratio (SNR), and the ability to deliver sufficient magnetic force to the particle. We note that here and in the rest of this dissertation whenever we refer to "resolution" we refer to the spatial resolution of the OCT system, not the MMOCT resolution (*i.e*. the ability to resolve two closely spaced magnetic particles). Similarly, "SNR" refers to the optical SNR of the OCT system, unless explicitly stated otherwise (*e.g.* "magnetic SNR"). For the second criterion, high volumetric throughput, we require a system with a large field of view (FOV) and a fast framerate (again, this refers to the OCT system framerate and not the MMOCT system framerate). OCT systems face fundamental tradeoffs between these two aims: to have a fine resolution, the FOV must also shrink, and because SNR is proportional to exposure time, faster framerates incur SNR losses. This is especially true of conventional OCT systems, which employ a point-scanning method to mechanically scan a focused spot across the entire transverse extent of one 2D cross-sectional image. In this case, the wider the FOV, the lower the framerate. One way to relax the tradeoff in speed and sensitivity is to employ a line-field configuration rather than a point-scanning one.

In a line-field OCT (LF-OCT) system, the light is focused into a line on the sample so that an entire 2D image is collected at once with no mechanical scanning [30]. If you can provide sufficient power to the sample, you can thus increase the framerate while maintaining a high SNR. Traditional supercontinuum (SC) sources which are able to provide this higher power have suffered from noise problems which limited the SNR achievable with them. However,

recent improvements in SC sources have reduced the noise level by using higher repetition rates and minimizing pulse-to-pulse variation [31]. By combining the line-field configuration with a SC light source and an optical design which carefully balances the need for fine resolution with a large FOV, we have designed an MMOCT system optimized for single magnetic particle detection.

This Ph.D. dissertation is organized as follows. Chapter 2 of this dissertation covers the optical design, implementation, and characterization of our LF-OCT system employing a SC source. To demonstrate the combination of high speed, high sensitivity, and high resolution, images recorded of beating cilia on *in vitro* human bronchial epithelial cells are shown. Chapter 3 is devoted to the design and implementation of the hardware and software necessary to convert the LF-OCT system to the LF-MMOCT system. This chapter also covers the theory of MMOCT and the characterization of the system hardware. In Chapter 4, the development of a new MMOCT imaging scheme, called frame-by-frame magnet modulation, is introduced, first on a point-scanning MMOCT system and then on the LF-MMOCT system. The LF-MMOCT system is then optimized for magnetic sensitivity and is used to image single magnetic micro-particles dispersed in an elastic, optically scattering medium. The vibration amplitude induced by the magnetic gradient force from an electromagnet is compared with the theoretical values. Chapter 5 summarizes the contributions of this dissertation and discusses future areas of investigation.

CHAPTER 2 - DEVELOPMENT OF LINE FIELD-SD OCT SYSTEM

As previously mentioned, OCT is a well-established biomedical imaging modality that produces 2D cross-sectional images from optically turbid media. The principle of OCT is low coherence interferometry [32] (coherence, in this case, referring to temporal coherence). The most widely used form of OCT is Spectral-Domain OCT (SD-OCT). In this chapter, I will give only a brief overview of SD-OCT since this theory has been extensively covered in previous works [33–35]. Next, I will discuss how SD-OCT theory is applied to line-field systems. By examining expressions for SNR in traditional SD-OCT and in LF-OCT, I will demonstrate why we are able to relax the fundamental tradeoff in speed and sensitivity inherent in SD-OCT systems by using the line-field configuration.

In Section 3, I will describe the optical design considerations for a LF-OCT system, the choice of optical elements for Version 1 of our LF-OCT system, the alignment procedure and the characterization of that system. Then I will discuss how the performance of Version 1 of the LF-OCT system informed the changes we made in the optical design to produce Version 2. Lastly, in Section 4, the LF-OCT system's high-speed, high sensitivity, and high resolution are demonstrated by imaging beating cilia on human bronchial epithelial (hBE) cells *in vitro*.

2.1 SD-OCT theory

OCT is an interferometric technique. Interferometry describes the splitting of light into two paths and the subsequent recombination of that light in an interferogram. When the light is recombined at the output of the interferometer, the two beams interfere either constructively or

destructively depending on the optical path delay (OPD) of the two beams. Importantly, the phenomenon of interference can only occur if the OPD is within the coherence length of the light source. Temporal coherence is analogous to the "memory" of the light. If the OPD between the beams is too large, then it is as if they no longer have any memory of the other when they recombine, and they will not interfere. If, however, the OPD is less than the coherence length, then the two beams retain some "memory" of each other and will interfere when recombined. The coherence length, l_c, (defined as the length over which the magnitude of the light source's temporal coherence function has dropped to $1/e$) is given by equation 2-1:

$$l_c = \frac{{\lambda_0}^2}{\pi \Delta \lambda} \tag{2-1}$$

where λ_0 is the center wavelength, $\Delta\lambda$ is the full width at half maximum (FWHM) of the source power spectrum, assuming a Gaussian emission spectrum. From this equation, it becomes clear that for a monochromatic source, the bandwidth is infinitely small so that the coherence length is infinite. This is why the temporal coherence is related to how monochromatic the light is; broadband light is by definition light with low temporal coherence. OCT is a form of low-coherence interferometry since it employs broadband light.

Commonly, SD-OCT systems use a Michelson interferometer: the incident polychromatic (meaning broadband spectrum) plane wave, with an electric field that can be expressed as $E_{inc} = s(k, \omega)e^{i(kz-\omega t)}$, is split into a reference beam, $E_R(k, \omega)$ and a sample beam, $E_S(k, \omega)$ (see Figure 2-1). In this expression, $s(k, \omega)$ is the electric field amplitude as a function of the spatial and temporal frequencies of each spectral component characterized by a wavelength, λ, and a frequency, v; the spatial and temporal frequencies are related to the wavenumber $k = 2\pi/\lambda$ and the angular frequency $\omega = 2\pi v$, respectively.

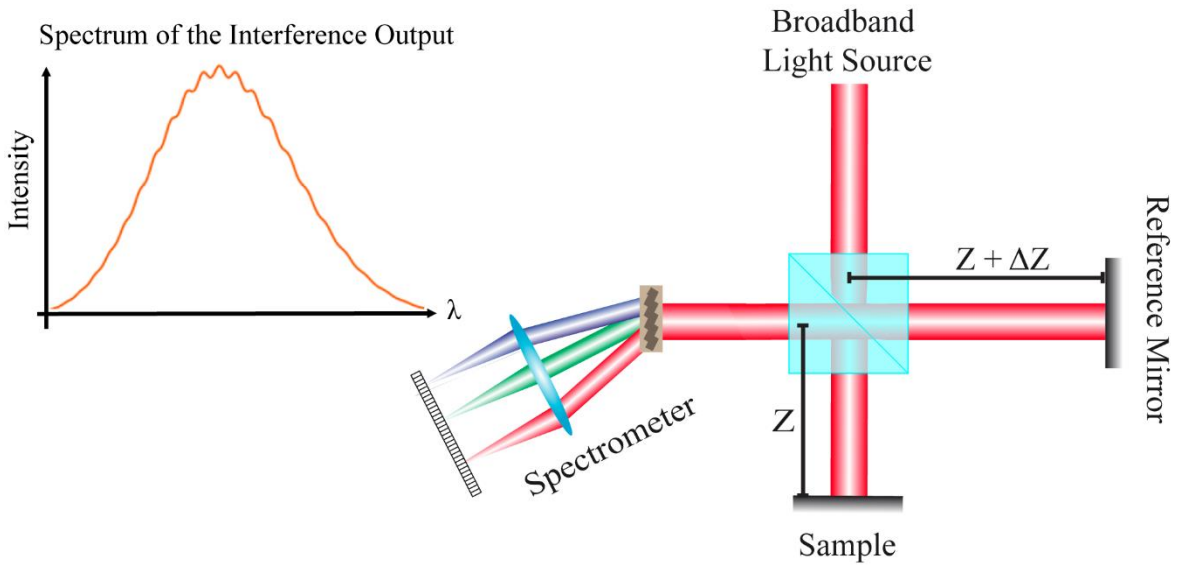

Figure 2-1 Schematic diagram of SD-OCT.
Schematic diagram of basic SD-OCT setup consisting of a broadband light source, a Michelson interferometer and a spectrometer. If the OPD between the two arms is within one coherence length, the recombined light exhibits interference. The recorded spectrum of the interference output carries a spectral modulation as a function of the OPD.

The light exiting the beam splitter, after having been reflected from the reference arm mirror and the scattering object in the sample arm, is recorded by a spectrometer composed of a diffraction grating and a camera. The camera records the intensity of the combined light, I_D, which is proportional to the square of the total field:

$$I_D(k,\omega) = \frac{\rho}{2}\left\langle \left| E_R + E_S \right|^2 \right\rangle \tag{2-2}$$

where ρ is the responsivity of the detector, the factor of ½ accounts for the power lost by passing through a 50:50 beam splitter, and the angular brackets denote averaging over the response time of the detector. The polychromatic plane waves in the reference and sample arms are reflected or backscattered by the reference mirror and the scatterers in the sample arm, respectively. The reference arm mirror is characterized by an electric field reflectivity, r_R, and the distance from the beam splitter to the reference mirror, z_R. Because optical power is proportional to the absolute

square of the complex field amplitude, the power reflectivity, R_R, is given by $R_R = |r_R|^2$. Likewise, the scatterers in the sample arm are characterized by their field reflectivities, r_{Si}, power reflectivities, R_{Si}, and distance from the beam splitter, z_{Sj}. Following the derivation in Ref [32], we can now write out a more explicit form of equation 2-2, assuming a series of N discrete, real, delta-function reflections from the sample:

$$I_D(k,\omega) = \frac{\rho}{2}\left\langle \left| \frac{s(k,\omega)}{\sqrt{2}} r_R \, e^{i(2kz_R - \omega t)} + \frac{s(k,\omega)}{\sqrt{2}} \sum_{j=1}^{N} r_{Sj} \, e^{i\left[2k\left(z_{SS} + n(z_{Sj} - z_{SS})\right) - \omega t\right]} \right|^2 \right\rangle \qquad (2\text{-}3)$$

where n is the refractive index of the sample, and z_{SS} is the distance from the beam splitter to the sample surface. Expanding the squared term in equation 2-3, we can write out the three terms that contribute to the detected intensity:

$$I_D(k) = \frac{\rho}{4}\left[S(k)\left(R_R + \sum_{j=1}^{N} R_{Sj} \right) \right]$$

$$+ \frac{\rho}{4}\left[S(k)\left(\sum_{j=1}^{N} \sqrt{R_R R_{Sj}} \left(e^{i2k\left(z_R - z_{SS} - n(z_{Sj} - z_{SS})\right)} + e^{-i2k\left(z_R - z_{SS} - n(z_{Sj} - z_{SS})\right)} \right) \right) \right]$$

$$+ \frac{\rho}{4}\left[S(k)\left(\sum_{m=1}^{N} \sum_{j \neq m=1}^{N} \sqrt{R_{Sm} R_{Sj}} \left(e^{i2kn(z_{Sm} - z_{Sj})} + e^{-i2kn(z_{Sm} - z_{Sj})} \right) \right) \right] \qquad (2\text{-}4)$$

In this expression, $\left\langle |s(k,\omega)|^2 \right\rangle$ is written as $S(k)$, the power spectral density of the light source (*i.e.* the optical power per frequency interval). Note that the detected intensity is now only a function of spatial frequency, k, because the time-dependent terms cancel out when the absolute square is taken. This makes sense from a practical interpretation as well because the optical frequency, ν, is much too fast to be sampled during the response time of the detectors typically

used in OCT. The first term has no dependence on the location, z_S, of the scatterers. This is usually called the "DC" term because it has no modulation in k, and it can be subtracted out of the OCT signal in post-processing. Generally, OCT images are collected with the sample arm and reference arm powers adjusted such that R_R is much larger than R_S (and biological tissues are generally weakly scattering with $R_S << 1$). In this case, the DC term dominates I_D. The second term is the cross-term. This is the term that contains useful information about the location of scatterers within an image because this term depends on the OPD between each scatterer and the fixed reference arm. For every scatterer in the sample arm, there is a corresponding contribution to the cross-term. The third term is called the auto-correlation term because it comes from the interference of light backscattered from scatterers at different depths in the sample.

The goal of OCT is to reconstruct the field reflectivity of the sample as a function of depth within the sample, $r_S(z)$. This reflectivity profile is what constitutes the structural images produced by OCT. To reconstruct the field reflectivity profile of the sample from the recorded spectral intensity, we make use of the Wiener-Khintchin theorem which says that the power spectral density is equal to the Fourier transform of the temporal autocorrelation of the electric field. We have recorded the spectrum using a spectrometer. This spectrum carries a spectral modulation with a period (in wavenumber) given by 2π divided by the OPD between the sample and reference arms, $2\pi/2[z_R - z_{SS} - n(z_{sj} - z_{SS})]$; each scatterer j at some depth z_{Sj} is characterized by its own spectral modulation frequency, with an amplitude scaled by its reflectivity r_{Sj}, and the modulated spectrum is a superposition of all the modulation frequencies. Now, we take an inverse Fourier transform (IFT) of $I_D(k)$ from equation 2-4 to reconstruct the field reflectivity profile of the sample as a function of depth, z, (our ultimate objective) convolved with the coherence function of the light source, IFT($S(k)$):

$$I_D(z) = \frac{\rho}{8}\left[IFT(S(k))\left(R_R + \sum_{j=1}^{N} R_{Sj} \right)\right]$$

$$+\frac{\rho}{4}\left[IFT(S(k)) \otimes \left(\sum_{j=1}^{N} \sqrt{R_R R_{Sj}} \left(\delta(z+\Delta z_j) + \delta(z-\Delta z_j) \right) \right)\right]$$

$$+\frac{\rho}{8}\left[IFT(S(k)) \otimes \left(\sum_{m=1}^{N} \sum_{j\neq m=1}^{N} \sqrt{R_{Sm} R_{Sj}} \left(\delta(z+\Delta z_{Sjm}) + \delta(z-\Delta z_{Sjm}) \right) \right)\right] \qquad (2\text{-}5)$$

where $\Delta z_{sjm} = 2n(z_{Sj}\text{-}z_{Sm})$ is the optical path delay between two scatterers located at depths z_{Sj} and z_{Sm} within the sample and $\Delta z_j = 2(z_R - z_{SS} - n(z_{Sj} - z_{SS}))$ is the optical path delay between the reference mirror and a scatterer located at a depth z_{Sj} in the sample.

Recall our initial assumption that the scatterers were a series of real, delta functions. We have now reconstructed these delta functions using the fact that the Fourier transform of a cosine function (re-writing the exponentials in equation 2-4 in terms of a cosine via Euler's rule) is a pair of delta functions. However, these delta functions are now broadened due to the convolution with the coherence function of the light source, IFT($S(k)$). Assuming a Gaussian emission spectrum both for convenience and because most light sources used in OCT typically have approximately Gaussian spectra, with bandwidth Δk, and wavenumber of center wavelength, k_0, we can write the coherence function of the light source as follows:

$$\gamma(z) = IFT(S(k)) = \frac{1}{\sqrt{\pi}} e^{-(z\Delta k)^2} e^{-(izk_0)} \qquad (2\text{-}6)$$

The complex exponential in equation 2-6 will drop out if we take the absolute value of the inverse Fourier transform (as in Figure 2-2), and is sometimes excluded from expressions of $I_D(z)$. By convolving the coherence function with the delta functions, we reconstruct the sample's reflectivity profile in depth, as shown in Figure 2-2, where we have subtracted the reference term

(the R_R component of the DC term in equation 2-5) and assumed that the autocorrelation terms are small enough to be negligible. The reference term, $I_D(k)_{ref}$, is subtracted by recording one or more images with nothing in the sample arm, averaging those frames (if applicable), and then subtracting this reference frame from each spectral interferogram. The assumption that the autocorrelation terms are small is justified by the way that the power is adjusted in the reference and the sample arms. Typically, the reflectivity of scatterers in the (biological) samples, r_S, is small compared to the reflectivity of the reference arm mirror, r_R, so that R_R dominates the detected intensity, $I_D(z)$. And, in fact, the ratio of reference to sample arm power is an important consideration for setting up an OCT system to image a particular sample; the sample must be illuminated with sufficient power such that the scatterers are detectable above the noise of the system without using so much sample power that the autocorrelation terms become problematic. The reference arm power is then adjusted so that the maximum amount of light is collected by the sensor without saturating it. A simplified expression for the reference-subtracted OCT signal is given in equation 2-7:

$$S_{OCT}(z) \approx \frac{\rho}{4}\left[\sum_{j=1}^{N}\sqrt{R_R R_{Sj}}\left(e^{-\left(z+\Delta z_j\right)^2\Delta k^2}e^{-i\left(z+\Delta z_j\right)k_0} + e^{-\left(z-\Delta z_j\right)^2\Delta k^2}e^{-i\left(z-\Delta z_j\right)k_0}\right)\right] \quad (2\text{-}7)$$

The two sets of exponentials in equation 2-7 represent an important aspect of OCT: a scatterer located at an OPD $+\Delta z$ from z_R and a scatterer located $-\Delta z$ from z_R will produce identical OCT signals. In order to avoid confusion or wrapping effects in the structural OCT image, we choose to set up the sample arm such that all scatterers are on the same side of the plane $z = z_R$. The mirror image produced in the region $z_R - \Delta z$ is called the conjugate image and is illustrated in Figure 2-12. Equation 2-7 also illustrates that the convolution of the coherence function with the delta function of the scatterer serves to broaden the delta function in our

reconstruction. In fact, the delta functions are all broadened by the coherence length of the coherence function. To better resolve the peaks in $r_S(z_s)$, a light source with a shorter coherence length should be used; this is why broadband sources are used for high-resolution imaging in spectrometer-based OCT. Each depth profile is called an A-line. If the beam in the sample arm is scanned across the surface of the sample, then we can build up an array of depth profiles and thereby create one 2D cross-sectional image, called a B-mode image.

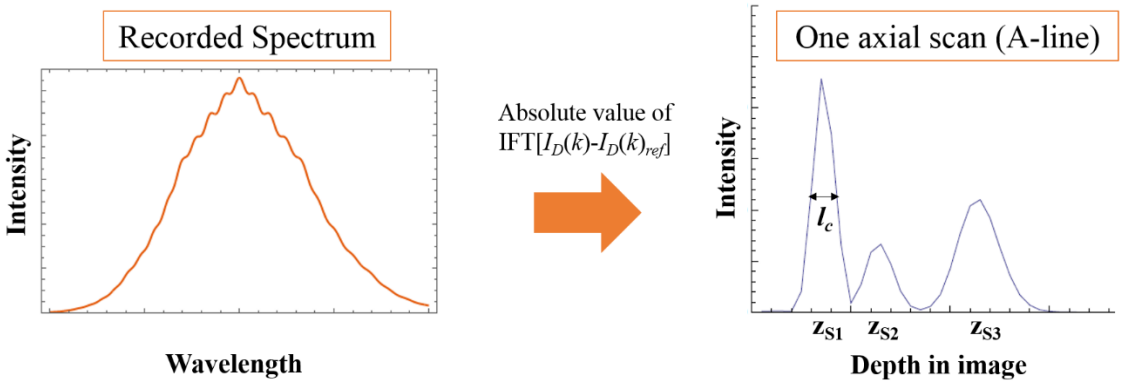

Figure 2-2 Illustration of A-line reconstruction in SD-OCT.
The spectral interferogram of the light recombined from the reference and sample arms carries a spectral modulation as a function of OPD between the reference mirror and each scatterer in the sample. Taking the absolute value of the IFT yields a reflectivity profile for one transverse location on the sample surface; each depth profile is called an A-line.

The axial resolution, Δz, is then given by the coherence length of the light source, and is typically defined in terms of the FWHM, rather than the $1/e$ width as in equation 2-1, of the temporal coherence function (the temporal autocorrelation function of the electric field of the light source). For a Gaussian emission spectrum, the FWHM is given by:

$$\Delta z = \frac{2\ln 2}{n\pi}\frac{\lambda_0^2}{\Delta\lambda} \tag{2-8}$$

where n is the refractive index of the sample and λ_0 and $\Delta\lambda$ are the source center wavelength and bandwidth, respectively. Importantly, the axial resolution in OCT is completely decoupled from the focusing optics, so a high axial resolution can be achieved independently of the sample arm objective lens used.

In traditional SD-OCT systems, the light is focused into a spot on the sample surface. The transverse resolution is given by the FWHM of the Gaussian intensity profile as a function of radial distance from the optical axis. For a Gaussian beam, assuming the incident beam is collimated so that the focused beam waist occurs a distance f away from the lens and that the divergence angle of the focused Gaussian beam is small ($2\theta \sim d/f$), the transverse resolution, Δx, is given by:

$$\Delta x = \frac{4\lambda_0 f}{\pi d} \tag{2-9}$$

where f is the focal length of the sample arm objective lens and d is the beam diameter on that lens [36]. This is called the diffraction-limited spot size, and is the same expression used in microscopy.

The axial ranging capabilities of OCT and the relatively large imaging depth are the primary differences between OCT and confocal microscopy. Several factors influence the maximum depth that can be imaged with OCT. The first major consideration is the limited spectral resolution of the spectrometer, the effect of which can be modeled by an optical SNR fall-off in depth. The depth at which the detected intensity falls off by ½ can be written:

$$Z_{1/2} = \frac{\ln(2)\lambda_0^{\,2}}{\pi\delta_r\lambda} \tag{2-10}$$

where $\partial_r\lambda$ is the spectral resolution of the spectrometer. The second major consideration for the maximum imaging depth in SD-OCT is how the spectral interferogram is sampled. Although the spectrum is continuous, it is sampled by a finite number of pixels. Recall that each A-line (depth-dependent reflectivity profile) is obtained by taking a Fourier transform of the modulated spectrum. The maximum depth that can be imaged is limited by the Nyquist sampling theorem, which gives the number of discrete samples needed to capture all the information contained in a continuous signal of finite bandwidth. The bandwidth of the broadband light source (after being spread by a diffraction grating) is sampled by N pixels, giving a wavelength sampling $\delta_s\lambda = \Delta\lambda/N$. We can write the maximum, one-sided imaging depth achievable by a spectrometer in terms of the bandwidth captured by the spectrometer, $\Delta\lambda$, the number of pixels, N, and the sample's refractive index, n:

$$Z_{\max} = \frac{N\lambda_0^{\,2}}{4n\Delta\lambda} \tag{2-11}$$

Both $Z_{1/2}$ and Z_{max} can be limiting factors for the practical imaging depth achievable by an OCT system; however, Z_{max} is typically the figure of merit used in SD-OCT publications as the imaging depth. One reason for this is that while the number of pixels is fixed by the sensor used, the sensitivity roll-off dictated by equation 2-10 can be mitigated by appropriately designing the spectrometer focusing optics, as it has been shown that the spot size of the beam on the spectrometer greatly affects the roll-off [37,38]. As long as the spot size is smaller than the width of two pixels, the roll-off will not be the limiting factor controlling the practical imaging depth [37], so the expression in equation 2-11 is the one typically used to estimate the imaging depth achievable for a given SDOCT system. In practice, the imaging depth is highly sample dependent and is often limited by the attenuation in depth from highly scattering samples. For the

NIR region, the imaging depth achievable in most biological tissues is limited to ~ 2mm by the scattering properties of the tissue itself [35]: scattering in biological tissues is primarily in the forward direction [39], which limits the number of mean free paths that can be imaged in depth due to multiple scattering, and sub-resolution sample heterogeneities give rise to further multiple scattering events, which is ultimately the most limiting factor for OCT imaging depth [40].

The final key parameter governing the performance of an SD-OCT system is the signal-to-noise ratio (SNR), which we use interchangeably with "sensitivity" throughout this dissertation. The SNR is a measure of the smallest amount of back-scattered light from a single coherence volume that can be distinguished from the background noise. For low-coherence interferometry, the SNR is defined as the ratio of the mean-squared OCT signal (equation 2-7) and the variance of the noise [31,41]:

$$SNR \equiv \frac{\left\langle S_{OCT}{}^{2} \right\rangle}{\sigma^{2}{}_{noise}} \tag{2-12}$$

From equation 2-2, the mean-squared OCT signal is proportional to the absolute square of the electric fields E_R and E_S. Because optical power is proportional to the square of the field, the mean-squared OCT signal is proportional to the product of the sample arm power and the reference arm power, $P_R \cdot P_S$. The noise, σ_{noise}^2, is given by the variance of the mean-squared OCT signal in regions of low backscattering and can be classified into three categories:

$$\sigma^{2}{}_{noise} = \sigma^{2}{}_{\mathrm{det}ector} + \sigma^{2}{}_{shot} + \sigma^{2}{}_{excess} \tag{2-13}$$

There are various ways to write the exact expressions for each term in equation 2-13, depending in part upon whether the light source follows Bose-Einstein or Poisson statistics and whether your detector is a charge-coupled device (CCD) or a complimentary metal-oxide

semiconductor (CMOS) sensor [42]. However, the most important consideration for this dissertation is the dependence on the power. The detector noise, $\sigma^2_{detector}$, has multiple components, most of which boil down to random fluctuations in the sensor electronics caused by thermal noise [41,43,44]. The detector noise is independent of the reference arm power. Shot noise, σ^2_{shot}, is a result of the quantum mechanical nature of light and the Heisenberg uncertainty principle. Shot noise is proportional to the reference power (recalling our assumption that the power exiting the reference arm is much greater than that of the sample arm) [42,43,45,46]. The third term, σ^2_{excess}, is photon excess noise caused by photon bunching. The exact form depends on the light source used but is proportional to the square of the reference arm power [47]. In the shot-noise limited regime (*i.e.* without photon excess noise), the SNR in decibels can be written:

$$SNR = 10 * Log_{10}\left(\frac{2\eta P_{Aline} T_{Aline}}{h\nu}\right) \tag{2-14}$$

where η is the quantum efficiency of the detector, P_{Aline} is the power in a single A-line incident on the sample, T is the exposure time of the detector for a single A-line, and $h\nu$ is the energy of the center wavelength of the light source [41]. For flying-spot OCT, the power per A-line is the total power in the sample arm because the entire beam is scanned over each transverse position, and the exposure time is 1/linerate of a linescan camera.

The dependence on the exposure time of the camera in this equation expresses a fundamental tradeoff in SD-OCT between imaging speed and sensitivity. The fastest line rate that can be used to collect A-lines is given by 1/T. For faster imaging, the exposure time must be shortened and the SNR is proportionally lowered as fewer photons are collected during a shorter pixel integration time.

The quantum efficiency of the detector, η, is determined by the choice of camera and the energy of the center wavelength is determined by light source. For a given SD-OCT system, these are fixed parameters. This means that for a given line rate, the only way to improve the SNR is to increase the sample power. However, the sample power cannot be arbitrarily increased without bound. For example, every light source has a maximum power output, and for typical broadband light sources used in SD-OCT, the maximum power output is a few hundred mW. More importantly, because OCT is a biomedical imaging modality, safety standards must be taken into consideration. For continuous-wave laser illumination of biological tissues, the figure of merit for damage thresholds is the peak irradiance of the light (*i.e.* the maximum power per unit area illuminated by the laser) [48]. For typical SD-OCT systems, the light at the sample is focused into a spot at the surface of the sample. Because the illuminated area is so small, the maximum power that can safely be used is limited.

One way to relax the fundamental tradeoff in speed and sensitivity inherent in SD-OCT while maintaining a safe intensity is to parallelize the detection. Two methods currently employed for detection parallelization are full-field time-domain OCT (most commonly called full-field OCT, or FFOCT) and line-field spectral-domain OCT (LFOCT). FFOCT produces *en face* images in the *X*-*Y* plane by illuminating the full 2D field of view on the sample surface with a low-coherent light source and detecting the back-scattered light on a 2D camera [49]. This technique achieves ultrahigh transverse resolution (0.7 μm reported in Ref [49]) and can produce volumetric imaging by mechanically scanning the sample in *Z*. While video-rate volumetric imaging has been achieved with FFOCT [49], the technique suffers (by comparison to spectral-domain OCT) from low sensitivity and from transverse resolution degradation due to crosstalk (from multiply-scattered light) [33]. An alternative method for parallelization of OCT

detection is line-field OCT, a spectrometer-based technique that offers sensitivity advantages with slightly more coarse transverse resolutions.

2.2 LF-OCT theory

Line-field OCT (LF-OCT) is a form of OCT in which the light in the sample arm is focused into a line rather than a spot at the surface of the sample. The spectral interferogram is then recorded on a 2D pixel array rather than a line scan camera, with one dimension being the wavelength and one dimension of the pixel array recording the transverse position. In this way, all A-lines are recorded simultaneously and we can reconstruct a 2D B-mode image from one camera frame without the need for mechanical scanning. These differences are illustrated in Figure 2-3.

It is immediately obvious that the line-field configuration presents a factor of N improvement in speed (N being the number of transverse A-lines recorded in a B-mode) because N A-lines can now be recorded during the same exposure time, T, that previously each A-line required. Additionally, because the sample power is spread across many A-lines, a higher total sample power can be used without damaging the tissue. This means that we can re-write the expression for SNR from equation 2-14 with a total sample power P_S that is N times higher than the power per A-line, P_{Aline}:

$$SNR_{LF} = 10 * Log_{10}\left(\frac{2\eta P_{Aline} NT}{h\nu}\right) \tag{2-15}$$

A higher total sample power can be used to achieve comparable SNR while maintaining a low intensity on the sample and with the factor of N improvement in speed [50], with the caveat that

photothermal heating has not been well characterized yet for line-field systems; the heat dissipation may be less effective in a light-sheet geometry than in point-scanning systems.

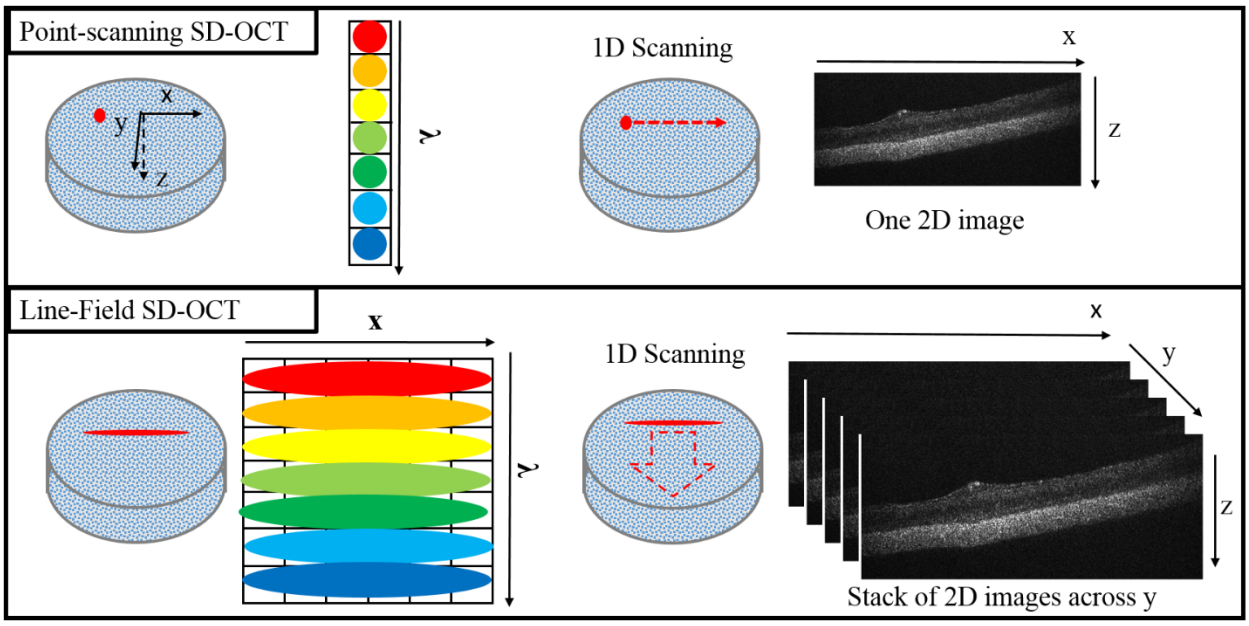

Figure 2-3 Schematic diagram of LF-OCT vs. point-scanning OCT.
Top panel: point-scanning SD-OCT employs a mechanically scanned focal spot at the sample and a 1D line-scan camera. Mechanical scanning is required to produce each 2D B-mode image. Bottom panel: line-field SD-OCT employs a line illumination at the sample and a 2D pixel area-scan camera so that a 2D B-mode image is formed without any mechanical scanning.

Related to the optical SNR is the phase noise of the optical imaging system. The phase noise is a measure of how constant the optical phase is over time when imaging a stationary object. The optical phase difference between light back-scattered from the reference mirror and an object in the sample arm is related to the OPD, $2n\Delta z$, according to $\Delta\theta = 2nk\Delta z$, where n is the index of refraction of the sample medium and k is the wavenumber. Therefore, a stationary object would ideally have a completely constant optical phase over time. However, every OCT system is subject to phase noise. The theoretical expression of phase noise for a shot-noise limited system can be found in Ref [51]; however, the more practical and easy to measure

quantity (which is the measure of phase stability typically used in the literature) is the phase resolution, $\delta\theta$ [51,52]. The phase resolution is considered the smallest phase change that can be reliably detected by a given system, and it is related to the SNR as follows [52]:

$$\delta\theta = \sqrt{\frac{1}{SNR(P_S, T, R_s)}} \tag{2-16}$$

The dependence of the SNR on the total sample power, exposure time, and reflectivity of the scatterer is shown. (R_s assumed to be 1 in equation 2-15, as this value is typically measured from mirrors and other nearly perfect reflectors.) The associated uncertainty in the displacement of a scatterer is then given by:

$$\delta z = \frac{\lambda_0}{4n\pi}\delta\theta \tag{2-17}$$

From Figure 2-3, it is also clear that the focusing of the beam onto the sensor in the *X* dimension is different in point-scanning and line-field OCT. In point-scanning OCT, the resolution in both *X* and *Y* is given by the same expression for the beam waist of a Gaussian beam, equation 2-9. This expression is the same for the out-of-plane resolution, Δy, in LFOCT. However, the in-plane transverse resolution, Δx, is determined by the ability of the collection optics (the series of lenses downstream from the sample) to focus light scattered by a point-particle onto the sensor. A more detailed explanation of how to calculate Δx requires an understanding of the LFOCT system setup, so it is reserved for after a description of the collection optics is given at the end of Section 2.3.1. The expressions for axial resolution and imaging depth remain the same for LFOCT systems.

In summary, for a line-field configuration, the equations governing performance are nearly all the same with an exception for the in-plane transverse resolution and for the fact that

the sample power is now spread across all A-lines so there is up to a factor of *N* improvement to speed. This means that if light sources exist which offer higher power over the wavelength ranges typically used in OCT, line-field OCT can offer a higher speed with a comparable SNR, thereby relaxing the tradeoff in speed and sensitivity.

Supercontinuum (SC) light sources are promising for high-power, broadband light sources for LF-OCT. A nonlinear optical process involving a photonic crystal fiber produces an ultrabroad bandwidth spectrum with more power than conventional OCT light sources. Historically, SC sources have been very noisy, making them unsuitable for OCT imaging because of the loss of SNR [53,54]. SC sources suffered from excess photon noise, meaning that they could not be operated in the shot-noise limited regime. In the shot-noise limited case, the SNR can be increased by increasing the power incident on the sample. When excess photon noise dominates, increasing the sample power does not result in increased SNR. However, recent advances in SC technology have produced lower noise sources suitable for OCT. In 2014, Brown *et al* demonstrated that a SC source from NKT Photonics with a repetition rate of 78 MHz could be operated in the shot-noise limited regime [31]. This new generation of SC sources uses a higher repetition rate (with some SC sources having rep rates of >300 MHz compared to older generation SC sources with repetition rates of 40 MHz [31]) and with less pulse-to-pulse variability to achieve lower noise. (In particular, NKT Photonics has developed a line of SC sources designed to be used specifically with OCT, and these are called their “low noise” systems, with some proprietary design that enables them to achieve better SNR than past generations.) These sources produce light over a very broad range: 400-2400 nm, covering the entire range of wavelengths commonly used in OCT and have output powers from ~2-20 Watts,

significantly more power than the super luminescent diodes and femtosecond lasers typically used in OCT.

2.3 Optical Design of a LF-OCT System

2.3.1 Optical Element Selection

The key optical element for LF-OCT systems is the cylindrical lens. Unlike spherical lenses which focus light into a circular spot by focusing in both planes orthogonal to the optical axis (referred to as the *X* and *Y* planes throughout this chapter), a cylindrical lens focuses a collimated input beam in only one transverse plane of the optical axis while the beam remains collimated in the other transverse plane. This produces a line illumination at the focal plane of the lens. The length of the line illumination is characterized by the 1/*e* fall-off in intensity of the Gaussian irradiance profile.

The introduction of the cylindrical lens adds a significant degree of complexity to the optical design of an OCT system, primarily due to the fact that 1) there are now twice as many design parameters to consider because the two transverse planes must be treated separately, and 2) the beam must now be significantly enlarged compared to the beam diameters typically used in OCT systems because the transverse FOV (*i.e.* the size of the line illumination at the sample) is determined by the collimated beam diameter (in the plane defined as *X* in Figure 2-3) output by the lens immediately before the sample. (This is different from point-scanning SD-OCT systems where the desired FOV is set by the sweep range of the mechanically scanned focused spot.) A large beam diameter is also desirable in LFOCT for achieving a fine transverse resolution, and that is true of both point-scanning and line-field systems. Working with a larger beam diameter means having to consider the beam diameter at every element because the

possibility of beam clipping on an optical element is high. Further, after passing through the cylindrical lens, the beam has a different diameter in the two transverse planes, *X* and *Y*, thus doubling the number of parameters that must be considered.

To begin any design, the first consideration is the application because this dictates what the figures of merit of the design are. The ultimate purpose of this LF-OCT system is the detection of endogenous magnetite particles. To achieve this, the requirements are: 1) sensitivity to single magnetic particle displacements above the phase noise of one resolution volume and 2) high throughput. The sensitivity to displacements created in one resolution volume of tissue by the induced motion of a single magnetic particle essentially has two dependencies: 1) the maximum displacement that can be induced on the particle (which is a function of the particle size/amount of Fe in the particle and the maximum magnetic gradient force that can be delivered by the electromagnet), and 2) the ability of the LFOCT system to detect the periodic phase shift caused by the displacement of the scattering medium. The smallest discernable phase is a function of the SNR, (SNR expression is given in equation 2-16), but it is not merely given by this relationship. Because we use lock-in detection (by taking the Fourier transform of the optical phase in time and selecting only motion at the magnet modulation frequency), the system may be sensitive to periodic displacements smaller than the value given by equation 2-17. Additionally, the smallest detectable phase shift created by the induced motion of a single magnetic particle is also dependent on the spatial resolution. The deformation of the tissue mechanically coupled to the magnetic particle will be largest in the area immediately surrounding the particle and will fall off with increasing distance from the particle. This means that the largest phase shifts will occur from the motion of scattering media closest to the particle. However, the optical phase of the OCT signal is the phasor sum of the light backscattered from every scatterer within one

resolution volume; this means that the optical phase we measure is a kind of weighted average (weighted by the reflectivity) of the phase shifts from every backscattered photon within one resolution volume. In the condition that the particle volume is much smaller than the resolution volume (as in the case of 50 nm diameter magnetite crystals with typical OCT resolution volumes), the larger the spatial resolution, the smaller the difference in the measured optical phase shift compared to stationary, neighboring resolution volumes. The relationship between the size of the resolution volume and the detectable displacement of a magnetic nanoparticle is discussed further in Chapter 3.

The second requirement of the LFOCT system for endogenous magnetite detection is high throughput, which we define here as the volume of tissue imaged per second (expressed as mm^3/s). High throughput is achieved by imaging as large a volume as possible and as quickly as possible. The volume of tissue imaged by a single B-mode is given by the product of the transverse FOV, the axial imaging depth, and the out-of-plane transverse resolution, Δy. The imaging speed is given by the OCT framerate. Multiplying the volume per frame and the framerate yields a measure of the volumetric throughput. The two system requirements for endogenous magnetite detection can thus be summarized as 1) Fine phase resolution (a function of SNR) and fine spatial resolution and 2) Large FOV (in X and Z) and fast framerates. As discussed previously, there is a fundamental tradeoff in imaging speed and SNR, but we can relax this tradeoff by using the line-field configuration. There remains another fundamental design tradeoff between high spatial resolution and large FOV, and this is true both in the transverse dimension, X, and in depth, Z. Essentially the problem rests on the fact that for each B-mode image, we can only get information from our array of $N \times N$ pixels (assuming that the spectral resolution is limited by the finite pixel size and not the spectral resolution of the

spectrometer). With a fixed number of data points, one cannot get information over an infinitely big area with an infinitesimally small resolution. So in general, in optical imaging systems such as OCT or microscopy, the bigger the transverse FOV, the coarser the resolution. Given these two sets of tradeoffs, we see that there is a fundamental tradeoff between the ability to detect single magnetic particles (with volumes less than the resolution volume) and the volumetric throughput of the imaging system. The optical design must carefully balance these tradeoffs, with the decision being made to favor the ability to detect single magnetic particles over volumetric throughput if we have to choose one or the other.

The optical design must take into consideration any fixed parameters. In the case of a LF-OCT system, there are two primary fixed parameters which result from the light source and the camera used: the diameter of the collimated output of the light source and the fixed size of the sensor. (The axial resolution is also limited by the available bandwidth of the light source, is not a limiting factor when a SC source is employed.) The general goal can be broken into two objectives. The first objective is to produce a line illumination at the sample with the desired transverse FOV (transverse FOV meaning the length of the line illumination at the sample) and the smallest possible transverse resolution. The second is to expand the beam to match the sensor size while simultaneously ensuring that each resolution element is being sampled by a sufficient number of pixels. To fill the sensor, we must match the beam diameter to the size of the sensor (in both dimensions of the 2D array) using beam expanders. These optical design considerations are summarized in Table 2-1.

Table 2-1 LF-OCT Optical Design Considerations

Fixed Parameters	Design Goals	Fundamental Tradeoffs
Initial Beam Diameter	Achieve desired transverse FOV and $\Delta x/\Delta y$ at sample	Small Δx & Δy vs. large Rayleigh range
Pixel Array Size	Match the beam diameter in both X and λ to the pixel array size with sufficient sampling	Small Δz vs. large imaging depth

The basic layout for the LF-OCT system is shown in Figure 2-4, and is adapted from the optical design used in [55]. The choice of each element was made as follows.

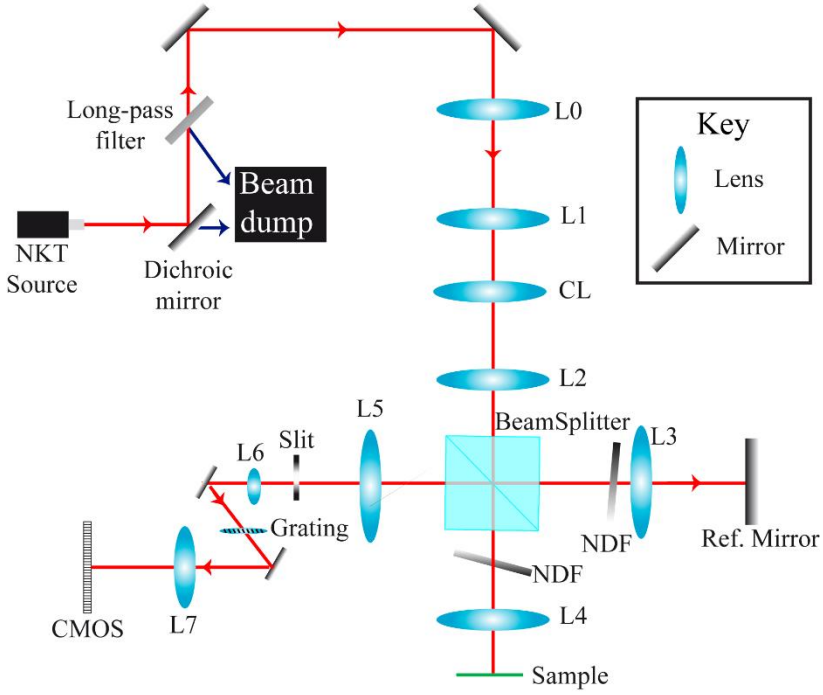

Figure 2-4 Schematic diagram of the LF-OCT system setup.
Broadband light from an NKT SC source is first filtered to a bandwidth of 300nm centered at 800nm. The beam is expanded by L0 and L1 and then enters a free-space Michelson interferometer. Light back-scattered from both arms is recombined and collected by a spectrometer composed of a diffraction grating and a 2D area-scan camera.

The Light Source. The first version of the LF-OCT system was designed for a demo light source loaned to us by NKT Photonics. It was an EXR9-OCT Low Noise SC source made specifically for use in OCT systems. The source has a repetition rate of 320 MHz (the high repetition rate contributing to the lower noise), a beam diameter of ~1 mm at 530 nm (as reported by NKT Photonics), and the output is a collimated, single-mode Gaussian. The source emits ultra-broadband light from 400 nm – 2400 nm with a total output power of 900 mW over the visible to near infrared (NIR) range (550-900 nm).

Optical Filters. A SC source offers the unique advantage to an OCT system design that you can select the desired bandwidth to use, and by changing the optical filters used, could change the design and application of the OCT system. The bandwidth dictates the application to some extent because, as mentioned in Section 2.1, the axial resolution and imaging depth both depend primarily on the source bandwidth, $\Delta\lambda$, and the center wavelength, λ_0. In terms of the Nyquist sampling criteria, equation 2-11, visible light OCT has a finer axial resolution, but lower imaging depth; conversely infrared (IR) OCT has a longer penetration depth but coarser axial resolution. The Nyquist sampling criteria is not the only factor governing the practical imaging depth achievable with OCT; the absorption and scattering properties of the sample itself will also serve to change the attenuation of the beam in depth. The beam attenuation is often the practical limit on the measured imaging depth. Using the Nyquist sampling criteria as a general sample-independent method for estimating the imaging depth, the bandwidth selection must weigh the benefit of high axial resolution against the corresponding cost in imaging depth. For our purposes, we desire high axial resolution, but we also need to maintain reasonably good volumetric throughput so we selected a broad bandwidth of 300 nm and a center wavelength of 800nm, because this allows us to achieve ultrahigh axial resolution while maintaining an imaging

depth > 0.5 mm; the use of shorter wavelengths (a branch of OCT called visible light OCT) can provide even finer axial resolution but at the cost of an even further reduced imaging depth [56]. From equations 2-4 and 2-5, this corresponds to a theoretical axial resolution of 1 μm and a maximum imaging depth of 564 μm in air (for an array of 1024 pixels, assuming Nyquist sampling). Using a dichroic mirror (Thorlabs DMLP950) to reflect light with wavelengths <950 nm and a long-pass filter (Chroma ET605lp) to transmit light with wavelength >605 nm, we filter the SC source's bandwidth down to ~350 nm. The wavelengths <605 nm and >950 nm are directed into a beam dump. We then align the beam on the camera sensor such that only the range 650-950 nm is captured by the camera, as discussed later in this section.

First Beam Expander (L0 and L1). The choice of the first beam expanders depends on the desired transverse FOV at the sample. To understand how the length of the line illumination depends on the focal lengths chosen, see Figure 2-5. The collimated output from the first beam expander (composed of lenses L0 and L1) is incident on the cylindrical lens, CL. From the figure below, it is clear that after the CL, the beam is always focusing in one of the two planes orthogonal to the optical axis (called the transverse and the spectral planes to distinguish between them at the camera sensor) and collimated in the other transverse plane. Because all the lenses are setup in a 4*f* configuration (meaning that each pair of lenses is separated by a distance equal to the sum of their focal lengths), the beam diameter of the collimated beam output when a collimated beam passes through a pair of lenses with focal lengths f_1 and f_2 is then $D_{L2} = (f_2/f_1)*D_{L1}$, where the notation D_{L2} signifies the beam diameter of a collimated beam at the output of Lens 2.

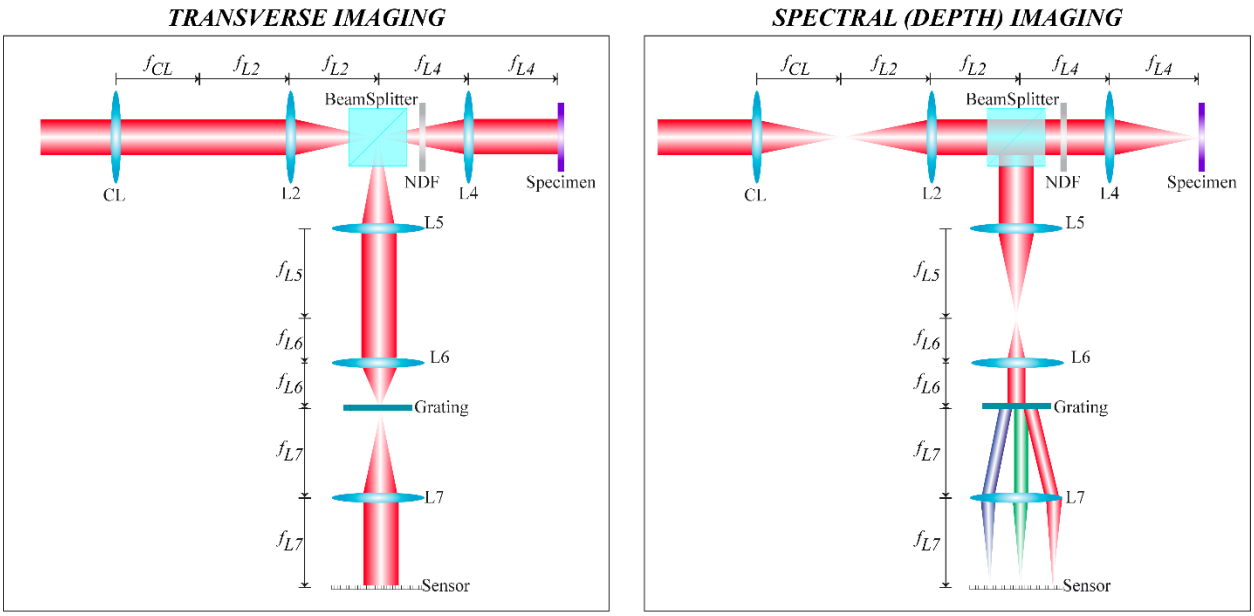

Figure 2-5 Transverse vs. Spectral Planes after Cylindrical Lens.
Schematic diagram illustrating how the beam in a LF-OCT system is focused in the two transverse planes after passing through the cylindrical lens, CL. The beam is always focusing in one plane and collimated in the other.

From Figure 2-5 it is clear that the choice of lenses for the first beam expander will affect all downstream parameters, so the optical design will be an iterative process rather than a simple formula. As a starting place, we chose a FOV of ~4-5 mm. From the expression for the transverse FOV in Table 2-2, we need a combination of four lenses (L0, L1, L2 and L4) whose combination increases the beam diameter of the collimated NKT output (measured to be roughly 0.7 mm) to 4 or 5 mm. In practice, you can make initial guesses for these four lenses and then tweak them as you fill in this chart of design parameters after choosing the downstream optical elements as well. Our choice of lenses was based in large part on which focal lengths were readily available. We used only achromatic doublets with an anti-reflective (AR) coating for the wavelength rage 650-1050 nm from Thorlabs, which limits the possible focal lengths considerably. Achromatic doublets are lenses composed of two separate pieces of glass cemented together, and they are preferable for our system because they produce fewer chromatic

aberrations which is a concern when using a bandwidth as broad as 300 nm. The AR coating is essential to prevent loss of power in applications requiring high SNR. For the beta version of the LF-OCT system, called Version 1 throughout this dissertation, we chose to make the first beam expander with focal lengths f_{L0} = 35 mm and f_{L1} = 200 mm to expand the beam to 4 mm. We then used a focal length of 100 mm for lenses L2 and L4 (and L3, to match the sample and reference arms) so that the theoretical transverse FOV at the sample was 4 mm. These four lenses together also determine the theoretical out-of-plane transverse resolution we can achieve at the sample, given by the focused beam waist as in equation 2-9. With the focal length of L4 being 100mm and the beam diameter incident on it being 4 mm, the theoretical transverse resolution is 25 μm. As stated previously, there is a fundamental tradeoff in transverse resolution and Rayleigh range. The Rayleigh range is the distance along the optical axis at which the radius of the focused beam waist of a Gaussian beam increases by a factor of the square-root of two, and is given by the following expression:

$$Z_R = \frac{\pi n(\Delta x / 2)^2}{\lambda_0} \tag{2-18}$$

The numerical aperture (NA) is proportional to the ratio of incident beam diameter to focal length. As shown in Figure 2-6, high NA focusing can achieve a tighter focus, but then defocuses a shorter distance along the optical axis, and conversely, low NA focusing does not achieve as small a transverse resolution, but maintains that resolution over a longer distance from the focal plane. The depth of field is defined as twice the Rayleigh range. The theoretical Rayleigh range given our theoretical transverse resolution is 853 μm for a sample refractive index of 1.34, and the depth of field is 1706 μm.

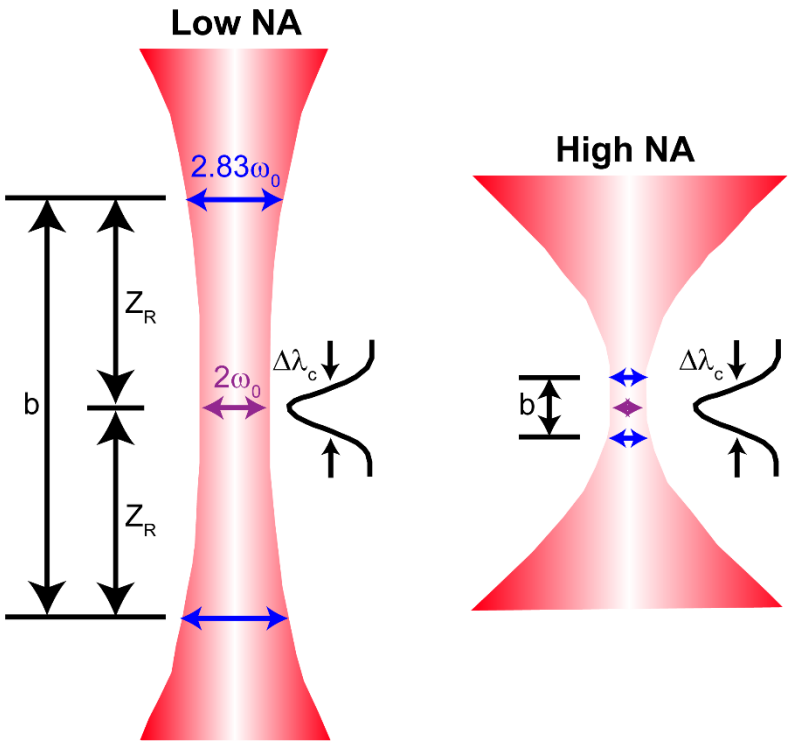

Figure 2-6 Illustration of High-NA vs. Low-NA Focusing.
Schematic diagram illustrating the inverse relationship between the focal spot, $2\omega_0$, (1/*e* diameter of a Gaussian intensity profile) achieved by a Gaussian beam and the corresponding Rayleigh range, Z_R. Low NA objectives (small incident beam diameter and/or long focal length lens) focus the beam to a larger spot size, but maintain a relatively uniform beam diameter over a longer range compared to high NA objectives which achieve a smaller focal spot but with greater beam divergence away from the focal plane. The depth of focus, *b*, is twice the Rayleigh range.

Collection Optics. After considering the first five lenses which bring us up to the sample plane, the next major consideration is matching the beam diameter in both the transverse and spectral planes to the size of the camera's pixel array. The pixel array in this system is a CMOS sensor of a Photron Fastcam SA3 camera. The 2D pixel array is composed of 1024 × 1024 square pixels with side-length 17 µm, making the total size of the array a square with side-length 17.4 mm. To match the spectral extent of the beam with the sensor size, we must consider the beam spread by the diffraction grating. Diffraction gratings exist in various forms, but we chose a transmission grating in which the diffracted light rays appear on the opposite side of the grating

from the incident light. A transmission grating is made of a transparent optical element with a set of regularly spaced grooves carved into the surface. These grooves are spaced by a separation distance, *d*. When light is incident at an angle α to the grating normal, a series of diffracted beams will appear on the other side. The diffraction of light through a transmission grating is shown in Figure 2-7.

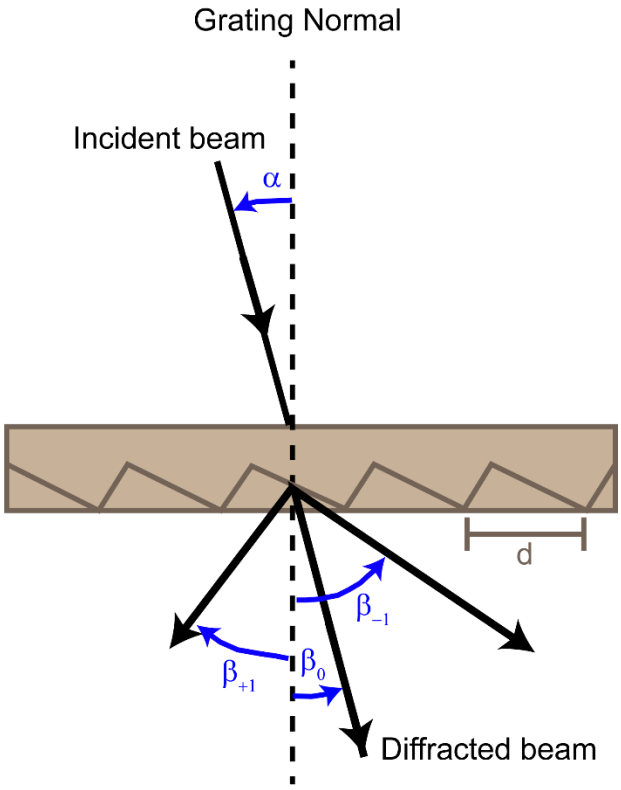

Figure 2-7 Diagram of a Transmission Diffraction Grating.
Light incident on a diffraction grating with groove spacing *d* and angle of incidence α is diffracted into multiple orders, with the angle of diffraction β being wavelength dependent.

The angular locations, $\beta_m(\lambda)$, of the intensity maxima are governed by the grating equation:

$$m\lambda = d(\sin\alpha + \sin\beta_m) \tag{2-19}$$

where *m* is the diffraction order. The intensity of the diffracted beam diminishes with increasing diffraction order. The zeroth order passes through the grating with no spread in λ, so we are

interested in the first diffraction order, where the intensity is highest of all the diffracted beams. The grating equation can also be written in terms of the groove frequency, $G = 1/d$:

$$Gm\lambda = \sin\alpha + \sin\beta_m \tag{2-20}$$

If the diffraction grating is placed at the focal plane of L7 and if we align the beam such that the diffracted center wavelength, λ_0, is orthogonal to the lens L7, as shown in Figure 2-8 below, the beamspread, χ, is estimated by the following expression:

$$\chi = 2 f_{L7} \bullet \tan\left(\frac{\beta_{\max} - \beta_{\min}}{2}\right) \tag{2-21}$$

where β_{min} and β_{max} are the found using equation 2-13, and λ_{min} and λ_{max} are found by determining the actual bandwidth captured by the spectrometer (proportional to the ratio of the beamspread to the sensor size if χ is larger).

Using a transmission grating with 600 lines/mm (Wasatch Photonics 2996-12), a focal length of 100 mm for L7, and an incident angle of 13°, the 1st diffraction order beamspread, χ, on lens L7 for our chosen wavelength range is 18.6 mm. This is the size of the beam in the spectral dimension on the camera. Because this is slightly larger than the length of the pixel array, we must account for the slight cropping in the actual bandwidth $\Delta\lambda$ recorded on the spectrometer. Given the ratio of the array length to the beamspread, the actual bandwidth captured is 280 nm. Being sampled by 1024 pixels, this gives a spectral resolution of 0.273 nm per pixel.

With the focal length of L7 chosen to match the beamspread with the size of the sensor (equation 2-21), that leaves L5 and L6 to be selected so that the beam diameter in the transverse plane of the sensor is also matched to the sensor size. The transverse extent in X is given by the transverse FOV at the sample multiplied by the magnification between the object and image planes. The magnification can be written:

$$M = \frac{f_{L7}}{f_{L6}} \cdot \frac{f_{L5}}{f_{L4}} \tag{2-22}$$

With $f_{L7} = f_{L4}$, the magnification is merely the ratio of f_{L5} and f_{L6}. These were chosen to be 100 mm and 50 mm respectively, yielding a magnification of 2 and a transverse extent at the sensor of 8 mm.

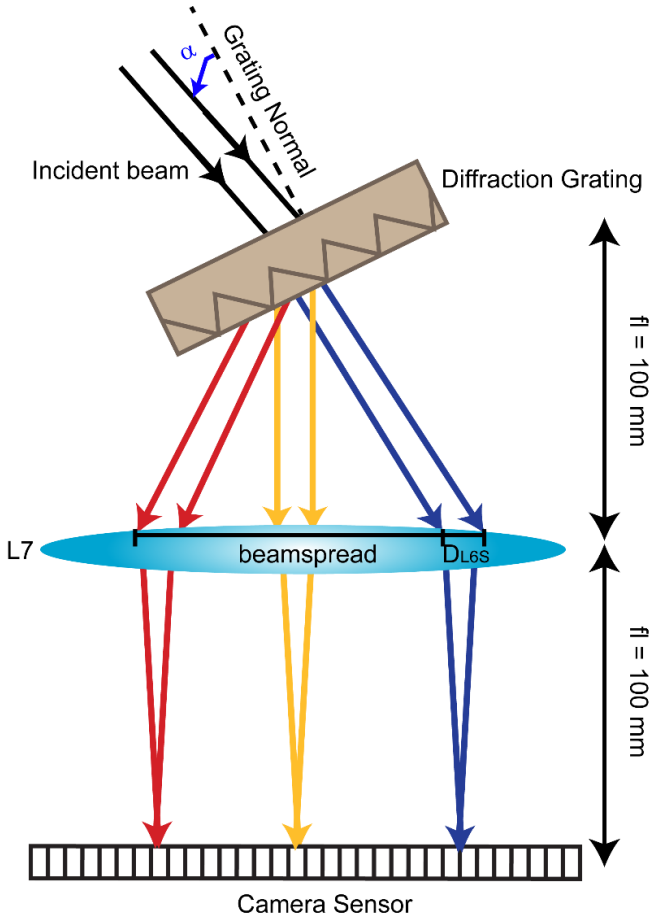

Figure 2-8 Illustration of Diffraction Grating Setup in LF-OCT System.
The diffraction grating is placed at the focal plane of L7 and at an angle such that the center wavelength λ_0 = 800 nm of the first diffraction order is perpendicular to the lens L7.

With an understanding of the setup of the collection optics in this LFOCT system, we can now treat the subject of the in-plane transverse resolution, Δx. Recall from our previous

discussion that the Δx is determined by the ability of the collection optics to focus light backscattered from a point source onto the sensor. Generally, a point particle in the sample may scatter light in any direction. The OCT system can only collect light that is scattered at some maximum angle relative to the optical axis, and that angle is determined by the limiting aperture (sometimes called the aperture stop) of the system. In a multi-lens system with no obvious limiting aperture, the limiting aperture is the rim of the lens which most limits the scattering angle that can be collected [57].

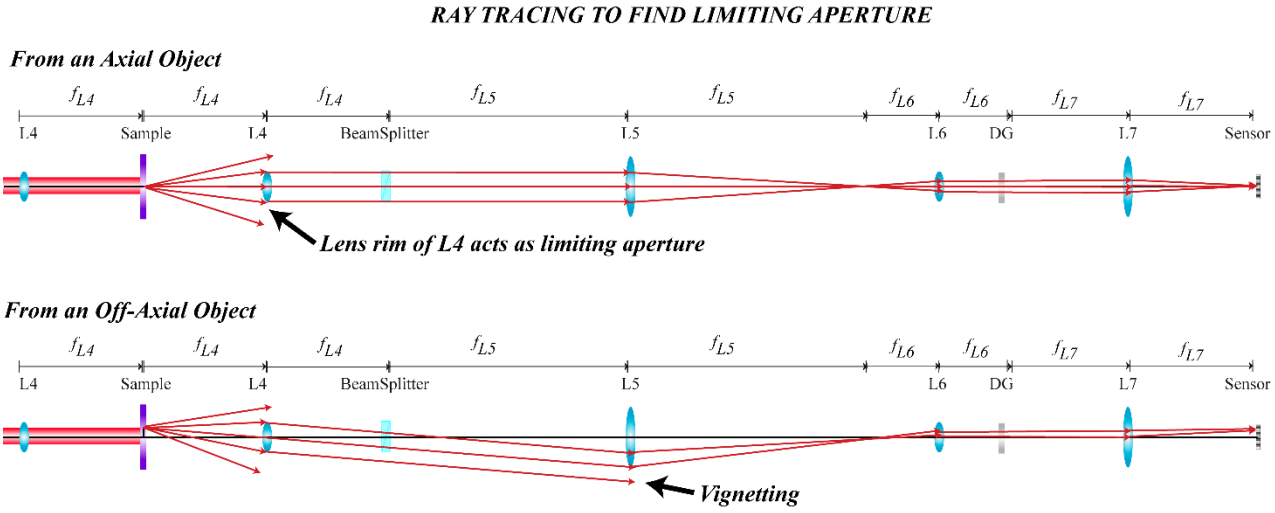

Figure 2-9 Ray Tracing Diagram to Determine Limiting Aperture.
A point source in the sample may generally scatter light in any direction. The limiting aperture determines which scattering angles can be collected and imaged onto the sensor. The diagram shown here (to-scale) illustrates that the rim of lens L4 acts as the limiting aperture in our LFOCT system (Top panel). The ray tracing of an off-axis point source (bottom panel) illustrates that our system suffers from vignetting, meaning that the extreme rays from off-axis points are not collected and therefore the intensity of those off-axis points will suffer.

To determine which lens in our collection optics (lenses L4-L7 in Figure 2-4) acts as the limiting aperture, we use ray tracing (a geometrical optics approach) from an on-axis object in the sample. (See Figure 2-9.) Somewhat counter-intuitively, using an on-axis point yields the

same information about limiting aperture as does ray tracing of an off-axis point; however, ray tracing of an off-axis point can provide useful information about intensity loss due to vignetting, the process by which not all the light back-scattered from off-axis points is collected resulting in non-uniformity in the transverse recorded intensity profile [57].

From Figure 2-9, we see that the diameter of the lens L4 is the limiting aperture of our LFOCT system. All the rays from an on-axis point source will be collected and mapped to the sensor as long as they are incident on the lens L4. The ability of the system to focus the light from that point source onto the sensor is then given by the expression for the focused Gaussian beam waist, as in equation 2-9, but now the focal length of the lens is the focal length of L7, and the beam diameter incident on L7 is given by the ratio of the focal lengths of L6 and L5 multiplied by the diameter of the lens L4, D_{L4}:

$$2\omega_{0sensor} = \frac{4\lambda_0 f_{L7}}{\pi\left(D_{L4}\frac{f_{L6}}{f_{L5}}\right)} \tag{2-23}$$

Given the focal lengths f_{L5}, f_{L6}, and f_{L7} of 100 mm, 50 mm, and 100 mm respectively and that L4 is a standard 1" optic (diameter of 25.4 mm), the size of the focused Gaussian beam waist is 8.02 μm at the sensor. Given a magnification of 2 between the object plane (at the sample) and the image plane (at the sensor) from equation 2-22, this results in a theoretical transverse resolution of 4.01 μm at the sample (*i.e.* the value for the theoretical transverse resolution in physical lab space). The full expression for the theoretical transverse resolution of the LFOCT system with the diameter of lens L4 as the limiting aperture is then the expression in equation 2-21 divided by the magnification, which simplifies to:

$$\Delta x_{LF} = \frac{4\lambda_0 f_{L4}}{\pi D_{L4}} \tag{2-24}$$

This is the expression for the focused Gaussian beam waist expected if L4 were focusing a beam with a diameter exactly equal to the diameter of the lens. Another consideration is that the focused transverse spot size of a single scatterer focused on the sensor, $2\omega_{0sensor}$, is sampled by a discrete number of pixels in the spatial dimension of the 2D camera. Any continuous function discretely sampled is subject to the Nyquist sampling criterion. For the transverse resolution, this means essentially that every focused spot in *X* on the sensor needs to be sampled by at least two pixels. Otherwise, the theoretical transverse resolution is given by the physical distance in *X* imaged by two pixels. Given that our transverse FOV is 8 mm on the sensor, we are not filling the entire array of pixels in the transverse dimension (sensor size being 17.4 mm). This means the 8 mm transverse FOV is sampled by (8/17.4)*1024 = 471 pixels, yielding 17 µm per pixel. This means that $2\omega_{0sensor}$ = 8.02 µm is not sampled by two pixels. So the theoretical transverse resolution of this Version 1 optical design will then be given by the distance in physical space (at the sample) represented by two pixels (for a magnification of 2, this is 17 µm). The expressions governing the optical design of a LFOCT system are summarized in Table 2-2, the chosen optical components for Version 1 are summarized in

Table 2-3, and the corresponding theoretical values are given in Table 2-4. The experimental values will then be shown alongside the theoretical values in Section 2.3.4, after a discussion of the system alignment and image processing steps.

Table 2-2 Summary of LF-OCT Optical Design Parameters

	Transverse Imaging		Spectral (Depth) Imaging	
Up to Sample	$D_{L4T} = \frac{f_{L4}}{f_{L2}} \bullet \frac{f_{L1}}{f_{L0}} \bullet D_{L0}$	Transverse FOV	$D_{L6S} = \frac{f_{L6}}{f_{L5}} \bullet \frac{f_{L2}}{f_{CL}} \bullet \frac{f_{L1}}{f_{L0}} \bullet D_{L0}$	
	$\Delta x = \frac{4\lambda_0 f_{L4}}{\pi D_{Lim\_ap}}$	In-plane Transverse Resolution	$\chi = 2 f_{L7} \bullet \tan\left(\frac{\beta_{\max} - \beta_{\min}}{2}\right)$	Beamspread (Beam diam. in λ on sensor) based on $\Delta\lambda_{inc}$
	$\Delta y = \frac{4\lambda_0 f_{L4}}{\pi D_{L4T}}$	Out-of-plane Transverse Resolution	$D_{L7S} = D_{L6S} + \chi$	Beam diameter on L7
	$Z_R = \frac{\pi n(\Delta x/2)^2}{\lambda_0}$	Rayleigh Range	$2\omega_{0\_\lambda} = \frac{4\lambda_0 f_{L7}}{\pi D_{L6S}}$	Focused size of each λ on sensor
Collection Optics	$D_{L7T} = \frac{f_{L7}}{f_{L6}} \bullet \frac{f_{L5}}{f_{L4}} \bullet D_{L4T}$	Beam diam. in *X* on sensor	$\frac{2\omega_{0\_\lambda}}{pixelsize}$	Spectral sampling (how well each λ is focused compared to pixel size)
	$2\omega_{0sensor} = \frac{4\lambda_0 f_{L7}}{\pi\left(D_{L4}\frac{f_{L6}}{f_{L5}}\right)}$	Focused size of each scatterer in X-dimension on sensor	$\frac{sensorsize}{\chi} \bullet \Delta\lambda_{inc.} = \Delta\lambda_{captured}$	Captured bandwidth, if $\chi >$ sensor size
	$\frac{2\omega_{0\_sensor}}{pixelsize}$	Focused spotsize in *X* compared to pixel size	$\lambda_{\max,\min} = 800nm \pm \frac{\Delta\lambda_{captured}}{2}$	λ_{min} & λ_{max} based on captured bandwidth
	$\frac{FOV/N}{\Delta x} = \frac{\mu m/pixel}{resolution}$	Spatial sampling (want to sample each resolution element with multiple pixels)	$\delta\lambda = \frac{\Delta\lambda}{N}$	Spectral resolution
	$M = \frac{f_{L7}}{f_{L6}} \bullet \frac{f_{L5}}{f_{L4}}$	Magnification between object plane (sample) & image plane (sensor)	$\Delta z = \frac{2\ln(2)\lambda_0^{\,2}}{\pi\Delta\lambda}$	Axial resolution
	$z_{1/2} = \frac{\ln(2)\lambda_0^{\,2}}{\pi\delta_r\lambda}$	Imaging Depth (SNR roll-off)	$z_{\max} = \frac{N\lambda_{\min}\lambda_{\max}}{4n\Delta\lambda}$	Imaging Depth (Nyquist sampling)

Table 2-3 Summary Components Used in LF-OCT System Version 1

LF-OCT System Components for Version 1	
Light Source	NKT Photonics EXR9-OCT Low Noise Collimated beam diameter of ~1 mm
Optical Filters	Chroma 605 nm longpass filter Thorlabs 950 nm shortpass dichroic mirror
L0	Thorlabs achromatic doublet, AR coating 650-1050 nm f = 35 mm diameter = 1”
L1	Thorlabs achromatic doublet, AR coating 650-1050 nm f = 200 mm diameter = 1”
CL	Thorlabs achromatic doublet, AR coating 650-1050 nm f = 100 mm diameter = 1”
L2	Thorlabs achromatic doublet, AR coating 650-1050 nm f = 100 mm diameter = 1”
L3/L4	Thorlabs achromatic doublet, AR coating 650-1050 nm f = 100 mm diameter = 1”
L5	Thorlabs achromatic doublet, AR coating 650-1050 nm f = 100 mm diameter = 1”
L6	Thorlabs achromatic doublet, AR coating 650-1050 nm f = 50 mm diameter = 1”
L7	Thorlabs achromatic doublet, AR coating 650-1050 nm f = 100 mm diameter = 2”
Beam Splitter Cube	Newport Broadband Non-polarizing 50:50 beam splitting cube 1” (10BC17MB.1)
Diffraction Grating	Wasatch Photonics 600 lines/mm 1”
Camera	Photron Fastcam SA3 1024 x 1024 CMOS pixel array with 17 µm square pixels

Table 2-4 Theoretical Values of Optical Design for LFOCT Version 1

			LF-OCT Version 1
			Theoretical Value
Transverse Imaging	D_{L4T}	Transv. FOV (mm)	4.0
	$\Delta x(n=1.34)$	In-plane Transv. Res. (μm)	17.0
	$\Delta y(n=1.34)$	Out-of-plane Transv. Res. (μm)	25.5
	$Z_R(n=1.34)$	Rayleigh Range in *Y* (μm)	822
	D_{L7T}	Beam diam. in *X* on sensor (mm)	583
	$2\omega_{0sensor}$	Focused size of each scatterer in *X*-dimension on sensor (μm)	8.02
	$\frac{2\omega_{0\_sensor}}{pixelsize}$	# Pixels sampling $2\omega_{0\_sensor}$	0.46
	$2(FOV/N)$	Object space mapped to 2 pixels (μm)	17.0
Spectral (Depth) Imaging	χ	Beam diam on sensor (mm)	21.4
	$2\omega_{0\_\lambda}$	Focused size of λ on sensor (μm)	60.5
	$\frac{2\omega_{0\_\lambda}}{pixelsize}$	# Pixels sampling $2\omega_{0\_\lambda}$	3.48
	$\Delta\lambda_{captured}$	Captured bandwidth (nm)	280
	$\lambda_{\min,\max}$	(nm)	660; 940
	$\delta\lambda$	Spectral resolution (nm/pixel)	0.273
	Δz	Axial resolution in air (μm)	1.01
	$z_{\max}$	Imaging Depth in air (μm)	524
	$z_{1/2}$	6dB Roll-off Depth in air (μm)	515

2.3.2 Optical Alignment

Many point-scanning SD-OCT systems are fiber-based. Because the beam in point-scanning systems can maintain a relatively small diameter from the light source all the way to the camera sensor, it is easier to align the system by launching the beam into a fiber coupler at the output of the laser source. Fiber-coupling is also desirable because the fiber aperture acts as a spatial filter which provides confocal gating (to reject multiply-scattered photons). Because LF-OCT requires a much larger beam diameter (on the order of many millimeters), fiber coupling is more difficult, requiring an array of fibers to image each transverse location along the line illumination. LF-OCT systems (to date) are therefore all free-space optical systems. Recall that three of the figures of merit of this LF-OCT system are high optical SNR (for sensitivity to small displacements), fine spatial resolution (to distinguish the phase shift caused by the motion of a single particle above the phase contributions from scatterers in the rest of the resolution volume) and large transverse and axial FOV with fast framerates (for high volumetric throughout). All three criteria require precise optical alignment. The theoretical transverse and axial resolutions are merely lower limits on the actual resolution of an SD-OCT system. The experimental resolutions will depend on how well the beam is collimated and aligned at each optical element in the system, as well as on the accrual of aberrations. There are different kinds of aberrations; some are avoidable with good alignment techniques, and some are inherent in this system.

Spherical aberrations occur when rays passing through the edges of a spherical lens focus at a different point than rays passing through the center. The difference in the focal length of a paraxial ray and an edge ray increases the further the edge ray is from the optical axis. Therefore, to minimize spherical aberrations, the beam diameter incident on a spherical lens should be small compared to the diameter of the lens so that all rays can be approximated as paraxial rays [58].

This is an important consideration for LF-OCT systems which employ unusually large beam diameters throughout the system. Spherical aberrations are a type of aberration inherent in the certain optical elements, but they can also be exacerbated by poor alignment. If the beam does not pass through the center of the lens but instead is shifted laterally or vertically, more spherical aberrations (and other aberrations described below) will be introduced.

Chromatic aberrations are another concern of any optical imaging system that employs a broadband light source because chromatic aberrations occur when different wavelengths focus at different points along the optical axis due to dispersion. For this reason, we use only achromatic doublets in this LF-OCT system. Spherical aberrations and chromatic aberrations are intrinsic to the type of lenses used and the broadband light source. They can be mitigated by careful choice of optical elements and by perfect alignment.

There are other types of aberrations inherent in LF-OCT which cannot be removed even with perfect lenses and perfect alignment. Astigmatism is one such aberration. Generally, astigmatism refers to the transverse planes having two different focal planes. There are two kinds of astigmatism: 1) rotational asymmetry and 2) oblique astigmatism. Astigmatism in systems not rotationally symmetric results from a lens having different curvatures in different planes. The two different curvatures cause rays (even for monochromatic rays originating from the optical axis) to focus at two different points in the two transverse planes. The rotational asymmetry could be an intentional design (as in the case of a cylindrical lens) or a lens imperfection. Oblique astigmatism refers specifically to the aberration resulting from off-axis points being focused into two different places in two transverse planes. Oblique astigmatism occurs even for perfectly symmetrical lenses. For a LF-OCT system, the wide FOV imaged will inherently result in off-axis objects being imaged.

The final type of aberration is called a coma. A comatic aberration results in off-axis points appearing to have a comet-like tail. This type of aberration results from a mechanism very similar to spherical aberrations. The off-axis points are deflected more steeply through the lens than on-axis points would be, producing an asymmetry in the rays at the image plane [58]. A tell-tale sign of comatic aberration is the spreading of the beam in the plane transverse to the optical axis.

To minimize aberrations and achieve the best possible resolution and SNR, it is essential that each optical element be aligned vertically and transversely (so the beam passes through the exact center of the element), be placed at exactly the right point along the optical axis to achieve a 4*f* configuration (the distance between each pair of lenses being equal to the sum of their focal lengths), and that the element face be orthogonal to the optical axis (without any tilt). For small beam diameters, it is fairly easy to ensure that the beam is centered laterally and vertically on the face of the optical element by attaching a pinhole aperture to each lens mount in turn and ensuring that the beam passes through the pinhole. For larger beams, we use an alignment target, placed over the lens mount, to check that the beam is centered on each lens.

When using a broadband NIR source, it is also important to consistently use an IR viewer to check the alignment of each lens. The shorter wavelengths of our 650-950 nm beam are visible by eye; however, most of the beam's power is spread across the IR wavelengths. Therefore, how the beam looks by eye is not necessarily how the beam looks through the IR viewer, which is closer to the total intensity distribution of the full 300 nm bandwidth. For every optical element, the general procedure for checking the lateral and vertical alignment as well as the tilt is to place two irises downstream of the element before inserting the element into the beam path. The two irises establish the optical axis. After inserting the optical element, adjust the

height of the element to ensure that the beam comes out vertically level on both irises; this means that the beam is centered vertically on the lens. Then attach a post collar to fix the height of the optical element. Next, slide the optical element laterally across the optical axis to align the beam on the first downstream iris. Then adjust the tilt to align the beam through the second downstream iris. This is an iterative process as changing one will affect the other. Once the beam is laterally centered on both irises, the optical element should be both laterally centered and orthogonal to the optical axis. An additional check is to ensure that the back reflection off the front surface of the lens is centered on an iris upstream of the newly inserted optical element. Once the beam is centered on the lens and there is no tilt in the lens, slide the lens along the optical axis to collimate the output (except for the very first lens, L0, which does not have a collimated output).

To collimate the output of each lens, the most consistent method is to use a shear plate interferometer [59], which consists of a plate of glass placed at an angle to the optical axis. The Fresnel reflections off the front and back surface of the glass are directed up through a diffuser and onto a fixed plate. Assuming the OPD travelled by the two beams is less than the coherence length of the light, the two beams will interfere on the fixed top plate. The fringes produced will be parallel to a reference line etched onto the top plate if the beam is collimated and will be at an angle to the reference line if the beam is converging or diverging.

Recall from equation 2-1 that the coherence length is inversely proportional to bandwidth. For our 300 nm bandwidth, the coherence length is ~1 μm, meaning that the shear plate interferometer cannot be used to collimate with the SC source directly. A far more monochromatic light source is needed to achieve a sufficiently long coherence length to employ a shear plate interferometer. For this reason we co-aligned a He-Ne laser (λ_0 = 632.991 nm) after

the optical filters but before the first lens as shown in Figure 2-10. Note that mirror M2a is on a flip mount so that you can easily switch between the NKT source for centering the beam on each lens and then the He-Ne for collimating its output. Further, because the cylindrical lens complicates the alignment significantly, we first align a spherical lens with the same focal length and replace this with the cylindrical lens toward the end of the alignment. The full alignment procedure can be found in Appendix 1.

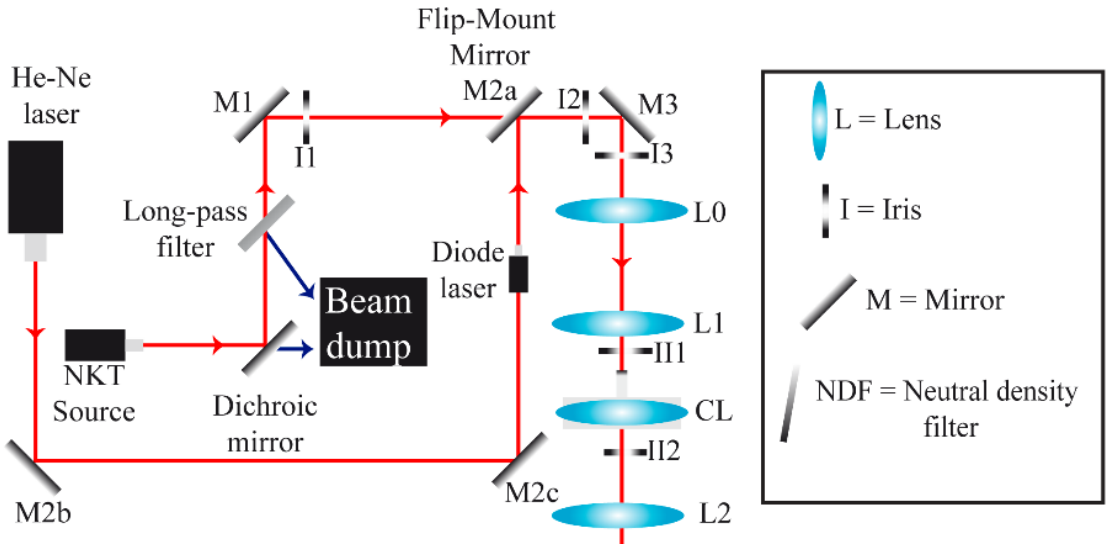

Figure 2-10 Schematic Diagram of LF-OCT Setup with He-Ne laser co-aligned.
A He-Ne laser and a diode laser are co-aligned with the SC source to help with the alignment. The SC source is used for aligning the transverse position of the optics. The He-Ne is used for collimating the output of each lens. The diode is used to center the output of the diffraction grating on the camera.

Using the shear plate interferometer is easy for the first few lenses because the interference fringes are perfectly or nearly perfectly straight, parallel lines. However, aberrations show up in the shear plate interferograms, and the optical aberrations are carried forward and compounded at each downstream optical element, so that the last few lenses are much more

difficult to collimate (as shown in Figure 2-11). A summary of how to interpret the shear plate interferograms in the presence of aberrations can be found in [59].

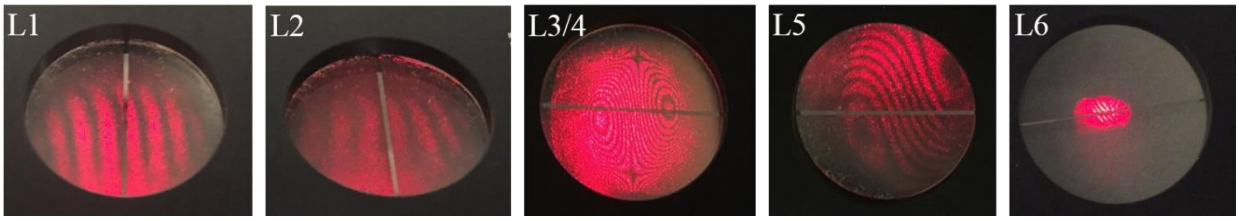

Figure 2-11 Photos of Aberrations on Shear Plate Interferometer.
After L1, small astigmatism. After L2, small astigmatism, small spherical aberration. After L3/L4 and L5, Astigmatism, spherical aberration and comatic aberration. After L6, small beam diameter obscures the aberrations and lines look parallel and straight again. Beam is slightly diverging so lines are at an angle to the reference line.

The shear plate interferometer also cannot be used to collimate the output of the last lens, L7 because 1) too much power is lost by the combination of 50:50 beam splitter and the diffraction grating to allow the He-Ne beam to be visible to the eye after L7, and 2) because the 633 nm wavelength of the He-Ne laser is diffracted at an angle such that it passes through one of the edges of L7 rather than through the center. The diffraction grating + L7 combination are aligned so that L7 is perpendicular to the center wavelength 800nm. For this reason, we co-aligned a diode laser (λ_0 = 780 nm) for use in aligning the camera with L7 (as shown in Figure 2-10*Figure 2-10*). We use the diode laser to align the camera such that 800 nm will be centered on it because we chose 800 nm as our center wavelength. Recall that the full bandwidth is then dictated by our choice of center wavelength and by the bandwidth captured by the spectrometer. Once the camera is roughly aligned with our center wavelength, the camera is slid back and forth along the optical axis in order to check the beam diameter after L7 and collimate its output.

Once the optical elements and the camera are all aligned, the final steps are to set up the sample arm so that the surface of the sample will be near the coherence zero position (the

position exactly path length matched to the position of the reference mirror) with the focal plane of the lens L4 below the sample surface to achieve approximately isotropic resolution throughout the imaging window (Figure 2-12). The imaging window of an OCT system is the region in the sample arm over which an image can be constructed. The top of that window, called coherence zero, occurs at the position along the optical axis in the sample arm such that the path length is exactly matched to the reference arm path length, call it z_0. The bottom of the imaging window is then given by $z_0 + z_{max}$, the maximum imaging depth the spectrometer is capable of capturing. Because light from one arm of an interferometer cannot distinguish between a path length difference of $z+\Delta z$ and $z-\Delta z$, the imaging window technically extends from $-z_{max}$ to z_{max} in the sample arm. Any scatterers in the sample arm located within z_{max} either above or below z_0 will interfere with light from the reference arm and will be resolved by the spectrometer. The region extending from z_0 to $-z_{max}$ is called the conjugate image. If the sample were placed in the region of the conjugate image, then the reflectivity profile of the scatterers in this region would appear wrapped around z_0 and would be overlaid on the depth profile of scatterers in the region from z_0 to z_{max}. To avoid confusion with the conjugate image, the sample is always placed only in the region z_0 to z_{max}.

Importantly, the focal plane of L4 and the coherence zero plane are two separate planes, in general. The focal plane of L4 is a set distance away from L4 and need not be within the imaging window. Because we place an identical lens in the reference arm, and because the reference mirror is placed at the focal plane of that lens, the focal plane of L4 should be in the exact same plane as z_0 by the nature of our design. Because we want the focal plane of L4 to be down in the sample we are imaging and not at the top of the image (typically left as an air gap), z_0 is intentionally shifted slightly toward the beam splitter, thereby pushing the focal plane down

~100-200 µm below z_0. In this configuration, there is a difference between the ranges $-z_{max}$ to z_0 and z_0 to z_{max}; now the focal plane of L4 is not in the conjugate image region, providing a preferred region to use.

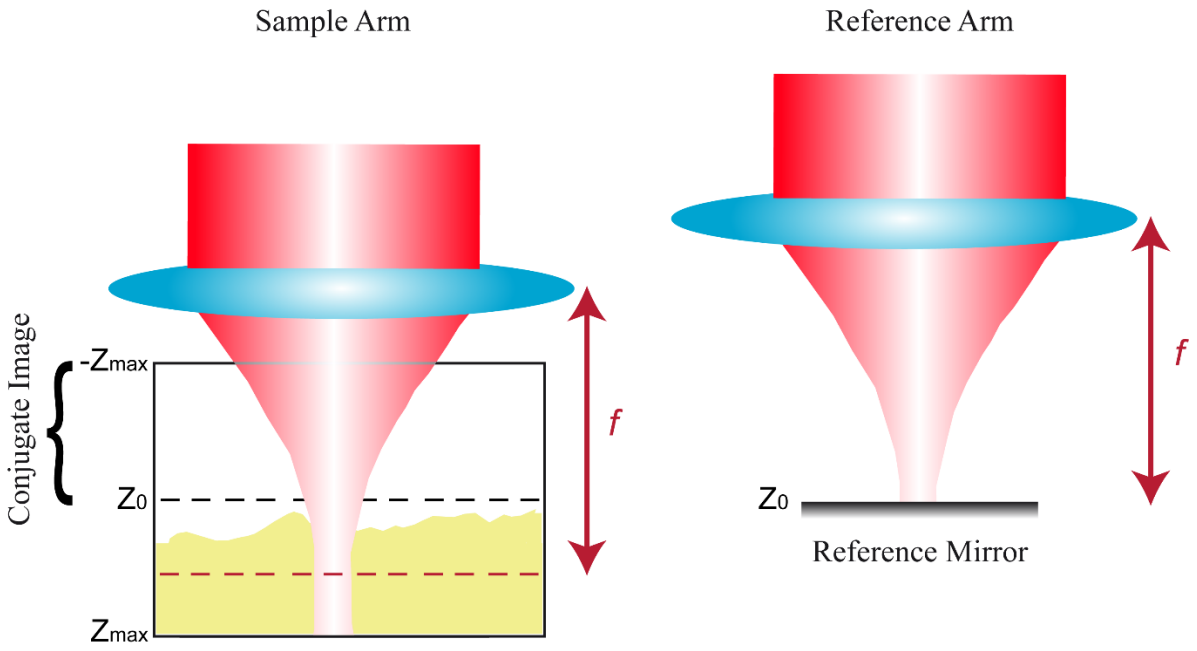

Figure 2-12 Sample Arm Setup.
Schematic diagram illustrating how the coherence zero position is set up relative to the reference mirror and relative to the focal plane of L4. The reference mirror + reference lens are shifted slightly toward the beam splitter so that z_0 is separate from the focal plane of L4.

2.3.3 Data Collection and Image Processing Algorithm Development

After aligning the LF-OCT system, the final step before image collection can begin is to do dispersion compensation. Dispersion describes the frequency dependence of the phase velocity of a light wave. One manifestation of dispersion is that the refractive index of a material has a wavelength dependence such that the optical path length (OPL) of rays passing though the material depends on the wavelength of the incident light. This in turn changes the total optical path length travelled by the various frequency components of polychromatic light through a

dispersive medium. There are three causes of dispersion that contribute to image distortion: interferometer imbalance, sample dispersion, and spectrometer nonlinearity in wavenumber, *k*. Interferometer imbalance results from any difference in path length between the sample and reference arms. This could be due to using different optical elements in the two arms, or a slight misalignment of optical elements, as well as manufacturing differences between the thicknesses of optical elements in the two arms. The sample also introduces dispersion as the light in the sample arm travels through the sample being imaged, as the refractive index of the sample may have wavelength dependence. Finally, diffraction gratings spread the polychromatic light linearly in λ, but the Fourier transform assumes that the data is sampled linearly in wavenumber *k* (which is inversely proportional to λ). We expect the ultra-broadband source used here to cause more dispersion than more narrowband sources used in other OCT systems; however, the imaging depth being inversely proportional to bandwidth means we also have a smaller imaging depth than typical SD-OCT systems, and therefore have a tradeoff in less sample dispersion.

Dispersion results in blurring of OCT images and resolution degradation. For high-resolution systems such as this one, it is therefore essential to compensate for dispersion. For a single imaging depth, it is relatively easy to compensate for interferometer mismatch using optical components. However, this is much more complicated over a large imaging range. To compensate for dispersion arising from the sample (at all image depths), as well as dispersion arising from the nonlinearity in *k* and the interferometer imbalance, we perform digital dispersion compensation in our reconstructed OCT images by employing an autofocus algorithm for dispersion compensation created by Daniel L. Marks [60]. After any realignment of the LF-OCT system, the first images recorded are always of a homogeneous distribution of TiO_2 point scatterers (Sigma Aldrich rutile powder, 224227, mean diameter 1μm) distributed in

Polydimethylsiloxane (PDMS) so that the autofocus algorithm can be used to find dispersion compensation parameters which minimize the point spread function (PSF) of the point scatterers across all depths of the imaging range. The index of refraction of PDMS does not exactly match that of water, but it does reasonably well and is useful for making stable point scattering targets that can be used over many years for doing dispersion compensation and spatial resolution measurements. Example B-modes of the TiO_2 point scatterers before and after digital dispersion compensation are shown in Figure 2-13.

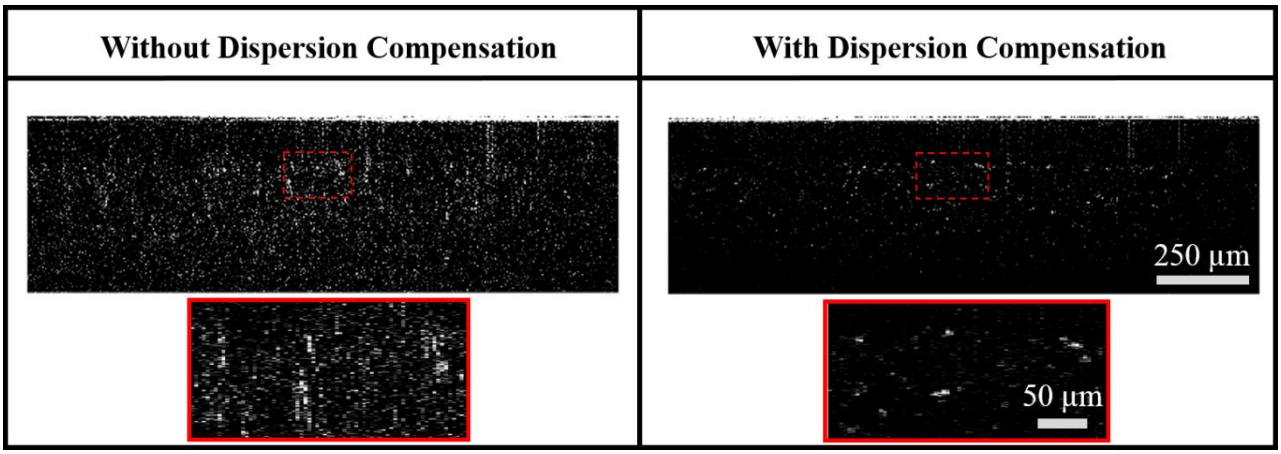

Figure 2-13 Comparison of B-mode Images before & after Dispersion Compensation. Comparison of B-mode images obtained with and without digital dispersion compensation. Inset (red) shows an enlarged view of the indicated region of interest. Images are of TiO_2 point scatterers embedded in PDMS.

From these images, it is clear that the digital dispersion compensation removes blurriness in the axial resolution so that the point scatterers are significantly more distinct from the background noise.

2.3.4 Characterizing the LF-OCT System Version 1

After choosing the optical design and aligning the system, the final step is to characterize the performance of Version 1 of the LF-OCT system. We do this by measuring the axial and transverse resolution, the SNR, and the axial and transverse pixel calibration (to get imaging depth and FOV). First, to calibrate to microns/pixel, we imaged a plastic ruler with millimeter tick marks.

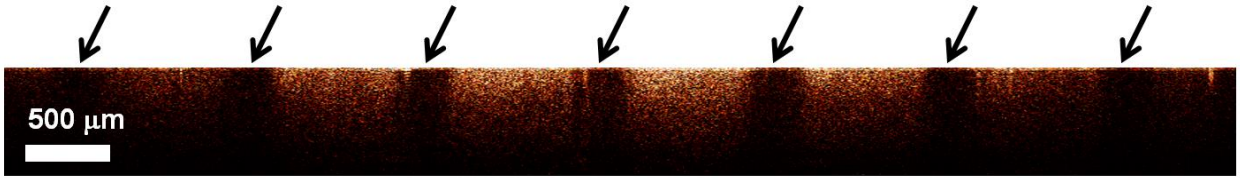

Figure 2-14 LF-OCT transverse calibration of Version 1.
Millimeter tick marks on a ruler are used to calibrate the transverse distance (arrows indicate the positions of the ticks, which attenuate the beam and create a shadowing effect).

Taking the average of the OCT signal amplitude of every column yields a transverse profile with dips corresponding to the black, millimeter tick marks (because the black lines on the ruler do not back scatter as much light as the clear plastic). Knowing the physical distance represented by each peak in the transverse profile, we find the average pixel calibration to be 8.58 μm per transverse pixel. Recalling from the optical design that the beam diameter in the X dimension of the sensor is only 8 mm (compared to the sensor size of 17.4mm), we are filling only 46% of the transverse pixels. This corresponds to a transverse FOV of 4.04 mm at the sample, compared with a theoretical value of 4.01 mm.

To calibrate the axial pixels, we image a flat, silver mirror. Because silver mirrors are nearly perfect reflectors ($R_S \sim 1$), we make use of a neutral density filter (NDF) to avoid saturating the camera. Using a micrometer-driven linear translation stage, the sample is lowered

in known increments and imaged at each depth. We then plot the row number in the image corresponding to the depth profile peak vs. the relative position of the mirror, Figure 2-15. Taking the slope of this line yields the axial calibration of 0.994 µm per axial pixel in air. For 512 spectral pixels (half of the 1024 array due to spectrum redundancy caused by the negative frequencies given by the inverse Fourier transform of the modulated interference spectrum), this corresponds to an imaging depth of 509 µm. The theoretical maximum imaging depth in air for the system is 524 µm.

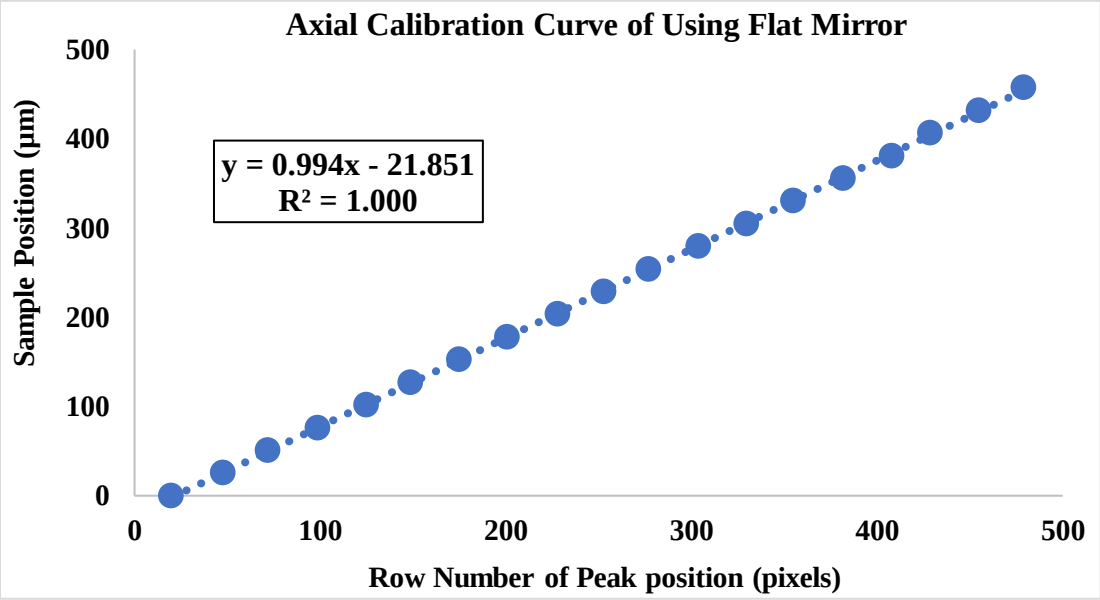

Figure 2-15 Axial calibration curve for LF-OCT System Version 1.
A flat silver mirror is lowered by known increments from coherence zero using a micrometer-driven translation stage. The sample position is plotted as a function of the center A-line in each image to obtain an axial calibration of 0.994 µm per pixel in air.

From the images of the mirror, we noticed that there is a smile artifact in the reconstructed images: the image of a mirror appears to curve downwards at the transverse edges of the frame. We computed the difference in row number between the peak in the depth profile of the center A-line compared to the peak in the depth profile of the most extreme A-lines and

found that the difference in row number of the peak was 2 pixels at depths up to 200 μm increasing to 5 pixels at 500 μm. The effect of such a curvature is distortion in the axial calibration for the transverse edges of the B-mode.

From the images of the flat silver mirror at various depths within the image, we also compute the SNR as a function of depth (see Figure 2-16). The images were recorded with a framerate of 1000 frames per second with an exposure time of 3.33 μs, and the total sample power incident on the NDF in the sample arm was ~400 mW. With the detector's quantum efficiency of 0.4, this gives a theoretical SNR of 104 dB. The sample power was attenuated with an NDF to ~8 mW. With a ref power of ~ 2 mW, the system was not set up in the shot noise limited regime. (We did not characterize the operating conditions needed for the shot-noise limited regime until after the demo NKT light source had been returned.) The experimental SNR of the system is taken to be 10*Log10 of the peak intensity of the center A-line (the mean-squared OCT signal) divided by the standard deviation of noise (which is the mean-squared OCT signal evaluated above and below the peak position). Adding back the 34 dB of optical attenuation, the maximum experimental SNR was 88 dB at a depth of 60 μm with a roll-off of -12 dB over ~250 μm in depth. We measured the power loss from every optical element in the collection optics, and found that the second pass through the beam splitter incurred a loss of 3 dB (as expected from a 50:50 beam splitter), the diffraction grating a loss of 10 dB (from the other diffraction orders), and the other lenses and mirrors a loss of 1.7 dB. The total losses of 14.6 dB in the collection optics brings the theoretical SNR down from 107 dB to 92.4 dB, in good agreement with our experimental SNR of 88 dB.

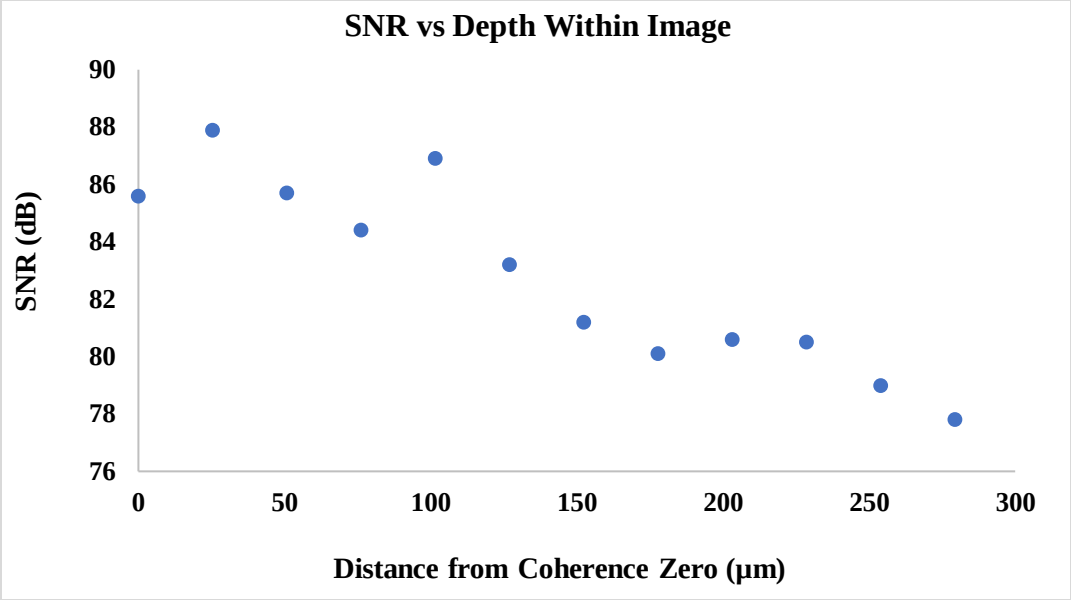

Figure 2-16 SNR vs depth for LF-OCT System Version 1.
There is a roll-off of ~10 dB over ~250 µm.

To measure the axial and transverse resolution, Δx, we imaged the same TiO_2 point scatterers used in the digital dispersion compensation algorithm. To measure the PSF of an optical imaging system, it is important to use point scatterers, which are particles with a mean diameter much less than the theoretical resolution. Because the physical dimensions of the point scatterer are smaller than the smallest resolvable element of the system, the intensity profile of the scatterer- the convolution of the system's point spread function (PSF) and a Gaussian profile with FWHM equal to the point scatterer's diameter- provides us a measurement of the system's PSF, both axially and laterally, as long as the point scatterer's diameter is much less than the system's PSF FWHM.

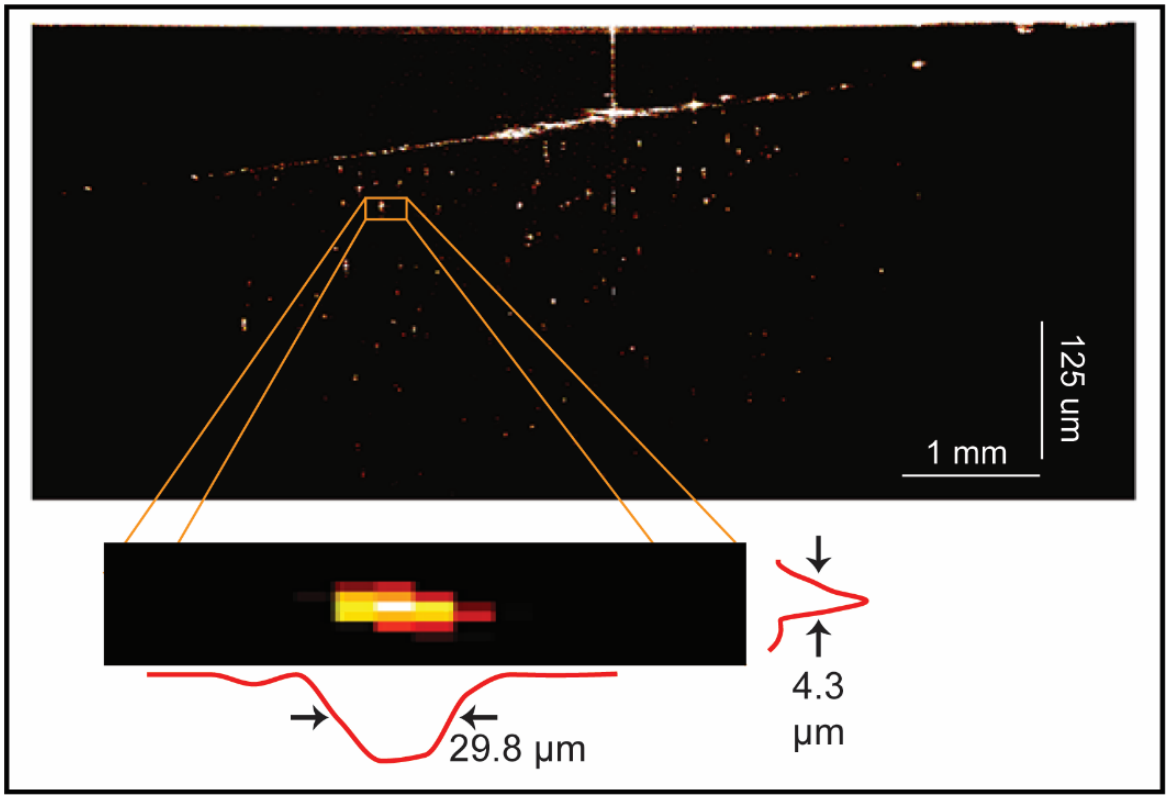

Figure 2-17 Image of Point Scatterers for Resolution Measurement.
Image of TiO_2 point scatterers embedded in PDMS. Twenty-five scatterers were selected and the FWHM of the axial and transverse profiles recorded.

Arbitrarily, we chose 25 scatterers, all with intensity greater than 700 arb. unit as illustrated in Figure 2-17. For each scatterer, we found the axial and transverse resolution (mean ± standard deviation) to be 2.4 ± 0.6 μm and 24 ± 3 μm respectively. The theoretical axial and in-plane transverse resolutions are 1.01 μm and 17.0 μm respectively. This means that the experimental axial resolution was worse than was expected. This may be explained by poor focusing of the lenses in the spectral plane (so-called, as in the right side of Figure 2-5, because this is the plane in which the beam is focused onto the spectrometer). The in-plane transverse resolution, Δx, is also worse than the theoretical lower bound; however, it is very consistent with the theoretical value for the out-of-plane transverse resolution, Δy, which is determined by the Gaussian beam waist focused by L4 (estimated to be 25.5 μm). We may be able to achieve an

experimental Δx closer to the theoretical lower bound with improved alignment techniques. Additionally, to check the spatial oversampling, with a magnification of 2, the size of Δx on the sensor is 2*24μm = 48 μm. With a pixel size of 17 μm, each resolution element is sampled by 2.9 pixels, so we are above the Nyquist sampling criterion. The Rayleigh range is estimated using the experimental value of 24 μm for Δx in equation 2-18; it is close to the Rayleigh range expected in Y because the experimental value of Δx is so close to the theoretical value of Δy.

We also used an image stack of the TiO_2 point scatterers in PDMS to measure the phase resolution of the system. We choose three of the brightest scatterers located near the top of the B-mode and compute the standard deviation of the optical phase in time, from a stack of 1000 frames recorded at 1 kHz. The average of those three standard deviations is 0.175 radians, and this is our estimate of the phase resolution. The theoretical value is computed using the measured SNR from the TiO_2 point scatterers which was 60 dB (with an exposure time of 167 μs and a sample power of 7.66 mW). The theoretical value of the phase resolution given a measured SNR of 60 dB is 0.124 radians.

One major concern about line-field OCT is the potential for crosstalk causing resolution degradation. Crosstalk occurs when multiply scattered light is recombined with light from one scatterer and is mapped to the same camera pixel. Most point-scanning OCT systems couple the light back into a single mode fiber, which acts as a confocal gate to reject multiply scattered photons. Because LF-OCT systems are free-space optical systems, they lack the same confocal gating, so crosstalk is a concern. The experimental value of Δx being larger than the theoretical could be an indicator of crosstalk; however, because the measured value is very close to the upper bound given by Δy we would not say that resolution degradation is a huge problem for this system. Indeed, we found in later optical designs and alignments that the experimental value of

Δx was in excellent agreement with the theoretical value. Possibly, the SC source has lower spatial coherence than the lasers and SLDs typically employed in point-scanning OCT systems. These results are summarized in Table 2-5.

2.3.5 Optical Design of LF-OCT System Version 2

Version 1 of the LF-OCT system was significantly improved in the next implementation, acknowledging that in Version 1, the transverse extent of the beam filled only about half of the pixel array, that the transverse resolution was larger than that typically achieved by SD-OCT systems, and that the SNR was relatively low. Additionally, the axial resolution was not as good as theoretically expected due to imprecise optical alignment techniques. With each subsequent realignment, the alignment procedure was improved step-by-step over the course of several years to eventually remove many of the alignment issues. In particular, the focusing in the spectral plane (transverse plane in which light is focused at the spectrometer, see Figure 2-5) was improved compared to the first alignment procedure used so that we were able to bring the experimental axial resolution down much closer to the theoretical limit. However, some of the poor performance of the first version of the LF-OCT system comes from the design itself. After purchasing our own SC light source, we chose to re-design the whole system to improve the transverse resolution and to better fill the entire pixel array.

After working with the demo SC source, we purchased an EXR15 from NKT Photonics, which has essentially the same power spectral shape as the demo source we were using, but with greater total power. We used a fiber-optic, hand-held spectrometer to measure the spectrum of both the demo source (an NKT Photonics EXR9) and the new SC source (and NKT Photonics EXR15). The normalized spectra are shown in Figure 2-18. The FWHM of the EXR15 is 20 nm

greater than that of the demo source and has a slightly more uniform, approximately-Gaussian shape (without the peak at 650 nm). The total power output over the 605-950 nm bandwidth (measured immediately after the long-pass filter in the optical setup) is 1.1 Watts.

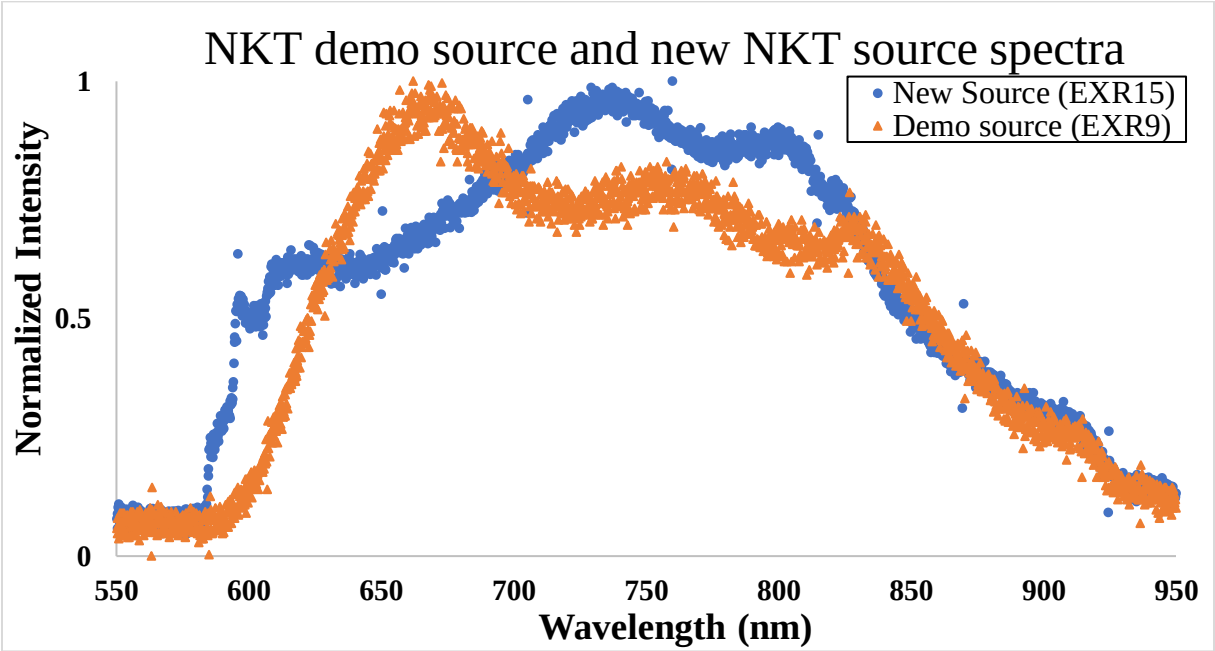

Figure 2-18 Normalized Spectra of the two SC sources.
The normalized spectra of the demo source and the purchased source as measured by a hand-held fiber-based spectrometer. The FWHM of the EXR15 is ~20 nm greater than that of the demo source and is slightly less peaked at the visible end of the spectrum.

To better fill the pixel array, and to improve the transverse resolution, the beam diameter on L4 needs to be expanded. To accomplish this, L1 (previously fl = 200 mm) was replaced with a lens of focal length 300 mm, and L5 was replaced by a lens with a focal length of 200 mm (previously fl = 100 mm). These lens changes increased the beam diameter incident on L3/L4 from 4 mm to 6 mm. The larger beam diameter on L4 shrinks the diffraction-limited spot size (*i.e.* the transverse resolution Δy) from 25 µm to 17µm. Because the measured value of Δx is something $\leq \Delta y$, we use the theoretical value of Δy to set the upper limit on what the measured Δx

will be. The magnification between the object and image planes was doubled from 2 to 4, meaning that we were able to fill the entire pixel array to ensure that all pixels were used. The focused spotsize in X on the sensor, $2\omega_{0sensor}$, is now 16.04 µm; since this is sampled by only one pixel, the theoretical value of Δx is given by the physical distance mapped to two pixels, 8.50 µm.

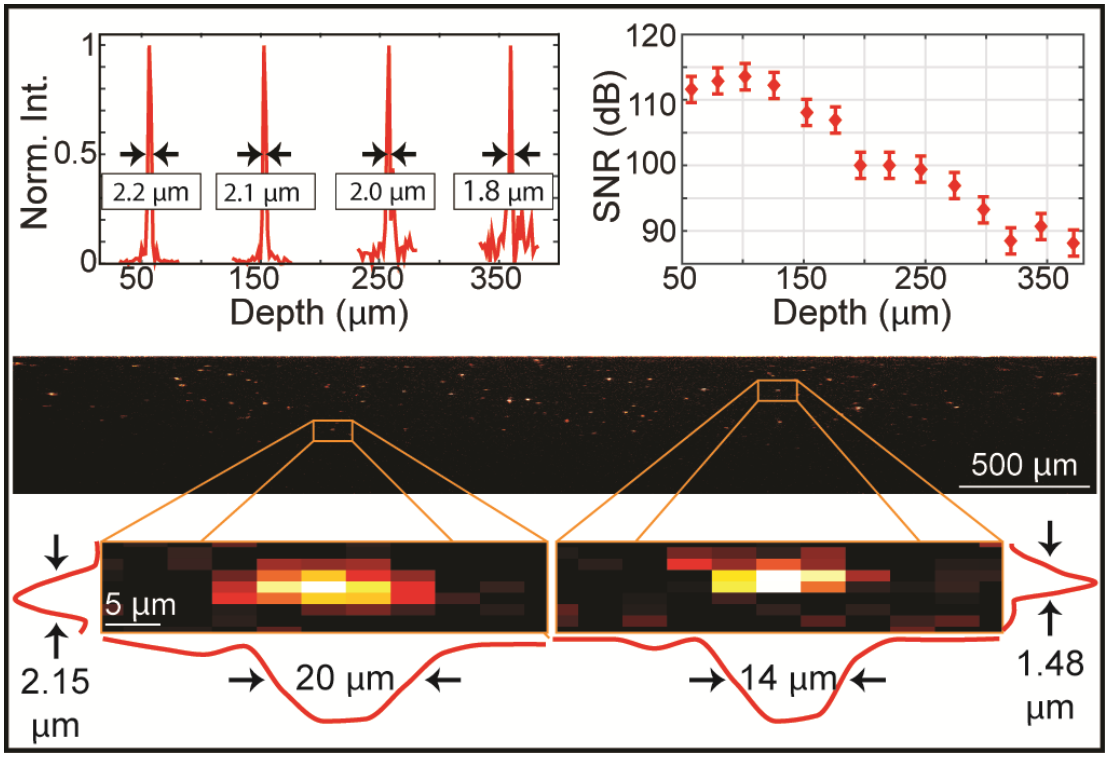

Figure 2-19 Summary of Characterization of LF-OCT System Version 2.
The axial and transverse resolution have been significantly improved since version 1 and are consistent with the theoretical values. The SNR roll-off in depth is ~20 dB over ~ 300 µm.

With more practice and fine-tuning of the alignment procedure, we were able to bring the experimental axial resolution down to 1.8 ± 0.2 µm in air, much closer to the theoretical value of 1 µm. To measure the maximum SNR achievable with the EXR-15 and the Photron Fastcam SA3, we again imaged a flat silver mirror at various depths within the sample arm. However, this

time we used the camera's maximum exposure time to measure the maximum SNR. At the camera's fastest framerate of 1000 fps, the maximum exposure time is 1/1000 = 1 ms. In order to avoid saturating the camera with the strong back-scattering from a silver mirror, we heavily attenuated the sample arm power with the NDF in the sample arm. Attenuation also ensures that the measured SNR is well below the dynamic range of the camera. The Photron Fastcam SA3 has a 12-bit sensor, meaning that the intensity recorded by each pixel is binned into an integer value ranging from 1 to 2^{12}. A 12-bit sensor therefore has a bit depth of $10*\text{Log}_{10}(2^{12}) = 36$ dB. To accurately measure the SNR of the system, the measured SNR should be below the bit depth. Therefore, the total sample arm power exiting the beam splitter was attenuated from 500 mW to 0.115 mW incident on the sample with the NDF. The theoretical SNR was 129 dB, and the experimental SNR (after adding back the 73 dB of optical attenuation) was 113 dB. The total losses of 14.6 dB in the collection optics brings the theoretical SNR down from 129 dB to 114.4 dB, in very good agreement with our experimental SNR of 113 dB. The system was characterized using the same methods as outlined for version 1. As shown in Figure 2-19, the SNR rolls off from a maximum value of 113 dB to ~88dB over a depth of 300 μm.

To measure the phase stability of the system, we imaged a silver mirror at 1000 fps with an exposure time of 0.2 ms and a total sample power of 4.86 mW. The measured SNR was 96 dB after adding back 34.3 dB of optical attenuation. The phase resolution expected from this SNR is 0.102 radians (equation 2-16). We estimate the phase resolution by taking the standard deviation of the optical phase of the brightest pixel in the center A-line across all 1000 frames. The standard deviation is 0.114 radians, in good agreement with the theoretical value. The results of version 2 are summarized and compared with version 1 in Table 2-5, and the optical elements

used in both versions are summarized in Table 2-6. The SNR and phase resolution (both values of the imaging parameters used rather than the optical design) are summarized in Table 2-7.

Table 2-5 Summary Comparing Performance of LF-OCT System, Versions 1 & 2

			LF-OCT Version 1		**LF-OCT Version 2**	
			Theoretical Value	**Measured Value**	**Theoretical Value**	**Measured Value**
Transverse Imaging	D_{L4T}	Transv. FOV (mm)	4.00	4.04	4.35	4.29
	$\Delta x(n=1.34)$	In-plane Transv. Res. (μm)	17.0	24± 3	8.50	14±3
	$\Delta y(n=1.34)$	Out-of-plane Transv. Res. (μm)	25.5	-----	17.0	-----
	$Z_R(n = 1.34)$	Rayleigh Range in Y (μm)	853	822	379	256
	D_{L7T}	Beam diam. in X on sensor (mm)	8.0	8.08	24.0	24.0
	$2\omega_{0sensor}$	Focused size of scatterer in X on sensor (μm)	8.02	48	16.04	56
	$\frac{2\omega_{0\_sensor}}{pixelsize}$	# Pixels sampling $2\omega_{0\_sensor}$	0.46	2.82	0.94	3.29
	$2(FOV / N)$	Object space mapped to 2 pixels (μm)	17.0	17.2	8.50	8.38
	Δz	Axial resolution in air (μm)	1.01	2.4 ± 0.6	1.01	1.8±0.2
	$z_{\max}$ (not sample-limited)	Imaging Depth in air (μm)	524	509	524	527

Table 2-6 Summary of Optical Components Used in LF-OCT System, Version 1 & 2

Component	LF-OCT Version 1	LF-OCT Version 2
Light Source	NKT Photonics EXR9-OCT Low Noise Collimated beam diameter of ~1 mm	NKT Photonics EXR15 Collimated beam diameter of ~1 mm
Optical Filters	605 nm long pass 950 nm short pass	605 nm long pass 950 nm short pass
L0	f = 35 mm	f = 35 mm
L1	f = 200 mm	f = 300 mm
CL	f = 100 mm	f = 100 mm
L2	f = 100 mm	f = 100 mm
L3/L4	f = 100 mm	f = 100 mm
L5	f = 100 mm	f = 200 mm
L6	f = 50 mm	f = 50 mm
L7	f = 100 mm	f = 100 mm
Beam Splitter Cube	Newport Broadband Non-polarizing 50:50 beam splitting cube	Newport Broadband Non-polarizing 50:50 beam splitting cube
Diffraction Grating	Wasatch Photonics 600 lines/mm	Wasatch Photonics 600 lines/mm
Camera	Photron Fastcam SA3 1024 x 1024 CMOS pixel array with 17 µm pixels	Photron Fastcam SA3 1024 x 1024 CMOS pixel array with 17 µm pixels

Table 2-7 Summary of SNR and Phase Resolution for LFOCT Versions 1 and 2

	LF-OCT Version 1			**LF-OCT Version 2**		
	Imaging Parameters	**Theoretical Value**	**Measured Value**	Imaging Parameters	**Theoretical Value**	**Measured Value**
SNR	Silver Mirror T = 3.3 µs Ps = 400 mW R_S = 1	107 - 14.6 = **92.4 dB**	**88 dB**	Silver Mirror T = 1.0 ms Ps = 492 mW R_S = 1	129 -14.6 = **114.4 dB**	**113 dB**
SNR	TiO_2 T = 167 µs Ps = 400 mW	124 - 14.6 = 109.6 dB	60 dB	Silver Mirror T = 0.2 ms Ps = 492 mW	123-14.6 = 108.4	96 dB
δθ (rads)	R_S = 1 1000 Frames @ 1 kHz	**0.124**	**0.175**	R_S = 1 1000 Frames @ 1 kHz	**0.102**	**0.114**

2.3.6 Summary of LF-OCT Systems to Date

Previously, the fastest LF-OCT was reported at 51.5k A-lines/s, but with a coarse axial and transverse resolution of 7.4 µm and 16.4 µm respectively and an SNR of 90 dB [61]. The highest reported SNR for a LF-OCT was 94 dB with an axial of 7.6 µm in air and an imaging speed of up to 100k lines/s, although the speed in reported images was slower due to image averaging [62]. The best reported resolution was 1.15 µm and 1.3 µm (axial and transverse) with an SNR of 86 dB and a frame rate of 10 fps [63]. Each of these three best metrics suffers in one or both of the other two areas. Our combination of an SNR of 113 dB with a frame rate of 1000 fps (1.02 million A-lines/s meaning each B-mode image is acquired in 1 ms), and an axial resolution of 1.8 µm represents the best combination of all three metrics [50]. This outstanding combination is made possible by the low-noise, high-power SC sources commercially available today used in conjunction with a line-field configuration.

2.4 ALI Imaging using LF-OCT

In order to demonstrate the high resolution, high speed and high SNR of the LF-OCT system, the system was used to image beating cilia of human bronchial epithelial (hBE) cells *in vitro*. One of the most important aspects of a LF-OCT configuration is that the simultaneous A-line acquisition allows us to spatially map features of dynamic samples; point-scanning OCT systems can capture the dynamics of a single A-line in time by not mechanically scanning the beam so that the A-lines are recorded in one transverse location; line-field OCT systems can more easily and more quickly capture the dynamics of an entire B-mode in time. The usefulness of this feature is demonstrated in the captured images of beating cilia.

Beating cilia of hBE cells are of particular interest because they are markers for many kinds of respiratory diseases [64]. Mucus provides a first line of defense against infection by trapping inhaled pathogens in our airways. Beating cilia propel mucus to the esophagus which expels pathogens from the airway [65]. Airway diseases such as chronic obstructive pulmonary disorder (COPD) and Cystic Fibrosis (CF) are characterized by a breakdown of mucociliary clearance resulting in chronic lung infections [66,67]. It is therefore beneficial to be able to assess ciliary activity at the respiratory epithelium. Previously, the beating of a single cilium tip has been tracked using a μOCT system with 1 μm axial resolution to make a direct measure of ciliary beat frequency (CBF) [68]. Although our parallel SD-OCT is not capable of spatially resolving individual cilia, it is fast enough to detect the rapid speckle fluctuations of beating cilia, which were previously described in Ref. [69]. Importantly, the quantitative measures of ciliary activity in [68,69] were limited to individual A-lines in time (M-mode), while the use of parallel OCT in this study enables assessment of ciliary dynamics over the entire B-mode frame.

In this study, well-differentiated cultures of hBE cells demonstrating mucociliary transport are prepared as previously described [70,71]. Briefly, primary human airway epithelial cells are isolated from excess tissue by the University of North Carolina Tissue Procurement and Cell Culture Core under protocols approved by the University of North Carolina Institutional Review Board. Then, cells are plated on collagen-coated membranes (MilliCell, Millipore, PICM03050, 0.4 μm, 30-mm diameter) and cultured at the air/liquid interface (ALI) using established protocols [70,71]. The cells form a pseudostratified mucociliary epithelium with abundant cilia at an ALI. Note that, in these studies, the culture insert is modified to create a circular track allowing mucus to be transported in a continuous circular path [72] (Figure 2-21 (a)). Cultures are examined by conventional wide-field microscopy, and those that have fully developed cilia and show continuous mucus transport are imaged with the LF-OCT system.

The hBE cells were imaged with a framerate of 1kHz using an exposure time of 100 μs with a total sample arm power of 259 mW. Three stacks of 1360 images were recorded, along with the corresponding stacks of 20 reference images. Representative B-mode images of the hBE cell cultures are shown in Figure 2-20. With the high SNR, the hBE cells are clearly visible above the background noise. The imaging depth and SNR roll-off are sufficiently good that the membrane under the hBE cells has fully developed speckle at a depth of several hundred microns within the image.

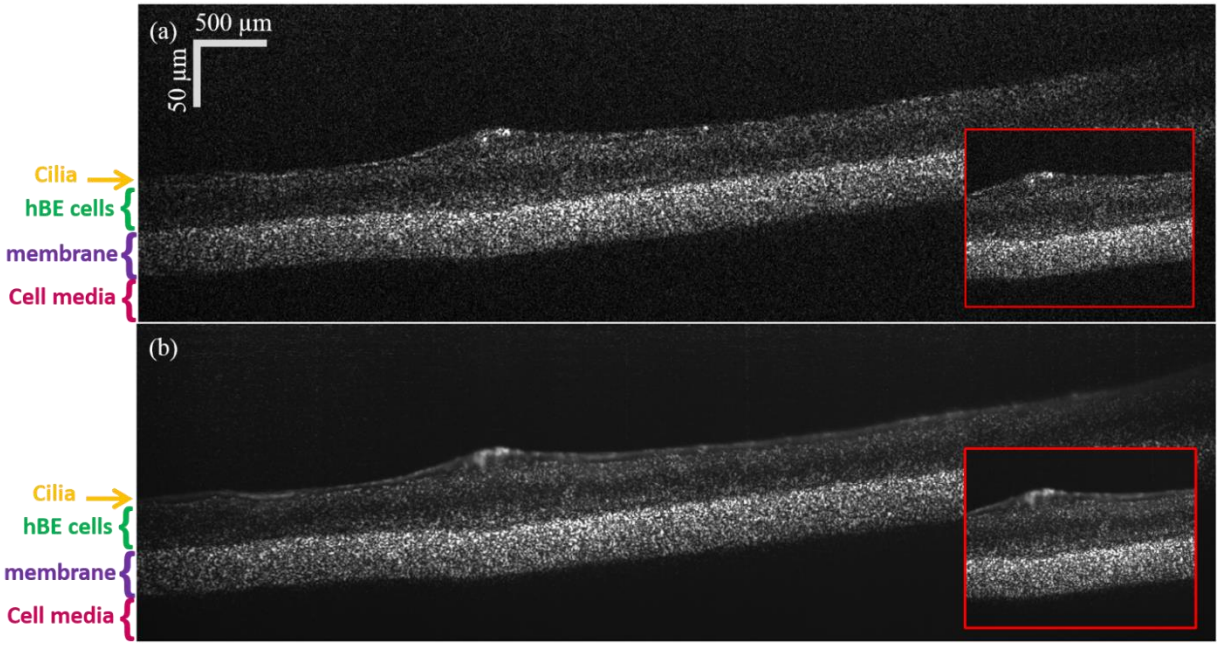

Figure 2-20 B-mode Images of Ciliated hBE Cells.
Representative B-mode images of ciliated hBE cells cultured on membranes. A) A single B-mode frame. B) A time average from a stack of 1000 frames. The beating cilia appear as a blurred line along the top of the hBE cells.

We compare a static B-mode image (Figure 2-21 b) with the known structure of the hBE cell culture (Figure 2-21 a). From the static image, only the membrane, air, and media regions are clearly distinguishable; it is not possible to distinguish the hBE cells, the periciliary layer (PCL) or the mucus. However, regions of rapid ciliary activity become apparent in video generated from successive B-mode frames. To quantify the dynamic information, we analyzed the speckle fluctuation spectrum at each pixel. Example fluctuation spectra are displayed for a single column in time in Figure 2-21 (c). In this data, the PCL is attributed to a rapidly fluctuating layer with high-frequency components (yellow arrow and bracket), the membrane is attributed to a highly scattering, stationary layer (purple bracket), and the hBE cells are in between (green bracket).

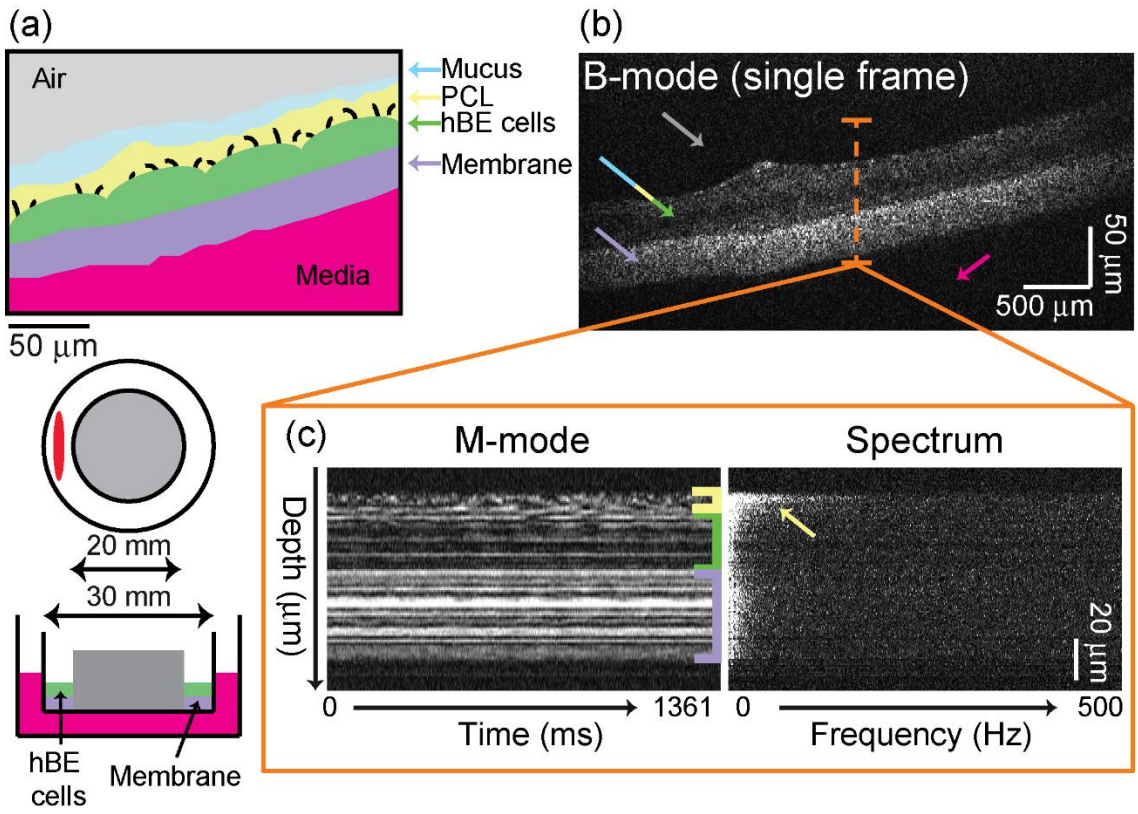

Figure 2-21 Spectral Analysis of Beating Cilia with LF-OCT.
LF-OCT of an *in vitro* ALI hBE culture. (a) Cartoon of an hBE culture cross-section (top) and diagram of imaging geometry (bottom). (b) B-mode OCT image of a single frame. Arrows indicate features color-matched to those in panel (a). (c) M-mode image reconstructed from one A-line in time of the B-mode stack and its corresponding Fourier spectrum. The depth of the M-mode and speckle fluctuation spectrum image spans from 103 µm to 247 µm.

Respiratory epithelial cilia are known to beat in a time-harmonic way with a distinct CBF. However, the power spectrum of the resulting OCT signal amplitude is expected to contain frequency components much larger than CBF because 1) the ciliary motion is not generally sinusoidal, and 2) amplitude and phase modulation results in further nonlinearity in the OCT signal amplitude. It was previously shown that the median frequency (f_m) of the speckle fluctuation spectrum, which is posited to be directly proportional to the CBF, is correlated with changes in ciliary activity under isoflurane treatment [69]. Here we measured f_m from the fluctuation spectrum at each pixel in the B-mode image by omitting the DC term, and subtracting

white noise (which was estimated as the average over the 300 – 500 Hz band). Because f_m in regions of low scattering can be large, a method for automatically segmenting the f_m map was developed to select only features with significant fluctuation amplitude. This method involves thresholding based upon the area under the curve of the fluctuation spectrum (after omitting DC and subtracting white noise). Since this value is, on average, two orders of magnitude lower in regions outside the cell culture than inside the culture, by setting a threshold on this value, the f_m map is automatically segmented.

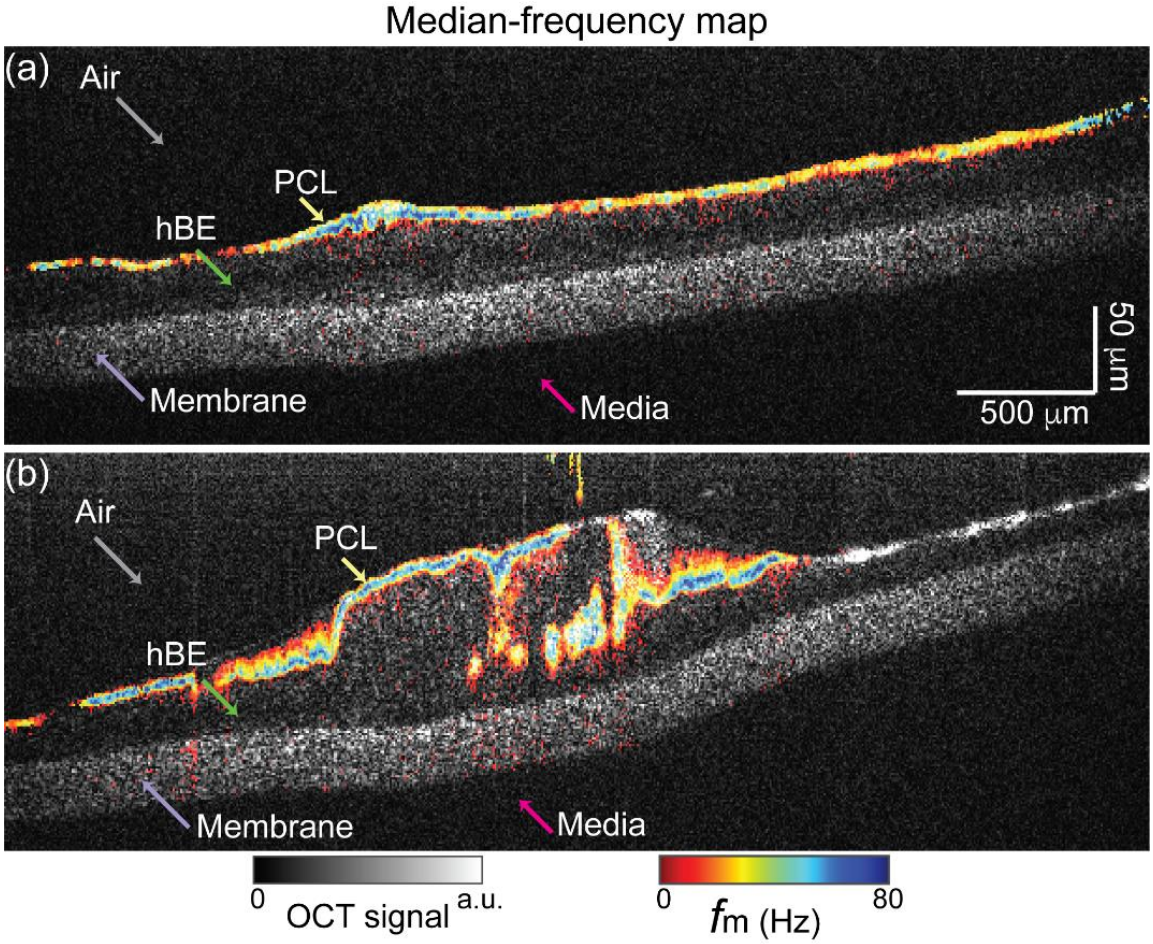

Figure 2-22 Median Frequency Map of Cilia.
Dynamic OCT imaging using the median-frequency map (f_m) for two hBE cultures (a) without mucus and (b) with mucus. Colored arrows indicate the different layers of the culture.

Figure 2-22 shows the f_m map overlaid in rainbow hue on the same B-mode image from Figure 2-20 of the *in vitro* hBE cell culture. Importantly, from this f_m map one can now distinguish between the PCL and the hBE cells, where f_m is a semi-quantitative measure of ciliary activity. In fact, the PCL shows up distinctly as a thin layer on the upper border of the hBE cells. Note that this image does not show a mucus layer because the hBE culture has been washed to remove any thick, turbid mucus. Next, dynamic imaging of hBE cells with endogenous mucus is performed. Rather than a mono-layer of cells (as in Figure 2-22 a), the area of the culture imaged in Figure 2-22 (b) has a gland-like structure such that there are cilia above and below the cells. The f_m analysis produces images that selectively contrast ciliary activity and enables identification of the PCL. For both cultures, the ciliary activity is characterized by f_m of ~ 50-80 Hz. This is larger than the actual CBF (typically 6-8 Hz for healthy adult airways [73]) but is known to change proportionally with changes in CBF [69].

One concern with using high-power SC light sources with OCT is the potential to damage live cells by photothermal heating. The amount of NIR absorption is sample dependent, and therefore any photothermal hearing will be sample dependent. These particular hBE cell cultures do not appear to be absorbing enough of the NIR to be significantly heated up or damaged. Heating is a transient effect, and we would therefore expect to see some change in CBF over time for long, continuous exposures if the cell cultures were heating up. We imaged the same culture three times back to back (for 1.36 seconds each time, with 1-2 minutes of continuous light exposure between each 1.36 second imaging cycle), and found that the median frequency corresponding to the ciliated regions did not change, as shown in Figure 2-23. These median frequency maps correspond to the same cell culture used in the bottom panel of Figure 2-22. There is no change in the median frequency after seven minutes of continuous exposure to the

SC light source. This suggests that the cells are not suffering from significant photothermal heating.

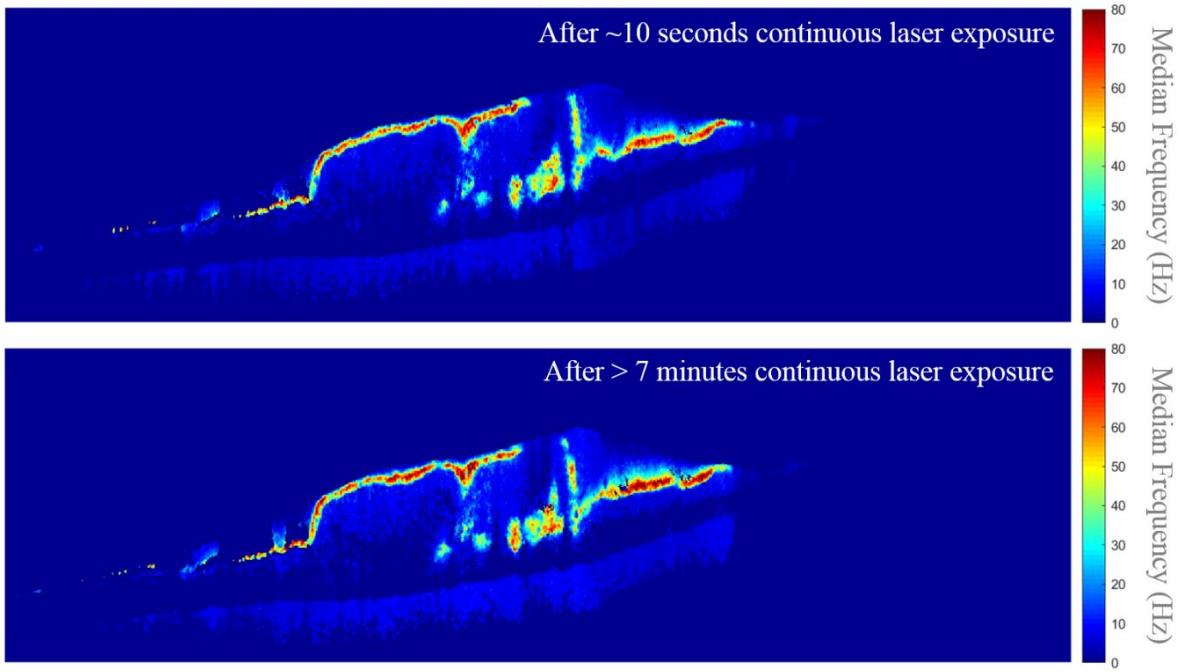

Figure 2-23 Photothermal Heating in Median Frequency Maps.
These median frequency maps were recorded ~ 7 minutes apart with continuous laser exposure from the SC source during that time. The lack of change in the median frequency maps suggests that the CBF did not change significantly, which in turn suggests that these cell cultures are not suffering from photothermal heating due to exposure to the high-powered SC source.

In summary, a broadband SC source has been implemented in a line-field SD-OCT system. The main advantages of this source are its wide spectral bandwidth providing ultrahigh-resolution images (axial resolution of 1.8 μm), and its high optical power which results in high-sensitivity images (maximum SNR of 113 dB). Importantly, the parallel SD-OCT geometry takes advantage of this increase of optical power by distributing it across a line focus. We have not observed any change in f_m by potential photothermal heating after more than seven minutes of continuous laser exposure, however, further investigation into heating in the line-focus geometry

is needed before use *in vivo*. The combination of this SC source with a high-speed camera in a parallel OCT configuration now enables kHz frame rates (with effective MHz line rates) with a competitive imaging performance compared with commercial SD-OCT systems. This will enable new applications in studying the dynamics of highly transient effects such as biological motility and magnetomotive imaging, which relies on the assessment of dynamic motion

CHAPTER 3 - DESIGN OF LINE-FIELD MMOCT SYSTEM

This chapter describes the theory of MMOCT and details about the development of a LF-MMOCT system. Section 1 begins with an overview of MMOCT theory. Then, in Sections 2 and 3, I describe the design of the hardware and software necessary to convert the LF-OCT system described in chapter 2 to a LF-MMOCT system. The first LF-MMOCT applications are discussed in Chapter 4.

3.1 MMOCT Theory

To begin the consideration of magnetic contrast agents for biological samples, we consider the magnetic properties of the biological samples under investigation. For endogenous magnetic nanoparticle detection, we are concerned with superparamagnetic iron-oxide nanoparticles (as found in certain species of magnetotactic bacteria [74]) and the surrounding biological tissues, which are typically slightly diamagnetic. All materials can be characterized by a magnetic susceptibility $\chi \equiv \partial M/\partial H$, where M is the magnetization and H is the magnetic field. In general, the magnetic susceptibility is largest at low fields ($H \sim 0$) and goes to zero at large fields as M approaches the saturation magnetization, M_{sat}. Diamagnetic materials have small, negative magnetic susceptibilities, meaning that the magnetic fields induced by the presence of an external magnetic field are anti-parallel to the external field. Biological tissues typically have magnetic susceptibilities approximately equal to that of water [75]. Paramagnetic materials, in contrast, generate induced magnetic fields in the presence of an external magnetic field which align with the external field. Superparamagnetism is a phenomenon in which the magnetization

of very small (nano-scale) ferromagnets (single-domain due to the small size scale) will randomly flip due to thermal fluctuations. Over long enough time scales (*i.e.* measurement times longer than the Néel relaxation time [76]), the magnetization is zero on average. Superparamagnetic particles have relatively large magnetic susceptibilities. For instance, the volume magnetic susceptibility of water (a diamagnetic material) is on the order of 10^{-5} and the magnetic susceptibility of superparamagnetic magnetite nanocrystals is on the order of 1 [5].

In the presence of an external magnetic field, a superparamagnetic particle embedded in a diamagnetic, elastic, optically scattering medium (*e.g.* biological tissue) will experience a magnetic force. The force on the superparamagnetic particle for $M << M_{sat}$ is typically written as follows

$$F = \frac{V\chi}{\mu_0}(B\bullet\nabla)B \tag{3-1}$$

where V is the volume of the particle, χ is the difference in the magnetic susceptibility of the particle and the surrounding medium, B is the magnetic flux density, and μ_0 is the magnetic permeability of free space (where we have made the approximation that, in weakly magnetic media, $\mu \approx \mu_0$) [4–8,77,78]. This can be understood in terms of the force on a magnetic dipole:

$$F = (m\bullet\nabla)B \tag{3-2}$$

where the magnetic dipole moment, m, can be written as the volume of the particle V multiplied by the particle's magnetization, M, and the magnetization can be written in terms of the magnetic susceptibility, χ, and the magnetic field H.

The orders-of-magnitude difference between the magnetic susceptibility of a superparamagnetic particle and a weakly diamagnetic medium means that, for a given external magnetic field, the force experienced by the superparamagnetic particle will be orders of

magnitude greater than the force experienced by the surrounding medium. The force on the superparamagnetic particle will displace the particle in the direction of the magnetic gradient. If the particle is mechanically coupled to the elastic medium, the medium will be displaced as well. The displacement of the optically scattering medium is detectable with OCT, and thus, superparamagnetic nanoparticles can be used as contrast agents in OCT. This concept is the foundation of MMOCT.

Importantly, the aim of this dissertation is single magnetic nanoparticle detection as a proof of concept that endogenous magnetite detection is possible using LF-MMOCT. As has been discussed in Chapter 2, the best axial resolution achievable with SD-OCT is on the order of 1 μm. The size of superparamagnetic nanoparticles is, by definition, on the nanoscale, meaning 1-3 orders of magnitude smaller than the best axial resolution of an SD-OCT system. From this information alone, it may seem that single magnetic nanoparticle detection with SD-OCT is impossible, and it is true that MMOCT is not capable of directly imaging magnetic nanoparticles. However, MMOCT does not involve imaging the magnetic nanoparticle itself, rather inferring the presence of the nanoparticle based on the behavior of the surrounding medium.

The mechanism underlying MMOCT theory is that displacement of a superparamagnetic iron oxide (SPIO) which is mechanically bound to an elastic, optically scattering medium will cause a deformation in the medium which is detectable with OCT. If a sinusoidally varying magnetic field is applied, the SPIOs will experience a sinusoidally varying magnetic gradient force in the axial direction. This time-varying magnetic gradient force combined with the elastic restoring force of the medium will together result in the periodic axial displacement of the SPIO. These periodic axial displacements will deform the surrounding scattering medium, creating a phase shift in the back-scattered light relative to the phase from the stationary reference mirror.

The change in time of the optical phase of the back-scattered light will be periodic (with a frequency equal to the modulation frequency of the magnetic field) and in-phase with the magnetic field. By detecting the resultant periodic phase shift in light back-scattered from the surrounding medium, we can infer the presence of superparamagnetic nanoparticles embedded in the sample, as illustrated in Figure 3-1.

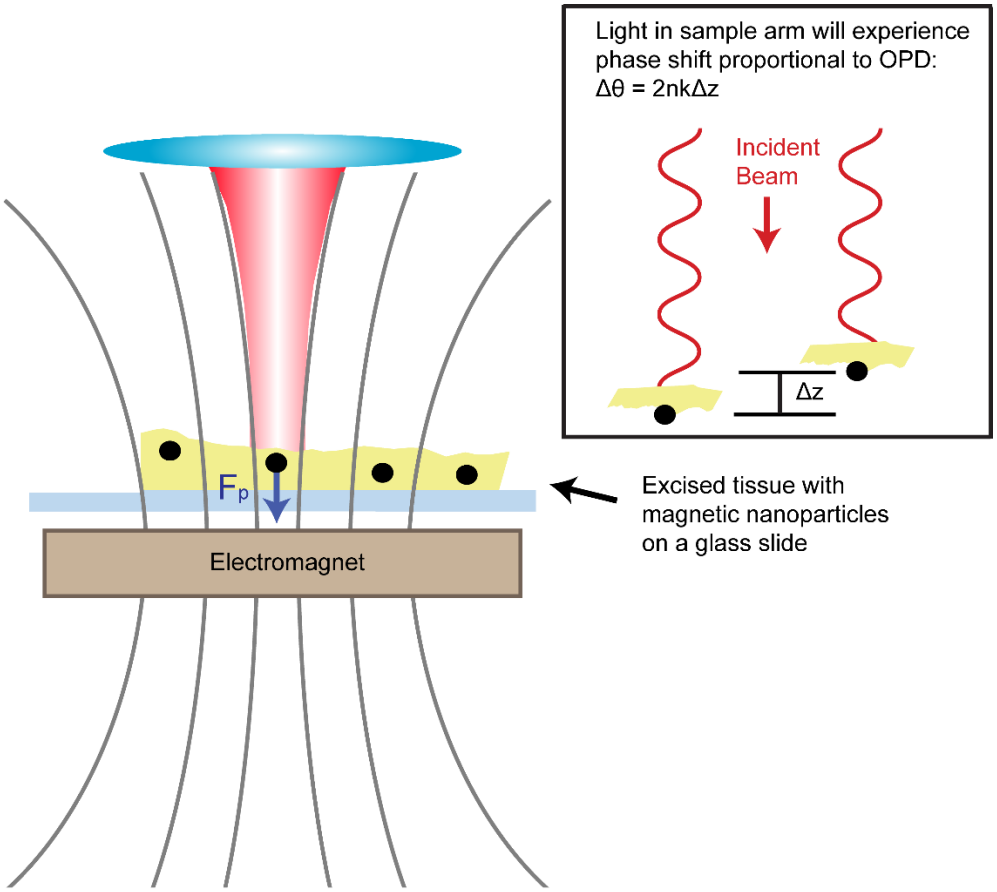

Figure 3-1 Illustration of the principle of MMOCT.
An electromagnet produces a sinusoidally varying magnetic gradient field in the imaging region of interest. SPIOs in this region feel a corresponding magnetic gradient force, F_P, and are axially displaced, causing the surrounding scattering medium to be periodically deformed. The displacement of the medium, Δz, creates a phase shift in the back-scattered light, $\Delta\theta$, which is detectable by phase-sensitive SD-OCT.

Recall that the optical phase is related to the OPD between a scatterer and the reference mirror, Δz, according to

$$\Delta z = \frac{\lambda}{4\pi n}\Delta\theta \tag{3-3}$$

Equation 3-3 tells us that the smallest detectable displacement, ∂z, between two consecutive frames is ~ 5 nm given that the measured rms phase noise, $\partial\theta$, of the LF-OCT system is ~0.1 radians (as reported in Chapter 2) and a center wavelength of 800 nm and a refractive index of 1.34. SD-OCT, by nature of being phase-sensitive, can detect sub-resolution movements; this LFOCT system in particular is sensitive to axial displacement three orders of magnitude below the axial resolution of 1.8 μm.

The displacement resolution is an estimate of the smallest displacement that can be reliably detected from the direct measurement of the optical phase shift produced by a single axial displacement, but the lock-in detection method used in MMOCT image processing makes the displacement sensitivity even higher. Understanding the sensitivity of this system to very small axial displacements is important to establish the motivation for using LFMMOCT for single magnetic particle detection. Therefore, a brief overview of the signal processing is outlined here, while a more detailed description is given in Section 3.3.2.

The MMOCT image processing steps are summarized in Figure 3-2. The force on the SPIOs is proportional to the square of the gradient of the magnetic field. Thus, to produce a sinusoidal magnetic gradient force, the applied magnetic field takes the form of a square-root-sine function. The resultant displacement of SPIOs is then a periodic function with a frequency equal to the magnet modulation frequency, f_{mag}. To select only motion which occurs at f_{mag}, we take a Fourier transform of the differential optical phase of each pixel in time. Using the Goertzel algorithm, we select only the component of the Fourier transform for which $f = f_{mag}$; this is the

frequency-locking step. Importantly, the discrete Fourier transform used in the Goertzel algorithm has an inherent SNR gain [79] proportional to the number of discrete samples recorded which makes the lock-in detection of periodic motion more sensitive than the displacement resolution, δz, of the SD-OCT system. In addition to frequency-locking, we employ phase-filtering to reject any motion that is not in-phase with the magnetic field (*e.g.* diamagnetic motion of the surrounding medium).

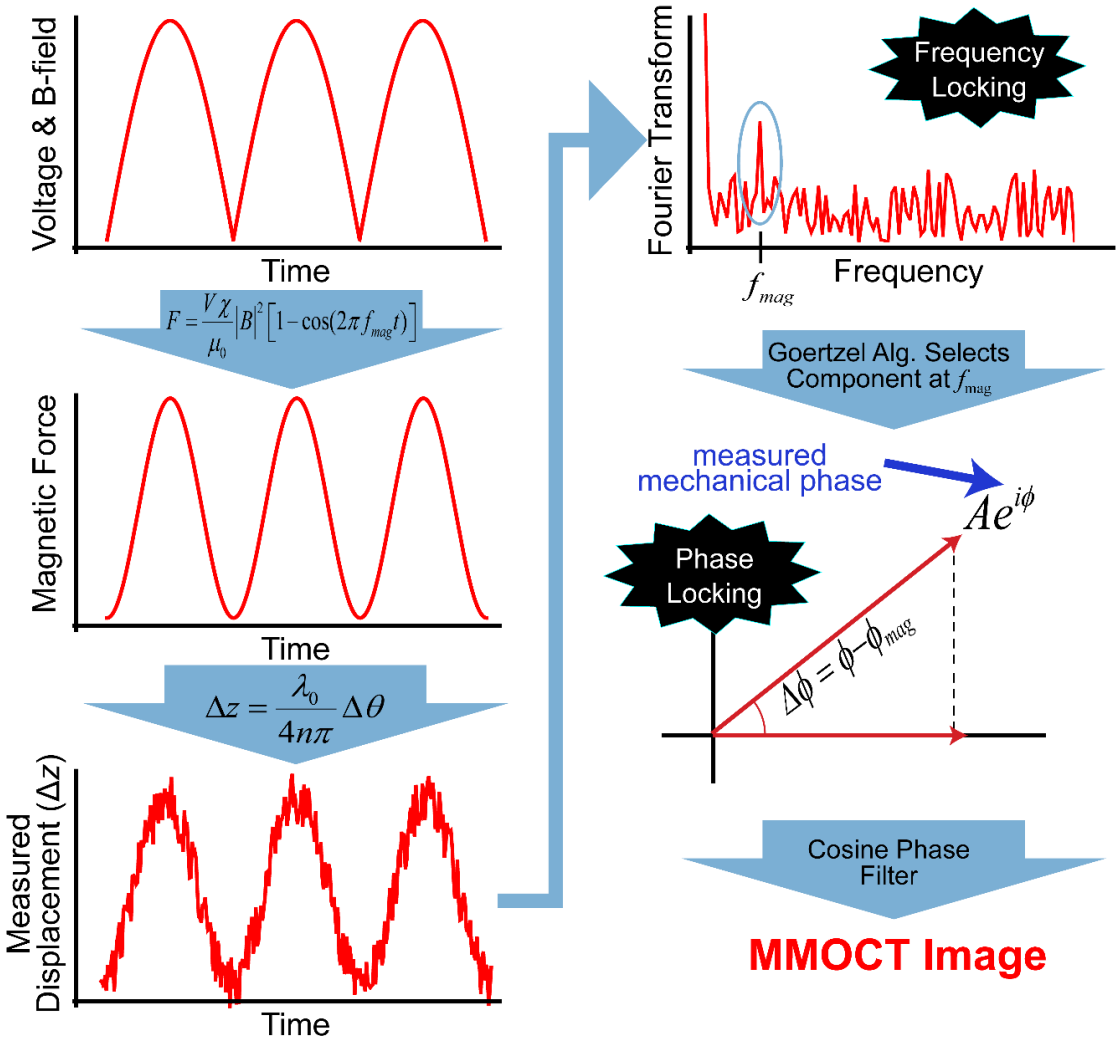

Figure 3-2 MMOCT Image Processing Steps.
Schematic diagram outlining the lock-in detection of both the frequency and phase of the displacement of magnetic particles subject to a sinusoidally varying magnetic gradient force.

The signal processing steps we use mean that this LF-MMOCT system is sensitive to displacements < 5 nm. We do not yet know what the theoretical minimum detectable size is for a superparamagnetic particle. To know this, we would need a noise model for the MMOCT signal in the absence of magnetic particles. Such a noise model would incorporate the shot noise of the light source, the phase noise of the OCT system, and the DFT bin size (the noise being the average DFT amplitude over the frequency bin centered on the magnet modulation frequency). Experimentally, we can detect anything that appears above the noise floor in the Fourier transform of the differentiated optical phase. This means that we may be able to estimate the minimum detectable particle size by imaging smaller and smaller particles and empirically determining what is the smallest size that gives some signal above the noise floor of the DFT.

The MMOCT theory and magnetic particle detection steps outlined thus far are true for any general MMOCT application. To specifically address the issue of single MNP detection, we need a model for the vibration amplitude of a single particle bound to an elastic medium and subject to a time-varying magnetic gradient force. For the discussion in the rest of this dissertation, the convenient acronym MNP is used to describe magnetic particles which are on either the nano-scale (*e.g.* endogenous magnetite in bacteria) or the micro-scale (*e.g.* the magnetic particles detected with the LF-MMOCT system in Chapter 4). This same problem has been investigated by ultrasound research groups interested in using the vibration amplitude of particles embedded in tissues to infer information about the biomechanical properties of the tissue [80–86]. Specifically, Aglyamov *et al* developed a model for the time-dependent vibration amplitude of a solid sphere bound to a viscoelastic medium under the influence of acoustic radiation forces [80]. The displacement of the solid sphere subject to a time-varying external force is multiplied by the impulse response of the elastic medium. (This is done in the frequency

domain.) Applying an inverse Fourier transform, the time-domain displacement of the solid sphere is obtained. In our case, the external force is the magnetic gradient force that takes the form:

$$F = \frac{V\chi}{2\mu_0}\nabla|B|^2\left[1-\cos(2\pi f_{mag}t)\right] \tag{3-4}$$

(This is the same expression as in equation (3-1), but here the time-dependence is made explicit.) Assuming that the external force is impulsive (acting on a very small region of space only), neglecting viscoelastic effects, and assuming the system is in a steady state, my lab mate Benjamin Levy worked out the math in order to arrive at the following expression for the time-dependent displacement (which is the same expression as the displacement of particles in his magneto-motive ultrasound system):

$$\begin{aligned}
z(t)_{SS} &= \frac{A}{6\pi\mu R}\left[1-C(\chi,\psi)\,\mathrm{Cos}\left(2\pi f_{mag}t-\Phi(\chi,\psi)\right)\right] \\
C(\chi,\psi) &= \frac{1}{\sqrt{\chi^2+\psi^2}} \\
\Phi(\chi,\psi) &= \mathrm{Tan}^{-1}\left(\frac{\psi}{\chi}\right) \\
\chi &= 1-\frac{\rho_{Med}(2\pi f_{mag})^2R^2}{9\mu}\left(1+2\frac{\rho_{MNP}}{\rho_{Med}}\right) \\
\psi &= 2\pi f_{mag}R\sqrt{\frac{\rho_{Med}}{\mu}}
\end{aligned} \tag{3-5}$$

where A is the amplitude of the external force, $\nabla|B|^2(V\chi/2\mu_0)$ as shown in equation 3-4, $\mu = E/2(1+\nu)$ is the shear modulus of the medium in terms of ν, the Poisson ratio, and E, the Young's modulus of the medium, R is the radius of the MNP, f_{mag} is the magnet modulation frequency, and ρ_{Med} and ρ_{MNP} are the densities of the medium and the MNP respectively. Writing out the steady state displacement in this way makes it clear that the displacement oscillates about

some mean, DC value (given by the first term in the equation for $z(t)_{SS}$). For biological tissues, the density of the medium is very close to that of water and is on the order of 10^3 kg/m^3. The shear modulus is proportional to the Young's modulus, which has values on the order of 10^3 – 10^4 Pa for the agarose and gelatin samples we use in MMOCT. This means that the ratio ρ_{Med}/μ in both χ and ψ is of order 10^0 or 10^{-1}. A typical order of magnitude for f_{mag} is 10^1. Then, for an MNP with a radius ~ 10^{-6} meters, χ is $(1 - 10^{-11}) \approx 1$, and ψ is ~10^{-7}. Because the ranges of biological relevance for both ρ_{Med} and μ are fixed, the term denoted $C(\chi,\psi)$ is dominated by the size scale of R and f_{mag}. For MNP with radii on the scale 10^{-6} – 10^{-9} meters, and $f_{mag} < 10^2$ Hz, $C(\chi,\psi) \approx 1$, and the time-varying displacement is merely a cosine function oscillating at the magnet modulation frequency with amplitude $A/6\pi\mu R$. For MMOCT, we can therefore approximate the average vibration amplitude as the DC term in equation 3-5:

$$z_{avg} = \frac{A}{6\pi\mu R} \tag{3-6}$$

The average vibration amplitude is proportional to the amplitude of the magnetic gradient force and inversely proportional to the radius of the MNP.

Equations 3-5 and 3-6 represent the vibration amplitude of the MNP, not the vibration amplitude of the medium coupled to the particle. We assume that the tissue, mechanically coupled to the magnetic particle, is displaced in-phase with the motion of the magnetic particle and with vibration amplitude proportional to the vibration amplitude of the magnetic particle. One difference between an experimental measurement of displacement amplitude and the theoretical vibration amplitude given in equations 3-5 and 3-6 is that MMOCT detects the phasor sum of all the photons backscattered from one resolution volume. This means that the measured vibration amplitude in one resolution volume will be a weighted average of the vibration amplitude at every point in the resolution ellipsoid. While there does not exist a simple analytical

model for what the measured vibration amplitude of a single MNP centered within a resolution element will be (taking into account the averaging over the resolution volume), we can estimate the ratio of the measured vibration amplitude over a resolution volume and the vibration amplitude of a single MNP. We do this by assuming uniform backscattering throughout the resolution volume and summing the vibration amplitude of the tissue produced by a force acting at a point in an infinite, elastic solid over every point in one resolution volume; the vibration amplitude of the tissue due to a point force acting on an infinite elastic solid is given by [87]:

$$u_{tissue} = \frac{A}{8\pi E}\frac{1+\nu}{1-\nu}\frac{(3-4\nu)r^2+(4-4\nu)z^2}{(r^2+z^2)^{3/2}} \tag{3-7}$$

where A is the force, ν is the Poisson ratio, E is the Young's modulus, and r and z are cylindrical coordinates. The analytic expression for the ratio of the measured vibration amplitude to the vibration amplitude of the MNP is a complicated function of elliptic integrals (from integrating over the resolution ellipsoid) weighted by the Gaussian intensity profile of the beam in X, and Y, and multiplied by the coherence function in Z (which imparts a depth-dependent phase to the back-scattered light). Such an analytical model is beyond the scope of this dissertation; instead, to estimate the measured displacement, we analytically integrated just the tissue displacement, u_{tissue} (as given in equation 3-7) over a sphere (*i.e.* we approximate the volume of the resolution element as a sphere to avoid elliptic integrals). Assuming uniform back-scattering throughout the resolution volume and neglecting the depth-dependent phase term from the coherence function, we estimated a simplified average vibration amplitude over a resolution volume by integrating equation 3-7 over a sphere (excluding the region at the origin corresponding to the magnetic particle), adding back the vibration amplitude of the particle and scaling the whole thing by the

resolution volume, we estimate the ratio of the measured displacement, $\Delta z_{measured}$, to the magnetic particle's vibration amplitude, Δz_{MNP}, as

$$\Delta z_{measured} = \frac{\iint \int_{R_{MNP}}^{R_{res}} u_{tissue}(r,z)dV + \iint \int_{0}^{R_{MNP}} u_{bead}dV}{V_{res}} \tag{3-8}$$

where R_{MNP} is the radius of the magnetic particle and R_{res} is the radius of the resolution volume. In this equation, u_{bead} is the vibration amplitude of the MNP, which is z_{avg} from equation 3-6, and we have divided the integral by the resolution volume, V_{res} to compute the average vibration amplitude over that volume. The ratio of measured vibration amplitude and the vibration amplitude of a single particle is then:

$$\frac{\Delta z_{measured}}{u_{bead}} = \frac{3}{2}\frac{R_{MNP}}{R_{res}} - \frac{1}{2}\frac{{R_{MNP}}^3}{{R_{res}}^3} \tag{3-9}$$

showing that the measured vibration amplitude falls off as approximately $1/R_{res}$. For Version 3 of the LFOCT system (as described in the next section), the spatial resolution in each dimension is approximately: $\Delta z \sim 2$ µm, $\Delta x \sim \Delta y \sim 6.6$ µm. Estimating the radius of the resolution sphere, $R_{res,}$ as 2.2 µm yields the same volume as the volume of the resolution ellipsoid described by the spatial resolution Δz, Δx, and Δy. We then plot this ratio as a function of R_{MNP} (Figure 3-3). This is only an estimation, but it serves to remind us that the measured displacement of a single MNP surrounded by scattering medium and centered in the resolution element is going to be some fraction of the theoretical vibration amplitude of the MNP. Because the displacement of the scattering medium falls off as $1/r$, where r is the distance from the MNP, having a fine spatial resolution is going to be essential for making endogenous magnetite detection possible.

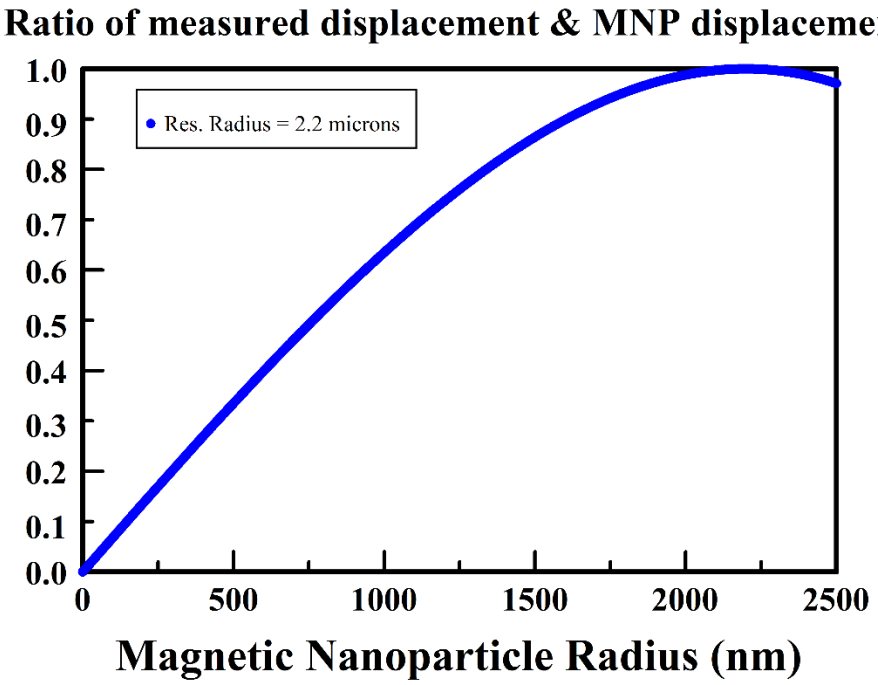

Figure 3-3 Ratio of measured MNP displacement to theoretical displacement. Approximating the resolution element as a sphere with radius of 2.2 μm, we plot an estimate of the ratio of the measured displacement (averaged over the resolution element) and the vibration amplitude of the MNP.

One final experimental consideration is the "halo" effect produced in MMOCT images. Because the medium is mechanically coupled to the particle, magnetic signal maps will exhibit a "halo" effect in which the magnetic signal bleeds out into the surrounding medium and is not confined to merely the resolution volume containing the MNP. In certain simplistic cases (*i.e.* homogeneous medium with identical magnetic particles) involving multiple particles (as we usually have in MMOCT), the halo effect in the magnetic displacement maps can be removed in post-processing by methods such as the model-based inversion of the displacement fields in magneto-motive ultrasound [88]. However, this dissertation is interested primarily in single magnetic particles, so we focus on the displacement of the MNP itself as a marker for magnetoreceptor detection.

3.2 MMOCT System Hardware

To convert the LF-OCT system to a LF-MMOCT system requires both hardware implementation and software development. In this section I will discuss the new hardware implemented to convert the LF-OCT system version 2 from Chapter 2 into a LF-MMOCT system. To the best of our knowledge, this is the first implementation of a LF-MMOCT system. The hardware changes consist of 1) re-designing the optics to improve the SNR roll-off (to increase the effective imaging depth) and to further decrease the transverse resolution (to improve the ability to detect single MNP above the noise floor of the resolution volume), 2) building the magnetic field delivery system (composed of a solenoid, power supply, and a water cooling system), and 3) incorporating the motorized stage to allow 3D image scanning.

3.2.1 Optical Re-Design for LF-OCT Version 3

During the design of the prototype LF-OCT system (Version 1), the figures of merit we used (SNR, axial and transverse resolution, transverse FOV, and axial imaging depth) are figures of merit for any optical imaging system. For our specific application of the LF-MMOCT system, we introduce a new figure of merit: the equivalent SPIO diameter. MMOCT systems are typically characterized by their Fe sensitivity. The Fe sensitivity describes the lowest concentration (of a homogeneous distribution of MNP) that an MMOCT system can detect above its noise floor. Because we are interested not in homogeneous distributions but in single MNP, we instead define something called the equivalent SPIO diameter which is the minimum size of a SPIO that could be detected by an MMOCT system. Without directly measuring this value, we can approximate it by measuring instead the minimum concentration of a homogeneous distribution of MNP that can be detected by the MMOCT system. After measuring the Fe

sensitivity of the MMOCT system (measured as the ratio of the mass of detectable Fe and the mass of the sample), and given the volume of a resolution element, the diameter of an SPIO particle that yields an equivalent ratio of grams Fe to gram sample (of a resolution element) is given by:

$$D_{equiv} = 2 \bullet \left(\frac{3V_{res}}{4\pi} \frac{\rho_{tis}}{\rho_{Fe}} \varsigma \right)^{1/3} \tag{3-10}$$

where ρ_{tis} and ρ_{Fe} are the density of the tissue and Fe respectively, V_{res} is the volume of a resolution element, and ς is the Fe sensitivity of the system measured in grams Fe per gram sample. This equivalent SPIO diameter metric assumes that the backscattering from the homogenous distribution and a single nanoparticle are the same, and that the displacement of a single, larger magnetic particle is equal to the sum of the displacements induced by a homogeneous distribution of smaller nanoparticles. We note that this metric does not account for the halo effect previously described; we would expect the halo effect to augment the measured vibration amplitude, so the equation 3-10 may be an underestimate of the equivalent SPIO diameter. An example of the size-scale of the equivalent SPIO diameter for a typical point-scanning MMOCT system employing a Ti:Sapph laser (bandwidth of 125 nm) with an axial and transverse resolution of 3 μm and 12 μm, respectively and a measured Fe sensitivity of ~ 30 μg/g sample (as reported in [12]), is 118 nm . The magnetite crystals found in magnetotactic bacteria are reported to have a diameter ranging from 35-120 nm [89]. Using this as a benchmark for the size particle we want to detect, we want to re-design our optics to decrease the transverse resolution from a theoretical value of 17 μm to 7 μm. Assuming we can achieve a similar Fe sensitivity of 30 μg/g, an axial and transverse resolution of 1.8 μm and 7μm respectively will

yield an equivalent SPIO diameter of 69 nm, within the range of the known size of endogenous magnetite crystals found in some bacteria. The measured Fe sensitivity is reported in Chapter 4.

The second major consideration for the optical re-design of the LF-OCT system was the SNR roll-off in depth. As reported in Chapter 2, the LF-OCT system version 2 had a roll-off of 25 dB over ~300 μm. Such a large roll-off effectively limits our imaging depth. In order to have high volumetric throughput for the LF-MMOCT system, we want to use all 500 μm of the theoretical imaging depth. To do this, we need to re-design the spectrometer. The roll-off in intensity of an A-line in SD-OCT is given by:

$$A(z) = \Delta x \, \mathrm{Re}^{-(a^2 R^2 z^2 / 4\ln 2)} \frac{\sin(\Delta x R z)}{\Delta x R z} \tag{3-11}$$

where Δx is the pixel width of a rectangular pixel, a is the FWHM of the spot size on the camera, R is the reciprocal linear dispersion of the spectrometer (dk/dx evaluated at λ_0), and z is depth within the image, as given in equation 5 of Ref [38]. The bigger the spot size on the camera, the greater the fall-off (for a fixed pixel width). In order to shrink the focused spot size on the camera ($2\omega_{0\_\lambda}$ from Table 2-2) and in order to improve the transverse resolution, Δx, we expanded the beam diameter at every point in system, starting at the first beam expander (L0 + L1). We changed the focal length of L1 from 300 mm to 400 mm and the focal length of the cylindrical lens from 100 mm to 75 mm. We also upgraded the camera to a Photron Fastcam SA1.1. The new camera has a 1024 × 1025 pixel array with 20 μm square pixels and a maximum framerate of 5400 frames per second. Lens L5 was also swapped for one of the same focal length but with a 2” diameter to accommodate the expanded beam size and to minimize vignetting (see Figure 2-9). The changed optical elements are summarized in Table 3-1.

Given the changed lenses, the theoretical out-of-plane transverse resolution for this configuration is 7.3 μm. The in-plane transverse resolution, Δx, is still given by the same limiting aperture (the diameter of lens 4) with a value of 4.01 μm. With a magnification of 4 between the image and object planes, the size of the focused spot on the sensor (in the X dimension) is 4*4.01 = 16.04 μm. This is not sampled by two pixels (pixel size is 20 μm for the new Photron camera), which means the figure of merit for the in-plane transverse resolution is the physical distance mapped to two pixels. This value is 2*(FOV/1024pixels) = 10.98 μm. With the expanded beam diameter in the spectral plane, a finer focused spot size on the camera (in the λ dimension) is achieved so that the expected roll-off has shrunk to -7 dB over 500μm. The beamspread, χ, is the same, but the sensor size of the new Photron camera is larger than that of the previous camera (20.5 mm compared to 17.4 mm). This means that the captured bandwidth is larger for Version 3 than Version 1 & 2: 330 nm compared to 280 nm for the previous versions. This makes the theoretical axial resolution smaller (0.85 μm compared to 1.0 μm).

We had to develop a new alignment procedure as well to accommodate the MMOCT hardware. The magnetic field delivery system requires that the sample arm have several inches of accessible space below the sample to accommodate the magnet, the water cooling tubes, and the magnet holder. To allow more space in the sample arm, the entire interferometer was lifted off the optics bench onto a separate breadboard. Two periscopes are added to lift the beam up onto the interferometer's breadboard and then to deflect it back down onto the level of the spectrometer. For a more thorough list of the alignment steps for Version 3, see Appendix 2.

Table 3-1 Summary of Optical Components used in LF-OCT system Version 1-3

Component	LF-OCT Version 1	LF-OCT Version 2	LF-OCT Version 3
Light Source	NKT Photonics EXR9-OCT Low Noise Collimated beam diameter of ~1 mm	NKT Photonics EXR15 Collimated beam diameter of ~1 mm	NKT Photonics EXR15 Collimated beam diameter of ~1 mm
Optical Filters	605 nm long pass 950 nm short pass	605 nm long pass 950 nm short pass	605 nm long pass 950 nm short pass
L0	f = 35 mm	f = 35 mm	f = 35 mm
L1	f = 200 mm	f = 300 mm	f = 400 mm
CL	f = 100 mm	f = 100 mm	f = 75 mm
L2	f = 100 mm	f = 100 mm	f = 100 mm
L3/L4	f = 100 mm	f = 100 mm	f = 100 mm
L5	f = 100 mm	f = 200 mm	f = 200 mm 2” Diameter
L6	f = 50 mm	f = 50 mm	f = 50 mm
L7	f = 100 mm 2” Diameter	f = 100 mm 2” Diameter	f = 100 mm 2” Diameter
Beam Splitter Cube	Newport Broadband Non-polarizing 50:50 beam splitting cube	Newport Broadband Non-polarizing 50:50 beam splitting cube	Newport Broadband Non-polarizing 50:50 beam splitting cube
Diffraction Grating	Wasatch Photonics 600 lines/mm	Wasatch Photonics 600 lines/mm	Wasatch Photonics 600 lines/mm
Camera	Photron Fastcam SA3 1024 x 1024 CMOS pixel array 17 µm pixels	Photron Fastcam SA3 1024 x 1024 CMOS pixel array 17 µm pixels	Photron Fastcam SA1.1 1024 x 1024 CMOS pixel array 20 µm pixels
All optics have a 1” diameter unless otherwise noted.			

The system was characterized using the same methods as described in Chapter 2. We measured an axial resolution of 2.5 ± 0.2 μm in air, an in-plane transverse resolution of 6.6 ± 3.4 μm in silicone, a transverse calibration of 5.02 μm/pixel in air, and an axial calibration of 0.90 μm/pixel in air. The larger standard deviation of the experimental transverse resolution (relative the size of the transverse resolution) is a product of the decreased Rayleigh range. In order to achieve a tighter focus with a higher NA, the Rayleigh range shrinks so that the beam defocuses more quickly away from the focal plane. This causes a spread in transverse resolution values measured at different depths within the image. The measured range of values for the in-plane transverse resolution covers exactly the range between the theoretical out-of-plane transverse resolution (which we found in Version 1 &2 to be a good estimator of what the measured in-plane resolution would be) and the theoretical in-plane transverse resolution given by the Nyquist sampling criterion of 2*(FOV/N pixels).

The SNR roll-off was found experimentally to be -9 dB at a depth of 450 μm in the image (as shown in Figure 3-4). This value is in good agreement with the theoretical roll-off and an improvement of 16 dB over the roll-off of Version 2. The maximum experimental SNR of Version 3 is 101 dB, 12 dB lower than the maximum SNR achieved with Version 2 (113 dB) even though the theoretical SNR is the same in both cases (same total power from the same light source, same maximum exposure time of 1 ms). The reason for this discrepancy is explained in large part by the larger beam diameter used in Version 3. The beam was expanded in order to shrink the transverse resolution, but the expanded beam size means that the amount of overfilling of the sensor in *X* was nearly doubled. This means that the sensor collects only 50% of the power collected by the sensor in the Version 2 design. A loss of 50% of the sample power results in an SNR loss of 3 dB. The remaining 9 dB in SNR loss of Version 3 compared to Version 2 can be

explained by the comparatively poor optical alignment achieved with Version 3. The larger beam diameter made the optical alignment significantly more challenging; the beam nearly filled each lens, making it harder to check the alignment on the targets. The larger beam size also introduces more aberrations, making lens collimation difficult. The system performance is summarized in Table 3-2.

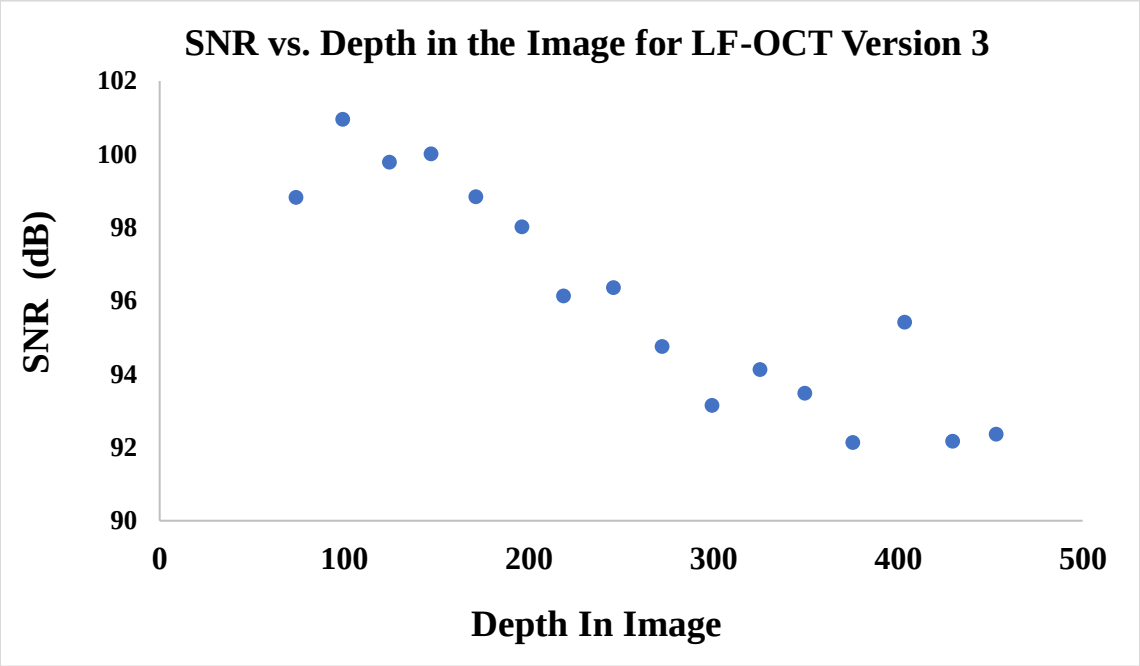

Figure 3-4 SNR vs depth for LF-OCT System Version 3.
Version 3 of the LF-OCT system exhibits a roll-off of -9dB at a depth of 450 µm within the image, an improvement of 16 dB over the roll-off of Version 2.

Table 3-2 Summary of System Performance of LF-OCT Version 1-3

		LF-OCT Version 1		LF-OCT Version 2		LF-OCT Version 3	
		Theoretical Value	**Measured Value**	**Theoretical Value**	**Measured Value**	**Theoretical Value**	**Measured Value**
Transverse Imaging	D_{L4T}	4.00	4.04	4.35	4.29	5.62	5.14
	$\Delta x(n=1.34)$	17.0	24± 3	8.50	14±3	10.98	6.6±3.4
	$\Delta y(n=1.34)$	25.5	-----	17.0	-----	7.31	-----
	$Z_R(n = 1.34)$	853	822	379	256	70	57
	D_{L7T}	8.0	8.0	24.0	24.0	50.8	50.8
	$2\omega_{0sensor}$	8.02	48	16.04	56	16.04	26.4
	$\frac{2\omega_{0\_sensor}}{pixelsize}$	0.46	2.82	0.94	3.29	0.80	1.32
	$2(FOV / N)$	17.0	17.2	8.50	8.38	10.98	10.04
	$\Delta z(n=1.0)$	1.01	2.4 ± 0.6	1.01	1.8±0.2	0.85	2.5±0.2
	$z_{\max}(n=1.0)$	524	509	524	527	445	461

Table 3-3 Summary of SNR and Phase Resolution for LFOCT Versions 2 & 3

	LF-OCT Version 2			LF-OCT Version 3		
	Imaging Parameters	**Theoretical Value**	**Measured Value**	Imaging Parameters	**Theoretical Value**	**Measured Value**
SNR	Silver Mirror T = 1.0 ms Ps = 492 mW R_S = 1	129 -14.6 = **114.4 dB**	**113 dB**	Silver Mirror T = 1.0 ms Ps = 492 mW R_S = 1	129 -14.6 = **114.4 dB**	**101 dB**
SNR	Silver Mirror T = 0.2 ms Ps = 492 mW	123-14.6 = 108.4	96 dB	Silver Mirror T = 1.0 ms Ps = 492 mW	129 – 14.6 = 114.4	88 dB
δθ (rads)	R_S = 1 1000 Frames @ 1 kHz	**0.102**	**0.114**	R_S = 1 1000 Frames @ 1 kHz	**0.106**	**0.161**

With the implementation of the new camera, we discovered that there was fixed-pattern noise (FPN) in the images. Fixed-pattern noise is a known problem of CMOS sensors and results from pixel-to-pixel variation in the photocurrent-to-voltage conversion [90]. Essentially this means that certain groups of pixels in the sensor have a higher gain than others resulting in artificially higher intensity readings from those pixels. The results is that B-mode images have vertical streaks, with some columns being brighter on average than others, as shown in the bottom left of Figure 3-5. To digitally compensate for the fixed pattern noise, we employ a method similar to that in Ref [90]. From the reference-subtracted spectral interferogram (the raw camera intensity values before taking a 1D FFT to recover the OCT signal), we take an average along the spectral dimension. From this plot, it is apparent that the fixed pattern noise has a period of 4 pixels in the transverse dimension; two columns are 'hot' (*i.e.* higher average intensity) and then two columns are 'cold' (*i.e.* lower average intensity). Averaging all the hot pixels together and all the cold pixels together yields one value for the gain of the hot pixels and one value for the gain of the cold pixels. These two values are then normalized by dividing each by the average of the two. We then divide every pixel in the 2D reference-subtracted spectral interferogram by either the hot or the cold normalized average value. This will compensate for the gain imbalance and will remove the vertical streakiness in the B-mode images.

In order to determine which spectral interferogram to use for calculating the hot and cold average values for the taps correction, we recorded images of a Lambertian surface (purely diffuse scattering), images with nothing in the sample arm, images with the sample arm blocked, and images with both the reference and sample arm blocked. From each set of images, we obtained a set of FPN correction values. To quantify the effect each set had on the reduction of the gain imbalance, we took a 1D DFT along the transverse dimension of a B-mode image of the

Lambertian surface (because these images should have uniform scattering throughout the entire FOV). Because the fixed pattern noise is periodic in the spatial dimension of the images, we can isolate the spatial frequency corresponding to this noise. The spatial modulation frequency has a period of 4 pixels. Because the index in the DFT along X corresponding to this spatial frequency is then given by $N/4$ where N is the number of samples (in this case, the number of pixels, 1024). As can be seen in the top panel of Figure 3-5, there is a sharp peak in the spatial DFT at the index 1024/4 = 256; this is the spatial modulation frequency of the fixed pattern noise. To quantify the effect that each set of taps correction values has, we examine the effect on the amplitude of this peak in the spatial DFT. The taps correction values found from images recorded with both arms of the interferometer unblocked but nothing in the sample arm reduced the peak's amplitude by the greatest amount, so these are the values we use for all images recorded with the Photron Fastcam SA1.1. A summary of the effect of the FPN correction is given in Figure 3-5: the amplitude of the DFT at the index corresponding to the spatial modulation frequency, then plots showing the average value of all the hot and cold pixels, and finally the B-mode images of a Lambertian surface.

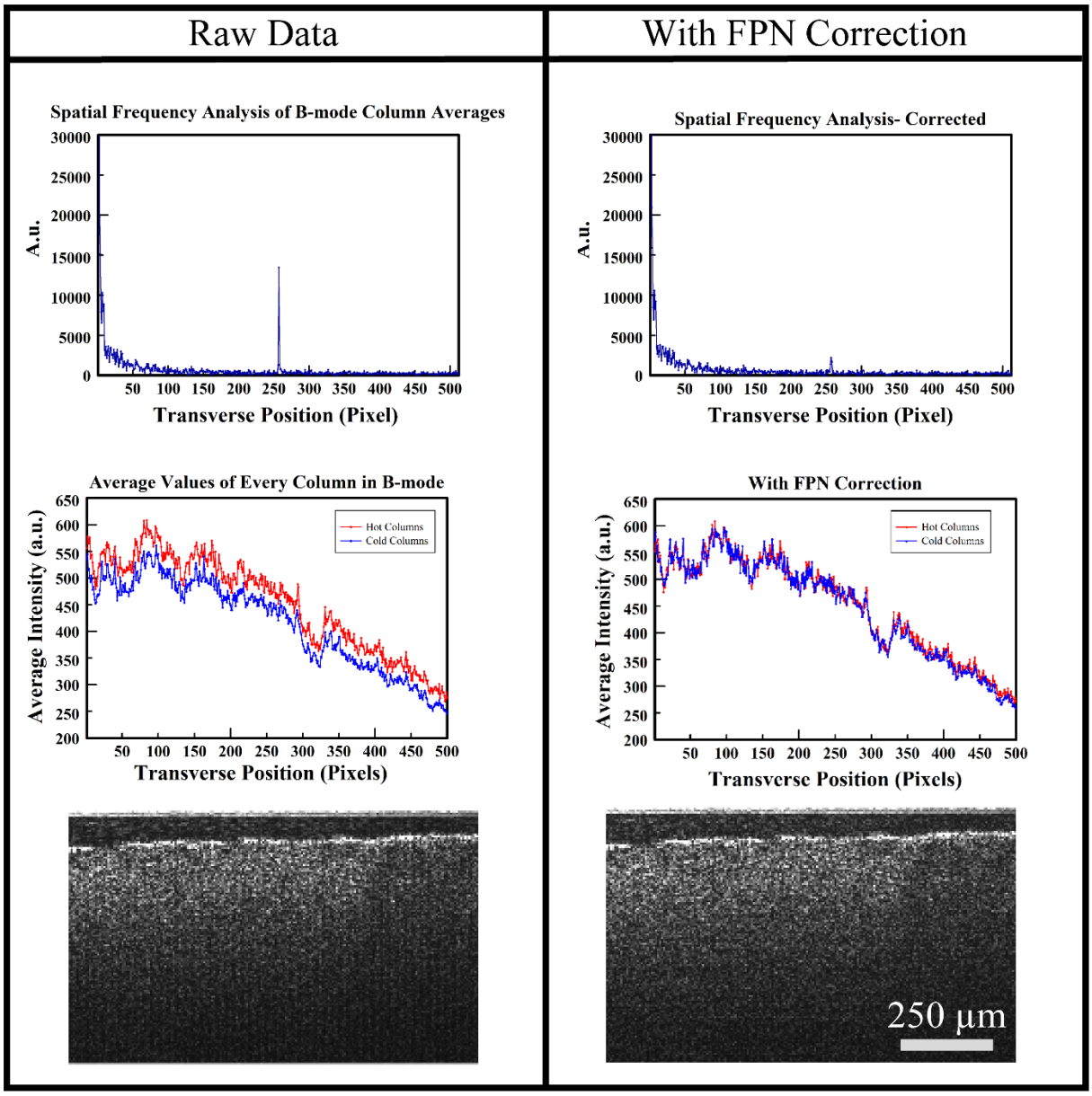

Figure 3-5 Fixed Pattern Noise Correction in Photron Camera SA1.1.
Top: Spatial FFT of the B-mode images of a Lambertian surface showing a peak at index 256, corresponding to the fixed pattern noise with a period of 4 pixels. Middle: The average values of every column in the B-mode images, separate into the hot and cold columns, showing that the uncorrected hot columns have a higher average. Bottom: Example B-mode images of the Lambertian surface show the vertical streaking disappears with FPN correction.

3.2.2 Magnetic Field Delivery System

The second major hardware consideration for the development of the LF-MMOCT system is the magnetic field delivery system, composed of the solenoid, the power supply, and the water-cooling system. We chose to set up the magnetic field delivery system with a single electromagnet placed below the sample (as shown in Figure 3-1). We want to maximize the component of the magnetic force that is along the optical axis, F_z, while minimizing the force component that is orthogonal to the optical axis, F_r (axial and radial directions shown in Figure 3-6). For our magnetic field delivery system, because the magnet is placed below the sample, the figures of merit governing the solenoid design are as follows: maximize B_z and maximize the gradient of B_z in our region of interest (to achieve the largest possible F_z), minimize the radial components B_r (to minimize any motion not along the optical axis), and retain some homogeneity in the force amplitude over our region of interest. There is a tradeoff in force homogeneity and the large field gradient, so this will have to be balanced carefully.

To simulate the magnetic field produced by a solenoid of given dimensions, there are four methods used in the literature: 1) approximate the solenoid as a dipole [91], 2) approximate the solenoid as a uniform, cylindrical current distribution [92], 3) approximate as a single helical winding [93], and 4) treat the solenoid as a collection of individual current loops of various radii and sum up the contributions from each [94]. The last expression is the most exact and can be used to find the magnetic field over all space, so this is the method we used. From Ref [94], the radial and axial components of the magnetic field at any point in space (r, z) produced by a current loop with radius a, are given by:

$$B_r = \frac{Cz}{2\alpha^2\beta r}\left[\left(a^2 + r^2 + z^2\right)E(k^2) - \alpha^2 K(k^2)\right] \tag{3-12}$$

and

$$B_z = \frac{C}{2\alpha^2\beta}\left[\left(a^2 - r^2 - z^2\right)E(k^2) + \alpha^2 K(k^2)\right] \tag{3-13}$$

where $\alpha^2 = a^2 + r^2 + z^2 - 2ar$, $\beta^2 = a^2 + r^2 + z^2 + 2ar$, $k^2 = 1 - a^2/\beta^2$, $C = \mu_0/\pi$, and $E(k^2)$ and $K(k^2)$ are elliptic integrals of the first and second kind. One important note is that these expressions use the permeability of free space, μ_0, to estimate the magnetic field produced by the solenoid. This is consistent with a solenoid having an air core. In our ultimate design (discussed later in this section), we use a ferrite core to amplify the magnetic field of the solenoid. In theory, we should use the value for the magnetic permeability of the ferrite core, μ, rather than μ_0 to correctly model the magnetic field of our solenoid. However, based upon practical advice given to us by graduate students who design magnetic coils for magnetic resonance imaging, we decided to use μ_0 and then expect to see ~2x amplification of the magnetic fields if a ferrite core is added later. The theoretical values for the permeability of ferrite range from $10^1 – 10^3$ [95]; however, we were advised that in practice, it is more common to see an amplification of only ~2 with a ferrite core. So using μ rather than μ_0 in the simulation may lead to a gross overestimation of the magnetic gradient force. As will be shown in this section, this advice turned out to be true for our case.

Because the elliptic integrals are computationally heavy to compute over an entire imaging region of interest (spanning the OCT FOV 5 mm × 0.5 m), we divide the magnet design into two steps. The first step is to coarsely step over a wide range of input parameters, computing only the magnetic field at a few points along the *Z*-axis (setting $r = 0$) to determine the maximum B_z and the maximum gradient of B_z achievable for each set of parameters. The design parameters of the solenoid consist of the inner radius, the outer radius, the height, the wire gauge, the

number of turns per layer, and the number of layers. Wire gauge number is inversely proportional to the wire diameter (smaller gauge numbers have larger diameters) and is proportional to the resistance per length of the wire (smaller gauge numbers have less resistance per length than larger gauge numbers). To impedance match the magnet and the power supply that will be used to supply current to the solenoid, we want the total resistance of the solenoid to equal that of the power supply. The power supply (Kepco ATE 36-8M) has a maximum voltage output of 36 Volts and a maximum output current of 8 Amps. This gives an impedance of 4.5 Ω. Thus, for each wire gauge, there is a total length of wire needed to give a total resistance of 4.5 Ω, based on the resistance per length of each wire gauge. We compute the axial component of magnetic field for an array of input parameters. First, it loops over a range of inner radii from 2.5 mm to 20 mm. Next, it looks over wire gauges 10 to 35. Third, it loops over possible height values from 5 mm to 50 mm. Given the total length per wire gauge for impedance matching, the simulation loops the wire until the total length is used up. Based on the previous constraints in place, this gives the number of turns per layer and the number of layers for each set of parameters.

After coarsely stepping through the initial parameter ranges, we narrowed down the parameter ranges based on general behavior of the magnetic field and the magnet geometry. As shown in Figure 3-6, the wider the inner radius, the better the field homogeneity. Conversely, the narrower inner radius produces a stronger magnetic field gradient. By setting a bound on the gradient so that the gradient cannot change by more than 10% over the 0.5 mm imaging depth of the LF-OCT system and then finding which parameters produce the largest gradient, we narrowed down the inner radius parameter range to between 2.5 and 5.0 mm, the height to between 5 and 25 mm, and the wire gauge to between 15 and 28. We also found that in general,

short and squat magnets are favored over long and skinny magnets given the design constraints. Curiously, all the best sets of parameters seemed to have a height:diameter ratio of 1:4.

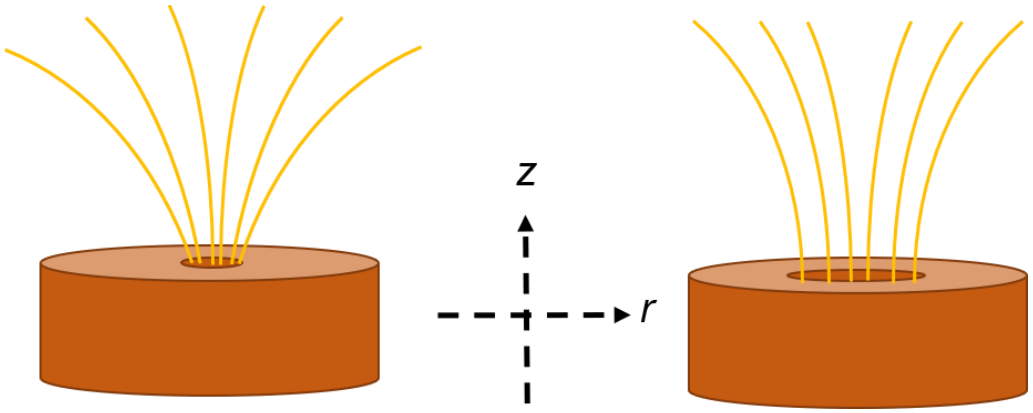

Figure 3-6 Effect of Magnet Geometry on Magnetic Field Gradient.

After step 1, we then move on to step 2 and compute the elliptic integrals from equations 3-12 and 3-13 to find the magnetic field produced at every point in our imaging region of interest for each set of input parameters found in step 1. As shown in Figure 3-7, the ROI for the magnetic field simulation is taken to be between z = 6.0 and 6.5 mm, based on the thickness of the solenoid water cooling jacket, the air gap between the magnet and the sample, the sample holder, and the sample itself. The maximum imaging depth is ~0.5 mm which means that we cannot image to the bottom of the 2-3 mm thick samples. We also typically leave a small air gap at the top of the B-mode image so that the sample surface does not wrap around the coherence zero position. This means that our imaging window is ~ 6 mm above the solenoid coil. The ROI in the radial dimension is -2.5 to 2.5 mm, given the transverse FOV of 5 mm.

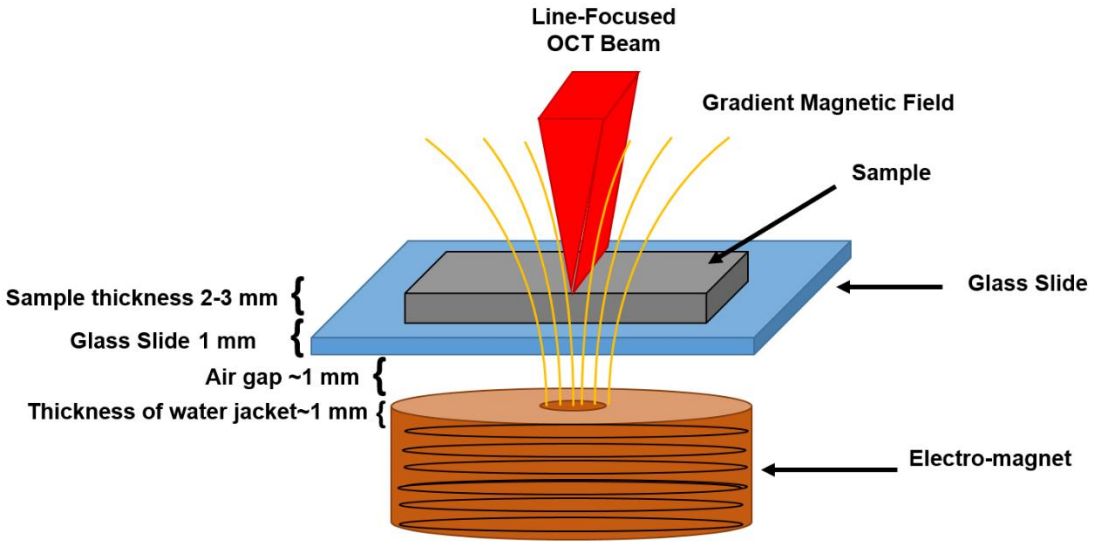

Figure 3-7 Illustration of LF-MMOCT Sample Setup.
The region of interest of the magnetic field simulation is taken to be between z = 6.0 and 6.5 mm above the top of the solenoid.

For each set of input parameters, we make contour plots of B_z, B_r, dB_z/dz, and dB_z/dr, as well as calculating the maximum and variance of F_z, F_r, and B_z. After several iterations of input parameters, each time making the step size between input parameter values smaller, we find the magnet geometry parameters which optimize F_z while maintaining a small F_z variance and which minimize the radial forces to be: an inner radius of 4.3 mm, an outer radius of 20.1 mm, and a height of 9.8 mm using 24 AWG copper wire. These parameters result in 31 layers of wire with 605 total turns.

Because we plan to send 8 Amps of current through the solenoid (24 AWG copper wire having a maximum current rating of 0.58 Amps), we need to cool the magnet. To do this, we encase the solenoid in a plastic water jacket attached to a chiller that continuously circulates cold water around the outside of the magnet. The chiller (Thermotek T257P) is set at 13 °C. Because the water can only circulate around the outside layer of the solenoid, we apply a layer of Cast

Coast adhesive between each layer when winding the magnet. Cast Coast is electrically insulating but thermally conductive so that heat can be dissipated from the inner layers. The solenoid water jacket is made of Ultem because this material is resistant to high temperatures, is long-lasting, and easy to machine. The Ultem solenoid water jacket is composed of two pieces: the inner bobbin for winding the solenoid, and the larger case that it fits snugly into. The two are epoxied together after the magnet has been wound and the wire ends passed through the Ultem water jacket, as shown in Figure 3-8. When winding the solenoid, a plastic spacer is taped to the inner bobbin to leave an air gap for water to flow.

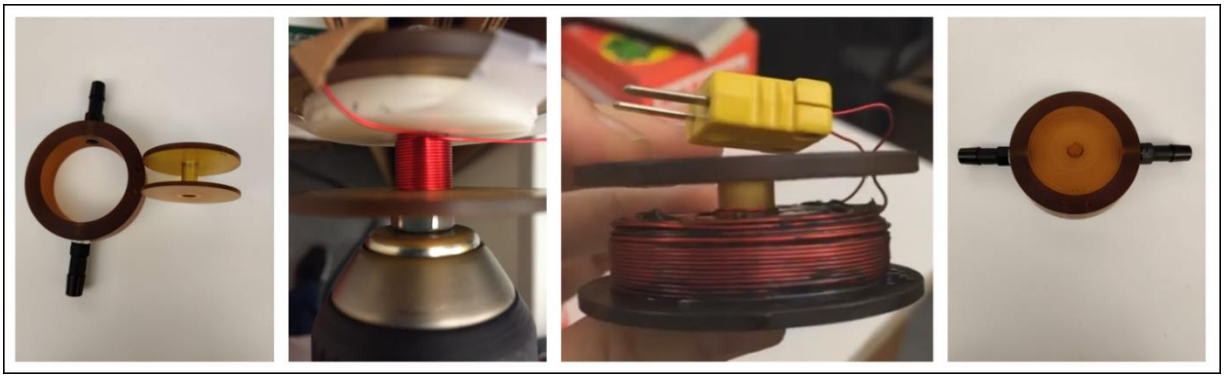

Figure 3-8 Photos of solenoid winding.
Far left, the two separate Ultem pieces, second from the left, the solenoid being wound around the inner bobbin with a white plastic spacer in place to leave a gap for water to flow, middle right, the wound magnet with spacer removed, and far right, the bobbin placed inside the Ultem case and epoxied together.

The final piece of the magnetic field delivery system is the power supply. The power supply (Kepco ATE 36-8M) has a set of programmable pins so that it can be controlled by an input signal of 0-10 volts. This allows us to control it with LabVIEW. The programmable pins can be set up either in fast or slow mode and in either voltage- or current-control mode. In slow mode, the power supply approaches an ideal voltage source. Heavy output and feedback

capacitors provide low output noise, excellent voltage stability, and good transient response. In fast mode, the output and main feedback capacitors are removed, providing characteristics of a wide-band amplifier, ideal for applications requiring a current stabilizer or for high-speed voltage or current programming. Loads cannot contain excessive capacitance. The voltage-control or current-control modes refer to whether the output is controlled by a 0-10 V external control signal (voltage-control mode) or a 0-1 V DC signal (current-control mode). We want to control in voltage-control mode because the DAQ card that converts the LabVIEW signal to an analogue signal has a 0-10 V supply voltage for the power supply. Based on information from the manufacturer of the power supply, an electromagnet operated at frequencies below 1 kHz should be set up in slow mode. While we typically use magnet modulation frequencies well below 1 kHz (typically, less than 100 Hz), it is worth mentioning that we supply a square root sine wave to the magnet, rather than a pure sinusoid because we have a uni-polar power suuply. The Fourier transform of a pure sinusoid is a delta function at $f = f_{mag}$; the frequency spectrum of a square root sine wave is a series of delta functions at all the multiples of f_{mag} (these are called the harmonics of f_{mag}). This means that the frequencies contained in the waveform we supply to the magnet may span a range an order of magnitude greater than the fundamental frequency, f_{mag}. For magnet modulation frequencies <100 Hz, one might expect the power supply to definitely perform best in the slow mode, but given the large range of harmonics presents in the square root sinewave spectra, this statement becomes less definitive. To choose which method to set the power supply up in, I tested the fast and slow modes (using the voltage-control mode). With a magnet modulation frequency of 10.8 Hz, we imaged a tissue phantom containing a homogeneous distribution of MNP. For the same 9 V input voltage from LabVIEW, the power supply in slow mode operation only drew 7 A of current, while the same power supply set up in

fast mode drew the full 8 A. We found that the fast mode configuration then produced a 5 dB greater magnetic signal than the slow mode, so we set up the programmable pins in the fast mode and voltage-control settings.

After winding the solenoid and setting up the power supply, we used a Hall probe (FW Bell 5180) to measure the magnetic field at various axial and radial points above the solenoid, using both an air core and a ferrite core. The Results are shown in Figure 3-9. The experimental values yield a winding efficiency of 0.7 compared to the predicted values (simulated by averaging the field expected over the area of the Hall probe sensor). The ferrite core amplifies the magnetic fields by a factor of ~1.5. The ferrite core combined with the winding efficiency of ~0.7 give us, in the end, experimental values slightly greater than the predicted values with an air core; the solenoid with the ferrite core produces a sufficient magnetic gradient to produce the magnetic force that it was designed to. In addition to increasing the axial component of the magnetic field, the ferrite core also amplifies the radial component by a factor of 1.5 - 2. This means that there will be greater field inhomogeneity across the transverse FOV, and there may be a small component of transverse displacement. However, the radial components of the B-field are < 10% of the axial components of the B-field for $|r| < 2$mm, so the majority of the FOV still meets our criteria for $B_r < 0.1B_z$.

With the ferrite core in, we made a more thorough measurement of the axial and radial components of the magnetic field produced by the solenoid over a region encompassing the imaging FOV. Using the same setup (a Hall probe mounted on a linear translation stage), we measured the magnetic field at various radial and axial (in increments of 0.5 mm) to produce 2D spatial maps of the magnetic field (Figure 3-10). From these, we can estimate the magnetic gradient force as a function of axial and radial position within our imaging ROI, understanding

that there is some multiplicative factor given by the volume and magnetic susceptibility of the particular sample being imaged needed for calibrating the measured axial displacements.

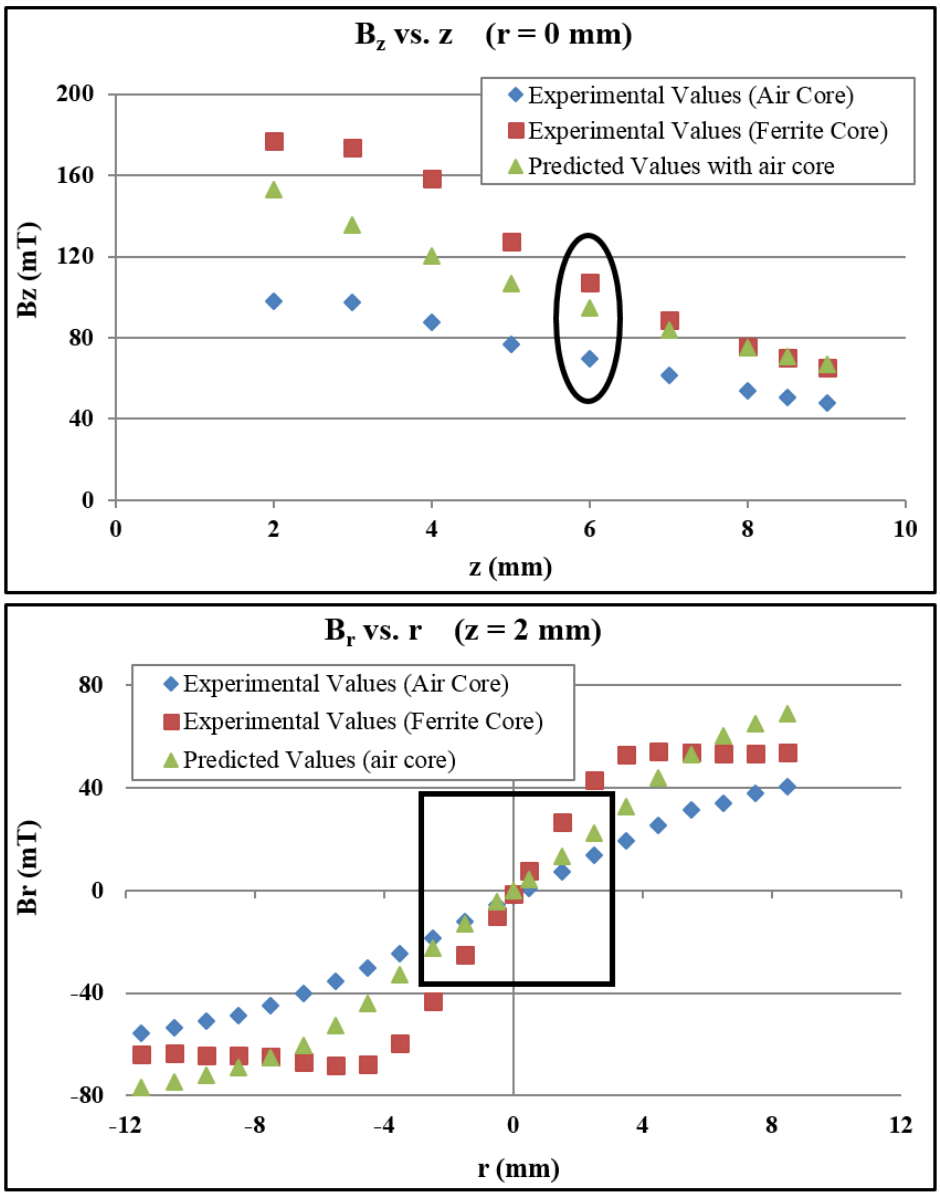

Figure 3-9 Comparing Solenoid Performance with Prediction.
Experimental values of the radial and axial components of the magnetic field produced by the solenoid, with both and air core and a ferrite core. The imaging ROI is indicated by the oval and rectangle.

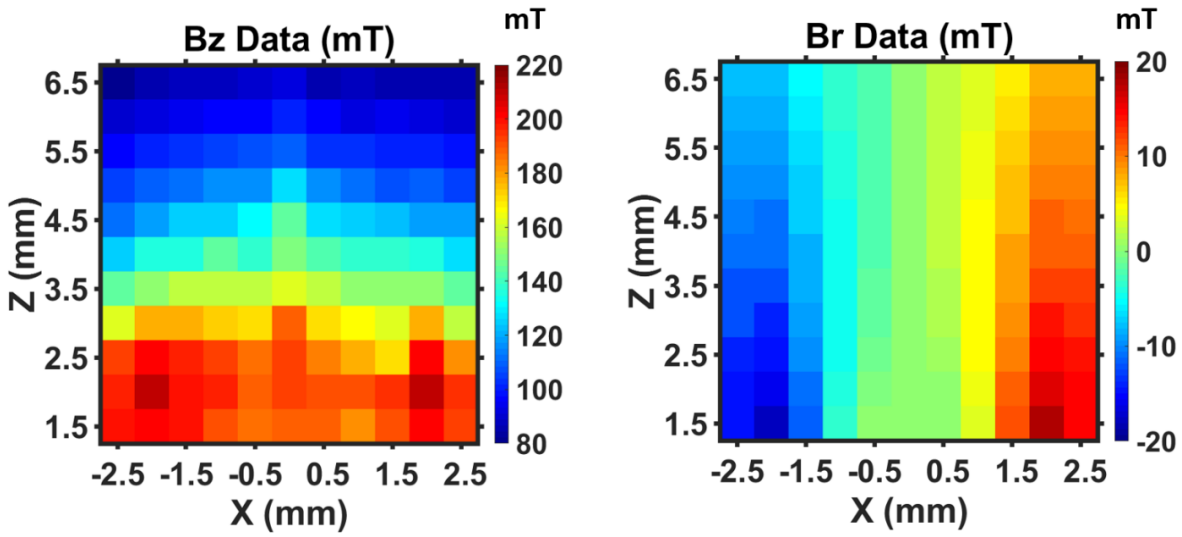

Figure 3-10 Magnetic Field Maps of Solenoid.
Measured values of the axial (left) and radial (right) components of the magnetic field produced by the solenoid with the ferrite core. Units are mT.

From these magnetic field maps in Figure 3-10, we made a map of the magnetic gradient force. It is helpful to write out the axial component of the magnetic force (equation 3-1):

$$F_z = \frac{V\chi}{2\mu_0}\left[2B_z\frac{dB_z}{dz} + 2B_r\frac{dB_r}{dr}\right] \tag{3-14}$$

Assuming the radius of the magnetic particle is ~1 μm, the volume is ~10^{-18} m^3. We estimate χ as 1 (since this is the order of magnitude for superparamagnetic particles), and we know the permeability of free space, μ_0, is $4\pi*10^{-7}$. Using these estimates, and equation 3-14, we made a map of the axial component of the magnetic gradient force by computing the axial and radial gradients from the magnetic field maps (Figure 3-11).

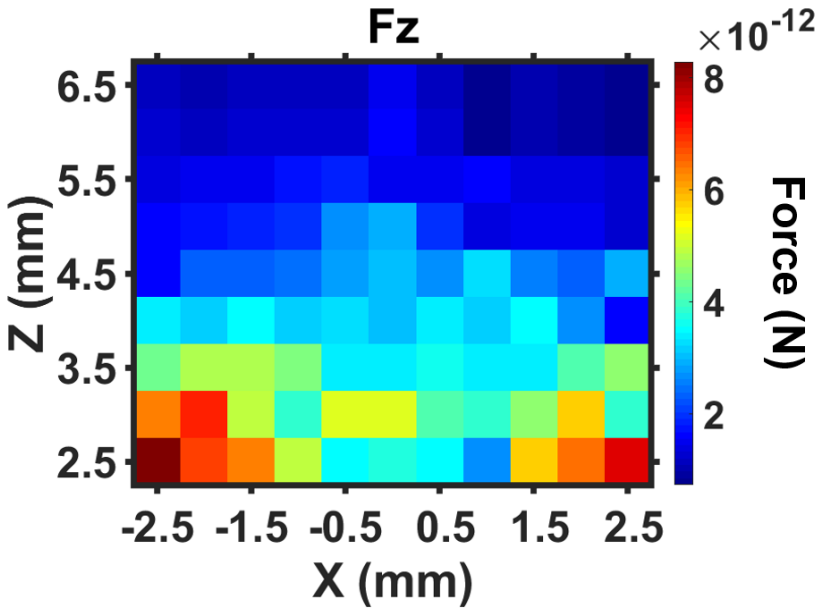

Figure 3-11 2D Map of Axial Magnetic Gradient Force Delivered by the Solenoid. Order of magnitude estimate of the axial component of the magnetic gradient force delivered by the solenoid to the sample region, for a particle with radius 1 μm and $\chi = 1$.

One concern with the ferrite core is that the large inductance will create a phase lag between the LabVIEW control voltage (which also triggers the camera to collect frames) and the magnetic field. This would affect the expected phase of the motion of paramagnetic particles embedded in the sample, a value we use in the cosine filtering step of the signal processing algorithm. To measure this phase lag, we used an oscilloscope to monitor the LabVIEW control voltage and the magnetic field simultaneously (with the ferrite core in place) for various magnet modulation frequencies. The magnetic field was measured with a Hall probe, and the Hall probe output monitored with the oscilloscope. The Hall probe was set up in AC mode, which has a sample time of 8 μs (sufficiently fast for sampling magnet modulation frequencies < 100 Hz) and a delay time of 30μs. The results are plotted in Figure 3-12. There is indeed a phase lag which increases linearly with the magnet modulation frequency from 10 Hz to 50 Hz. Assuming that

this phase lag is due the inductance, we modeled this phase lag with the frequency response of the phase of a LR circuit:

$$\theta(f) = -\tan\left(\frac{2\pi fL}{R}\right) \tag{3-15}$$

where θ represents the phase difference between the applied voltage and the voltage drop across the solenoid as a function of the magnet modulation frequency, f. The solenoid is described by a resistance, R, and an inductance, L. The minus sign indicates that the voltage at the solenoid lags behind that of the power supply. We used nonlinear least squares curve fitting to fit this model to the data, with R and L both being free fit parameters. To estimate the initial value of R we simply measured the resistance of the solenoid using a multimeter. We measured a value of 4.3 ± 0.1 Ω. To estimate the inductance, L, we used the following equation from Ref [96] for the low-frequency inductance of small air-core solenoids (keeping in mind the same comment from the solenoid design that we can approximate the solenoid as an air core and just multiply the result by ~1.5 to account for the ferrite core):

$$L = 0.4\pi^2 n^2 \frac{r_m^{\,2}}{l + \Delta r + r_{out}} AB$$

$$A = \frac{10l + 12\Delta r + 2r_{out}}{10l + 10\Delta r + 1.4r_{out}}$$

$$B = 0.5 Log_{10}\left[100 + \frac{14r_{out}}{2l + 3\Delta r}\right] \tag{3-16}$$

In this expression, n is the total number of turns of the solenoid, r_{out} is the outer radius, Δr is r_{out} - r_{inner}, r_m is r_{inner} + ½ Δr, and l is the length of the solenoid. Given an inner radius of 4.3 mm, an

outer radius of 20.1 mm, and a length of 9.8 mm with 605 total turns, we estimate the inductance to be 3.9 mH. This expression does not account for the magnetic permeability, μ, of the ferrite core. We found that measuring this value is generally very tricky, and we can estimate the value from the measured value of the magnetic field with and without the ferrite core (Figure 3-9). We found that the ferrite core amplified the magnetic field by a factor of ~1.5. So we estimate that for our solenoid, the ferrite core has an effective magnetic permeability of ~1.5. This means we expect the inductance with the ferrite core to be approximately 1.5* 3.9 mH = 5.9 mH. Equation 3-15 is plotted alongside the data in Figure 3-12. From the least squares curve fitting, we estimate $L = 5.1 \pm 0.8$ mH and $R = 4.3 \pm 0.7$ Ω. While we did not measure the phase response of the solenoid without the ferrite core in place, the fact that the fitted values for the resistance and inductance are so close to the predicted values (with our permeability estimate of ~1.5), these results suggest that the phase lag is due to the inductance. However, the most important fact is that we have characterized the phase lag as a function of f_{mag} so that it can be accounted for in the phase-locking step of the signal processing algorithm. We use the parameters from this least squares curve fitting to set the phase value used in the phase filtering step of the MMOCT image processing algorithm based on the magnet modulation frequency used.

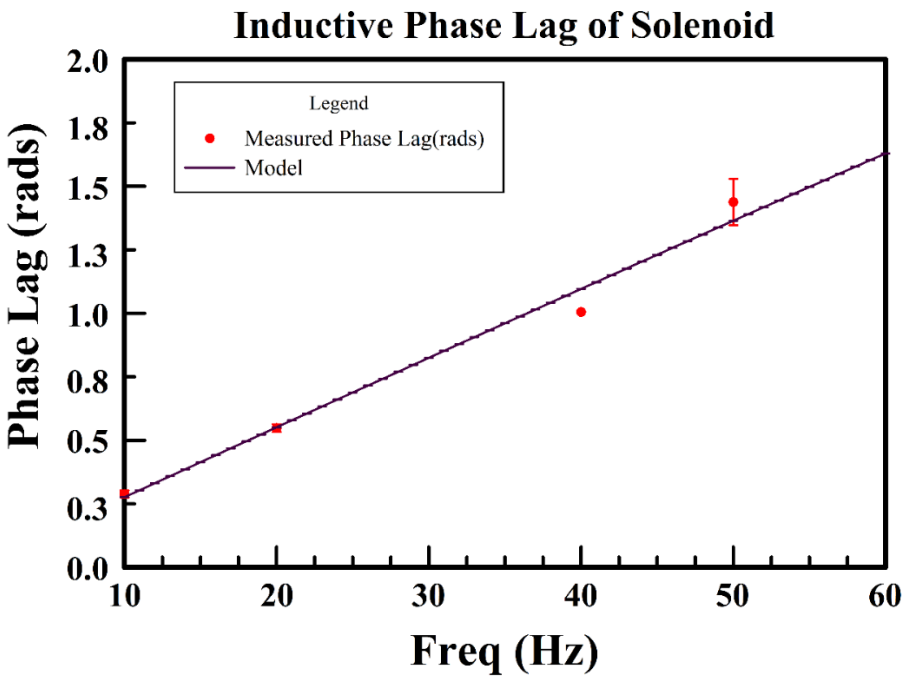

Figure 3-12 Frequency Response of the Inductive Phase Lab.
The voltage of the solenoid lags behind the applied voltage from the power supply. The frequency response of the phase of the LR circuit models this behavior well.

Likewise, the amplitude of the magnetic field decreases approximately linearly with magnetic modulation frequency. The frequency response of the voltage amplitude for an LR circuit is given by:

$$|V(f)| = \frac{R/L}{\sqrt{(2\pi f)^2 + (R/L)^2}} \tag{3-17}$$

Using the same initial values of *R*, and *L*, we used nonlinear least squares curve fitting to fit equation 3-16 to the measured B-field amplitude as a function of magnet modulation frequency (Figure 3-13).

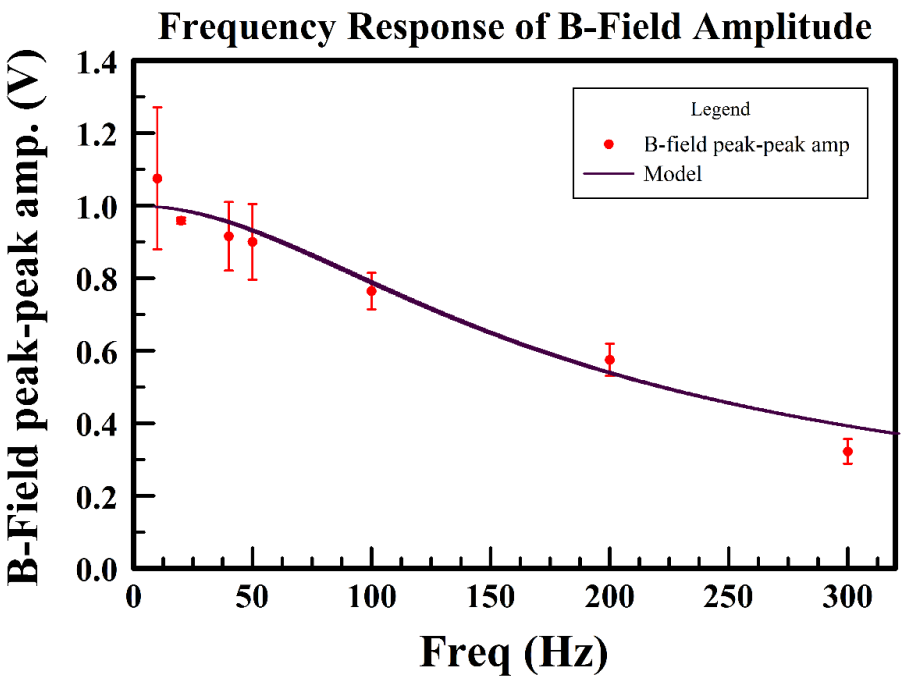

Figure 3-13 Frequency Response of B-Field Amplitude.
The magnitude of the inductor voltage has a fall-off with increasing magnet modulation frequency which is modeled in terms of the frequency response of an LR circuit.

From the least squares curve fitting, we estimate $L = 5.5 \pm 0.2$ mH and $R = 4.4 \pm 0.2$ Ω. The reduction in magnetic field amplitude means that if we try to modulate the magnet at frequencies higher than 50 Hz, we will have > 10% drop in amplitude. This means that the range of magnet modulation frequencies we can use is currently limited by the inductance of the magnet. It is possible that we could re-design the circuit to make a resonant LRC circuit and remove this inductive amplitude loss. In that case, we could move to higher values of f_{mag}, but we would have to consider both the high-frequency properties of elasticity and the viscoelastic effects. The frequency-dependent elastic properties include the resonance properties of the sample (typically in the kHz range for biological tissues, but this is geometry dependent) as well as the frequency-dependent elasticity (medium stiffness increasing with increasing frequency) [97]. Sample viscoelasticity may cause the vibration amplitude to fall off with increasing f_{mag} if the

viscoelastic response time (which causes a lag in the sinusoidal tissue deformation compared to the applied force) is much longer than the excitation time [98].

3.2.3 Motorized Stage

The final hardware element of the LF-MMOCT system is the motorized linear stage. Although no scanning is needed to produce a 2D image with LF-OCT, mechanical scanning is required for volumetric imaging. Typically SD-OCT systems accomplish volumetric imaging by mechanically scanning the beam using galvanometer-controlled mirrors. Because the beam is so large in LF-OCT, it is easier to mechanically scan the sample rather than scanning the beam. To accomplish this requires a motorized linear stage that is controllable by LabVIEW and which has sufficiently large range of motion, sufficiently small incremental step size and is highly accurate. There are generally two kinds of motors used to control motorized linear stages: stepper motors and DC servo motors. Stepper motors are cheaper but noisier. DC servo motors are not precise unless they have a position encoder- this is what makes high-precision DC servo motors expensive. Because MMOCT is very sensitive to any mechanical vibrations in the sample, we require the least noisy motor possible. For this reason, we chose a Newport linear motorized stage (XMS50) with a DC servo motor, a maximum range of 50 mm, a minimum step size of 1 nm and a position accuracy of 200 nm.

3.3 MMOCT System Software

3.3.1 Graphical User Interface for hardware control

To synchronize the LF-MMOCT hardware, we created a graphical user interface (GUI) that controls the camera, the magnet's power supply, and the motorized linear stage. To control

the magnet, the user selects the following parameters: the maximum output voltage (for the 0-10 V signal that is sent to the power supply), the camera framerate, the number of frames to be collected, N, and the temporal sampling of the magnetic field (the number of frames per magnet cycle). A square root-sine waveform is generated with N points spaced by Δt = 1/framerate. The magnet modulation frequency is then defined as the framerate divided by the temporal sampling. To engage the motorized stage, the user can set a starting position, a final position, and a velocity. To record MMOCT images, a preset button is pressed first which primes the waveform to be sent to the power supply. Then, when the record button is pressed, the camera begins recording images at the same time that the waveform is sent to power supply. (The motorized stage will also initialize if it has been set to do so.)

In addition to controlling image acquisition, the GUI can also be used to help set up the samples. If operated in live mode, the GUI will display the intensity recorded by the camera in real time as a 12-bit gray scale image. The intensity recorded by the camera is the spectral interferogram rather than a B-mode OCT image. Because it is far easier to set up the sample position within the coherence gate if you can see the B-mode image rather than the raw spectral interferogram we added an option to display a "real-time" 1D Fourier transform of the raw spectral interferogram. This option will display B-mode images at 20 frames per second.

3.3.2 Signal Processing Algorithm

To detect magnetic signal from an OCT image, we wrote an image processing algorithm (outlined in Figure 3-14). The camera records the intensity of the combined electric field from the sample and reference arms (as in equation 2-2). We record a stack of images in time. First, a 1D Fourier transform (along λ) of the reference-subtracted image stack reconstructs the complex

analytic OCT signal, S_{OCT}. Digital dispersion compensation is done at the same time as the FT. The absolute values of the S_{OCT} of each frame in the image stack is a B-mode image. The argument of S_{OCT} of each frame yields a stack of optical phase in time. Differentiating the optical phase in time produces a stack of N-1 frames of $\Delta\theta$ in time. In order to select only oscillations at the magnet frequency, $f_{mag,}$ we take a 1D Fourier transform along the time dimension of the $\Delta\theta$ stack. The Goertzel algorithm selects only the Fourier transform component, $F(\omega)$, for $\omega = 2\pi f_{mag}$. This component has an amplitude, A_{mag}, and a phase, φ_{mech}. The phase is the mechanical phase of the magnetic particles' response. To reject any motion that is out of phase with the expected phase of paramagnetic particles, φ_{para}, a cosine filter is applied:

$$A_{mag} = A_{mag} \bullet \frac{1+\cos(\varphi_{mech} - \varphi_{para})}{2} \tag{3-18}$$

(The value of φ_{para} is computed as the difference of $\pi/2$ and the phase lag given by equation 3-15.) This weights the magnetic signal, A_{mag}, by a value ranging from 1 if the mechanical phase is equal to the paramagnetic phase to zero if the mechanical phase is π radians out of phase. We then convert A_{mag} to a displacement in nm. This is done by writing out the expression for the discrete Fourier transform of the differential optical phase in terms of Δz (which is related to the displacement Δz by equation 3-3) and then solving for Δz. They are related by

$$\Delta z = \frac{\lambda_0}{4\pi^2 n f_{mag}} \frac{A_{mag}}{\Delta t N} = \gamma A_{mag} \tag{3-19}$$

where Δt is the spacing of the discrete samples (1/framerate) and N is the number of discrete samples. The multiplicative factor, γ, converts the magnitude of the DFT to a displacement in nm. The same steps are repeated for an image stack recorded with no magnetic modulation. We take the difference of the magnetic signal with the magnet modulated and the magnet off and

apply an intensity threshold mask to the difference. The intensity threshold mask is made from the time-averaged B-mode image, and we apply it because we only expect meaningful phase information from bright scatterers. The thresholded difference Δz_{Bon} - Δz_{Boff} is what we call the magnetic displacement and is the metric used in this dissertation for single magnetic particle displacement measurements. For homogenous distributions of MNP, the metric typically used is the magnetic SNR which is defined as the magnetic displacement divided by displacement from the stack with no magnet modulation and is given in dB by taking the logarithm (10Log_{10}) of that ratio.

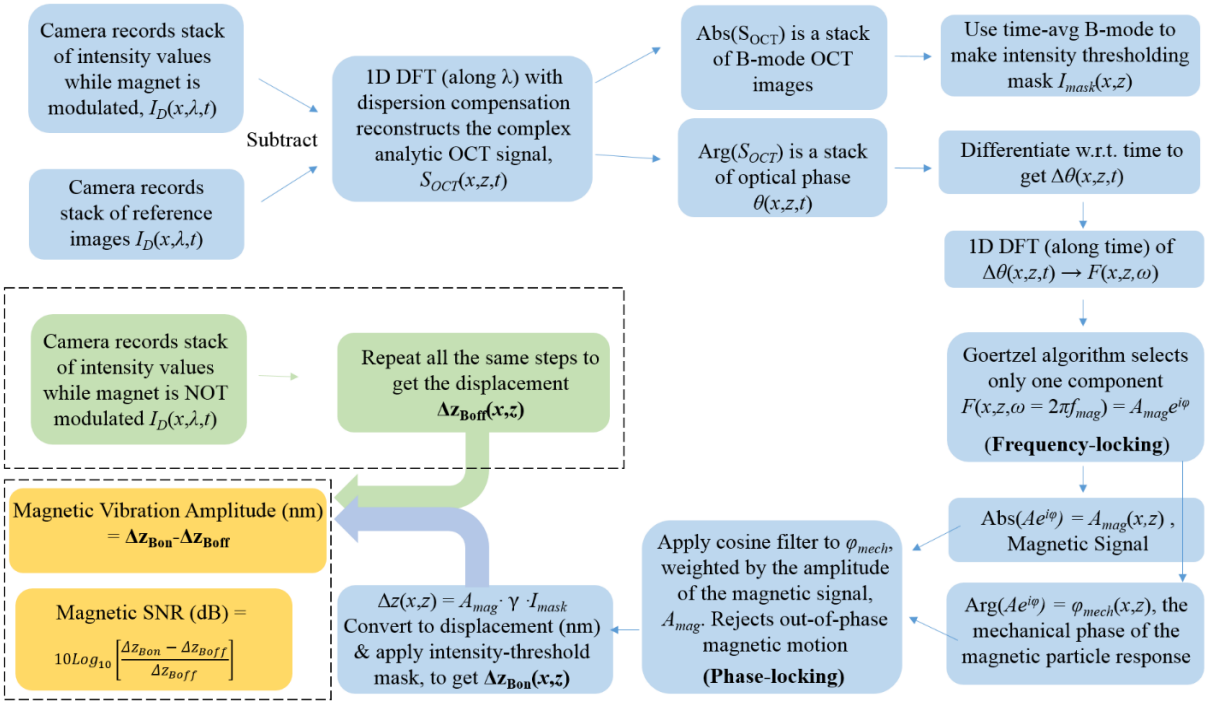

Figure 3-14 Flowchart of MMOCT signal processing algorithm.

3.4 Conclusion

The LF-MMOCT system described in this chapter is one specifically designed for single magnetic particle detection. In order to achieve an equivalent SPIO diameter on the order of the size of endogenous magnetite crystals found in some species of bacteria, we have re-designed the optics to achieve a smaller resolution volume with an axial and transverse resolution of ~2 μm and ~7 μm respectively. The spectrometer was re-designed to improve the roll-off so that the effective field of view could be extended to the full 500 μm. The magnetic field delivery system was designed to produce a sufficiently high magnetic gradient at a distance of 6 mm from the solenoid and to maintain force homogeneity over an unusually wide FOV of 5mm. With the implementation of the new camera with a framerate of 5400 frames per second, the LF-MMOCT system has the potential to increase the volumetric imaging speed by an order of magnitude compared to the only other reported volumetric MMOCT system [20], while simultaneously achieving a better sensitivity to single magnetic particles through the combination of high SNR and fine spatial resolution. The first demonstration of LF-MMOCT is given in the following chapter.

CHAPTER 4 - LF-MMOCT OPTIMIZATION & SINGLE MNP DETECTION

After designing and characterizing the LF-OCT system and then converting that LF-OCT system to a LF-MMOCT system with the hardware and software developments described in the previous chapter, the next step was to develop imaging protocols and to characterize the LF-MMOCT system before finally demonstrating the ability of LF-MMOCT to detect single magnetic particles. In Section 1 of this chapter, I describe the protocols developed for LF-MMOCT sample preparation. In Section 2, I describe the development of the imaging scheme used. Section 3 covers an attempt we made to image magnetotactic bacteria using the new (faster) imaging scheme. The work described in sections 2 and 3 was done using a point-scanning MMOCT system built by a previous student in our lab (but using my new imaging scheme and signal processing algorithms). This work was done while the LF-MMOCT system was being developed. Section 4 is the first demonstration of the LF-MMOCT system. This section includes the work on optimizing the imaging parameters for best magnetic sensitivity. Then, using those optimal imaging parameters, Section 5 includes the detection of single magnetic particles with the LF-MMOCT system, and a comparison of the measured vibration amplitude with the theoretical vibration amplitude expected based on the theory described in Chapter 3, section 3.1.

4.1 Sample Preparation Protocols

For system characterization, we use tissue-mimicking phantoms rather than biological samples. This allows us better control over the relevant properties of the sample (such as optical

scattering and elastic modulus) as well as ensuring that the samples will last for a long time so that repeated imaging over the course of many months will yield comparable results. For MMOCT, the relevant metrics for a tissue phantom are the optical scattering and the elastic properties of the phantom. Following the sample preparation protocol given in Ref [5], we first made samples using silicone because the elasticity is easy to manipulate by diluting cross-linking PDMS with non-cross linking silicone oil. Oldenburg *et al* reported that a ratio of 90.4% silicone oil (50 cSt viscosity), 8.8% PDMS part A and 0.8% PDMS part B (the curing agent) produced tissue phantoms that qualitatively matched the mechanical properties of soft human tissue [5], with an elastic modulus of approximately 12 kPa [99]. To match the scattering coefficient of biological tissues, TiO_2 micro-particles were added at a concentration of 4.1 mg/g. This concentration was found by comparing the peak OCT signal and OCT signal attenuation in depth to that of 2% intralipid, which is representative of human skin (as reported in Ref [100]).

Using this protocol as a starting point, we found that a similar ratio worked well for us. We combine 89.1% silicone oil (pure PDMS, 50 cSt viscosity, Clearco Products), 9.9% Sylgard 185 Silicone Elastomer Kit part A, (the base), and 0.99% of the elastomer kit part B (the curing agent). We add TiO_2 micro-particles (Sigma Aldrich rutile powder, 224227, mean diameter 1μm) at a concentration of 4.11 mg/g, and we add varying concentrations of Fe_3O_4 nanopowder (Sigma Aldrich, 637106, mean diameter 50-100 nm) to make samples with homogeneous distributions of paramagnetic nanoparticles for characterizing the MMOCT system. The TiO_2 nanopowder is highly electrostatic and tends to settle out of the silicone polymer matrix and stick to the sides of the glass or plastic sample holder during the ~36 hours that it takes the silicone to cross-link. The protocol that we ultimately found to produce the most homogenous distribution of both the TiO_2 and the Fe_3O_4 (with the least settling out of the nanopowders) is as follows. To make an entire

array of silicone samples with varying concentrations of Fe_3O_4, make three large batches of the silicone mixture, one with no Fe_3O_4, one with a high concentration, and one with an intermediate concentration. These three are then be combined in varying ratios to produce individual samples with the desired concentration of Fe_3O_4. Working in large batches this way minimizes systematic errors from measuring small amounts of the Fe_3O_4 nanopowder. For each batch, pour all the components (silicone oil, PDMS parts A and B, TiO_2 and Fe_3O_4) into a 200 mL glass beaker. Manually stir the contents for five minutes. Then place in a sonicating bath and leave for three hours. Manually stir each batch right before combining them in the desired ratio into each individual sample mold. Cure the samples overnight at 70°C and then cure at room temperature for 24 hours.

The benefits of the silicone samples are that silicone stays cross-linked for many years. This means that the same samples can be used to measure the Fe sensitivity of an MMOCT system over long time scales, ensuring that the results are always comparable with previous measurements. While silicone is the best choice for longevity, it presents problems for LF-MMOCT samples. As shown in Figure 3-7, the magnet in the LF-MMOCT system is placed below the sample because with our large line illumination, it would be difficult to image through the magnet bore. Because the magnetic field gradient drops off steeply with distance, we need the magnet to be as close as possible to the portion of the sample being imaged. This limits the thickness of the sample we can use in LF-MMOCT because we can only image ~ 0.5 mm deep into the tissue and we need the magnetic field gradient not to have fallen off too much at this distance from the magnet. As described in section 3.2.2, the magnetic field delivery system was designed to be used with samples ~2 mm thick. Making such thin samples proved challenging because the TiO_2 and Fe_3O_4 settles out and clings to the bottom of the sample mold when such a

thin layer of the silicone mixture is poured. The optical scattering of the 2mm-thick silicone samples was greatly reduced compared to ~8mm-thick samples made for a point-scanning MMOCT system (in which the magnet is placed above the sample so sample can be much larger).

We tried using gelatin rather than silicone to make thin samples for the LF-MMOCT system, but the melting point of the gelatin (37°C) was so low that the gels melted under illumination from the high-powered SC source in the LF-OCT system. Ultimately, the best protocol we found for making 2 mm-thick samples for the LF-MMOCT system was to use agarose powder (Sigma Aldrich A0169). The agarose has a melting point of 87°C and has never shown any sign of melting after many minutes of continuous exposure to the line illumination in the LF-OCT system. Evidence of melting can be seen by taking an image stack of the agarose or gelatin sample over time. If the processed B-mode images are converted to a video, the surface of the sample lowers in the image over time if the sample is melting. Additionally, a hollow with approximately the same dimensions as the line illumination will appear on the surface of the gel. For all the samples made in this dissertation, we use an agarose concentration of 0.4% by weight (*e.g.* for a typical sample size, combine 10 mL of distilled water and 42 mg of agarose powder). From Ref [101], we can estimate the elastic modulus of this agarose concentration as ~13 kPa. This is a biologically relevant elasticity because the range of the Young's modulus of soft tissues varies from ~10^{-1} kPa – 10^{1} kPa [102]. In fact, we are at the upper end of the biologically relevant range of Young's moduli meaning that the displacements we measure will be smaller (and therefore harder to detect) in these samples compared to soft tissues with smaller Young's moduli. (From equation 3-6, the vibration amplitude of an MNP mechanically coupled to an elastic medium is inversely proportional to Young's modulus, so smaller Young's moduli will produce larger displacements.) If we can detect magnetic motion in these agarose samples, we can expect

to expect similar or even larger displacements in soft tissues.

The agarose sample preparation is as follows. Heat water to at least 90°C and pour into a 50mL centrifuge tube, and then add the agarose powder, the TiO_2, and the Fe_3O_4. (Note that using a smaller and narrower centrifuge tube results in the TiO_2 and Fe_3O_4 getting stuck in the tip of the centrifuge tube.) Immediately mix using a vortexer, and then place in a 90°C water bath. Keep the agarose mixture in the hot water bath for 20 minutes, vortexing periodically. After 20 minutes, remove the water bath from its heat source and allow it to begin cooling. Continue to vortex the sample periodically. Once the agarose mixture has cooled to 55°C, pour into the sample molds, cover, and refrigerate for 20 minutes. If the agarose samples are kept hydrated and in an air-tight container in the fridge, they will last for many months.

4.2 Development of frame-by-frame MMOCT imaging scheme

To improve the volumetric imaging speed of the LF-MMOCT system, we propose not only to take advantage of the parallelization of A-line acquisition given by the line illumination + 2D pixel array, but also to change the imaging scheme that has been employed in previously published MMOCT work. The first MMOCT system developed by Amy L. Oldenburg used a magnet modulation scheme in which the magnetic field was modulated while the imaging beam was scanned along the transverse extent of the sample [4,5]. Only three B-mode images are needed to reconstruct a 2D magnetic signal map. A 1D DFT is applied to the spatial dimension of each B-mode image (the spatial dimension, *X*, being coupled to the magnetic modulation in time), the DFT is band-pass filtered around the magnet modulation frequency, and then an inverse DFT is applied to reconstruct a 2D spatial mapping of the magnetic signal (with some loss of transverse resolution due to the bandpass filtering). Two of the images are recorded with

no magnet modulation and are used for background noise subtraction. The third image is recorded while the magnet is modulated. We refer to this imaging scheme as line-by-line MMOCT because the magnet is modulated within a B-mode frame.

While line-by-line MMOCT is a viable method if some loss of transverse resolution and imaging speed is acceptable, for applications such as single magnetic particle detection, the limitations placed on the imaging speed and transverse resolution make this imaging scheme untenable. Because each magnet cycle needs to be sampled by several A-lines (minimum of two, to meet the Nyquist sampling criterion), and because it is desirable to have several magnet cycles per resolution element in order to increase the magnetic SNR and in order to ensure that the structural OCT image is separable from the magnetic signal in frequency space (after taking the DFT), a constraint is placed on the linerate according to:

$$mf_{mag} < f_s < cf_{mag} \tag{4-1}$$

where m is the temporal sampling factor (the number of A-lines per magnet cycle), f_s is the linerate, and c is the spatial oversampling factor in X (*i.e.* the number of A-lines per resolution element). To meet the Nyquist sampling criterion, m must be >2. For a typical magnet modulation frequency f_{mag} = 100 Hz, with heavy spatial oversampling of 75 A-lines per resolution element, the linerate is limited to a few thousand lines per second, well-below the maximum linerates of ~70kHz commercially available in 2020 (although at the time that MMOCT was developed, frame-by-frame MMOCT was not a viable option because sufficiently fast linerates were not yet available). Using a larger spatial oversampling factor is possible but impractical because the total number of A-lines, N, required to image a given FOV is determined by $N = c*(\text{FOV}/\Delta x)$, where Δx is the transverse resolution. So increasing the spatial oversampling increases the total number of A-lines required to image a given FOV, which in turn

reduces the framerate. To summarize: for the line-by-line imaging method, because the spatial dimension, *X*, is coupled to the magnet modulation in time, the effective framerate is limited by the need to spatially oversample the image. Additionally, the transverse resolution is degraded by the bandpass filtering required to select for magnetic motion in the spatial DFT. If we could de-couple the spatial dimension, *X*, and the time, *t*, we could increase the MMOCT framerate and prevent the loss of transverse resolution.

A more efficient imaging scheme is called frame-by-frame MMOCT, and it consists of modulating the magnetic field across frames rather than within frames. This effectively decouples *X* and *t*. Now, the limitation on imaging speed can be written:

$$mf_{mag} < f_s < cf_{mag} \tag{4-2}$$

where the sampling rate, f_s, is now the framerate, and the spatial oversampling factor, *c*, is the number of frames per resolution element in *Y* rather than in *X*, and the temporal sampling factor, *m*, is the number of frames per magnet cycle (rather than the number of A-lines per magnet cycle). The requirement on the spatial oversampling is only true for volumetric MMOCT. If the sample is held stationary (without scanning in Y), there is no theoretical upper limit on the framerate. However, even for volumetric MMOCT, the parallelization of Aline acquisition combined with the fact that the magnetic signal is now decoupled from the spatial dimension means that the overall volumetric imaging rate is greatly improved; heavy spatial oversampling is no long required because the magnetic signal is inherently decoupled from the structural OCT image. Fewer A-lines per resolution element combined with faster framerates means higher volumetric throughput. Further, because the structural OCT image is decoupled from the magnetic signal, we no longer need to bandpass filter the DFT to select the magnetic motion; instead, we use the Goertzel algorithm to select only the spectral component $f = f_{mag}$. This

collapses the 3D stack of B-mode images recorded in time to a 2D magnetic signal map. This method means that the transverse resolution is not degraded by bandpass filtering the spatial image. For these reasons, we propose to use the frame-by-frame imaging scheme in the LF-MMOCT system. The relevant imaging parameters that characterize an MMOCT system with the frame-by-frame method are summarized in Table 4-1.

Table 4-1 Frame-by-Frame MMOCT Imaging Parameters

	Parameter	Definition	Written in terms of other variables
Independent Imaging Parameters	f_s (optical framerate)		
	N (# frames)		$m*P$
	f_{mag} (Hz)		
Dependent Imaging Parameters	m (images/cycle)	f_s/f_{mag}	
	T (total imaging time)	N/f_s	
	P (# magnet cycles)	$T*f_{mag}$	$(N/f_s)*f_{mag}$
DFT Parameters	ΔT (spacing of discrete samples)	$1/f_s$	
	Nyquist Frequency (Hz)	$f_s/2$	
	Δf (DFT frequency bin spacing)	$1/T$	f_s/N
	n_{fmag} (index of DFT frequency bin centered at f_{mag})	$f_{mag}/\Delta f$	$(N/f_s)*f_{mag} = P$

While the LF-MMOCT system was being developed, we tested the frame-by-frame imaging scheme on a point-scanning MMOCT system. The system is described more fully in Ref [11], but briefly, the system is composed of a Ti:Sapphire laser (KMLabs, INC, with a bandwidth of 120 nm centered at 810 nm), a free-space Michelson interferometer, galvo-

controlled mirrors that allow scanning in *X* and *Y*, and a line-scan CCD camera (Dalsa Piranha with a maximum linerate of 70kHz). The system has an axial resolution of 2 μm, a transverse resolution of 16 μm, and an SNR > 95 dB.

As an initial demonstration that the frame-by-frame imaging scheme worked at least as well as the line-by-line imaging scheme, we measured the Fe sensitivity of the MMOCT system using both methods. The Fe sensitivity is defined here at the minimum concentration of Fe in a sample that is needed to produce a magnetic SNR distinguishable from that of a control sample (containing no Fe) with 95% confidence ($p < 0.05$). We made an array of silicone samples with Fe concentrations ranging from 2 μg Fe/g sample to 713 μg Fe/g sample. For the line-by-line imaging method, each sample was imaged in two transverse positions on the surface of the sample. At each position, we recorded one reference image, 5 images with the magnet modulated and 5 images with the magnet off (for background noise subtraction). The magnet modulation frequency of 80 Hz was used, the FOV in *X* was 0.4 mm, the number of A-lines per B-mode was 2500, and a linerate of 2000 lines/sec was used. This yields a temporal sampling factor of 25 A-lines per magnet cycle and a spatial oversampling factor of 75 A-lines per transverse resolution element. Between each pair of magnet off + magnet modulated images, there was a rest period of 5 seconds to prevent magnet overheating. A random number generator was used to select the order in which to image the samples so that any time-dependent effects over the course of the experiment would not be linked to certain samples. The frame-by-frame data was collected with a magnet modulation frequency of 10.8 Hz, a linerate of 69.252 kHz, a FOV of 0.4 mm, 500 A-lines per B-mode (giving an optical framerate of 108 fps and a spatial sampling in *X* of 15 A-lines per resolution element), and 100 images are recorded in each image stack. These parameters yield a temporal sampling of 10 frames per magnet cycle. Two image stacks (one

with the magnet modulated and one with the magnet off) are recorded at two different positions on the sample's surface, with three image stacks recorded at each transverse position.

For line-by-line signal processing, the magnetic signal is calculated by taking the average of the absolute value of the pixels that pass through the bandpass filtering, weighted by their mechanical phase. This is done for the image recorded with the magnet modulated and the image recorded with the magnet off. The magnet-off magnetic signal is subtracted from the magnet-modulated magnetic signal. The results are plotted in Figure 4-1. For the frame-by-frame method, the signal processing steps are outlined in the last section of Chapter 3; a Goertzel algorithm selects the component of the DFT of the differential optical phase in time for which $f = f_{mag}$. The magnetic signal (the absolute value of the Goertzel output) is background-subtracted. We then take the log of the background-subtracted signal to report values in dB. The Fe sensitivity found by comparing the background-subtracted magnetic signal of each sample to that of the control sample (containing no Fe) was found to be 37.6 µg Fe/g sample from the line-by-line method and 20.0 µg Fe/g sample from the frame-by-frame method. This was a proof of concept that the frame-by-frame imaging method at the very least is not less sensitive than the traditional line-by-line method. In fact, we see evidence that the magnetic signal given by the frame-by-frame method saturates at Fe concentrations above 300 µg/g, so that the signal appears to decrease for very high Fe concentrations. We made a similar measurement of the Fe sensitivity of the LF-MMOCT system after its implementation, which is discussed later in Section 4.4. We note that Ahmad *et al* first published a demonstration of the frame-by-frame MMOCT magnet modulation scheme in 2014 [20]; our work was developed independently from that group's work, but with similar conclusions as to the method's viability and improved speed for volumetric applications.

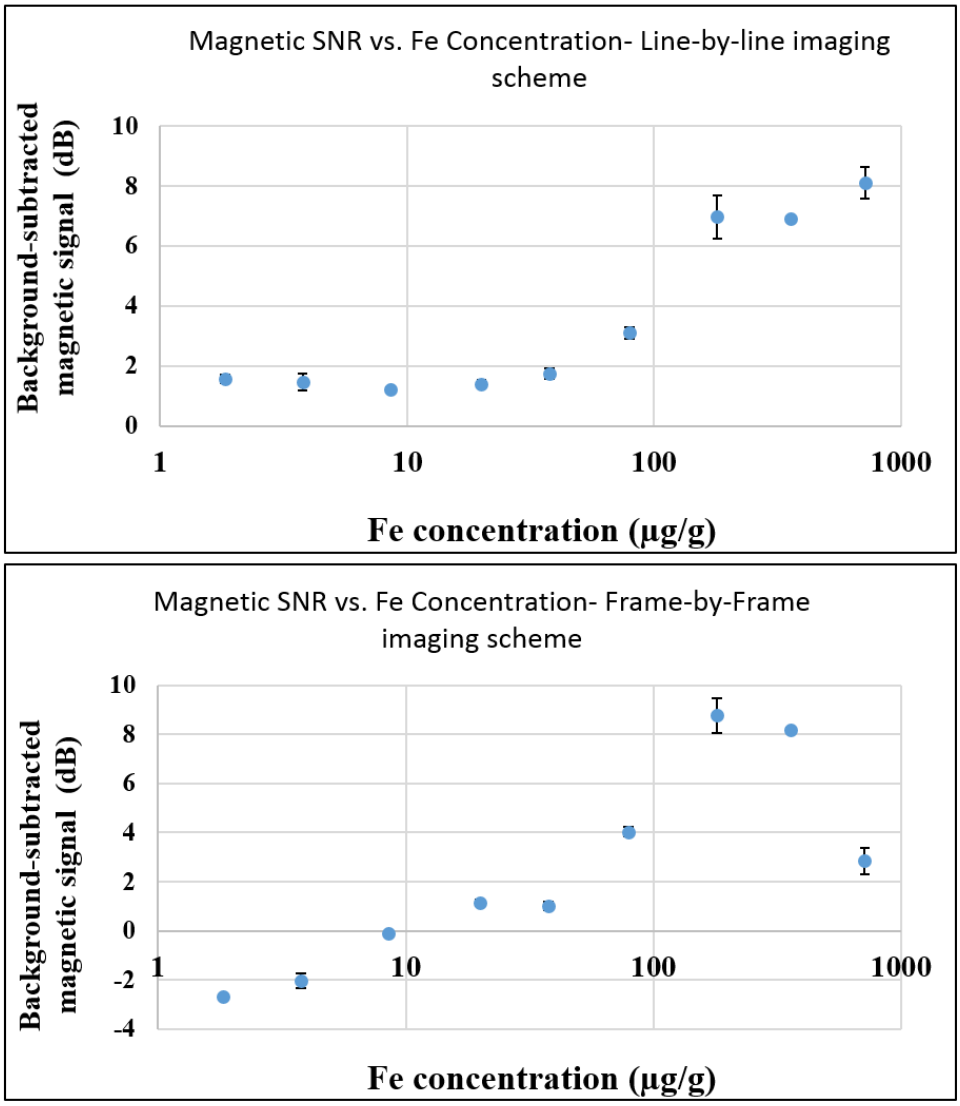

Figure 4-1 Fe Sensitivity of Line-by-Line and Frame-by-Frame MMOCT.
Plot of the background-subtracted magnetic signal as a function of Fe concentration measured using the line-by-line imaging method (top) and the frame-by-frame imaging method (bottom). In the frame-by-frame method, there is evidence of signal saturation at Fe concentrations above 300 µg/g, so that the signal appears to decrease for very large Fe concentrations.

After verifying that the frame-by-frame method is as sensitive as the line-by-line method, we could more carefully think about how to make the frame-by-frame method as fast as possible. Although we no longer need to heavily spatial oversample, as we do in the line-by-line method, to be conservative when measuring the Fe sensitivity, we still used a relatively high amount of

spatial oversampling of 15 A-lines per resolution element in *X*. We also recorded 10 magnet cycles with a temporal sampling of 10 frames per magnet cycle. Using the same data displayed in the bottom panel of Figure 4-1, we used frame decimation and A-line decimation to determine which parameter (spatial oversampling, number of magnet cycles, and temporal sampling) had the greatest effect on the background-subtracted magnetic signal to determine if the amount of data collected can be reduced without significantly effecting the Fe sensitivity. We tried decimating the number of frames by a factor of 2. The total imaging time remains the same, so the spacing in the DFT of the differential phase in time remains the same. The Nyquist frequency is halved. We also decimated the A-lines by a factor of 8. This was to reduce the spatial oversampling to only 2 A-lines per resolution element. The third data reduction technique was to reduce the total number of frames processed; this reduces the number of magnet cycles. Of the 100 recorded frames, we processed only the first 80, reducing the number of magnet cycles from 10 to 8. We tried each metric individually. To quantitatively compare the effect of each data reduction method, we computed the background-subtracted magnetic signal in the exact same manner as that described previously. We then computed the sum of the squared errors between each back-ground subtracted magnetic signal with all the original data and that obtained using the data reduction metric. We also tried combining all three metrics. The results are summarized in Table 4-2. Decimating A-lines by a factor of 8 had the smallest effect on the background-subtracted magnetic signals and has the greatest effect on reducing the amount of data needed of any single metric. Based on these results, we conclude that heavy spatial oversampling has a small effect on the Fe sensitivity when the frame-by-frame imaging scheme is used. In order to increase the volumetric throughput, a spatial oversampling of approximately 2 A-lines per resolution element provides a good balance between sufficient sampling and imaging speed.

These results informed our design of the LF-MMOCT system, described in Chapter 3. We expanded the transverse FOV to 5 mm, and with a transverse resolution of ~ 7μm and 1024 transverse pixels, the LF-MMOCT system has a fixed spatial oversampling factor of ~ 1.4 A-lines per resolution element.

Table 4-2 Summary of Data Reduction Metrics

	Decimating A-lines ×8	Decimating Frames ×2	Reduce # magnet cycles by 20%	All 3 metrics combined
Sum of squared errors (dB)	0.54	5.11	1.24	12.90
Percent of original data kept	12.5 %	50 %	80 %	5 %

4.3 MMOCT of Magnetotactic Bacteria

After familiarizing myself with the MMOCT imaging procedures, sample preparation protocols, and measuring the Fe sensitivity of the point-scanning MMOCT system, we used this system to image magnetotactic bacteria. Magnetotactic bacteria are known to contain chains of magnetite crystals, which allow them to sense the Earth's magnetic field [74,89]. Because the ultimate goal of the LF-MMOCT system is to detect endogenous magnetite crystals (which may or may not be present in other animals), imaging a sample that we know contains endogenous magnetite is a logical starting place.

Working with collaborator, David Ernst, in the Lohman Lab in the Biology Department of UNC-Chapel Hill, we made several attempts to image the magnetotactic bacteria after embedding them in agarose. The bacteria are *Magnetospirillum magneticum* (strain AMB-1), and were grown in a liquid media bath (ATCC magnetic spirillum growth medium). These bacteria

are anaerobic, which means that special equipment is needed to culture them. Our collaborators received the bacteria from another lab, which means that we could not control the concentration that we received. Likewise, we discovered that these bacteria are very difficult to count without special equipment because they are an unusual size (a size that does not work well with the cell counting techniques available to use on UNC's campus).

The general plan of our experiments was to first use cell counting techniques to estimate the number density of the bacteria. Then, use microscopy methods to image the bacteria. From the microscopy images, estimate the size and number of magnetite crystals in each bacterium. Combined with the number density estimate, we use this information to estimate the total amount of Fe in the samples we made of bacteria embedded in agarose. Finally, perform MMOCT imaging of the bacteria embedded in agarose.

The biggest challenge with imaging the magnetotactic bacteria was getting a reliable estimate of the number density. We first tried using a bright line hemocytometer. The hemocytometer is a glass slide with ruled lines etched on the surface. You drop a known volume on the glass slide and then count the cells in each of 25 squares. Dave and I both counted 1900 cells per cubic mm from the first batch of magnetotactic bacteria that we received. This is equivalent to 1.9e6 cells/mL. However, this method had several drawbacks. The bacteria are smaller than the cells that this particular hemocytometer was designed to be used with, meaning that there could have been overlapping in the axial direction. Typically, the raised sides on the hemocytometer are very close to the diameter of the cells being counted to ensure a single layer of cells is spread across the grid. Further, there were a lot of debris and some other types of cells (identified by Dave) mixed in with the magnetotactic bacteria which may lead to over estimating

the bacteria number density. And finally, the bacteria are transparent and were very hard to see with the magnification available with that hemocytometer.

Next, we asked for help from the Flow Cytometry Lab on UNC's campus. Using a Luna cell counting machine, a lab technician made four measurements of the cell density in that first batch of magnetotactic bacteria. The average value was 2.1e4 cells/mL ± 0.2e4 cells/mL. This value is two orders of magnitude lower than the hemocytometer estimate, and neither method was well-suited to counting these bacteria. The Luna cell counting machine requires such small volumes of liquid that the estimate was based on very small numbers of cells (<10 cells per measurement). The low numbers and the fact that there were debris and other cells in the media mean that we were not confident that either method provided a good estimate of the number density.

To estimate the number and size of magnetite crystals in the bacteria, we imaged the bacteria using microscopy. Vicky Madden in the Microscopy Services Lab took transmission electron microscopy (TEM) images of the bacteria (without any dye) dried on a film. A representative image is shown in Figure 4-2. From these images, we estimate that the magnetite crystals have a diameter of ~50 nm, and that there are approximately 30 magnetite crystals per bacterium.

Although we were uncertain what the true number density of the bacteria was, we tried MMOCT imaging to see if the bacteria were detectable above the noise floor of the system. We first had to embed the bacteria in agarose because MMOCT requires the magnetic particles to be elastically bound to an optically-scattering medium. The agarose sample was made by combining distilled water, agarose powder, TiO_2 nano-powder, and the bacteria suspended in distilled water

in a concentration of 1.7% agarose by weight (elastic modulus of approximately 184 kPa, neglecting any effects from the bacteria [101]) and 4.1 mg/g TiO_2.

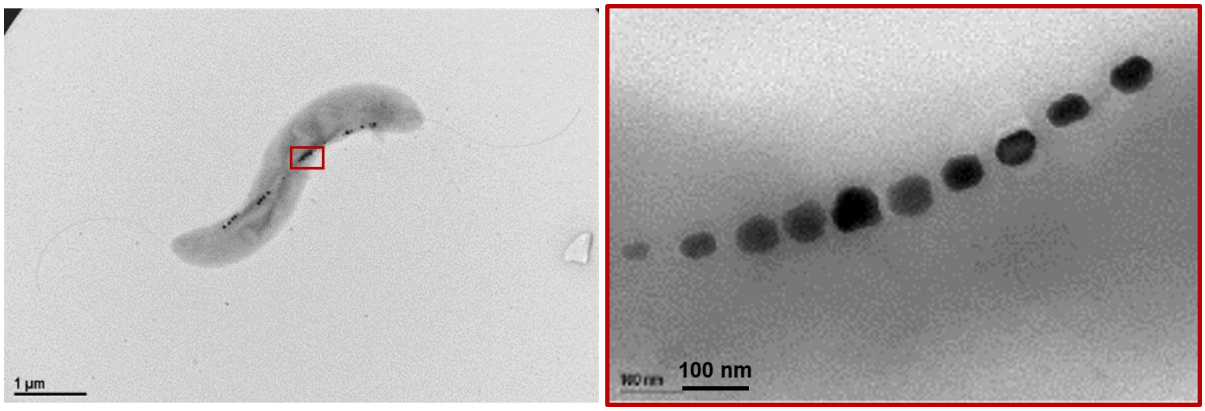

Figure 4-2 TEM images of magnetotactic bacteria.
The bacteria are ~ 3 µm in length with chains of magnetite crystals spanning nearly the entire length of the bacteria. Magnetite crystals have diameter of ~ 50 nm.

The elastic modulus of these samples was an order of magnitude larger than the Young's modulus of the typical 0.4% concentration agarose that we use for LFMOCT samples. If the bacteria imaging were repeated, a lower concentration of agarose could be used to produce larger vibration amplitudes. We pipetted 400 µL of the agarose sample into three micro-wells. The samples were allowed to cool in the fridge for 20 minutes. After gelling, we removed the gels from the micro-well plate, turned them upside down and returned them to the micro-well plate (in case the bacteria settled out on the bottom of the plate while the gel was gelling).

We imaged the bacteria embedded in agarose using the line-by-line MMOCT imaging method. With 1000 A-lines per image, a linerate of 1 kHz, an exposure time of 38.1 µs, a transverse resolution of 0.4 mm, and a magnet modulation frequency of 100 Hz, we recorded 3 images of each sample with the magnet modulated and 3 images with the magnet off. We also

imaged positive and negative control samples (agarose + TiO_2 samples with either 1.0 mg/g Fe_3O_4 or no Fe). Representative images are shown in Figure 4-3.

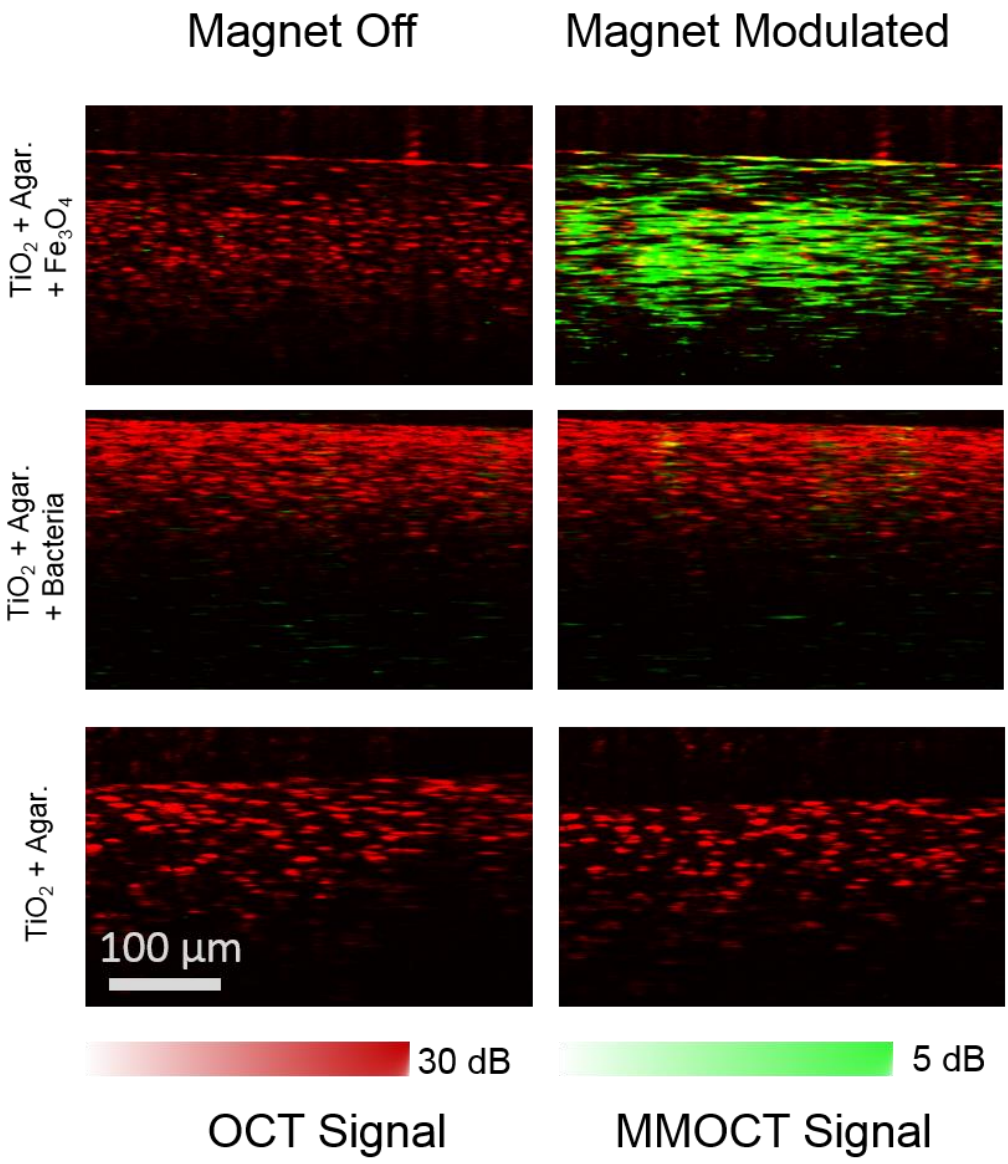

Figure 4-3 MMOCT images of magnetotactic bacteria.
The structural OCT images are displayed in red with the magnetic SNR overlaid in green. The images on the left side were recorded with the magnet off and those on the right side with the magnet modulated. The positive control sample (top row) shows strong magnetic signal throughout, as expected. The bacteria embedded in agarose (middle) show some localized magnetic signal, and the negative control sample (bottom) shows no magnetic signal.

The structural OCT image is displayed in red with the magnetic SNR map overlaid in green. The positive control sample shows strong magnetic signal throughout the entire B-mode image, as expected, while the negative control sample shows no magnetic signal, also as expected. Interestingly, the images of the bacteria embedded in agarose do show some localized regions of magnetic signal.

To quantify the results, the magnetic SNR is averaged across each 2D map. Then, the mean of the mean value of each of the three images is computed. These values are displayed in Figure 4-4, where the error bars are given by the standard error of the three measurements. The samples with bacteria have an average magnetic SNR of 2.3 dB ± 0.5 dB, compared to 0.52 dB ± 0.14 dB for the negative control and 8.1 dB for the positive control (which has only one image, the other two recorded with the shutter closed). These are exciting results as they potentially represent the first MMOCT detection of a sample with endogenous magnetite.

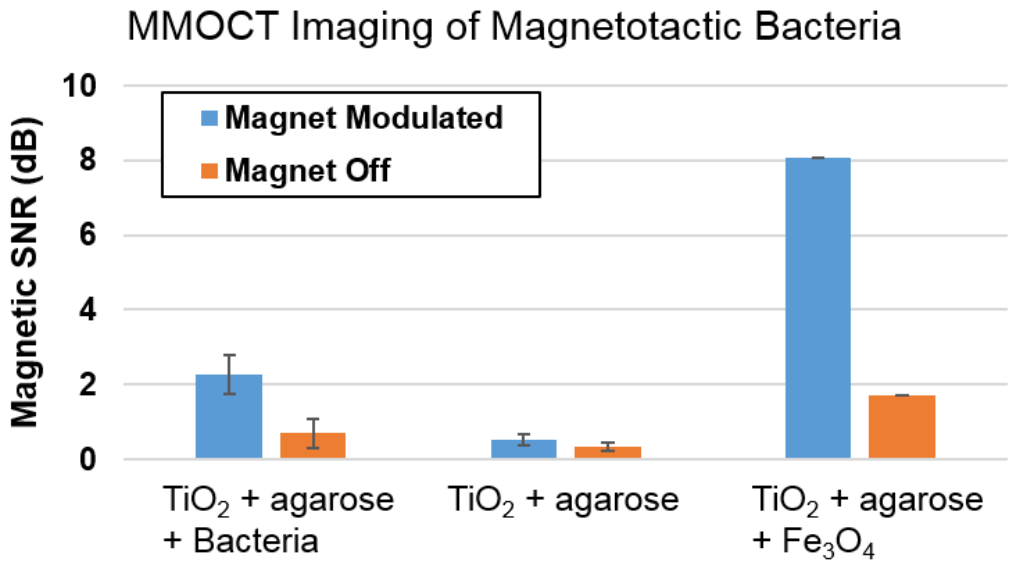

Figure 4-4 Magnetic SNR from MMOCT of magnetotactic bacteria.
The magnetic SNR of the agarose samples for the positive and negative control samples as well as the samples containing magnetotactic bacteria, showing that the bacteria are producing a measurable magnetic signal.

Knowing the dilution we used to make these agarose samples, and using the data gathered from the TEM images, we can estimate the amount of Fe in the agarose + TiO_2 + bacteria samples that we imaged and compare this estimate to the measured Fe sensitivity of the point-scanning MMOCT system. Assuming that each bacterium has 30 magnetite crystals, each with a diameter of 50 nm, we can estimate the mass of Fe in each bacterium (given that Fe_3O_4 is 72.359% Fe by mass). The volume of a single magnetite crystal is $4/3*\pi*r^3$; for r = 25 nm, the volume is $6.54*10^{-17}$ cm^3. Multiplying the volume by the number of crystals per bacterium (30), the density of Fe_3O_4 (4.8 g/cm^3), and by the mass ratio of Fe (0.7259), the mass of Fe in each bacterium is approximately $7.96*10^{-15}$ grams. Now we can estimate the number of bacteria in each gram of agarose sample. The bacteria solution are added to the agarose mixture in a ratio of 1:3, so the bacteria solution represent ¼ of the total volume and mass of the sample (assuming the bacteria solution and agarose mixture both have a density equal to that of water because they are both primarily water). Estimating the density of the solution as 1 $gram/cm^3$, the number of cells per gram sample is just the product of the $cells/cm^3$ and 1 $gram/cm^3$. We then divide by 4, because the bacteria solution is diluted 1:3 with the agarose mixture. This gives $4.75*10^5$ cells per gram sample. Now the mass of Fe per gram sample is just the product of the mass of Fe per bacterium ($7.96*10^{-15}$ grams) and $4.75*10^5$ cells per gram sample; we estimate that the bacteria embedded in agarose samples imaged had ~0.0038 µg Fe per gram sample. This is 4 orders of magnitude below the measured Fe sensitivity of the point-scanning MMOCT system (~30µg Fe/gram sample). However, there are several possible contributing factors to the apparent detection of magnetic signal from these samples. For one, the estimated number density from the hemocytometer was not very good. We could not even get order of magnitude agreement between that estimate and the estimate from another method (the Luna cell counting machine).

Second, the Fe sensitivity is a measure of the smallest detectable concentration of Fe when homogeneously distributed in the elastic medium. We know that the Fe is not homogeneously distributed in these samples, rather it is concentrated within the bacteria. (In fact, if we roughly estimate the density of the bacteria as that of water, and approximate the shape of the bacterium as a cylinder with length 3μm and radius 0.5 μm, then following the same estimation as above, each bacterium has ~3300 μg Fe per gram tissue.) The equivalent MIO diameter for the magnetite crystals in a single bacterium (estimated as the radius of a single sphere that has the same volume as 30 crystals each with a diameter of 50 nm) is 155 nm, well above the minimum detectable MIO diameter of 118 nm for the point-scanning MMOCT system. This means that we would expect to detect magnetic signal from each bacterium, assuming that it is successfully coupled to the agarose and if the surrounding agarose provides sufficient back-scattering. Further, the bacteria may clump together in the agarose. We try to distribute the TiO_2 and bacteria homogeneously throughout the agarose, but because we cannot see the bacteria by eye or directly image them with the OCT system, we cannot verify that clumping is not occurring. Given all the confounding factors, it seems possible that the detected signals are true magnetic signal from the magnetotactic bacteria. We would like to get a better, more accurate and repeatable estimation of the number density of the bacteria in order to say for sure that we are detecting them. This would also enable us to vary the concentration of bacteria in the agarose gels and then correlate the changing magnetic SNR with bacteria concentration. We were advised that the best method to use to count these bacteria is a continuous flow centrifuge. If we could find someone on UNC's campus who has one, the magnetotactic bacteria are worth returning to in the future.

4.4 First Implementation of LF-MMOCT

After implementing all the hardware on the LF-OCT system to add magnetomotive functionality, we characterized the Fe sensitivity and optimized the imaging parameters for providing the best Fe sensitivity possible with current limitations. First, we measured the Fe sensitivity in the same manner as we did for the point-scanning MMOCT system. I made an array of 2 mm-thick agarose samples (0.4% agarose concentration by weight with 4.1 mg/g TiO_2) with homogenous distributions of Fe_3O_4 in varying concentrations from 0.0 to 1.0 mg Fe/gram sample. Even though we are making very small samples (2 mm thick and 35 mm in diameter), we discovered that it is necessary to make very large amounts of each Fe concentration in order to decrease the uncertainty on the mass of Fe added to each agarose gel. So we made ~200 mL of each sample, even though we use only 2 mL to make each 2mm thick sample.

The imaging parameters we could use with the point-scanning system are limited largely by the framerates available on the point-scanning system. There is a much wider array of imaging parameter values that we could use on the LFMMOCT system with optical framerates up to 5400 fps possible, and the ability to record 48,000 images in one go using the camera's on-board memory. As a starting point, we chose imaging parameters comparable to those used with the frame-by-frame magnet modulation scheme on the point-scanning MMOCT system. Using an optical framerate of 1000 fps, an exposure time of 0.5 ms, a magnet modulation frequency of 10 Hz, we record 1000 frames with the magnet modulated and 1000 frames with the magnet off. This is one image stack and is used to compute the magnetic SNR. For each agarose sample in the array, we record three such image stacks while the magnet is actually turned on and three image stacks while the magnet is turned off. The average magnetic SNR measured is shown in

the plot in Figure 4-5, where the vertical error bars are the standard deviations. The horizontal error bars represent the uncertainty in the concentration of Fe in each sample, calculated as the percent uncertainty in the mass of Fe in the sample from an uncertainty of 0.4 mg in the digital balance used to measure out the Fe_3O_4 nano-powder. The magnetic SNR from the control sample (with no Fe) is shown in red in the plot at an arbitrary x-axis position for comparison with the other values on the Log scale. With a p value < 0.05, a concentration of 35 µg Fe per gram sample is distinguishable from the control sample. This is consistent with the Fe sensitivity we measured with the point-scanning MMOCT system. These images constitute the first (to our knowledge) demonstration of a LF-MMOCT system.

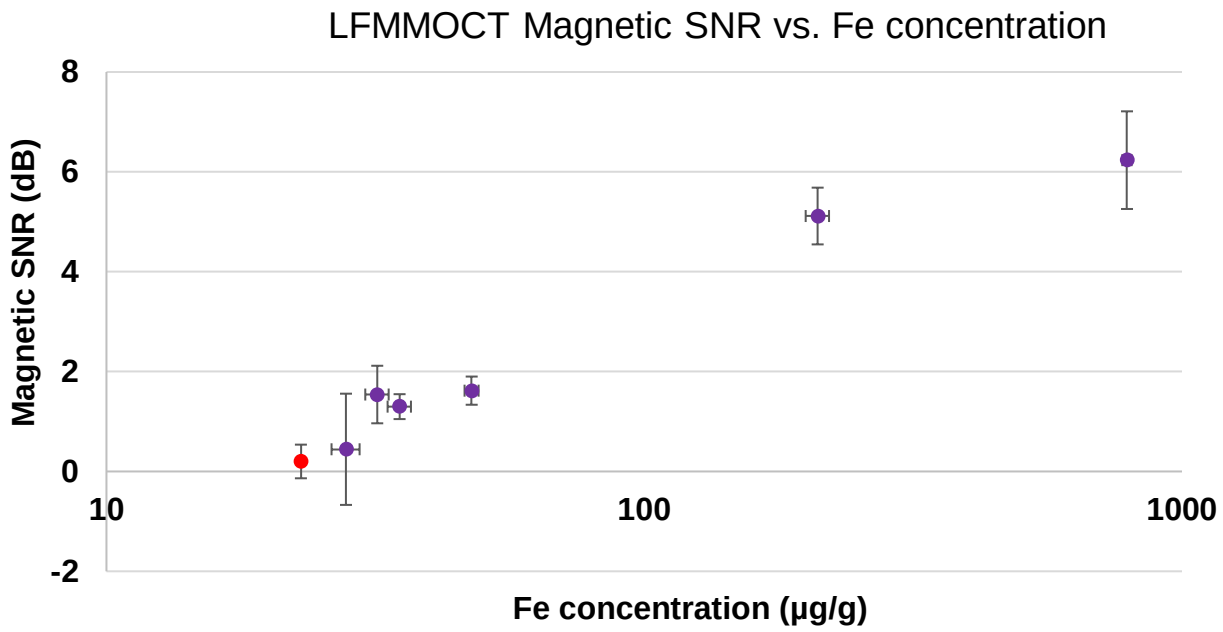

Figure 4-5 Measuring the Fe sensitivity of the LF-MMOCT System.
The average magnetic SNR from three image stacks is plotted as a function of the concentration of Fe in the sample. The control samples (with no Fe) is shown in red for comparison. With p < 0.05, we find a concentration of 35 µg Fe per gram sample to be distinguishable from the control sample.

After measuring the Fe sensitivity with imaging parameters comparable to those used with the point scanning MMOCT system, we wanted to more fully characterize how the magnetic signal was affected by each of the different imaging parameters so that we could choose imaging parameters that optimize the magnetic sensitivity. The imaging parameters that dictate the magnetic sensitivity of a LFMMOCT system essentially boil down to three things: the magnet modulation frequency, f_{mag}, the number of magnet cycles recorded, P, and the temporal sampling of the frame-by-frame magnet modulation scheme, m (called the "temporal sampling" as in Ref [20] because the magnet cycles are being sampled in time and not in the transverse dimension, as in line-by-line magnet modulation). As summarized in Table 4-1, these three parameters are dictated by the choice of optical framerate, f_s, and the number of frames collected, N. The temporal sampling is given by f_s/f_{mag}. The number of magnet cycles recorded is the product of the total imaging time and the magnet modulation frequency: $(N/f_s)*f_{mag}$. Note that the temporal sampling and the number of magnet cycles are inversely related for a fixed N. So we want to explore how each parameter affects the magnetic signal since there will be a tradeoff in these two parameters.

First, we investigate the effect of the temporal sampling by varying the optical framerate for a given f_{mag} and a given number of magnet cycles. (To hold the number of cycles constant at different optical framerates, the number of images recorded, N, must be changed as well.) The imaging parameters used are summarized in Table 4-3.

Table 4-3 Imaging Parameters for Testing Effect of Temporal Sampling

		Set 1	Set 2	Set 3	Set 4	Set 5
f_{mag} = 10 Hz	f_s (fps)	1000	500	250	125	60
	N (# frames)	1000	500	250	125	60
	m (images/cycle)	100	50	25	10	6
	P (# magnet cycles)	10	10	10	10	10
f_{mag} = 25 Hz	f_s (fps)	1000	500	250	125	60
	N (# frames)	400	200	100	50	30
	m (images/cycle)	40	20	10	5	3
	P (# magnet cycles)	10	10	10	10	10
f_{mag} = 40 Hz	f_s (fps)	1000	500	250	125	
	N (# frames)	250	120	60	30	
	m (images/cycle)	25	12	6	3	
	P (# magnet cycles)	10	10	10	10	

Using the imaging parameters given above, we imaged an agarose sample with a homogeneous distribution of Fe_3O_4 in a relatively high concentration (0.991 mg Fe/gram sample). For each set of imaging parameters, we recorded three sets of 20 reference images, three image stacks with the magnet turned off and three image stacks with the magnet turned on. The magnetic SNR as a function of m for each f_{mag} is shown in Figure 4-6. The magnetic SNR increases with increasing sampling of the magnet cycle.

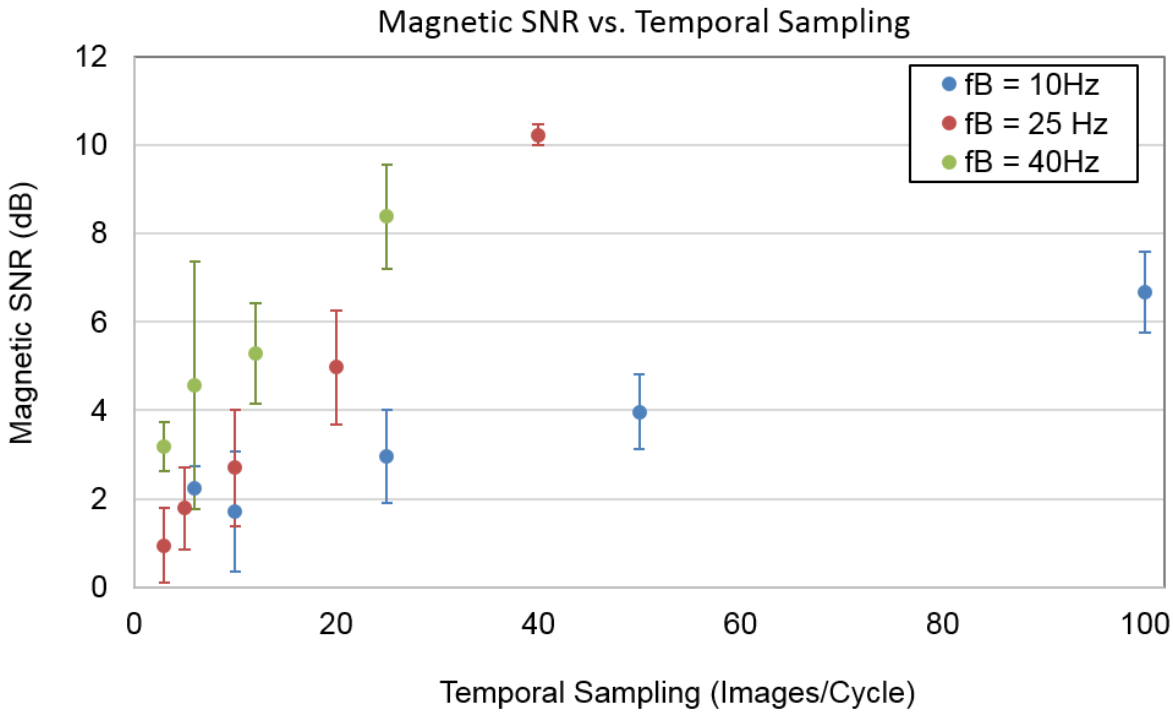

Figure 4-6 Magnetic SNR vs. Temporal Sampling.
The magnetic SNR as a function of temporal sampling is shown for three magnet modulation frequencies, 10 Hz, 25 Hz, and 40 Hz. The number of magnet cycles is fixed at 10. The magnetic SNR increases with increasing sampling.

We can model the effect of the temporal sampling by considering the effect that the sampling parameters have on the discrete Fourier transform (DFT). As outlined in Chapter 3, the signal processing algorithm we use is based on a DFT of the differential optical phase in time. The differential optical phase can be written as follows:

$$\Delta\theta(t) = A\cos\left(2\pi f_{mag} t - \pi/2\right) \tag{4-1}$$

where A is the amplitude of the differential phase (proportional to the vibration amplitude), and the $\pi/2$ phase shift comes from differentiating the optical phase. This continuous function is discretely sampled by our camera with a sample rate, f_s, and the number of samples, N. The

samples are evenly spaced in time, with a sampling interval of $1/f_s$ (as summarized in Table 4-1). We can then write the discretely sampled differential phase as a function of the sample index, *k*:

$$\Delta\theta(k) = A\cos\left(2\pi f_{mag}\frac{k}{f_s}\right) \tag{4-2}$$

We can neglect the π/2 phase shift because this will not affect the magnitude of the DFT. Recall our definition of the number of magnet cycles, $P = (N/f_s)*f_{mag}$. From this we see that we can re-write $1/f_s$ as $P/(N*f_{mag})$. The DFT of the differential optical phase is now written:

$$F(n) = \sum_{k=0}^{N-1} A\cos\left(2\pi k\frac{P}{N}\right)e^{-i2\pi kn/N} \tag{4-3}$$

where *n* is the index of the frequency bin. The closed form expression for the DFT of a real cosine function is a well-known expression in the digital signal processing world. Following the derivation in Section 3.15 of Ref [79], we can write that closed form expression of the sum over *k*:

$$F(n) = \frac{A}{2}e^{i\left(\pi(P-n)-\pi(P-n)/N\right)}\frac{\sin\left(\pi\left(P-n\right)\right)}{\sin\left(\pi\left(P-n\right)/N\right)} \tag{4-4}$$

This expression ignores the redundant negative frequency components. The magnitude of the DFT frequency response is then simply:

$$\left|F(n)\right| = \frac{A}{2}\frac{\sin\left(\pi\left(P-n\right)\right)}{\sin\left(\pi\left(P-n\right)/N\right)} \tag{4-5}$$

We care only about the frequency bin centered on the magnet modulation frequency, n_{fmag}. The index of this frequency bin is equal to *P*, as shown in Table 4-1. However, we can't evaluate $\left| F(n_{fmag} = P) \right|$ directly because sin(0)/sin(0) is undefined:

$$\left|F(n_{f_{mag}})\right| = \frac{A}{2}\frac{\sin\left(\pi\left(P-P\right)\right)}{\sin\left(\pi\left(P-P\right)/N\right)} = \frac{A}{2}\frac{\sin\left(0\right)}{\sin\left(0\right)} \tag{4-6}$$

Instead, use L'Hopital's rule to evaluate. The result is below:

$$\left|F(n_{f_B})\right| = N\frac{A}{2}\frac{\cos\left(0\right)}{\cos\left(0\right)} = N\frac{A}{2} = mP\frac{A}{2} \tag{4-7}$$

This is the well-known result for the magnitude of the frequency response of the DFT of a real cosine input; the magnitude is linear in *N*, the number of samples. The number of samples is equal to *P***m*, so we expect the magnetic signal, $\left| F(n_{fmag}) \right|$, to be linearly proportional to both the number of magnet cycles and the temporal sampling.

To test how well our experimental data follows the expected linear trend in magnetic signal as a function of temporal sampling, we used least squares curve fitting to fit a line to the magnetic signal (defined as $\left| F(n_{fmag}) \right|$, which is different from the magnetic SNR shown in Figure 4-6) as a function of *m*. From equation 4-7 we expect $\left| F(n_{fmag}) \right|$ to be linearly proportional to *m*. The results are shown in Figure 4-7. Both the slope and the y-intercept were free fit parameters. All three sets of data (each of the three values of f_{mag}) have R-squared values >0.92 with varying slopes (the slope is larger for larger f_{mag}).

As previously mentioned, we do not yet have a noise model for MMOCT, so we don't have a model to fit to the magnet-off data sets. However, we can make some educated guesses about the expected behavior. The shot noise of the light source is proportional to square root of

the sample power, as discussed in Chapter 2. From this we may expect a square root dependence on the magnitude of the DFT (in the absence of magnetic signal) as a function of *N*. We used nonlinear least squares curve fitting to fit an equation of the form *A**Sqrt(*m*)+*B* to the magnitude of the DFT from image stacks when the magnet was off (so no magnetic signal, only noise is expected). The results are plotted alongside the linear dependence on *m* when the magnet is modulated in Figure 4-7. When the magnet is off, the noise appears to have a square root dependence on *m*, plateauing to a value of ~ 6 over the range of temporal sampling factors we can achieve with this system.

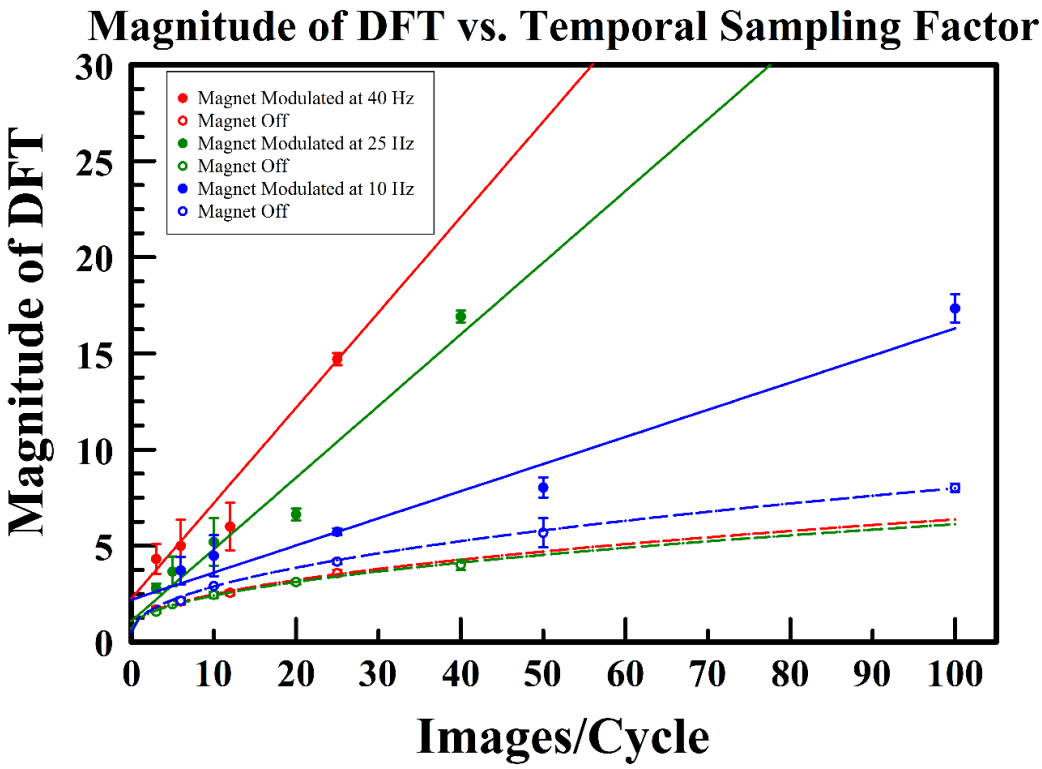

Figure 4-7 Magnitude of DFT as a function of temporal sampling.
The magnitude of the DFT is plotted as a function of the temporal sampling for three magnet modulation frequencies: 10 Hz (blue), 25 Hz (green), and 40 Hz (red). The closed circles are data points with the magnet modulated (roughly linear in *m*), and open circles are magnet-off data (appears to show a square root dependence on *m*).

To investigate the effect of the number of magnet cycles, we used some of the same data recorded for test above. We took the data recorded with a framerate of 1000 fps, f_{mag} = 10 Hz, and N = 1000 and used frame decimation to change the number of magnet cycles processed (which also changes N) while keeping m constant. From equation 4-7, we expect $\left|F(n_{fmag})\right|$ to be linear in P for a constant m. The average values of the magnitude of the DFT for the three image stacks (magnet modulated and magnet off) are displayed below, along with the fitted equations for the linear (magnet on) and the square root dependence (magnet off) on the number of magnet cycles. The magnetic signal is more clearly linear in this case (we now have the ability to get evenly spaced data points and more data points). Again, the noise (the signal when the magnet is off) appears to show a square root dependence.

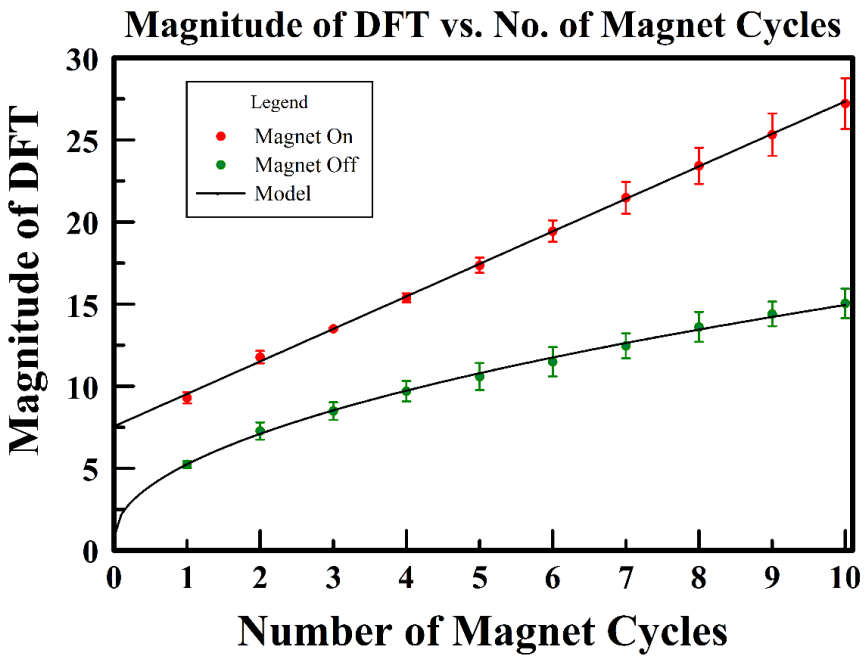

Figure 4-8 Magnitude of the DFT as a function of No. of Magnet Cycles.
The magnitude of the DFT is linear in the number of magnet cycles (when the magnet is being modulated), for a fixed m. The noise in the Magnet Off images appears to have a square root dependence on P.

We summarized the findings of the LFMMOCT imaging parameters in Table 4-4. If the magnetic signal is linear in $N = m*P$, and if the noise is proportional to the square root of N, then we can expect the magnetic SNR to increase with increasing number of magnet cycles and temporal sampling. However, in practice, there is a tradeoff in the temporal sampling and the number of magnet cycles. Based on the system constraints (maximum total imaging time, available framerate, useful f_{mag} range), we chose two sets of optimal imaging parameters that maximize the Fe sensitivity. One set has 40 magnet cycles with 25 images/cycle and one has half the magnet cycles with double the temporal sampling.

Table 4-4 LFMMOCT Imaging Parameter Optimization Summary

Parameter	Useful range	Limiting Factors	**Optimal Imaging Parameters for magnetic sensitivity**	
			Set 1	**Set 2**
f_{mag}	10-50 Hz	Loss in B-field amplitude with increasing f_{mag}	20 Hz	40 Hz
f_s (fps)	0.5k – 2k	-Need 1ms exposure time for optical SNR - Camera has fixed options	1kHz	1kHz
N (# frames)	1000-2000	Can't run magnet for more than a few seconds (overheating)	1000	1000
m (images/cycle)	25+	Need small f_{mag} or large f_s	50	25
P (# magnet cycles)	More is better	Need large f_{mag} or small f_s	20	40

To test whether or not these two sets of optimal imaging parameters do produce a greater magnetic signal than the set of imaging parameters that are more comparable with the point-scanning MMOCT system, we imaged the homogeneous agarose sample with 0.991 mg Fe per

gram sample with all three sets of parameters. The mean value of three image stacks recorded with each set of imaging parameters is shown in Figure 4-9. The magnetic SNR is 2-3 dB larger with the optimal imaging parameters, compared to the first set of imaging parameters (f_{mag} = 10 Hz, f_s = 1000, and m = 100). Interestingly, these three imaging parameter sets all have a fixed value of $N = P*m$ = 1000. So while the magnitude of the DFT is linear in N, the magnetic SNR, defined as $10*\text{Log}_{10}$(magnet on – magnet off signal), appears to show that, in the tradeoff between P and m, P is slightly more important in terms of getting the largest magnetic SNR. The set with f_{mag} = 40 Hz, P = 40 cycles, m = 25 had the highest magnetic SNR, so we use this set of parameters for the single magnetic particle imaging in the next section. The error bars (standard deviation) are large enough that the difference in magnetic SNR between the optimal imaging parameter sets 1 and 2 may merit further investigation to definitively say that set 2 produces higher magnetic SNR.

As a final test of the LFMMOCT system, we made an agarose inclusion sample for testing the volumetric throughput. Making the inclusion sample is non-trivial because it is hard to make inclusions that are smaller than the 0.5 mm imaging depth of the LFMMOCT system. After trying several methods for preparing the inclusions, we found one method that works to a certain degree. We made the usual agarose sample of 0.4% w/w agarose with 4.1 mg/g TiO_2 (no Fe_3O_4). We poured this into the sample mold and allow it to cool for ~10 minutes so that it has gelled somewhat but not entirely. We also made an agarose sample (same concentration of agarose and TiO_2) that had 0.991 µg/g Fe. Using a 10 µL pipette tip, we pipetted as small a volume as possible of the Fe-laden agarose into the cooling agarose mold. We allowed the sample to cool fully (at least 20 minutes), and then make another agarose sample without any Fe_3O_4. We pipetted a very thin layer of the iron-free agarose over the top of the Fe inclusion and

allowed it to cool. This protocol only works to a certain degree because it seems to produce Fe-laden inclusions, but, the TiO_2 in the surrounding agarose never seems to have a homogenous distribution, meaning that the Fe-laden inclusion is visible in a B-mode OCT image. Ideally, we would like the inclusion to be invisible in B-mode images, blending in seamlessly with the backscattering of the surrounding agarose. However, this method works for creating a small inclusion to test the volumetric throughput of the LFMMOCT system.

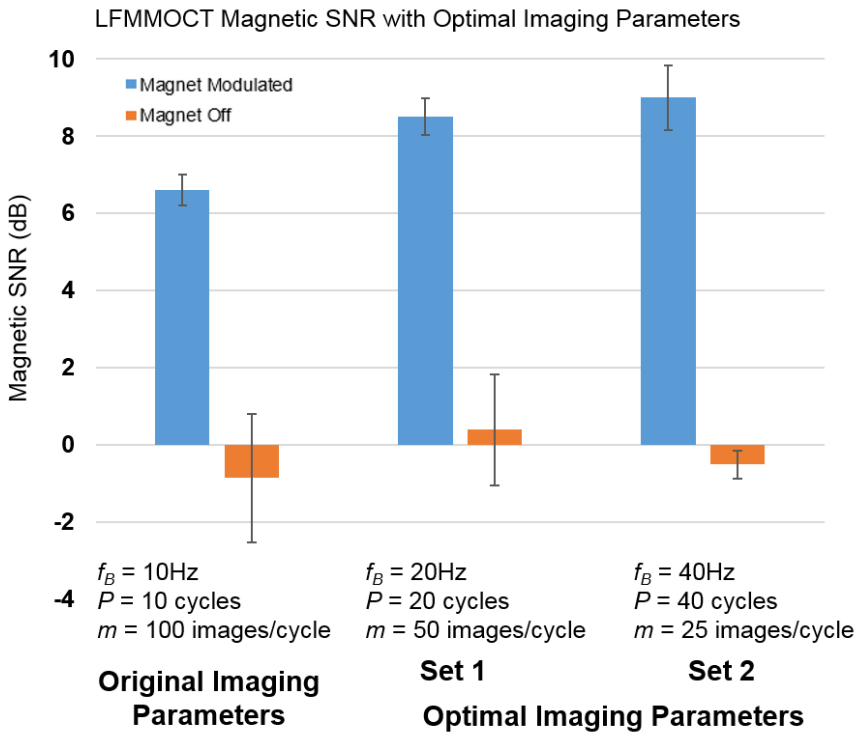

Figure 4-9 LFMMOCT Optimal Imaging Parameters for Magnetic Sensitivity.

These three sets of imaging parameters for fixed N (N = 1000) demonstrate that the number of magnet cycles is slightly more important for getting a high magnetic SNR than m is, as long as m is large enough to avoid phase wrapping effects.

Using an optical framerate of 2 kHz, N = 1000 frames, f_{mag} = 40 Hz, we set the motorized stage to move 1 mm in Y at a constant velocity of 2mm/s. After recording an image stack while

the magnet is off, we return the motorized stage to its starting location and record another image stack while the magnet is modulated. To compare our results to those in Ref [20], we alter our signal processing algorithm slightly. Rather than using a Goertzel algorithm to select only the component of the DFT of the differential optical phase in time for which $f = f_{mag}$ (thereby collapsing the 3D image stack to a 2D map of magnetic signal, mapped in the *XZ* plane), we bandpass filter the DFT (taken in the *Y* dimension, because this is the dimension coupled to time) around f_{mag}. Then we take an inverse DFT to return the image stack to a 3D volume in *X*, *Y*, and *Z*. The bandpass filtering of the DFT is necessary to reconstruct a 3D map of the magnetic signal, but it does come at the cost of loss of spatial resolution. For the images shown in Figure 4-10, we use a filter window of 20 Hz – 60 Hz (centered at f_{mag} = 40 Hz), which corresponds to a transverse resolution of 50 μm in *Y*. Future work on this system could include an exploration of the filter window size that optimizes magnetic sensitivity given the trade-off in a narrow filter window and a fine transverse resolution.

The images shown in Figure 4-10 were recorded with a volumetric imaging speed of 2.5 mm^3/s. This is calculated as the total volume (0.5 mm in *Z*, 5 mm in *X*, 1 mm in *Y*) divided by the imaging time of 1.0 s (1000 frames at 2000 frames per second for each stack- one magnet on and one magnet off). The only other published work on volumetric MMOCT employed a point-scanning MMOCT system that captured a larger FOV (2.2 mm in *Z*, 3.2 mm in *X*, 3.2 mm in *Y*) at an optical framerate of 300 fps (using the maximum possible linerate of 92 kHz), with 2100 frames recorded [20]. Although the volume imaged is ~8x larger than ours, the imaging time is 14x longer, so a total volumetric imaging speed of 3.22 mm^3/s is achieved.

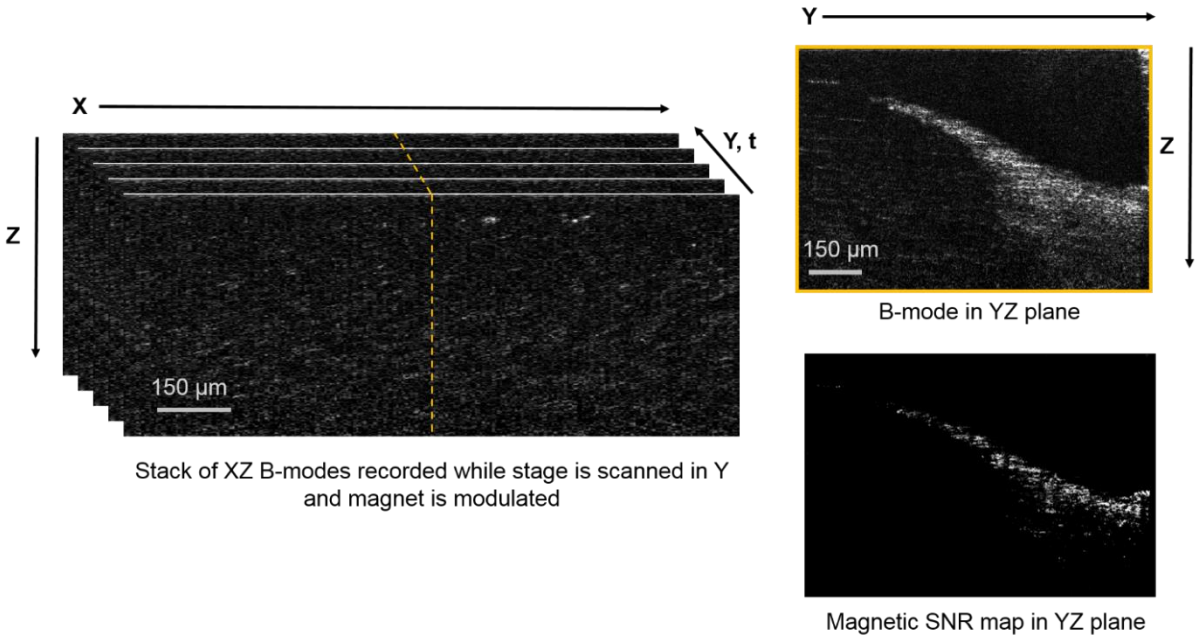

Figure 4-10 Magnetic Signal Map from Volumetric LFMMOCT.
On the left is a representation of the image collection. A stack of B-mode images (in X-Z) are recorded while the motorized stage scans the sample across the imaging beam at a constant velocity of 2 mm/s. On the right is an example of a Y-Z B-mode slice taken from the center A-line in time. The Fe-laden inclusion is visible as having much brighter backscattering than the surrounding agarose. The magnetic SNR map is displayed in grayscale below.

This system has the to-date highest volumetric imaging speed, but it is using the maximum possible linerate and FOV, and uses a total imaging time (7 seconds) that is 7x larger than the longest imaging time we use (which is a conservative guess about how long we can run the magnet without overheating it). Their system also employs complex conjugate removal, which double their imaging depth. We have demonstrated a volumetric imaging speed very close to theirs, without pushing the LFMMOCT system to its highest framerates of 5.4 kHz and without using the maximum possible transverse FOV in *Y*. The LF-MMOCT system has the potential to offer an order of magnitude improvement to the volumetric imaging speed by using higher framerates and larger FOV in Y (by sacrificing some spatial sampling in *Y* or by using a longer total imaging time); however, to maintain high magnetic sensitivity we would have to be able to

use correspondingly higher magnet modulation frequencies so that the same number of magnet cycles are recorded in a shorter time. For example, if we could use f_{mag} = 100 Hz, then we could record 2000 frames at 5000 fps (which would give P = 40 and m = 50 as in our optimal imaging parameters) and with a FOV in Y of 2 mm, we would have a volumetric imaging speed of 12.5 mm^3/s. This possibility is discussed further at the end of this chapter.

4.5 Single Magnetic Particle Imaging

Before doing animal imaging with the LF-MMOCT system, we want to verify that the system is capable of detecting single magnetic point particles. To do this, we embedded magnetic point particles in a sparse distribution in an agarose gel. A point particle is any particle with a diameter less than the resolution of the LFOCT system. Our finest spatial resolution is in the axial direction and is ~ 2 μm. As a starting point, we chose magnetic micro-spheres that are as large as possible while still being point particles because we want the best chance of detecting the particles as we are still refining the technique. We purchased fluorescent microspheres from Bangs Labs with a diameter of 1.63 μm. These microspheres are extremely monodisperse in size and are 42% magnetite by mass.

In order to get a calibrated measurement of the vibration amplitude, from equation 3-6, we need to characterize the amplitude of the magnetic gradient force and the Young's modulus of the agarose gel that the microspheres are coupled to. To characterize the force amplitude, we have already characterized the magnetic field components and field gradients (Figure 3-11), but we also needed to characterize the magnetic susceptibility of the magnetic microspheres.

We estimated the magnetic susceptibility of the microspheres using vibrating sample magnetometry (VSM). A volume of the microsphere solution is dropped onto a small glass coverslip. The water evaporates, leaving the microspheres dried to the coverslip. This is called a dropcast sample. The coverslip is then glued to a long glass rod and placed in a super-cooled, 8-Tesla electromagnet. The sample is mechanically moved through a coil while an external magnetic field is applied. The resulting current induced in the coil is recorded as a function of the applied magnetic field. The resultant data is a direct measure of the magnetic moment as a function of magnetic field. By knowing the volume of the microsphere solution that was dropped onto the coverslip, we can estimate the volume magnetic susceptibility from the curve of magnetic moment as a function of magnetic field, $\mu(H)$. Using equation 1 from Ref [11], we used nonlinear least squares curve fitting to fit the following equation to the VSM data:

$$m(H) = M_s m_s \left[\coth\left(\frac{3\chi_s H}{M_s} \right) - \frac{M_s}{3\chi_s H} \right] + \chi_m m_m H \qquad (4\text{-}8)$$

In this equation, m_s and m_m are the mass of the Fe and the diamagnetic background medium (coverslip, glue, etc), M_s is the saturation magnetization, χ_s and χ_m are the magnetic susceptibilities of the Fe and the diamagnetic background, and H is the magnetic field. We let M_s, χ_s, and χ_m m_m,be free-fit parameters.

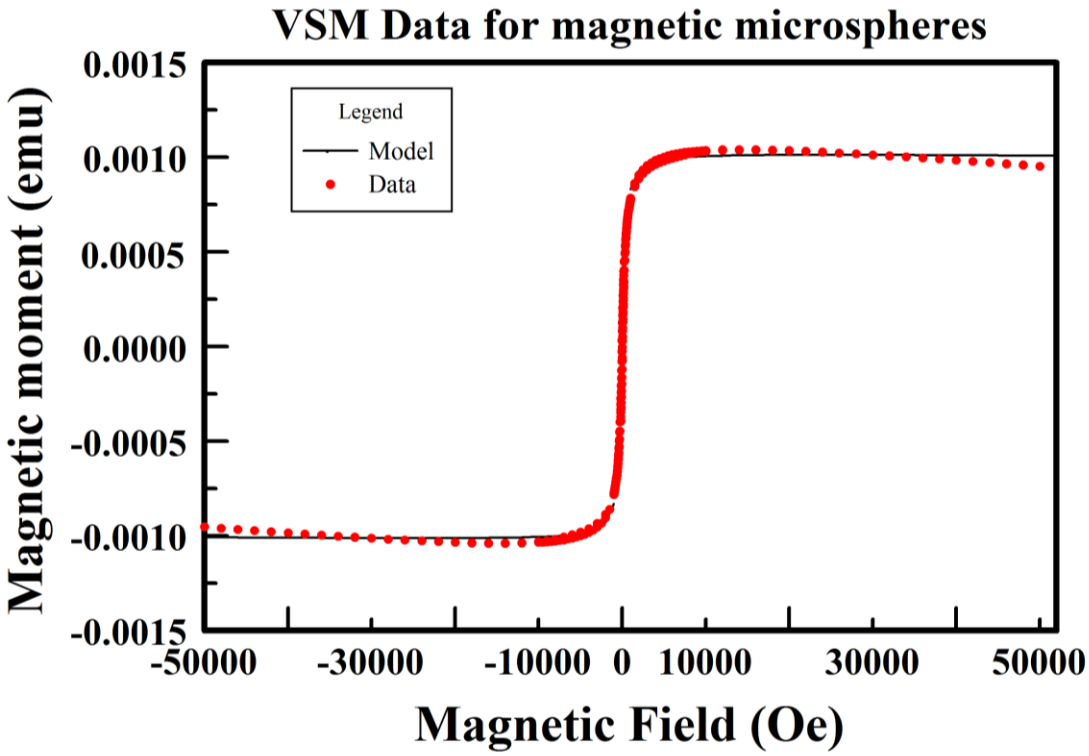

Figure 4-11 VSM Data for characterizing magnetic microspheres.
The raw data from the VSM (red) is plotted alongside the nonlinear least squares fitted curve. From this model we can estimate the magnetic susceptibility of the magnetic microspheres.

From two dropcast samples which had nearly the same volume of microsphere solution, we measured two very different values of magnetic susceptibility. The volume of liquid that was dropped onto the two coverslips must have been different. It was difficult to pipette very small (20µL) volumes. In order to account for the uncertainty in the mass of the microspheres, we report the mean value of the two fitted curves with an uncertainty range of 16%, to cover the range of fitted values. In this way we estimate the mass magnetic susceptibility to be 0.116 ± 0.018 emu/g Fe. The dropcast samples had a number density of $5.9*10^8$ MP/mL, meaning that in each 20 µL dropcast sample, there were about $1.2*10^7$ MP. This corresponds to a volume magnetic susceptibility of 1.23 ± 0.19.

Finally, we characterized the Young's modulus of the agarose in order to get a calibrated measurement of the vibration amplitude. We used a texture analyzer, which slowly compresses the agarose and produces an applied force vs displacement curve (Figure 4-12). The slope equals the Young's modulus. We made an agarose cylinder with a diameter of 64.83 mm, and a height of 25.67 mm. The mean value of the slopes of the four true stress vs true strain curves is 13.9 kPa ± 0.7 kPa.

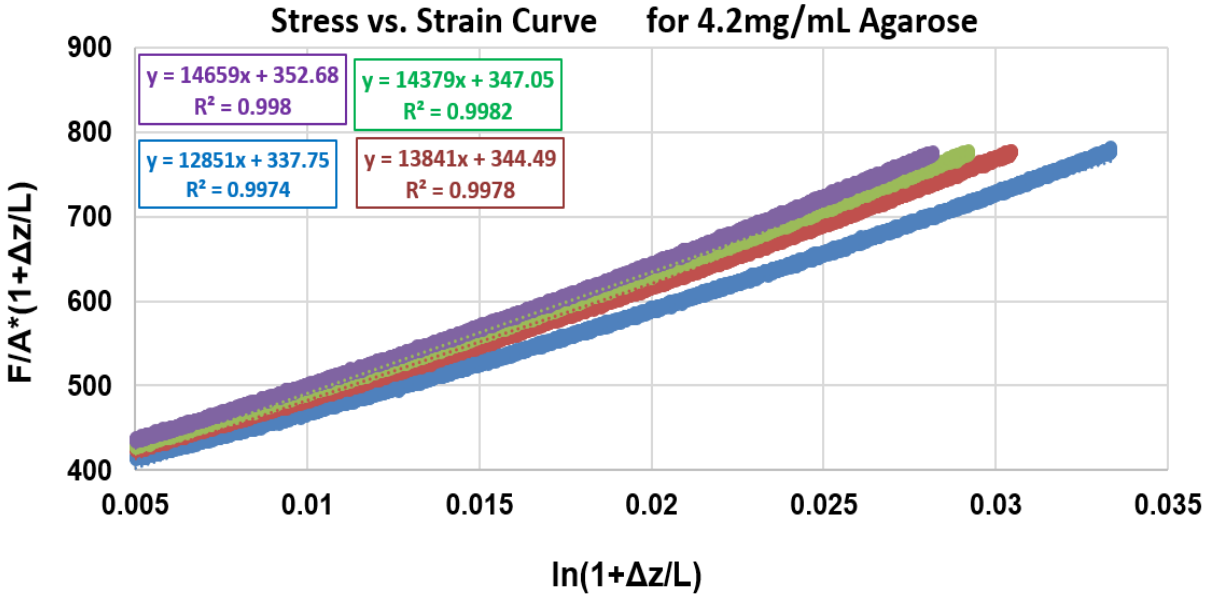

Figure 4-12 Stress vs Strain Curves for measuring the Young's modulus of agarose.

Four measurements with the texture analyzer give four true stress vs true strain curves. We use these to measure the Young's modulus of the 4.2 mg/mL (0.4% w/w) agarose. In this plot, F is the applied force, A is the area of the agarose cylinder, L is the length of the agarose, and Δz is the displacement of the compression.

We can now get a calibrated measurement of the vibration amplitude of these magnetic microspheres across our entire imaging ROI. The vibration amplitude is given by $A/6\pi\mu(E)R$, where A is the amplitude of the magnetic gradient force, R is the magnetic particle radius, and

$\mu(E)$ is the shear modulus (computed with $\nu = 0.495$). Given our micro-particle size and susceptibility, we made a map of the magnetic gradient force amplitude, A, shown in Figure 4-13.

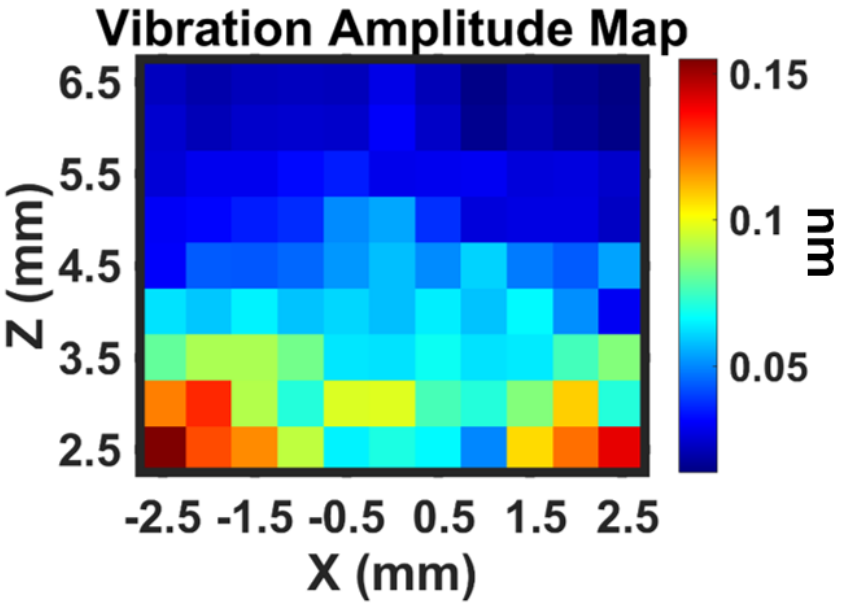

Figure 4-13 Theoretical vibration amplitude map for point particle imaging. The vibration amplitude (nm) is mapped across the entire region above the solenoid for the magnetic microspheres with diameter of 1.63 μm, $\chi = 1.23$, embedded in agarose with Young's modulus of 13.9 kPa, and $\nu = 0.495$.

Given the Young's modulus of 13.9 kPa, and assuming a Poisson's ratio of 0.495, the shear modulus is 4.65 kPa. In the region $x = 0$ mm and $z = 5$ mm (consistent with the ROI we choose for processing the magnetic microsphere images), the theoretical vibration amplitude is 0.05 nm. The uncertainty on this estimate comes from the propagation of uncertainty from the measured magnetic field, the measured magnetic susceptibility, and the measured elastic modulus. Combining the percent uncertainties in quadrature from each of these measurements

yields a total uncertainty on the vibration amplitude of 16%. The theoretical vibration amplitude is then estimated to be 0.05 nm ± 0.01 nm.

We made 2 mm-thick agarose samples (with 4.2 mg/mL agarose concentration) with magnetic microspheres at a number density of $2.42*10^7$ spheres/mL. We did not add any TiO_2 because we first want to see if we can directly image the magnetic microspheres before adding homogeneous optical scattering and then having to pick the magnetic microspheres out of that background. We used the LFMMOCT imaging parameters that are optimized for magnetic sensitivity. With an optical framerate of 1 kHz, a magnet modulation frequency of 40 Hz, and recording 1000 frames, we recorded 5 image stacks with the magnet modulated and 5 image stacks with the magnet off. We also recorded three image stacks each of a positive and negative control for comparison. The controls were the agarose + TiO_2 samples used to measure the Fe sensitivity. The negative control had no Fe_3O_4 and the positive control had 0.991 µg/g Fe_3O_4.When processing the images, we applied an intensity threshold mask to the magnetic displacement because the noise from low-intensity pixels is on the same size-scale as the sub-phase resolution displacements we expect of 2 nm. Representative images are displayed in Figure 4-14. The top panel shows a single B-mode and the corresponding intensity threshold mask. The middle panel shows the magnetic displacement from the magnet off and the magnet on image stacks. Then the bottom row shows the Bon-Boff vibration amplitude with and without spatial filtering. From the displacement maps (Figure 4-14 parts c and d), it is clear that there is a difference in the magnetic signal between the magnet off and the magnet modulated stacks.

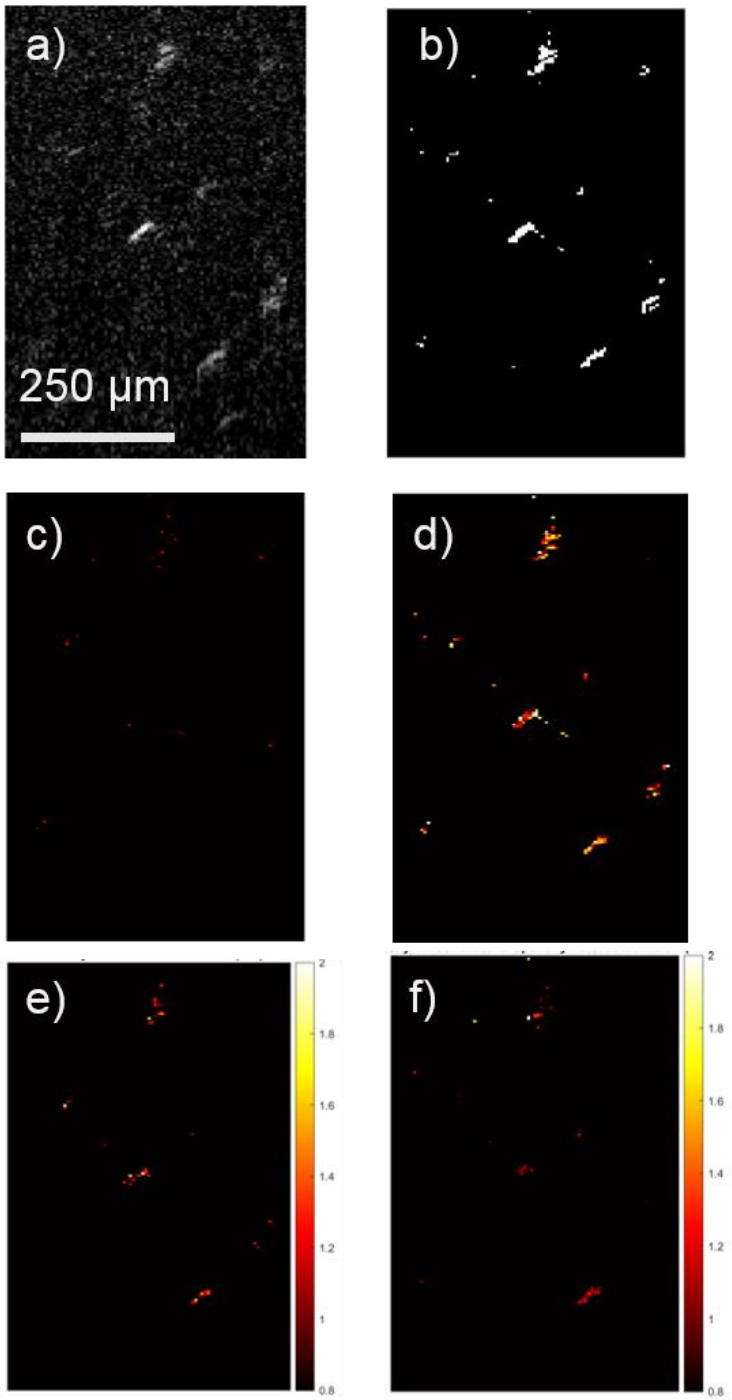

Figure 4-14 LFMMOCT Images of magnetic point particles.

First demonstration of single magnetic particle detection with LFMMOCT. a) A single B-mode image. b) The intensity threshold mask. c) The vibration amplitude of the magnet-off stack. d) The vibration amplitude of the magnet-on stack. e) The Bon-Boff vibration amplitude map. f) the Bon-Boff displacement map with spatial filtering. Colorbars show the vibration amplitude (nm).

To quantify the results, we manually selected the center of three beads in each ROI. Then, we compute the average vibration amplitude in one resolution volume centered on the center of the bead. We do the same for the positive and negative controls- manually selecting regions of bright scattering to compute the vibration amplitude over. The results are summarized in Figure 4-15. Any manually selected ROI that does not have an average intensity value >400 is automatically rejected. The mean value of those that pass through the intensity threshold is 0.96 nm ± 0.27 nm for the magnetic microspheres, compared to 27.6 nm ± 5.2 nm for the positive control and 0.21 nm ± 0.36 nm for the negative control (with no Fe).

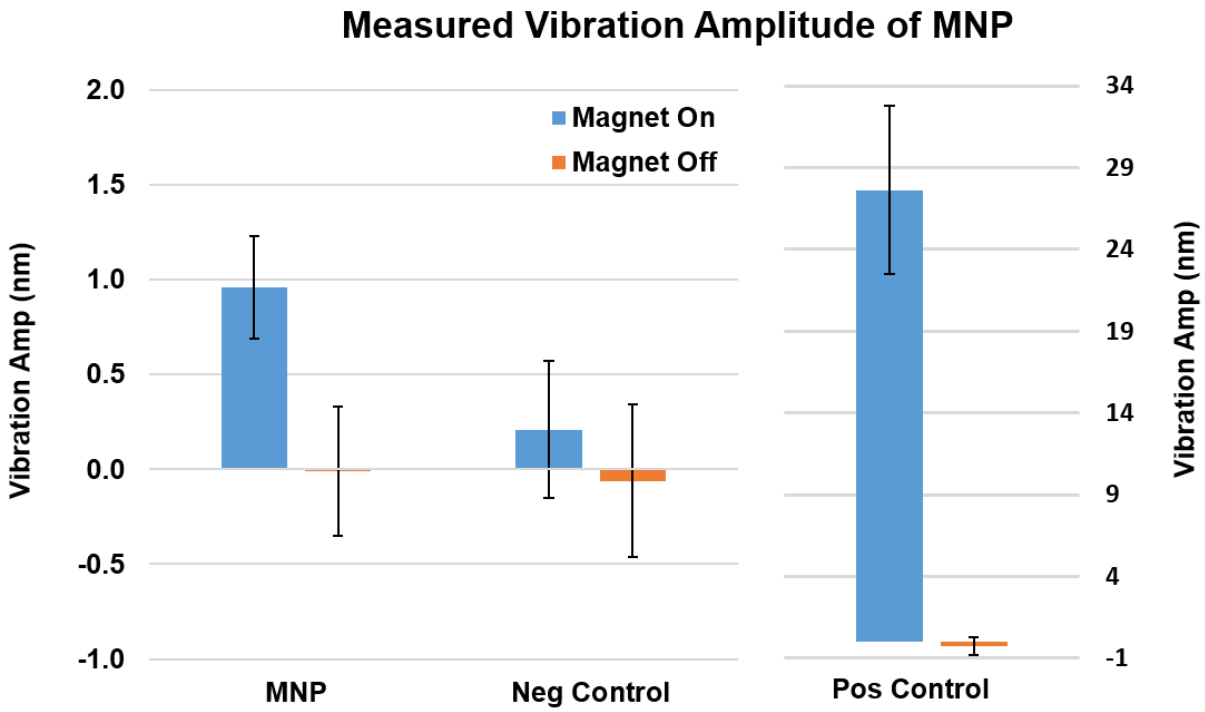

Figure 4-15 Measured vibration amplitude of magnetic microspheres.
Left: The average value of the intensity-thresholded vibration amplitude from all the manually selected ROIs in the magnetic microspheres sample compared to that from the negative control sample (no Fe). Right: The average value of the vibration amplitude for the positive control sample is shown with a different scale bar.

The average measured vibration amplitude from the MNP is 0.96 nm ± 0.27 nm compared to the theoretical vibration amplitude of 0.05 nm ± 0.01 nm. There is no overlap in the standard deviation bars from the MNP magnetic signal compared to the magnetic signal from the control sample, which has an average vibration amplitude of 0.2 nm ± 0.36 nm. The positive control sample (with its large, homogeneous concentration of Fe_3O_4) has an average vibration amplitude of 27.6 nm ± 5.2 nm. The magnetic signal from the negative control sample is considered to be a measure of the noise floor of the system. With the current samples and the given constraints on the imaging parameters, the magnetic signal we are detecting from the MNP is very close to the noise floor. At the end of this section, we discuss future ways in which the magnetic sensitivity could be increased further. It is somewhat surprising that we measure a larger vibration amplitude than the theoretical prediction. However, there may be several possible explanations. First, the Young's modulus of the sample being imaged may be lower than the estimated 13.9 kPa for two reasons: 1) mechanical damage to the gel from repeated vibration of the magnetic microspheres, and 2) heating of the gel from the high-power line illumination (the Young's modulus is known to be highly temperature dependent). Second, the magnetic microspheres may be partially aggregated within the sample. The manufacturer notes that these spheres are "stickier" than other magnetic particles. Given the relative sizes of the resolution and the spheres, groups of 2-3 microspheres would appear to have the same size in the B-mode image as a single sphere. Additionally, the diagonal shape of the spherical point particles in Figure 4-14 is due to field curvature, which is apparent in all of the B-mode OCT images captured with the Version 3 LF-OCT design. This field curvature could be corrected in the future with corrective optics.

This is an important proof of concept that LMMOCT can be used to image magnetic point particles, which had never been done before with MMOCT. There are several important steps left on the road to endogenous magnetite detection. First, the MNP imaged for this dissertation have diameters of 1.63 μm. This is ~30x larger than the diameter of the endogenous magnetite crystals found in magnetotactic bacteria. While we can't be sure that endogenous magnetite crystals in larger animals (if they exist) would have the same size scale as those in bacteria, we take the 50 nm diameter of the magnetite in bacteria as an estimate of the size of the magnetic particles we would like to be able to detect with LFMMOCT in order to perform endogenous magnetite detection. Although it may seem discouraging that we are measuring displacements of only ~ 1 nm (very near the level of the background noise) for the 1.63 μm diameter MNP, there are several reasons to believe that, with further work, endogenous magnetite detection may be possible. The avenues of further investigation outlined below include two main components: increasing the sensitivity to smaller MNP detection and imaging samples which more closely mimic the scenario of endogenous magnetite embedded in soft tissue.

In terms of increasing the LFMMOCT system's sensitivity to smaller MNP, the factor that can potentially have the greatest effect is increasing the displacement sensitivity by increasing N, the number of discrete samples. The most limiting factor on the largest N we can use currently is the total imaging time. N is a product of temporal sampling and P, the number of magnet cycles. For a given magnet modulation frequency, P is limited by the total length of time that current can be supplied to the magnet without overheating it and ruining it. There are two ways that we could increase the total imaging time (which we currently limit to 1-2 seconds): 1) we could investigate the heat dissipated by the solenoid, either by building a second magnet and experimentally measuring the temperature of the solenoid after varying lengths of excitation or

by searching the literature for guidelines on time-dependent heat dissipation in solenoids with water cooling, and 2) we could use higher magnet modulation frequencies. The reason to investigate the heat dissipation is that we may find we can double or triple the length of time that the magnet is modulated without risking damaging it. The current limitation of 1-2 seconds is a conservative guess. Using a higher magnet modulation frequency would allow us to record more magnet cycles for a fixed total imaging time. For example, if we can modulate at 100 Hz rather than 40 Hz, we can record 200 magnet cycles in 2 seconds rather than the maximum of 80 that we are currently limited to. (And if we are able to use longer total imaging times, say 5 seconds, and higher magnet modulation frequencies of ~100Hz we could imagine recording 500 magnet cycles.) Using higher magnet modulation frequencies would involve designing a resonant LRC circuit as discussed in Chapter 3.

Another method to increase the LFMMOCT system's sensitivity to smaller MNP is to amplify the magnetic gradient force further to produce larger vibration amplitudes. We could also replace the current ferrite core with one that exactly fills the solenoid bore (or design a new solenoid with a bore size exactly equal to a given ferrite core diameter) because removing the small air gap we currently have between the solenoid and the ferrite core would doubtless increase the effective permeability of the core. We could also try removing the ferrite core and again measuring the phase lag at higher frequencies. If the ferrite core contributes greatly to the inductance, we could re-design the magnet to have an air core that produces a magnetic gradient force comparable to that of our current solenoid with a ferrite core. Careful re-design of the magnet could enable us to get an order of magnitude increase in the number of magnet cycles recorded and could also produce a larger magnetic gradient force. These two things would greatly improve the LFMMOCT system's sensitivity to magnetic nanoparticles. A third way to

improve sensitivity to small displacements is to improve the SNR of the LFMMOCT system. With a better SNR, the phase noise of the system will be lowered, and the sensitivity to small displacements compared to the controls would be improved. We have never measured an SNR with Version 3 of the LFOCT design that was as a good as that of Version 2. The SNR from Version 2 was consistently 10 dB higher. With better alignment we may be able to improve the SNR achieved with Version 3 by 6 dB.

A fourth easily achievable method of increasing the sensitivity to smaller magnetic particles is to prepare agarose samples with lower Young's modulus. We chose to use 0.4% w/w agarose with a Young's modulus of 13.9 kPa, which is slightly larger than the high end of the values typically measured for soft tissues, which fall on the range 0.1 kPa – 10 kPa [102]. With a Young's modulus 1 – 2 orders of magnitude smaller, we would expect to measure vibration amplitudes 1 -2 times larger, because the two are inversely related. For example, a magnetite particle with a diameter of 50 nm has a theoretical vibration amplitude of 0.007 nm in a medium with Young's modulus 13.9 kPa, which increases to 0.08 nm at 1.39 kPa, and to 0.8 nm at 0.139 kPa (assuming the current limitations on magnetic gradient force and N). Getting one more order of magnitude improvement to N and/or the magnetic gradient by re-designing the magnet would easily push the vibration amplitude of a 50 nm diameter magnetite crystal embedded in 0.1 kPa agarose into the region of detectable values. Another consideration is that the theoretical vibration amplitude assumes a single, isolated magnetic particle. Recalling the earlier discussion of the magnetotactic bacteria, it is very possible that the endogenous magnetite may exist in chains or other groupings which would increase the equivalent MIO diameter by an order of magnitude: in the bacteria, the chain of 30 crystals with 50 nm diameters yields an equivalent MIO diameter of 155 nm. To summarize: we have detected the vibration amplitude of single,

1.63 μm diameter MNP embedded in fairly stiff agarose. By re-designing the magnet to enable operation at higher modulation frequencies, possibly getting a higher magnetic gradient with improving the ferrite volume filling of the solenoid bore, by using less stiff agarose (to better match that of soft tissue), and by improving the SNR of the LFMMOCT system, endogenous magnetite detection may well be possible with this system.

In addition to the future work outlined in the previous paragraphs which deals with increasing the magnetic sensitivity, there are other experiments to do before we move on to animal imaging. These include adding TiO_2 to the MNP + agarose samples and then detecting and spatially locating the MNP within a homogeneous back-scattering background. If we are able to spatially locate the magnetic microspheres against a background of optically turbid media, this takes the system one step closer to mimicking the scenario of endogenous magnetite embedded in turtle tissue. Another step to take before small animal imaging would be to try to image the magnetotactic bacteria embedded in agarose again. I recommend using a lower concentration of agarose to embed the bacteria in. We may have been detecting the bacteria even in the very stiff agarose (1.7% by weight with Young's modulus of ~184 kPa); using a lower, more biologically relevant agarose concentration would produce vibration amplitudes 1 – 3 orders of magnitude greater. This combined with the use of a continuous flow centrifuge to accurately estimate the number density would remove the ambiguity about whether or not we were detecting magnetic signal from the bacteria. This would be the first instance of endogenous magnetite detection with MMOCT and would be a highly interesting result. Imaging a biological sample which we know contains endogenous magnetite would be a natural first step before then imaging animals which may or may not contain magnetite.

CHAPTER 5 - CONCLUSIONS

This dissertation describes the design and implementation of the first line-field MMOCT system. The system is composed of a LF-OCT system that uses a novel, supercontinuum light source and an optical design which together achieve the best combination of speed, sensitivity, and resolution of any LF-OCT system to date [50]. The LF-OCT system was then converted to a LF-MMOCT system with additional hardware and software components. This LF-MMOCT system has a speed comparable to the fastest reported volumetric throughput of any MMOCT system to date, with the potential be offer a further order of magnitude improvement in speed. After optimizing the imaging parameters to achieve the best possible magnetic SNR, the system was used to demonstrate the first detection of a single magnetic point particle using MMOCT and to measure a vibration amplitude consistent with the theoretical value. The ability to detect single magnetic point particles provides a necessary proof of concept that LF-MMOCT may be used for endogenous magnetite detection in the excised tissue from animals that are known to use geomagnetic navigation. The future work needed to prepare the system for endogenous magnetite detection is described at the end of Chapter 4. The broader impacts and potential utility of this work are described in the following paragraphs.

We demonstrated the ability of the second version of the LF-OCT system to image dynamic biological samples. The line-illumination combined with the high-speed camera, the excellent SNR, and the high axial resolution allowed us to image beating cilia of human bronchial epithelial cells in a unique way. Rather than having to study a single A-line in time as in Ref [69], we were able to examine the dynamic behavior of the cilia across an entire 2D

cross-sectional image because, in this system, each A-line is well correlated with the subsequent A-line in time. The study of ciliary beat frequency is of great interest for the study of human respiratory diseases such as cystic fibrosis and chronic obstructive pulmonary disorder. The ability to spatially map changes in the ciliary beat frequency over some cross-sectional area is useful for the study of mucociliary clearance, an indicator of the health of the airway. Future uses of the version 2 LF-OCT design presented here include not only further study of beating cilia in human airway cells, but any dynamic biological sample that can be studied in an *in vitro* scenario. For example, the motility of cancer cells in response to certain chemotherapy drugs is another process studied by our lab (using a point-scanning OCT system) that requires high-speed imaging and the ability for subsequent frames to be well correlated in time. Motility is a metric of healthy cell activity so it is used to study the efficacy of certain drugs [103,104].

The development of the MMOCT frame-by-frame imaging scheme demonstrated an improvement in MMOCT imaging speed by decoupling the spatial dimension X from the magnet modulation in time. Although we were not the first to publish this method, we developed the method independently and in parallel with Ahmad *et al* [20]. While increasing the MMOCT framerate, this method maintains the same Fe sensitivity as the previously published line-by-line MMOCT imaging scheme. Higher MMOCT imaging speed is essential for volumetric MMOCT. This new imaging scheme makes MMOCT a more viable method for applications such as endogenous magnetite detection, in which large volumes of tissue must be imaged. It was also essential for the development of a LF-MMOCT system: because all A-lines are recorded simultaneously in the line-field configuration, line-by-line MMOCT is not possible with LFOCT.

The LF-MMCOT system presented here is the first demonstration of an MMOCT system with the line-field configuration and the first MMOCT using a supercontinuum light source. By

combining the imaging speed improvement of the line-field configuration with the frame-by-frame imaging scheme and the high-power supercontinuum light source (which gives high optical SNR and high axial resolution) we built a system with the potential to be the fastest MMOCT system to date and one that has a sufficiently fine resolution and sufficiently high magnetic sensitivity to detect single, magnetic point particles. We have optimized the MMOCT imaging parameters to produce the highest magnetic SNR possible at kilohertz framerates. This is a key step on the path to endogenous magnetite detection.

We also present a summary of three optical designs with the subsequent figures of merit of the optical imaging system. This makes the LF-OCT system adaptable for different applications. For example, a LF-MMOCT system built using the version 2 optical design would offer increased SNR and increased resolution homogeneity across the entire imaging region of interest if a sacrifice in transverse resolution is acceptable. This may be the preferred setup for applications in which the goal of the MMOCT imaging is to detect the presence of multiple particles rather than single, point-like particles. One such application is the detection of magnetic gold nanorods which may be used to measure the porosity of mucus or other polymers by relating the diffusion of the magnetic gold nanorods to the polymer pore size [105,106]. In summary we have designed, built, characterized, and optimized a novel imaging system with the potential to be used for a wide variety of biological and biomedical applications currently under investigation by this lab and by our collaborators.

APPENDIX 1: LF-OCT ALIGNMENT PROCEDURE VERSION 1

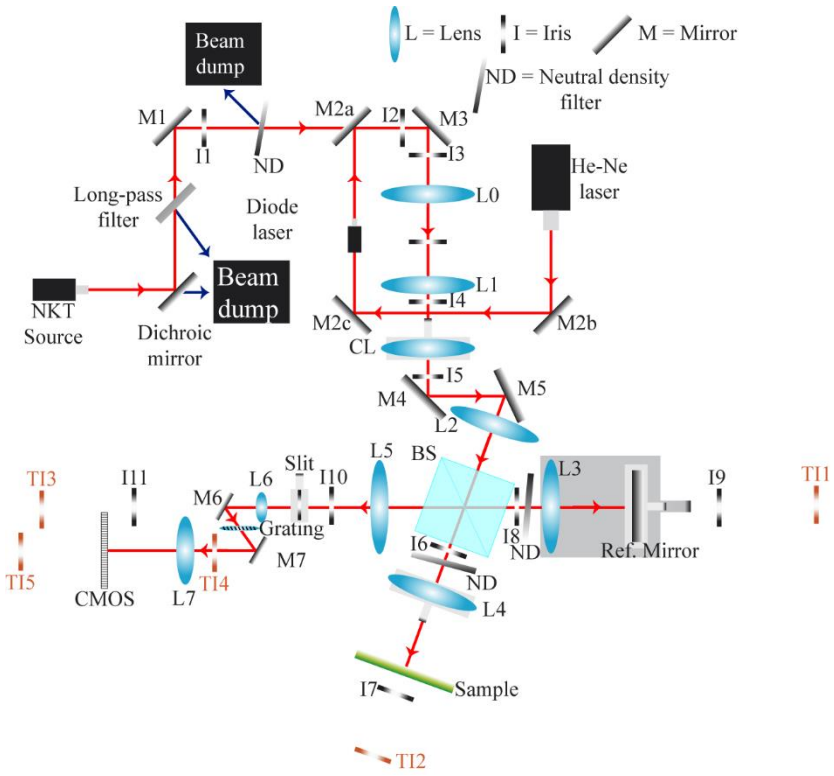

NOTE- Ultimately we need the beam to be at the height of the center of the camera pixel array. We also want the beam to be level with the table so that it doesn't enter any of the lenses at an angle. Ideally the height of the light sources would be set to the height of the camera. Set NKT and diode laser height so that both beams emerge at the height of the center of the camera array. We have found that if the beam is not at the right height, then you have to use M6/M7 to set the height. This means that the beam enters the diffraction grating with some vertical tilt. In this case, when you rotate the DG in order to make horizontal lines truly horizontal on the camera, you shift the beam up or down and it will no longer be centered on the pixel array.

I. Front end through first beam expander

1) Set "alignment irises": Set two irises to height at laser head. Then add the collars which fix the height of the post in the post holder but allow you to turn the iris. These are used as temporary alignment irises throughout setup (for any place where there isn't enough room to leave irises permanently)
2) NKT reflecting from dichroic: Set alignment irises along row of holes on breadboard which are right angle to direction that NKT source is being emitted. This way we know dichroic mirror is set to 45 degrees. Make sure 2 beams (including 1st Fresnel reflection) are coming off mirror (otherwise it may be dumping a bunch of power into the optic holder). One reflection will be visible and one IR (IR because it has been transmitted through first surface and is reflected off back surface). Make sure the beam dump is collecting what's transmitted (950 nm-2400 nm). The visible beam should be centered on the two irises. Translate DM to get beam through first iris; change tilt of DM to get visible beam through second iris.
3) NKT through LP filter: Insert LP (long-pass) filter between DM and M1. It won't change the path of the beam at all. Put at angle so that reflected beam (400 nm – 605 nm) goes into same beam dump as DM transmitted beam.
4) NKT off M1 & thru I1: Now set same two alignment irises along row of holes on breadboard which are right angle to the path of the beam reflected from DM. This way M1 is set to 45 degree angle. Set mirror so that beam is centered through both irises. Then set I1 to block the IR beam and pass the visible one.
5) NKT through variable attenuator: Put at angle so that reflected beam goes into 2nd beam dump.

6) Set M3: Now set height of two more irises to the height at laser head. These will be I3 and I4 and are permanent alignment irises. Then set them along a row of holes on the breadboard after where M3 will be inserted. Insert M3. Use dichroic mirror and M1 to align through I3 and I4. After setting, M3 should ever be touched. Dichroic mirror and M1 are used to align NKT through I3/I4; M2b and M2c used to align He-Ne through I3/I4; diode mount and M2a used to align diode through I3/I4.
7) He-Ne alignment: (Note that the He-Ne is necessary for checking collimation using shear plate interferometer. NKT is too polychromatic and diode isn't bright enough. We use the He-Ne laser to collimate the beam because all lenses are achromatic doublets). Set He-Ne up as shown in diagram. Use the two alignment irises to make sure He-Ne beam is coming out approximately in a straight and level line along a row of holes on the breadboard. Then set 3 mirrors (M2a, M2b and M2c) at 45 degree angles as shown in diagram. Make sure that where the He-Ne beam crosses the path between L0-L1-CL won't intersect with any optical elements. Then adjust the position and tilt of these two mirrors to get the He-Ne through I3 and I4.
8) (**General lens alignment procedure**): As with all lenses going forward, two downstream irises should be identified before putting in the lens and the lens adjusted transversely so as not to deflect the beam, and also tilted so that the surface is exactly perpendicular to the beam path. NKT power needs to be at least 50% for lens alignment; we noticed that the beam shape seems to change at lower powers and it's harder to see the beam to align it well.
9) (**General collimation procedure**): Use a shear plate collimator with He-Ne beam everywhere possible. (For all lenses, even for the lens after the diffraction grating). This process does not work for the cylindrical lens

All of the following steps should be done using the NKT unless otherwise noted

10) L0: First place a second iris immediately after L0 after setting iris height at laser head; drop in L0; Align with this new iris and I4. Note beam is highly divergent so irises must be within ~30 cm of L0.

11) Set I5: Place additional iris immediately before M4 after setting iris height at laser head.

12) L1. Place L1; Align L1 with I4 and I5. Adjust axial position to collimate the output beam. Re-check alignment on I4 and I5. Once L1 is set, place a large iris between the 2 lenses captures back-reflection off the second lens.

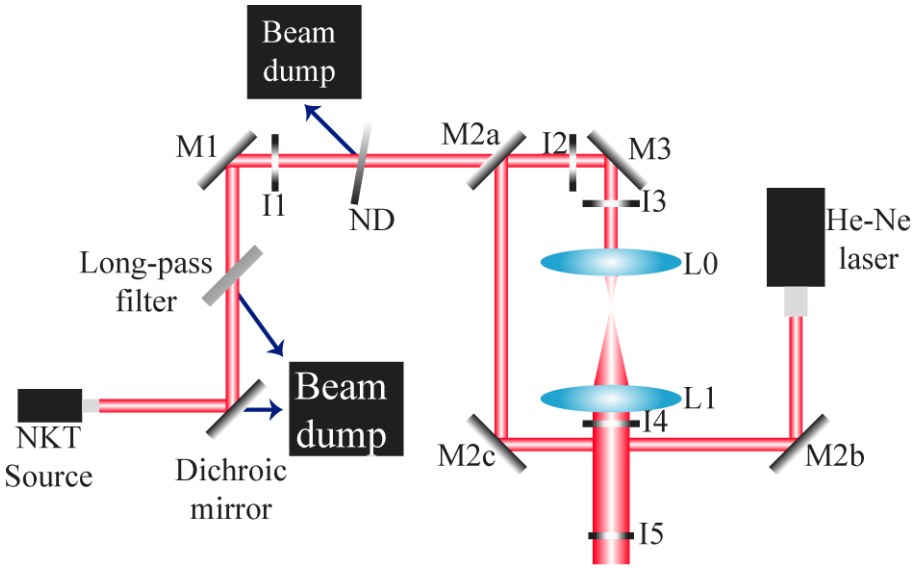

II. The Michelson

1) **(General Strategy):** Align as much as possible without the CL (up to L5) although the exact distance of the ref mirror and sample will not be able to be set yet. Then put in the CL and align ref mirror (we'll be able to see focus), L6, diffraction grating, and L7. Ideally this brings the system to where the beam is approximately collimated in transverse and focusing in spectral directions (from the ref arm), whereas the sample hasn't been checked at all yet.

The diode laser will be used with CMOS translation to get the spectral direction from the ref mirror into focus. A point-like scatterer on the sample will be translated to bring transverse direction of the sample into focus. Then using the diode laser again the spectral focus of the sample will be checked – and if need be, the camera (NOT the sample) will be moved. Then iterate back to the ref mirror spectral adjustment. Then the ref mirror+lens translated together to align the OPD to just above the sample. We already know that the ref mirror+lens motion doesn't modify the spectral direction focus significantly, so as long as it doesn't move terribly far, it should remain in focus along that direction.

2) Setting I6-I9 and Beam splitter:
   a) Set height of I6-I9: set 4 irises to height at laser head
   b) Place I6 and I7: Put I6 and I7 in approximate location of sample arm. (If aligning for first time, you won't know exactly what angle this should be. The angle between the line M3-L0-L1 and the sample arm should be ~25-30 degrees.)
   c) Two mirrors- coarse horizontal adj: Downstream of the planned position of the CL, two mirrors can be used to direct the beam at an angle through the beam splitter. Position the mirrors so that the beam is directed approximately along the line established by I6/I7
   d) Two mirrors- vertical adj Use vertical tilt adjustment of M4 and M5 and I6/I7 to make sure that the beam height is constant in sample and ref arms.
   e) Place I8 and I9: Screw I8 and I9 directly onto breadboard along a row of holes; this is important because we screw the ref arm translation stage directly to row of holes and we want to ensure that when we translate the ref stage, the beam stays aligned
   f) Beam splitter:
      i) Beam should enter prism marked with a black dot.

ii) Placed at an angle slightly different than 45 degrees to avoid back reflections into the camera (and so that the ref arm is along a row of holes on the breadboard).

iii) Place at an angle so that beam is roughly along the same row of holes as I8/I9

iv) Use I8 and I9 to check the out of plane tilt of the beam splitter to ensure that beam height in ref arm is constant. Adjust tilt of beam splitter plate if necessary.

g) Two mirrors- fine horizontal adj: Adjust tilt of M4 and M5 to align beam through I8 and I9.

h) Set lateral position of I6/I7: Shift I6 and I7 laterally to align with beam.

i) Iterate as needed until beam passes through beam splitter and is aligned with all 4 irises

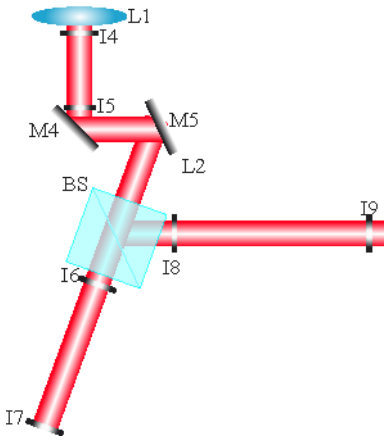

3) L2: Place in about 1 focal length from the beam splitter and align with I6/I7. Also check that beam is centered on L2. Note that the exact distance from beam splitter doesn't matter- after CL insertion, we will check the collimation after L2 to make sure CL+L2 distance is right.

4) L2+L3 reference adjustment: Place the variable neutral density filter into the ref arm first**. Set one of the temporary alignment irises (TI1) after I9 and along same row of holes. Place L3 on a translation stage and align with I9 and TI1. Collimate the output beam.

5) Ref mirror coarse adj: place ref mirror approx. one focal length from L3. Retro-reflect the beam exactly back through I8 and I1. Note that the axial position of the ref mirror will be

aligned more accurately later. We use I8 and I1 because we need two points to be able to exactly retro-reflect the beam. The beam is shifted transversely coming out of the Michelson so we can't set I10 and I11 until after the beam is perfectly retro reflecting.

6) <u>L2 + L4 sample adjustment:</u> Place the variable neutral density filter into the sample arm first**. Place another temporary alignment iris (TI2) after I7. Place L4 on a translation stage. Then, align L4 with I7 and TI2. Collimate the output beam. (The actual sample will be dealt with later). *NO NEED TO TILT L4.*

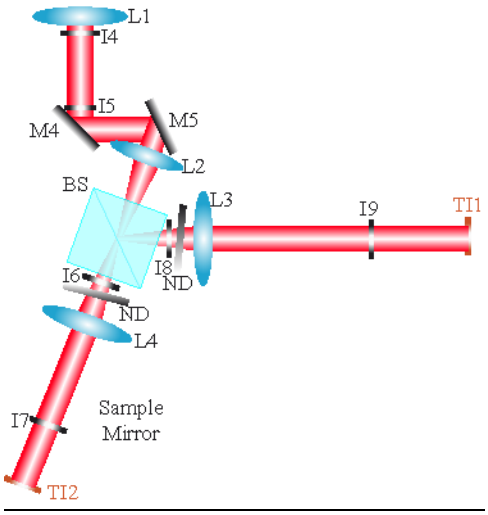

7) <u>Sample mirror coarse adj:</u> place a mirror in sample arm approx. one focal length from L4 and retro-reflect back through I6 and I1. (We setup mirror in sample arm so that we can check that L5 is collimated by checking with both ref arm and sample arm.)

8) <u>Positioning I10 and I11 and verifying ref and sample coaxial:</u> Set I10/I11 to height at laser head. Note that I10/I11 can't be screwed directly to the breadboard because the beam emerges from the beam splitter slightly shifted transversely.

9) <u>L3 + L5 adjustment:</u> With the ref arm only, align L5 with I10/I11 and collimate the output beam.

10) L4 + L5 adjustment: Now block ref arm and unblock sample and check that beam from L5 is still collimated and passing through I10/I11.

**Note: this is used to balance the dispersion and OPD from the filter in the reference. We might explore, if needed, using a slightly thicker flat to force the focus a little deeper than the coherence zero. However, since the transverse focus of the ref arm probably doesn't matter (it's a mirror) the added flat here may not even be needed at all – recognizing that the imbalanced dispersion can be compensated digitally.

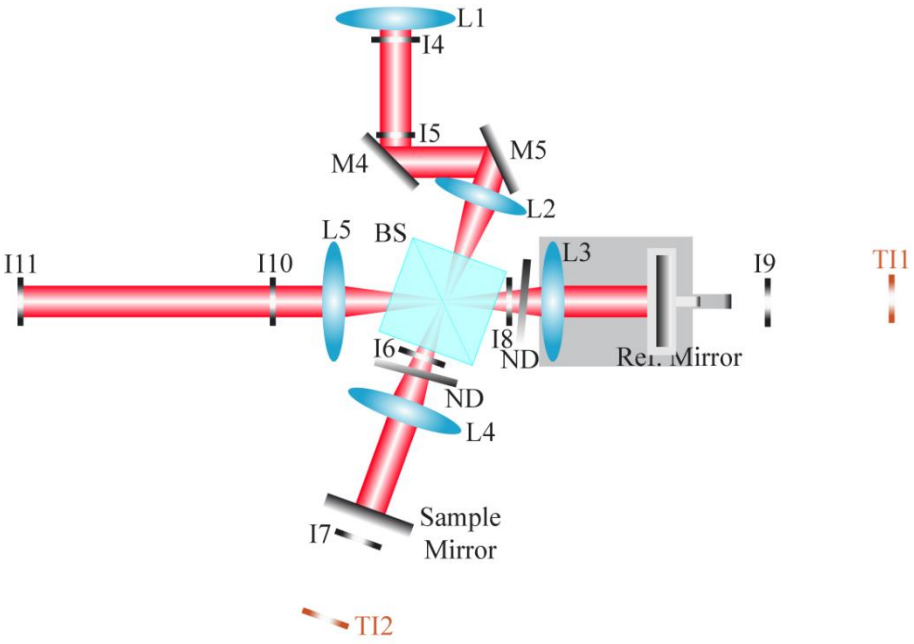

III. The Camera Coarse Positioning with Ref Arm Beam Only

(Use the ref arm beam for all alignments in this section).

1) Insert 100 mm fl lens: Before inserting CL, insert a 100 mm fl spherical lens on an axial translation stage where the CL will later go. Because, we can't use shear plate with elliptical beam. Center beam on I5 and I6/I8. Translate axially until beam after L2 is collimated.
2) Ref mirror axial adjustment: Slide the ref mirror along the beam axis (while keeping L3 stationary) to collimate the beam after the BS (output of the Michelson) but before L5. You

will also want to carefully check the retro-reflection back through I8 and I5– the ability for the ref arm to exactly retro-reflect automatically sets the system so that it will be sensitive only to exact backscattering from the sample object. Ref mirror should be at the focal plane of L3 if all is right. Because the shear plate is our most sensitive collimation tool, once we set this distance, we fix the position in space of the ref mirror and where the camera will end up being. Note this ref mirror stage micrometer value.

3) Setting up sample arm: Insert a mirror to deflect the beam down onto the optics bench. Using a mirror as the sample, set the location and angle of the new mirror until the beam is retro-reflected back through I6 and I1. Check that two arms (ref and sample) are coaxial: first check that two arms are coaxial with NKT source by checking at I10 and at the slit.

4) Sample mirror axial adjustment: translate the vertical stage in the sample arm until the output of the Michelson (before L5) is collimated.

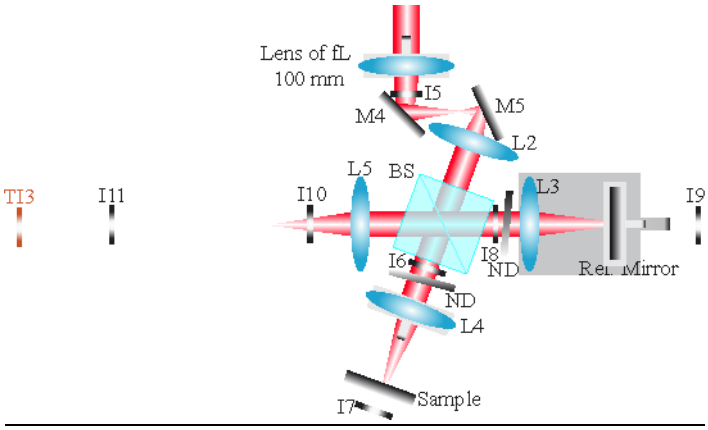

5) Build relay system: If beam after L6 is smaller than 5 mm, we won't be able to use the shear plate to collimate so instead use a 150 mm fl lens and a 100 mm fl lens to expand the beam after L6.

6) L5 + L6 adjustment: Place one of the temporary alignment irises (TI3) after I11 and along the same row of holes. Drop in L6 and align with I11 and TI3. Collimate the output from L6

using the He-Ne lase. Set transverse and height position of the L6 lens using NKT and without the lens of fL 100 mm.

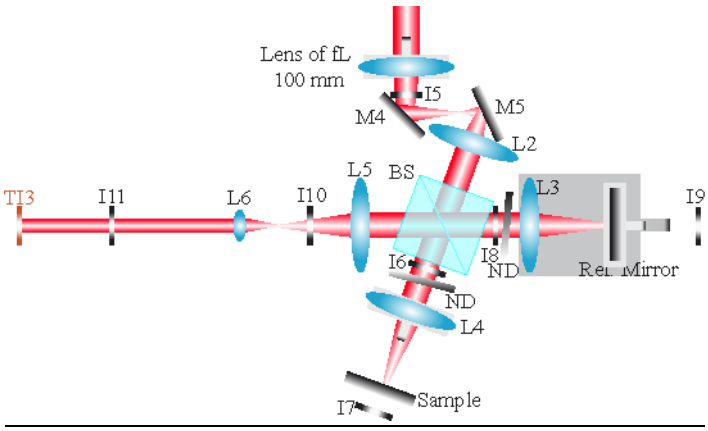

7) Slit coarse adjustment: Insert slit at focal plane between L5 and L6 on a lateral translation stage.

8) M6 at Littrow angle: Now place M6 after L6. Set horizontal tilt of M6 such that if the DG is placed parallel to the row of holes L5-L6, the beam from M6 will enter the DG at Littrow angle. Place mirror as close to L6 as possible, because focal length of L6 is only 5 cm and need diffraction grating to be at focal plane (after M6).

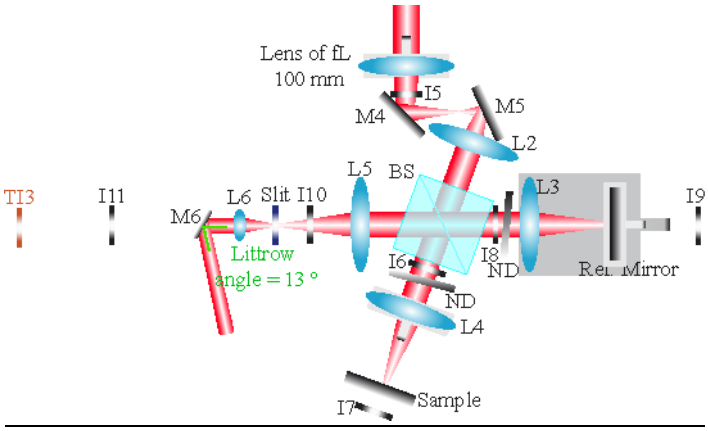

9) Diffraction grating (DG) positioning: Remove 100 mm fl lens. Position the DG at the approximate focus in the transverse imaging plane. Note that the rotation angle of the DG will be checked later.

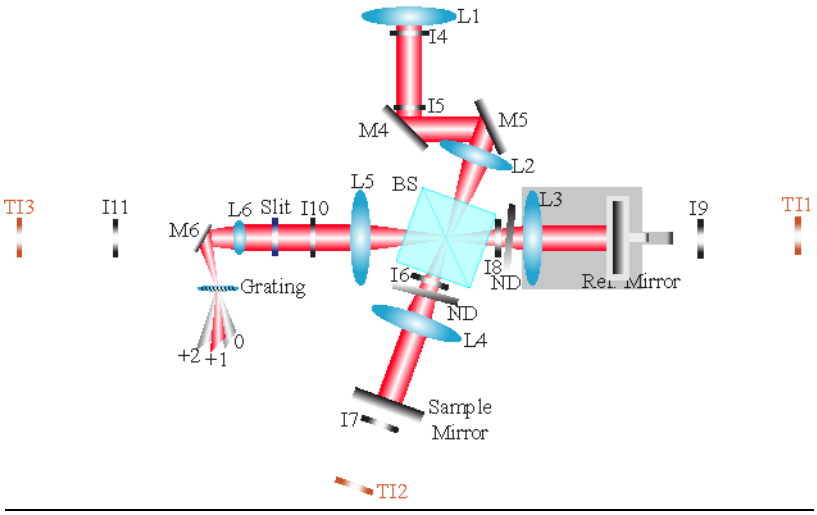

10) Replace 100 mm fl lens: Align with I5 and I8/I6.

11) M7 approximate placement: Place M7 at roughly the right location so that first order is directed roughly along a row of holes.

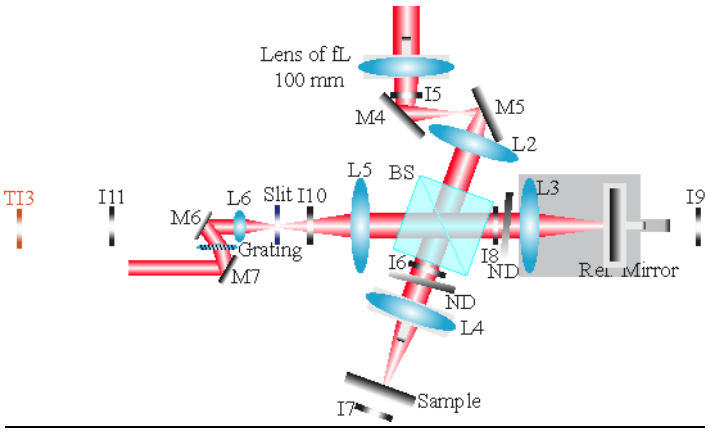

12) Diode laser off flipper mirror (M2a) and M3: Choose a row of holes that is perpendicular to the beam path between M1 and M3; insert the two alignment irises along this row of holes. Now insert the diode laser so that the beam is going at least approximately through both irises. Adjust the tilt of the diode laser mount and M2a (flip mirror) to center the diode beam through I3 and I4. Do not move M3, which was set with the NKT.

13) Set TI4 and TI5: Set height to height at laser head (note that this may not be the same height as the camera, so don't worry too much about height). These irises will be used to set horizontal tilt only. Place irises after M7 along a row of holes.

14) Horizontal tilt of M7: With the diode laser, translate M7 and adjust horizontal tilt to align diode through TI4 and TI5. Note that the height will be set later.

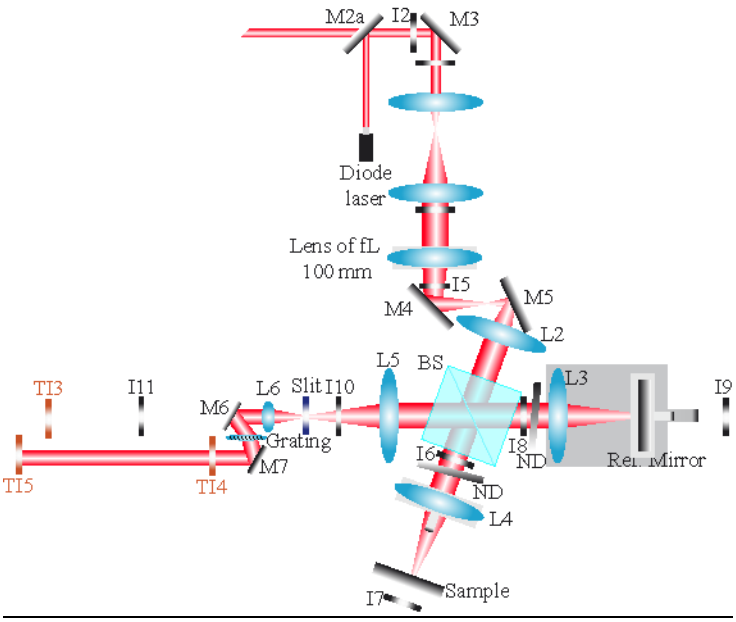

15) Vertical line toward camera: With NKT: Remove TI4 and TI5. Place camera along same row of holes as TI4 and TI5. Mark two axial positions along this row of holes (~10" apart). At the first position, adjust vertical tilt of M6 to center height on camera (using line profile tool in PFV software). Slide camera to second position and adjust vertical tilt of M7 to center beam vertically on camera. Iterate until beam is level with table and centered on camera at both axial positions.

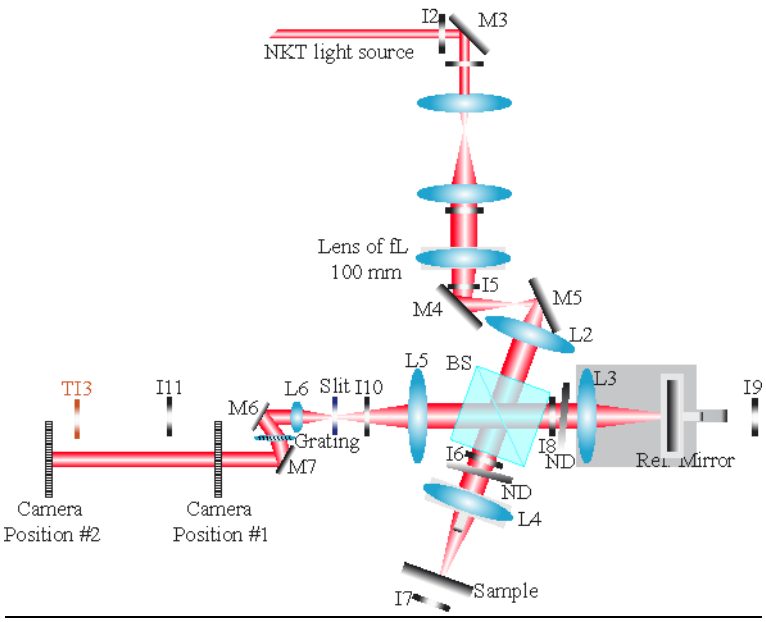

16) Remove 100 mm fl lens

17) Set height of L7: Set L7 on axial translation stage (axial position will be set later). with NKT source- using the same general procedure as step 15 above, slide the camera between two axial positions to set the height of L7 so that NKT beam is centered vertically on camera at both axial positions. Then add a collar to L7 so that height is fixed.

18) Set transverse position of L7: Once height is set and is fixed by collar, again translate the camera between two axial positions and adjust transverse position of L7 as well as tilt of L7 to get NKT beam centered laterally on camera at both axial positions of camera.

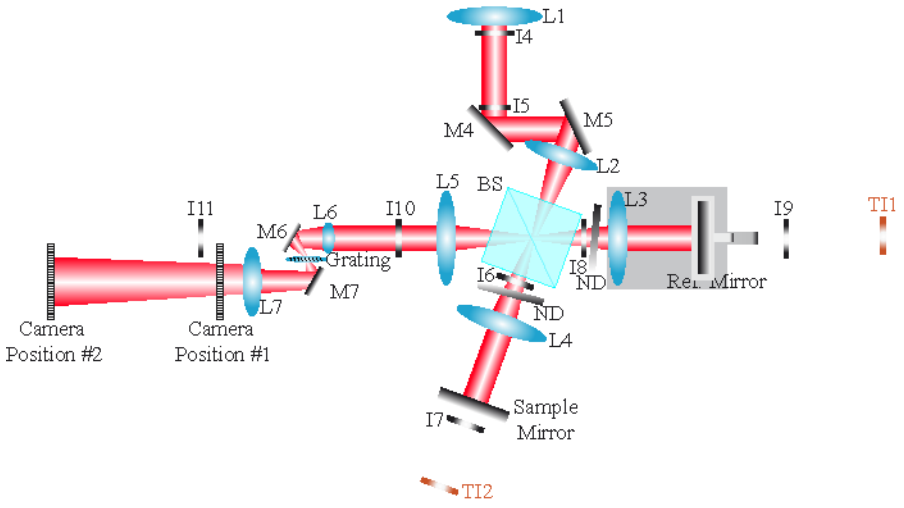

19) L7 collimation: NKT: Set axial position by checking collimation using He-Ne laser and the shear plate.

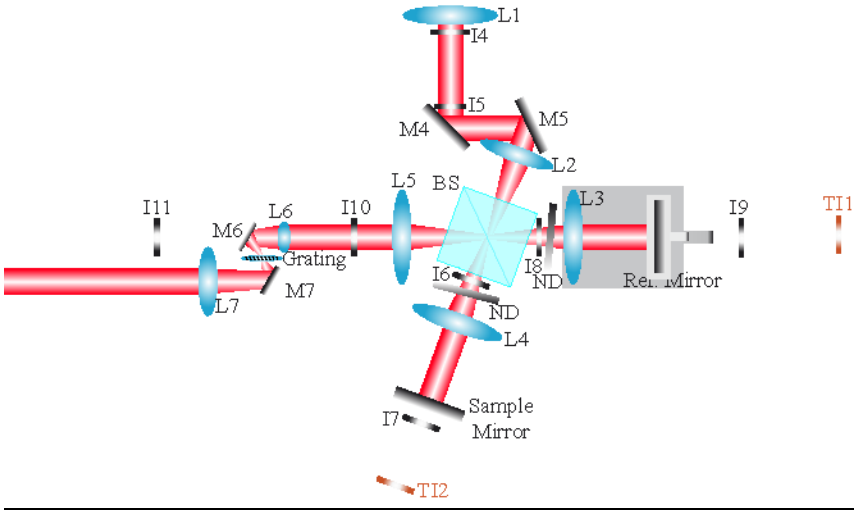

20) Insert 100 mm fl lens

21) Camera coarse positioning: Switch to the diode laser and ref arm only. Align the camera so that it is centered on the diode beam and perpendicular to the beam axis. Then screw in two rails along the feet of camera so that it can be moved axially without being tilted laterally. Adjust the axial position of the camera to focus the beam from just the ref arm onto the sensor. Carefully remove rails and clamp camera legs to table.

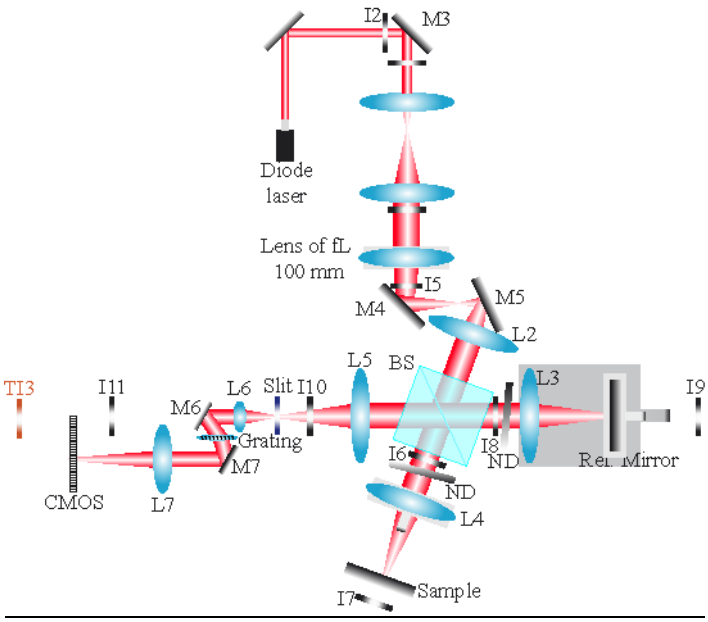

22) Fine camera position with sample arm: Using diode laser. Block ref arm and unblock sample arm. With sample mirror at focal plane of L4 (step 4 of this Section), adjust finely the axial position of the camera to focus the point source from the sample arm onto the sensor. Adjust ND filter angle until you get the smallest width of diode spot on camera.

23) Re-check collimation of L4: If you changed the ND filter angle: Because we have changed the ND filter angle, we may have slightly affected the collimation of L4.

24) Check ref. mirror position: Using diode laser. Block sample arm and unblock reference arm. Check if the point source produced by the reference arm is the smallest, if not move the axial position of the reference mirror (kept L3 fixed).

25) DG rotation angle. With NKT- Adjust the DG rotation angle to make one of the central lines exactly horizontal. (need 100 mm fl lens in to be able to see horizontal lines on camera). If height of beam on camera changes when DG rotation angle is changed, go back to step 15 in section III. Keep 100 mm fl lens in but remove L7 and repeat steps up to this point.

26) Remove 100 mm fl lens

27) CL insertion: NKT: Insert CL approximately CL+L2 away from L2 and use I5 and I6/I8 to align CL. Change tilt to center beam on target; adjust lateral position and axial position to align with irises. Check that beam is centered through lens by rotating the CL in its mount. You should see the beam rotate about the center of I5 is beam is centered through CL. Adjust tilt of CL mount to align the retro-reflection from CL on I4.

28) Check retro-reflection of ref mirror: note that the filter wheel needs to be at least attenuation. Otherwise one side of beam is much less bright and it makes aligning hard.

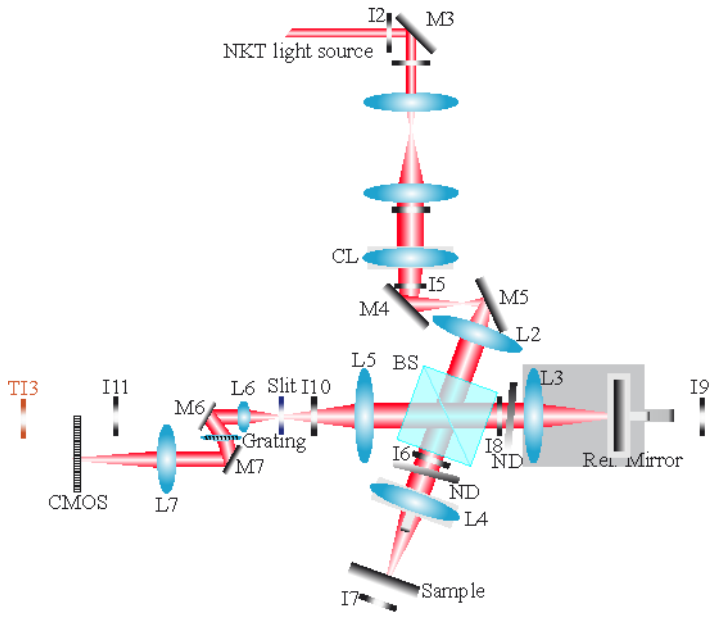

29) CL collimation: After beam is aligned, switch to diode laser. Block reference arm and unblock sample arm. Change axial position of CL until the width of vertical-line beam on camera is the narrowest. For this position, the beam after L2 is collimated.

30) Check ref. mirror position: Using diode laser. Block sample arm and unblock reference arm. Check if the vertical line produced by the reference arm is as narrower as possible. If not, move the axial position of the reference mirror (again without changing the L3 lens).

31) CL rotation angle: Using diode laser, fine-tune the CL rotation angle so that the focused line is exactly vertical on the camera.

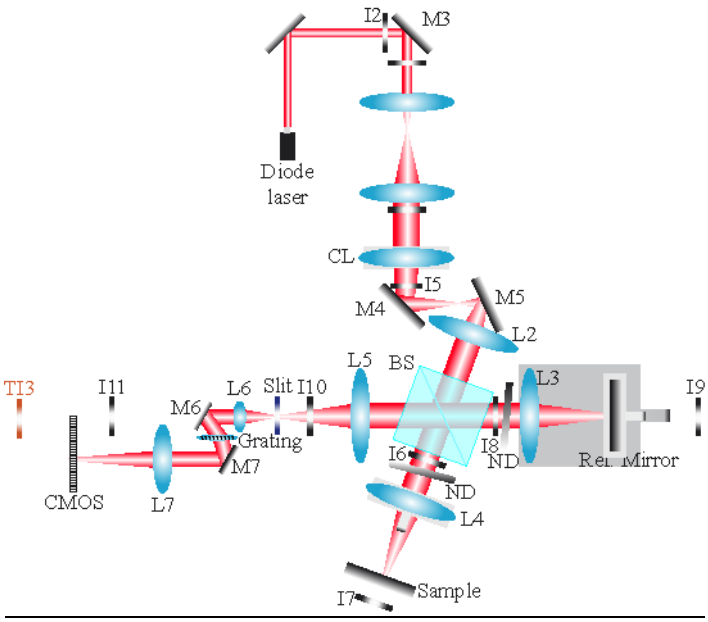

32) Check that both arms are coaxial: Using diode laser, make sure that two arms are perfectly overlapping on camera (the two vertical-line beam should overlap completely).

33) Slit fine transverse position: Using the NKT: Fix slit to translation stage that moves laterally across beam axis. Now, using the NKT source and the ref arm mirror on the camera, close slit almost all the way. Center the light that is passed onto the camera. Then open the slit slowly. You should see the beam fill the camera symmetrically. If not, iterate between centering slit when slit is closed almost all the way and opening the slit to pass the entire beam. Note the position of the slit-width micrometer once the slit is centered and closed as much as possible because the slit needs to be opened wider to pass diode.

ǂ *We recognize that the 100 mm fl lens and the cylindrical lens probably don't have the exact same focal length. This is ok because we are only using the 100 mm fl lens to set the positions of the ref and sample mirrors and L6. These positions are independent of whether we use the 100 mm fl lens or the cylindrical lens. Once the 100 mm fl lens is replaced with the cylindrical lens, we simply adjust the axial stage that the cylindrical lens is on in order to collimate the output of L2.*

IV. Sample Object Focusing and Fine-Tuning

(Use the sample arm beam for all alignments in this section).

1) Sample at transverse (x) focus. With NKT. Tape a thin wire (or a needle) to a piece of black paper as your sample (something reflective but with limited transverse extent). Place the wire onto the sample mirror, perpendicular to the beam. Using the camera, translate the sample axially until the wire/needle is focused (vertical dimensions as small as possible). This step is independent of the CL.

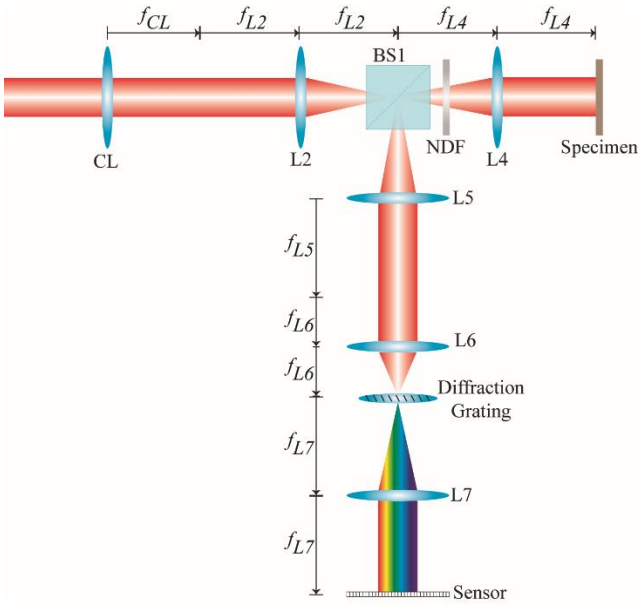

2) Match the transverse focus with the spectral focus

   a) OCT image of the wire/needle. Reconstruct the OCT image of the wire. Determine the axial position of the wire in the reconstructed OCT image.

   b) OCT image of the sample mirror. Remove the wire and translate the mirror axially until its OCT image is placed at the exact same row of the image of the wire (setup in a)).

   c) Fine CL position: Switch to diode laser. Move axially the CL until the width of the vertical line is focused onto the camera. If you have moved the CL significantly, then

move the position of the reference mirror (step 29 of Section III). The movement of CL does not affect the performance of the transverse focusing.

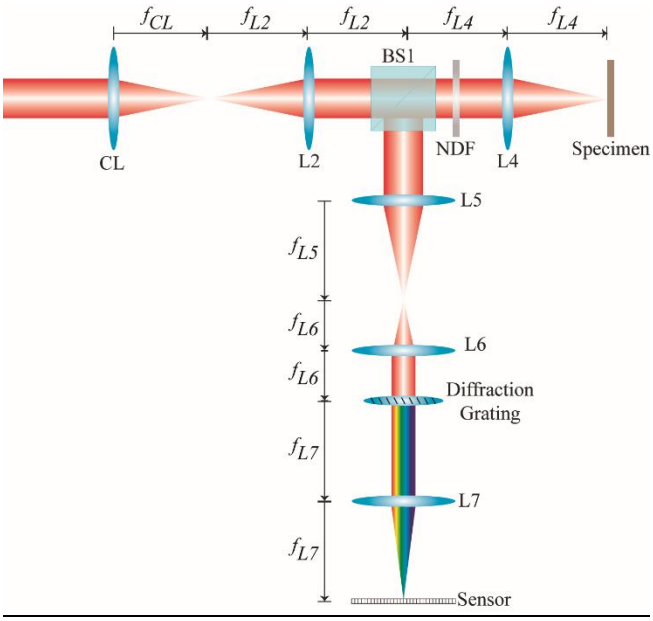

V. Final OPD and sample adjustments

1) <u>OPD adjustment.</u> With the mirror and NKT, moving the ref mirror and L3 together, (which should not modify its focus on the camera). Adjust the OPD to get the maximum fringe visibility on the camera. Determine the coherence zero of the reference stage. When it is centered, you know that the coherence zero delay position is co-incident with the sample focus

2) <u>Switch to phantom:</u> replace mirror with phantom. Tilt sample holder so that specular reflection from plastic behind phantom isn't retro-reflected. Then adjust sample vertical stage until tilted surface of phantom is back at coherence zero

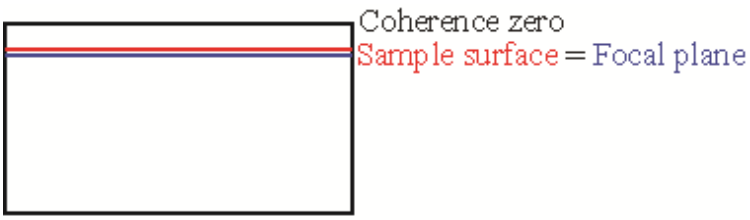

3) Adjust coherence gate– intentionally move ref stage (L3 + ref. mirror together) ~200 microns closer to the BS to shift coherence zero up relative to the focus/surface (sample surface and focal plane should be in middle on image).

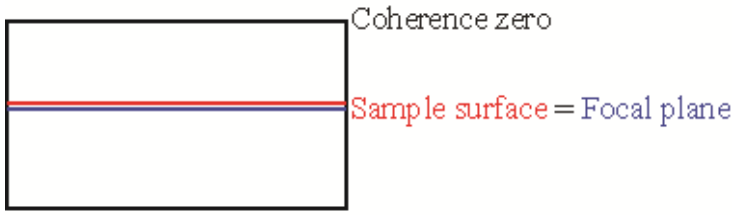

4) Sample position adjustment. At the same time, you want to move the sample ~100 microns closer to the BS so that it is still slightly below coherence zero, but slightly above the focal position.

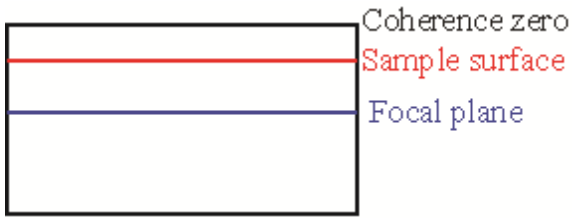

5) Imaging other samples. In general, only the sample position would need to be translated to bring the surface to the correct position, once the correct relative positions of the coherence and confocal gates are set by step 1 above.

Troubleshooting tests

1. Horizontal line shape. Looking at a sample bead, move it around (up and down) and note whether the horizontal line on the camera becomes curved at certain positions; make a drawing. If it "smiles" at the edges of the field, we might want to use a different lens and/or consider digital correction methods to compensate.
2. Vertical line shape. Same as above except using He-Ne with ref mirror. Since the curvature might depend on moving that last mirror for the He-Ne, might have to wait for the more centered 780nm laser.
3. Field curvature – horizontal. Looking at the sample bead, pay attention to the horizontal line thickness at the edges versus the center (position it to focus it as best as possible). It is fuzzier on the edges than the center or vice versa? Now hold a coverslip in front of the CMOS and see if that flips where things look fuzzy (the coverslip will slightly shorten the focal length). If we see this effect would might be able to purchase a field curvature correction optical window element.
4. Field curvature – vertical. Same test as above except on the spectrum.

APPENDIX 2: LF-OCT ALIGNMENT PROCEDURE VERSION 2

Parallel OCT Initial Setup and Alignment Procedures

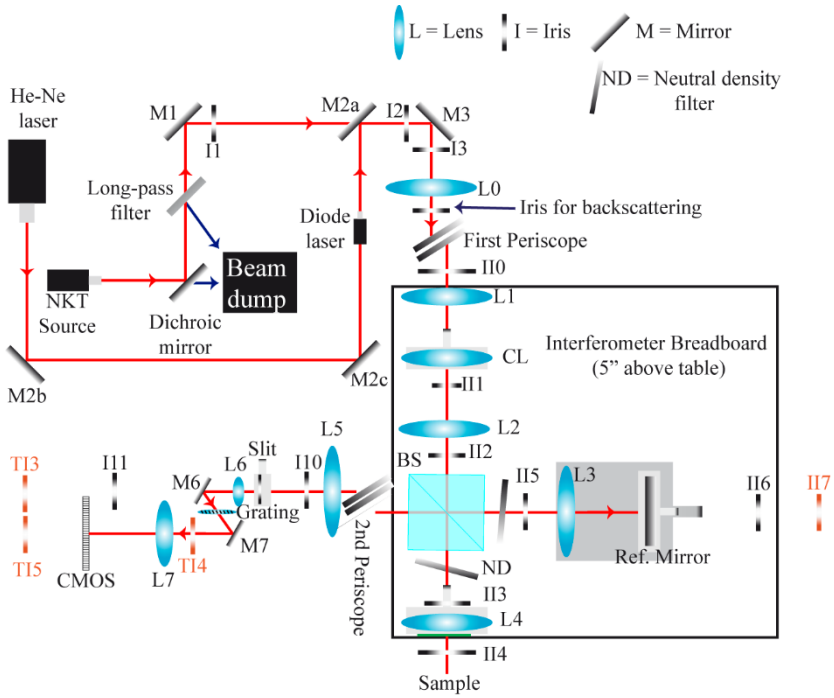

NOTE- Ultimately we need the beam to be at the height of the center of the camera pixel array. We also want the beam to be level with the table so that it doesn't enter any of the lenses at an angle. Ideally the height of the light sources would be set to the height of the camera. Set NKT and diode laser height so that both beams emerge at the height of the center of the camera array. We have found that if the beam is not at the right height, then you have to use M6/M7 to set the height. This means that the beam enters the diffraction grating with some vertical tilt. In this case, when you rotate the DG in order to make horizontal lines truly horizontal on the camera, you shift the beam up or down and it will no longer be centered on the pixel array.

Note- ALWAYS START WITH THE NKT LIGHT SOURCE AT ITS MINIMUM POWER. EVEN THIS MAY DAMAGE THE LEAVES OF THE IRIS WHEN SETTING HEIGHT.

I. Front end through first beam expander

1) Set "alignment irises": Set two irises to height at laser head. Then add the collars which fix the height of the post in the post holder but allow you to turn the iris. These are used as temporary alignment irises throughout setup (for any place where there isn't enough room to leave irises permanently)
2) Place NKT: fix NKT in place such that beam is coming out approximately level and along a row of holes.
3) NKT reflecting from dichroic: WARNING: THIS STEP IS DANGEROUS. EVEN AT LOWEST SETTING, NKT POWER IS ~300mW. YOU WILL HAVE TO HAVE HANDS VERY CLOSE TO BEAM PATH WHEN SETTING DICHROIC. Set alignment irises along row of holes on breadboard which are right angle to direction that NKT source is being emitted. This way we know dichroic mirror is set to 45 degrees (because 45 degree AOI optimizes reflectance/transmittance). Make sure 2 beams (including 1st Fresnel reflection) are coming off mirror (otherwise it may be dumping a bunch of power into the optic holder). One reflection will be visible and one IR (IR because it has been transmitted through first surface and is reflected off back surface). Make sure the beam dump is collecting what's transmitted (950 nm-2400 nm). The visible beam should be centered on the two irises. Translate DM to get beam through first iris; change tilt of DM to get visible beam through second iris. (*Or use the tilts of the DM mount and the tilts of the NKT source if the beam is close to being aligned through the two irises but needs fine-tuning*.)

4) NKT through LP filter: Insert LP (long-pass) filter between DM and M1. It won't change the path of the beam at all. Put at angle so that reflected beam (400 nm – 605 nm) goes into same beam dump as DM transmitted beam.
5) Set two irises: to same height in front of NKT. Place along row of holes between where L0 and L1 will go.
6) NKT off M1 & M2: adjust to get beam aligned with two irises from previous step.
7) Drop in two irises between M1 and M2 to check alignment in future.
8) He-Ne alignment: (Note that the He-Ne is necessary for checking collimation using shear plate interferometer. NKT is too polychromatic and diode isn't bright enough. We use the He-Ne laser to collimate the beam because all lenses are achromatic doublets). Set He-Ne up as shown in diagram. Use the two alignment irises to make sure He-Ne beam is coming out approximately in a straight and level line along a row of holes on the breadboard. Then set 2 mirrors (M2b and M2c) at 45 degree angles as shown in diagram. Make sure that where the He-Ne beam crosses the path between L0-L1-CL won't intersect with any optical elements. Then adjust the position and tilt of these two mirrors to get the He-Ne through I1 and I2.
9) Place L0: drop in L0; Align with irises from step 5. Note beam is highly divergent so irises must be within ~30 cm of L0. Place on both an axial and a transverse translation stage. This way we can roll L0 out of the beam path when aligning periscope.

Option: set a temporary iris way beyond I4 and co-align all 3 beams (in sequence above) through I3/I4 and the temporary one.

10) (**General lens alignment procedure**): As with all lenses going forward, two downstream irises should be identified before putting in the lens and the lens adjusted transversely (horizontally and vertically) so as not to deflect the beam, and also tilted so that the surface is

exactly perpendicular to the beam path. NKT power needs to be at least 50% for lens alignment; we noticed that the beam shape seems to change at lower powers and it's harder to see the beam to align it well.

11) **(General collimation procedure)**: Use a shear plate collimator with He-Ne beam everywhere possible. (For all lenses, even for the lens after the diffraction grating). This process does not work with the cylindrical lens in place or with broadband sources. Note about aberrations: spherical aberrations (due to large beam size) will become compounded. We have found that after 4 lenses, the fringes on the shear plate are no longer straight, parallel lines. We first tested the collimation by using a piece of graph paper and checking the diameter far away. Then we saw what this corresponded to on the shear plate.

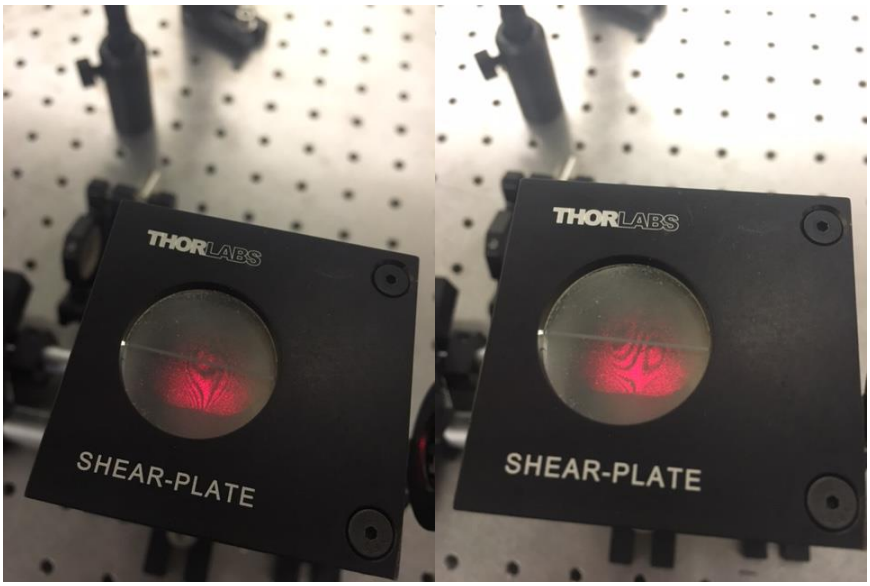

Not Collimated (with spherical aberrations) *Close to collimated (with spherical aberrations)*

All of the following steps (except collimation) should be done using the NKT unless otherwise noted.

12) Coarse periscope setup: setup periscope immediately after iris that is immediately after where L0 will go. Adjust so that beam is coming out at approximately the height on top of the interferometer breadboard that you want all interferometer optics at. (So set up the interferometer breadboard on its posts. Choose an axial position, set an iris to the height that you want all optics at, then adjust periscope so that the beam is centered on this iris.)
13) Set II1-II3: set three irises to be the height on top of the interferometer breadboard that you want all your interferometer optics to be at (Do this by placing each iris in the exact same position on the interferometer breadboard as the position at which the first iris in the previous step was set. In this way, all irises will now be at the same height.) Screw two of them onto breadboard along row of holes that L1, L2, BS, and L4 will be on.
14) Set height of periscope: Set interferometer breadboard on posts. Then align periscope mirrors so that beam is coming out at a level height using II1 and II3. This is done before placing lenses because the beam is still small and easier to align accurately.
15) Set horizontal tilt of periscope: so that beam comes out going along a row of holes on interferometer breadboard (because these holes are offset by ½" from holes on optical table).
16) Set II0 & II4: Also set additional 1.5" irises to same height, but these will be placed at edge of optical table in ref arm. This will be used to align beam splitter and L3.
17) Place L0: drop in L0; Align with II0 and I4. Note beam is highly divergent so irises must be within ~30 cm of L0.
18) Screw interferometer breadboard down: Set approximate position of breadboard so that L1 will be collimated right on the edge of the breadboard. Screw in posts of breadboard at this position on optic axis.

19) Move first iris on row 3 of interferometer breadboard to row 6 because it will be in the way of L1. (Needed it at row 3 because beam is so diverging after L0 that you want iris as close as possible to L0)

20) L1. Place L1; Align L1 with II1 and II4. Adjust axial position to collimate the output beam (note: any time "collimate" is mentioned one switches to He-Ne, otherwise assume NKT is used). Re-check alignment on II1 and II4. Once L1 is set, place a large iris between the 2 lenses captures back-reflection off the second lens.

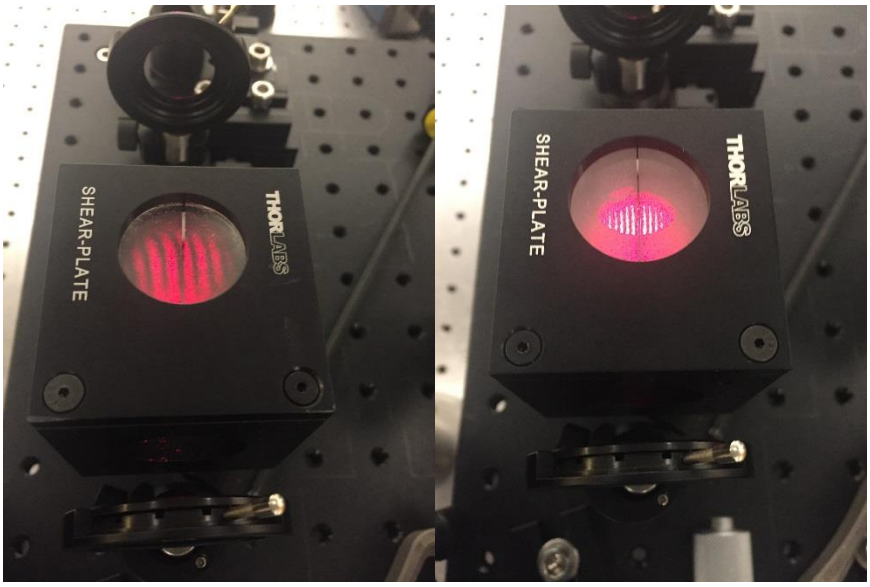

Fringes on a) large shear plate and b) small shear plate. Note that we are able to see the presence of aberrations in the form of curved fringes much more clearly in a) than in b) due to the size of the fringes.

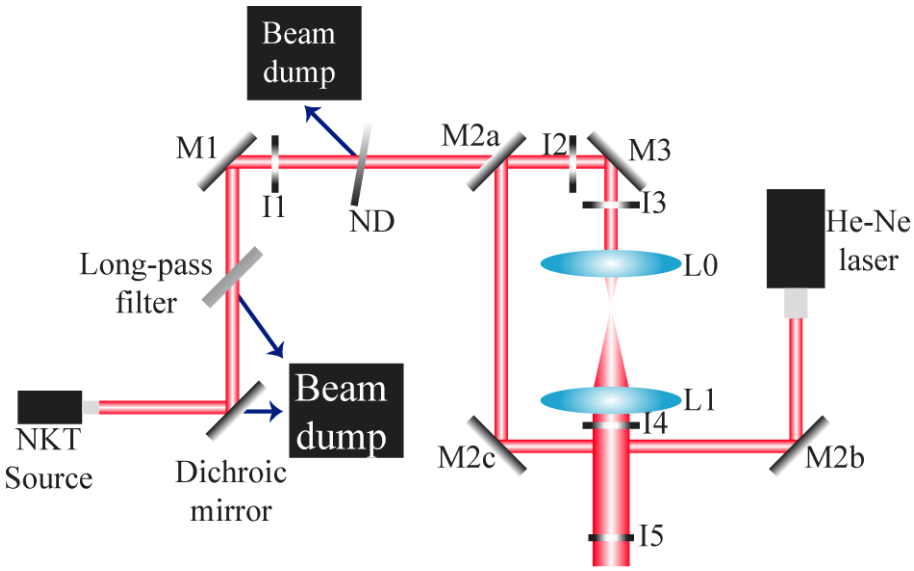

II. The Michelson

1) (**General Strategy**): Align as much as possible without the CL (up to L5) although the exact distance of the ref mirror and sample will not be able to be set yet. Then put in the CL and align ref mirror (we'll be able to see focus), L6, diffraction grating, and L7. Ideally this brings the system to where the beam is approximately collimated in transverse and focusing in spectral directions (from the ref arm), whereas the sample hasn't been checked at all yet. The diode laser will be used with CMOS translation to get the spectral direction from the ref mirror into focus. A point-like scatterer on the sample will be translated to bring transverse direction of the sample into focus. Then using the diode laser again the spectral focus of the sample will be checked – and if need be, the camera (NOT the sample) will be moved. Then iterate back to the ref mirror spectral adjustment. Then the ref mirror + lens translated together to align the OPD to just above the sample. We already know that the ref mirror + lens motion doesn't modify the spectral direction focus significantly, so as long as it doesn't move terribly far, it should remain in focus along that direction.

2) Set II6 & II7: set one iris along row of holes where ref beam will come out of beam splitter. Set one farther away (not on interferometer breadboard but along same row of holes).

3) Setting Beam splitter:

   a) Beam should enter prism marked with a black dot.

   b) Place at an angle so that beam is roughly along the same row of holes as II6 and II7.

   c) Use II6 and II7 to check the out of plane tilt of the beam splitter to ensure that beam height in ref arm is constant. Adjust tilt of beam splitter plate if necessary. Note that you must also use the back reflection from the front surface of the beam splitter to check height because it is possible to have beam at correct height through II3 and II5 and have the back reflection completely off. We found that you need to adjust both tilts on the beam splitter plate in order to get both the back reflection and the beam in ref arm to be at same height.

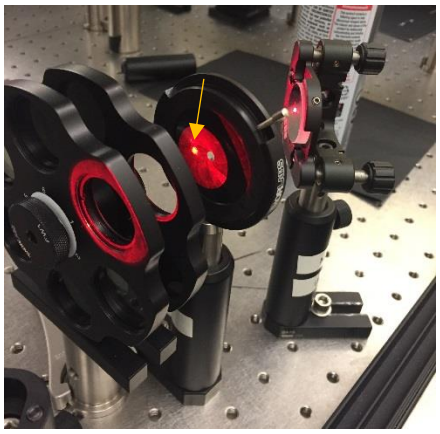

Yellow arrow points to reflection from front surface of beam splitter on I1 (with M1 behind). Use to set vertical tilt of beam splitter.

4) L2: Place in about 1 focal length from the beam splitter and align with II4/II6 as well as back reflection on II1. Also check that beam is centered on L2. Note that the exact distance from

beam splitter doesn't matter- after CL insertion, we will check the collimation after L2 to make sure CL+L2 distance is right.

5) NDFs and fix irises: Place the variable neutral density filter into the ref arm first. Then place NDF in sample arm. Try to set at approximately same angle. Note that NDF's should be placed at angles such that same side of beam enters the filter first. And beam should be centered on wheel in each arm. After spherical lens is inserted, beam will be clipped by filter wheels so the outputs of each arm will be different sizes if the wheels aren't both centered.
6) L2+L3 reference adjustment: Place L3 on a translation stage and align with II6 and II7. Collimate the output beam.

Fringes on larger shear plate after L3. This was after we checked beam diameter ~40" away from lens to determine collimation since unclear from spherical aberrations on plate.

7) Ref mirror coarse adjustment: place ref mirror approx. one focal length from L3. Retro-reflect the beam exactly back through I8 and I1. Note that the axial position of the ref mirror will be aligned more accurately later. We use I8 and I1 because we need two points to be able to exactly retro-reflect the beam. The beam is shifted transversely coming out of the Michelson so we can't set I10 and I11 until after the beam is perfectly retro reflecting.

8) Add temp iris after L4: set another iris after II4. This will be used to set L4.

9) L2 + L4 sample adjustment: Place L4 on a translation stage. Then, align L4 with II4 and temp iris from previous step. Collimate the output beam. (The actual sample will be dealt with later).

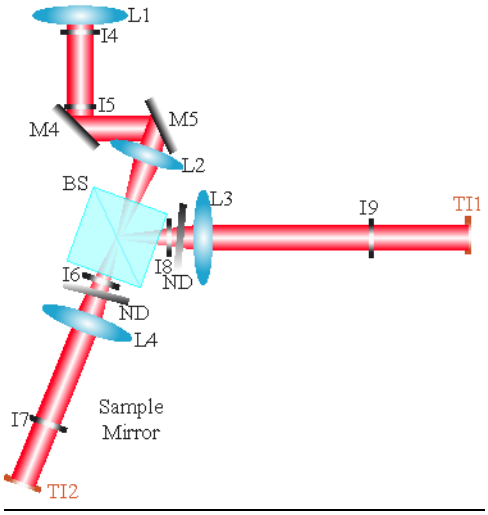

10) Sample mirror coarse adjustment: place a mirror in sample arm approx. one focal length from L4 and retro-reflect back through I6 and I1. (We setup mirror in sample arm so that we can check that L5 is collimated by checking with both ref arm and sample arm.)

11) Set height of I10: Set an iris to the height of the center of the camera sensor, as best you can tell by eye.

12) Place I10: place iris close to the output of the second periscope.

13) Coarse vertical adjustment of 2nd periscope using camera height: adjust the height and vertical tilt of 2nd periscope to get beam vertically centered on camera. Then, at that same axial location, set I10 to the same height (so that as you close I10, you can see the beam on the camera closing symmetrically). (We note that the vertical tilt may still be off at this point.)

14) Set I11: move I10 further away from 2nd periscope and along the same row of holes. Now insert I11 in the exact same place where I10 was previously. Set the height of I11 such that beam is centered on it. Now we know that I10 and I11 are at the exact same height.
    a) Repeat this step for two additional irises! We will need these later on to ensure that everything in the spectrometer is at the same height.
15) Second Periscope: set mirrors of periscope so that output of the Michelson is directed through I10/I11, horizontally and vertically.
16) L3 + L5 adjustment: With the ref arm only, align L5 with I10/I11 and collimate the output beam.

Fringes on Large shear plate after L5. Again this was after checking beam diameter ~40" from lens.

17) L4 + L5 adjustment: Now block ref arm and unblock sample and check that beam from L5 is still collimated and passing through I10/I11.

**Note: this is used to balance the dispersion and OPD from the filter in the reference. We might explore, if needed, using a slightly thicker flat to force the focus a little deeper than the coherence zero. However, since the transverse focus of the ref arm probably doesn't matter (it's

a mirror) the added flat here may not even be needed at all – recognizing that the imbalanced dispersion can be compensated digitally.

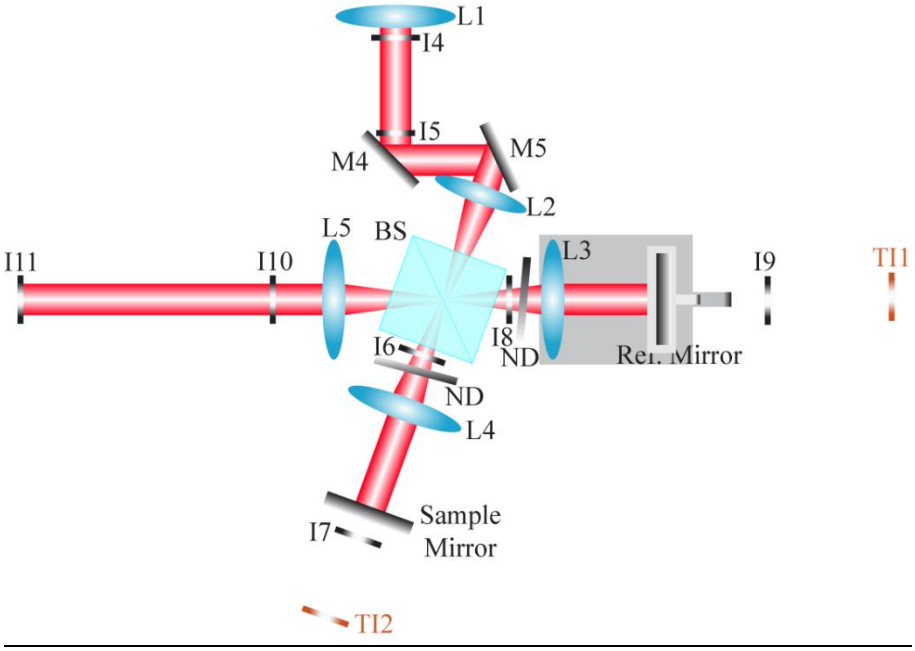

III. The Camera Coarse Positioning with Ref Arm Beam Only

(Use the ref arm beam for all alignments in this section).

1) Insert spherical lens: Before inserting CL, insert a spherical lens with the same focal length as the CL on an axial translation stage where the CL will later go. (Because we can't use the shear plate with an elliptical beam.) Center beam on I5 and I6/I8. (Beam may not look centered on I10/I11, possibly because beam is shifted vertically coming out of the beam splitter. When this lens is removed, beam should again look aligned on I10/I11.) Translate axially until beam after L2 is collimated. ǂ

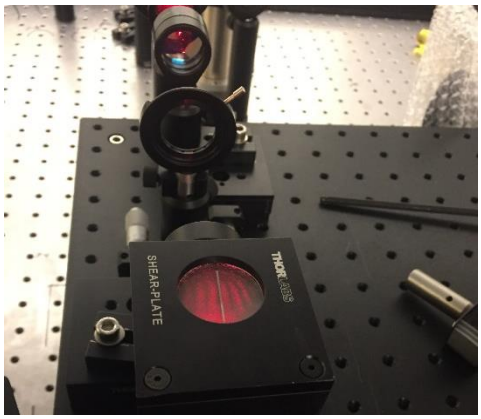

Fringes on large shear plate after L2 (changing spherical lens to collimate). Note fewer spherical aberrations after these 4 lenses than after L3 is collimated also with 4 lenses in place.

2) Ref mirror axial adjustment: Slide the ref mirror along the beam axis (while keeping L3 stationary) to collimate the beam after the BS (output of the Michelson) but before L5. You will also want to carefully check the retro-reflection back through I8 and I5– the ability for the ref arm to exactly retro-reflect automatically sets the system so that it will be sensitive only to exact backscattering from the sample object. Ref mirror should be at the focal plane of L3 if all is right. Because the shear plate is our most sensitive collimation tool, once we set this distance, we fix the position in space of the ref mirror and where the camera will end up being. Note this ref mirror stage micrometer value.
3) Setting up sample arm: Insert a mirror to deflect the beam down onto the optics bench. Using a mirror as the sample, set the location and angle of the new mirror until the beam is retro-reflected back through I6 and I1. Check that two arms (ref and sample) are coaxial: first check that two arms are coaxial with NKT source by checking at I10 and at the slit.
4) Sample mirror axial adjustment: translate the vertical stage in the sample arm until the output of the Michelson (before L5) is collimated.

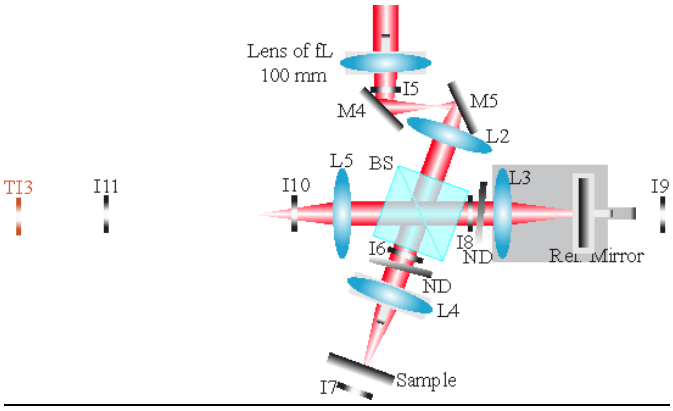

5) Build relay system: If beam after L6 is smaller than 5 mm, we won't be able to use the shear plate to collimate so instead use a 150 mm fl lens and a 100 mm fl lens to expand the beam after L6.

6) L5 + L6 adjustment: Place one of the temporary alignment irises (TI3) after I11 and along the same row of holes. Drop in L6 and align with I11 and TI3. Collimate the output from L6 using the He-Ne laser. Set transverse and height position of the L6 lens using NKT and without the lens of FL 100 mm. Iterate between the two steps as needed.

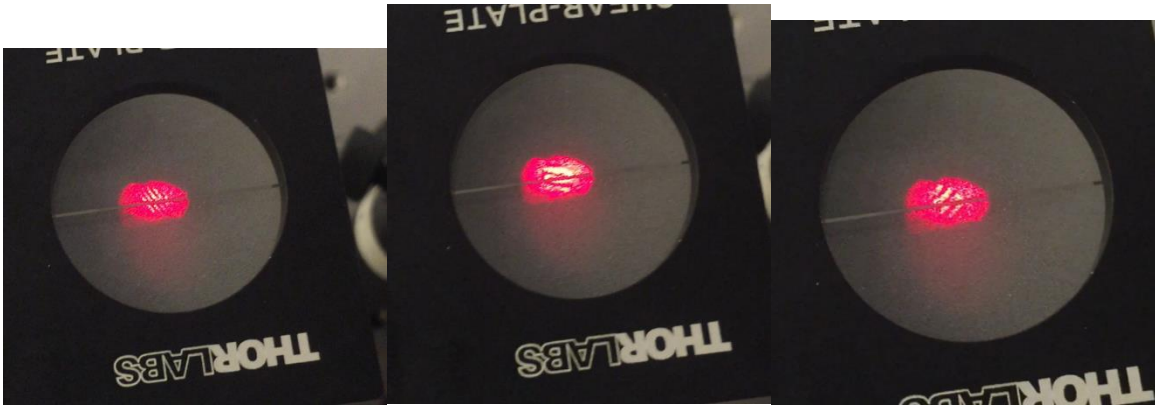

Fringes on small shear plate after L6 as L6 is being translated axially. Hard to see b/c beam so small, but you can tell where lines are parallel with line on shear plate.

7) Replace 100 mm fl lens

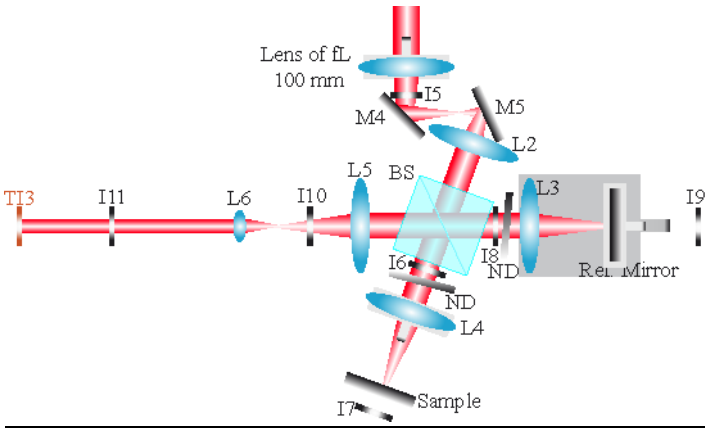

8) Slit coarse adjustment: Insert slit at focal plane between L5 and L6 on a lateral translation stage.

9) M6 at Littrow angle: Now place M6 after L6. Set horizontal tilt of M6 such that if the DG is placed parallel to the row of holes L5-L6, the beam from M6 will enter the DG at Littrow angle. Place mirror as close to L6 as possible, because focal length of L6 is only 5 cm and need diffraction grating to be at focal plane (after M6).Use the two irises from step 11a of section II to set vertical tilt of M6 so that beam is level with table.

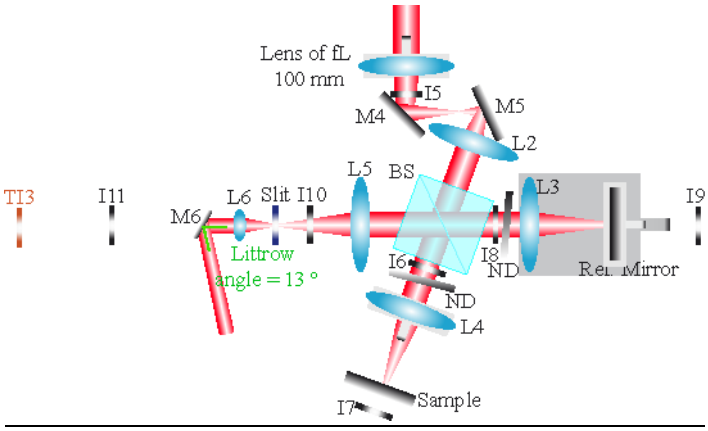

10) Remove 100 mm fl lens

11) Diffraction grating (DG) positioning: Position the DG at the approximate focus in the transverse imaging plane. Note that the rotation angle of the DG will be checked later. Set the coarse DG rotation angle such that the various orders coming out of the DG are all at the

same height, as dictated by sliding the two irises from step 11a of section II along the orders and checking the height at various positions.

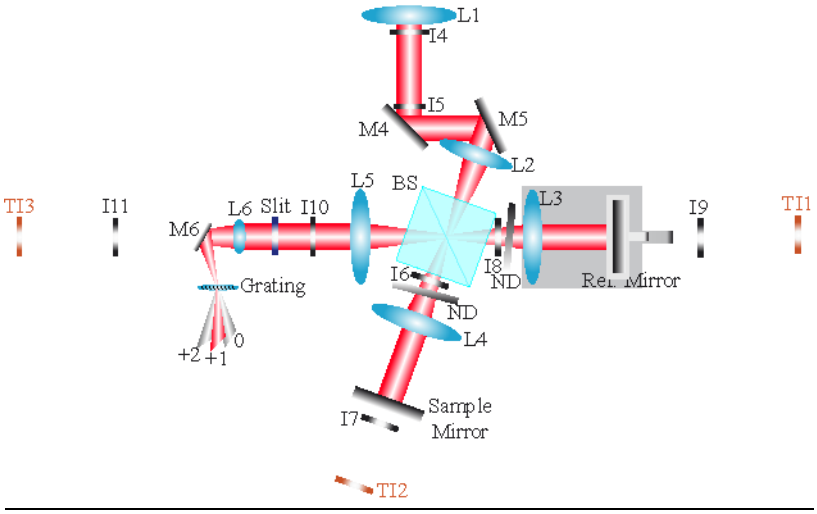

12) Replace 100 mm fl lens: Align with I5 and I8/I6.

13) M7 approximate placement: Place M7 at roughly the right location so that first order is directed roughly along a row of holes.

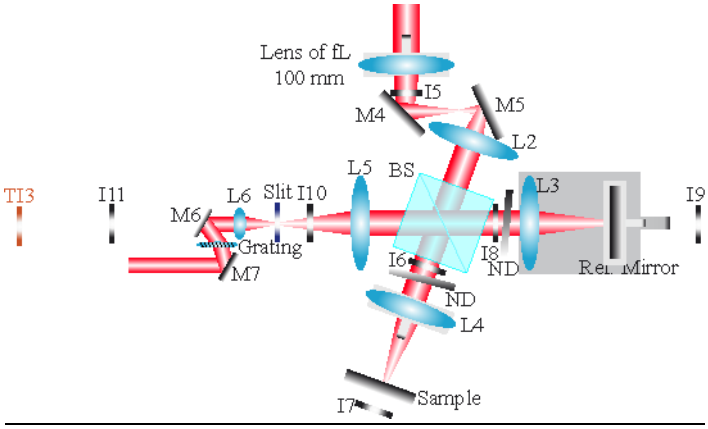

14) Insert Thorlabs 800nm filter between L5 and L6.

15) Horizontal tilt of M7: With NKT & 800 nm filter translate M7 and adjust horizontal tilt to align through TI4 and TI5. Note that the height will be set later.

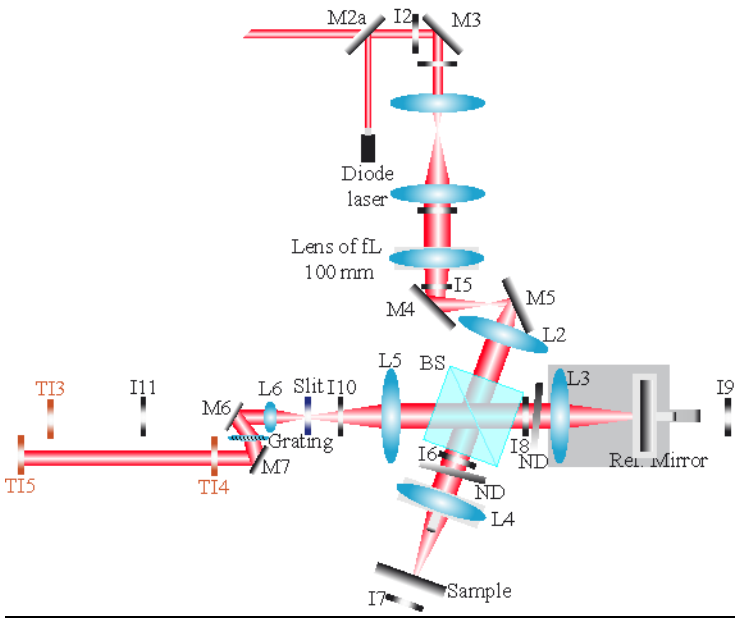

16) <u>Vertical line toward camera:</u> With NKT: Remove TI4 and TI5. Place camera along same row of holes as TI4 and TI5. Mark two axial positions along this row of holes (~10" apart). At the first position, adjust vertical tilt of M6 to center height on camera (using line profile tool in PFV software). Slide camera to second position and adjust vertical tilt of M7 to center beam vertically on camera. Iterate until beam is level with table and centered on camera at both axial positions.

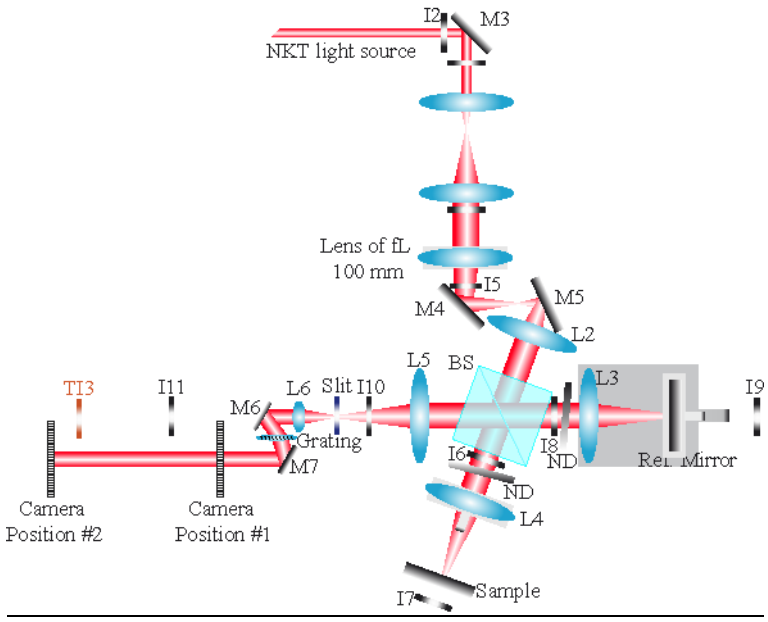

17) Set height of L7: Set L7 on axial translation stage (axial position will be set later). with NKT source- using the same general procedure as step 15 above, slide the camera between two axial positions to set the height of L7 so that NKT beam is centered vertically on camera at both axial positions. Then add a collar to L7 so that height is fixed.

18) Set transverse position of L7: Once height is set and is fixed by collar, again translate the camera between two axial positions and adjust transverse position of L7 as well as tilt of L7 to get NKT beam centered laterally on camera at both axial positions of camera.

19) Remove 75 mm fl lens

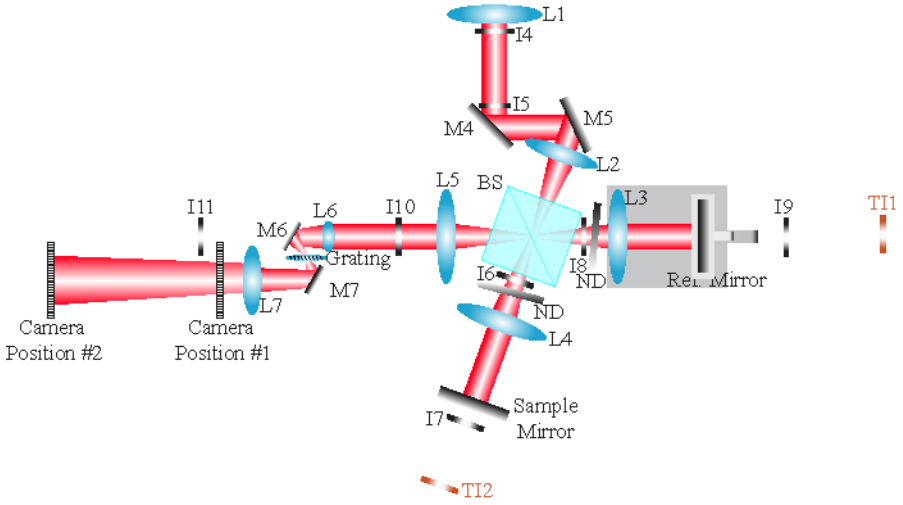

20) L7 collimation: NKT: Try to set axial position by checking collimation using He-Ne laser and the shear plate. On most recent alignment, we couldn't see fringes on shear plate. Instead checked beam diameter ~40" from L7 with graph paper. Note that when we close I0, the beam seems to be focusing. When all irises are open, the beam seems collimated both for 800 nm and for all wavelengths.

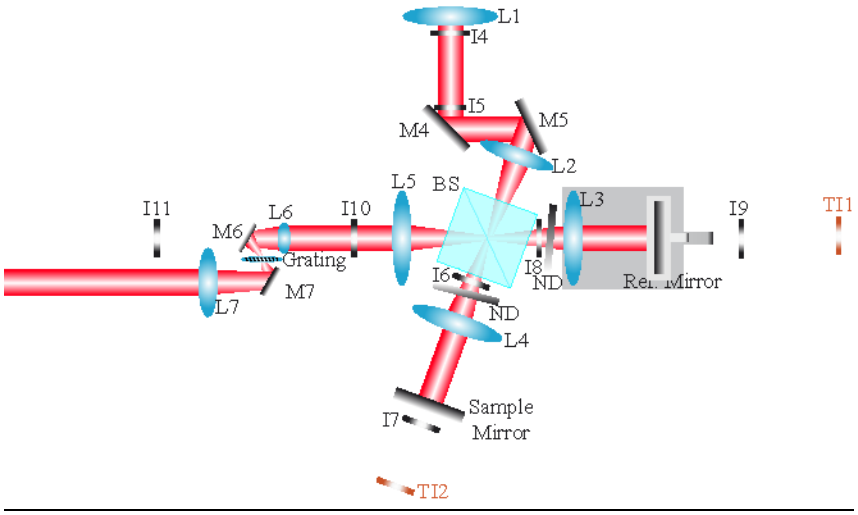

21) Insert 100 mm fl lens. Re-check alignment and collimation

22) Camera coarse positioning: With ref arm only. Align the camera so that it is centered on the NKT/800nm filter and perpendicular to the beam axis. Then screw in two rails along the feet of camera so that it can be moved axially without being tilted laterally. Adjust the axial position of the camera to focus the beam from just the ref arm onto the sensor. Carefully remove rails and clamp camera legs to table.

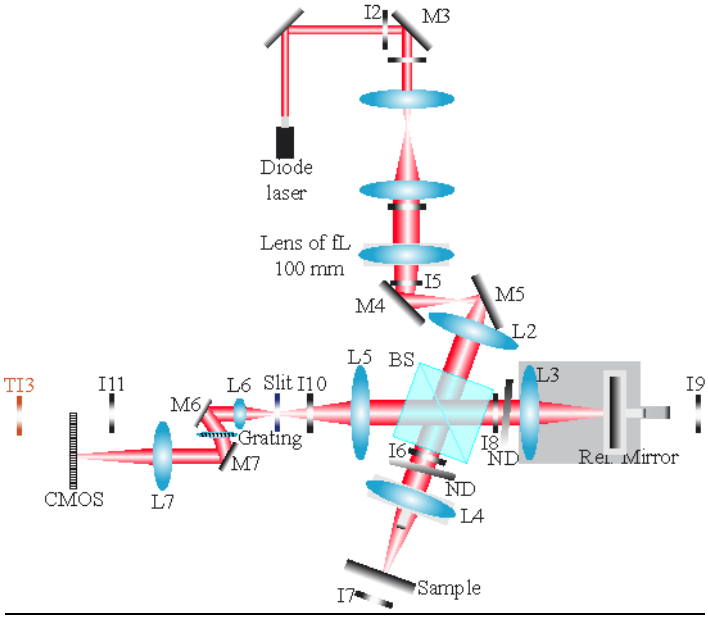

23) Fine camera position with sample arm: Using diode laser. Block ref arm and unblock sample arm. With sample mirror at focal plane of L4 (step 4 of this Section), adjust finely the axial position of the camera to focus the point source from the sample arm onto the sensor. Check ref. mirror position: Using diode laser. Block sample arm and unblock reference arm. Check if the point source produced by the reference arm is the smallest, if not move the axial position of the reference mirror (kept L3 fixed).

24) DG rotation angle. With NKT- Adjust the DG rotation angle to make one of the central lines exactly horizontal. (Need spherical lens in to be able to see horizontal lines on camera.) If height of beam on camera changes when DG rotation angle is changed, go back to step 17 in section III. Keep spherical lens in but remove L7 and repeat steps up to this point.

25) Remove 100 mm fl lens

26) CL insertion: NKT: Insert CL approximately CL+L2 away from L2 and use I5 and I6/I8 to align CL. Change tilt to center beam on target; adjust lateral position and axial position to align with irises. Check that beam is centered through lens by rotating the CL in its mount. You should see the beam rotate about the center of I5 is beam is centered through CL. Adjust tilt of CL mount to align the retro-reflection from CL on I4.

27) Check retro-reflection of ref mirror: note that the filter wheel needs to be at least attenuation. Otherwise one side of beam is much less bright and it makes aligning hard.

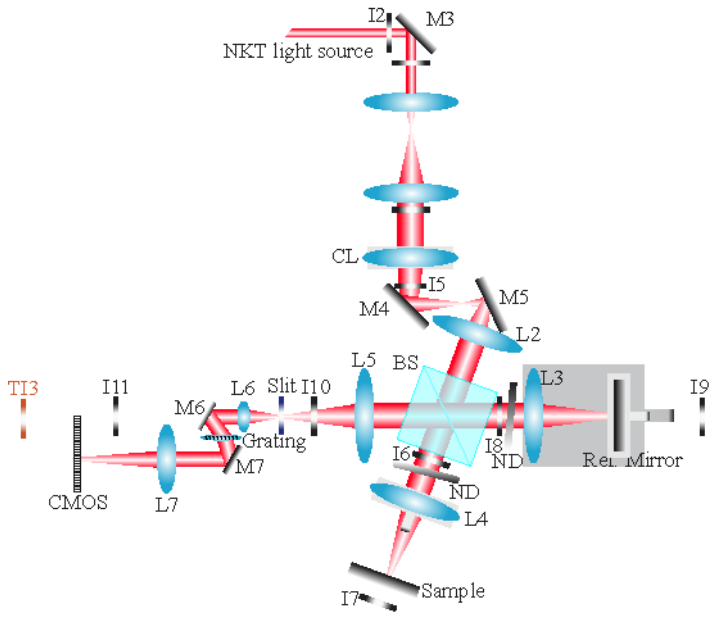

28) CL collimation: After beam is aligned, switch to NKT w/ 800 nm filter. Block reference arm and unblock sample arm. Change axial position of CL until the width of vertical-line beam on camera is the narrowest. For this position, the beam after L2 is collimated.

29) Check ref. mirror position: Using diode laser. Block sample arm and unblock reference arm. Check if the vertical line produced by the reference arm is as narrow as possible. If not, move the axial position of the reference mirror (again without changing the L3 lens).

30) CL rotation angle: Using diode laser, fine-tune the CL rotation angle so that the focused line is exactly vertical on the camera.

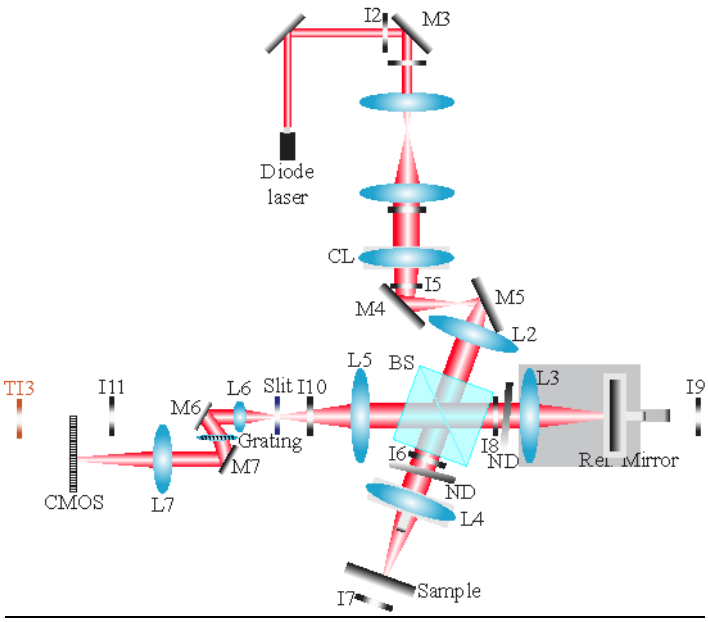

31) Check that both arms are coaxial: Using diode laser, make sure that two arms are perfectly overlapping on camera (the two vertical-line beam should overlap completely).

32) Slit fine transverse position: Using the NKT: Fix slit to translation stage that moves laterally across beam axis. Now, using the NKT source and the ref arm mirror on the camera, close slit almost all the way. Center the light that is passed onto the camera. Then open the slit slowly. You should see the beam fill the camera symmetrically. If not, iterate between centering slit when slit is closed almost all the way and opening the slit to pass the entire beam. Note the position of the slit-width micrometer once the slit is centered and closed as much as possible because the slit needs to be opened wider to pass diode.

ǂ *we recognize that the 100 mm fl lens and the cylindrical lens probably don't have the exact same focal length. This is ok because we are only using the 100 mm fl lens to set the positions of the ref and sample mirrors and L6. These positions are independent of whether we use the 100 mm fl lens or the cylindrical lens. Once the 100 mm fl lens is replaced with the cylindrical lens, we simply adjust the axial stage that the cylindrical lens is on in order to collimate the output of L2.*

IV. Sample Object Focusing and Fine-Tuning

(Use the sample arm beam for all alignments in this section).

1) Sample at transverse (x) focus. With NKT. Tape a thin wire (or a needle) to a piece of black paper as your sample (something reflective but with limited transverse extent). Place the wire onto the sample mirror, perpendicular to the beam. Using the camera, translate the sample axially until the wire/needle is focused (vertical dimensions as small as possible). This step is independent of the CL.

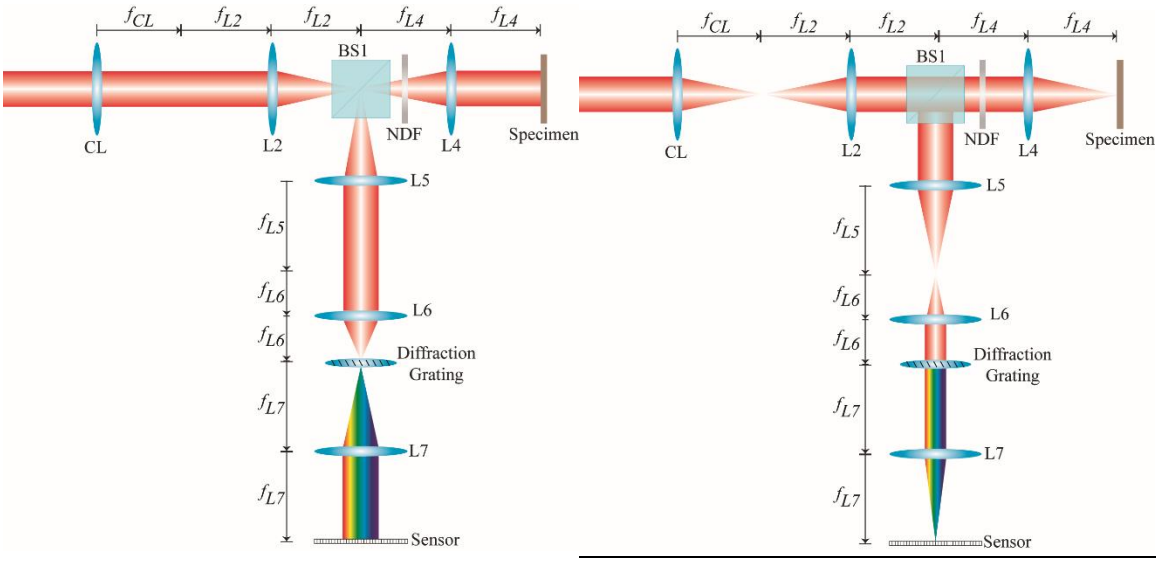

2) Match the transverse focus with the spectral focus

   a) OCT image of the wire/needle. Reconstruct the OCT image of the wire. Determine the axial position of the wire in the reconstructed OCT image.

   b) OCT image of the sample mirror. Remove the wire and translate the mirror axially until its OCT image is placed at the exact same row of the image of the wire (setup in a).

   c) Fine CL position: Switch to diode laser. Move axially the CL until the width of the vertical line is focused onto the camera. If you have moved the CL significantly, then

move the position of the reference mirror (step 32 of Section III). The movement of CL does not affect the performance of the transverse focusing.

V. Final OPD and sample adjustments

1) OPD adjustment. With the mirror and NKT, moving the ref mirror and L3 together, (which should not modify its focus on the camera). Adjust the OPD to get the maximum fringe visibility on the camera. Determine the coherence zero of the reference stage. When it is centered, you know that the coherence zero delay position is co-incident with the sample focus

2) Switch to phantom: replace mirror with phantom. Tilt sample holder so that specular reflection from plastic behind phantom isn't retro-reflected. Then adjust sample vertical stage until tilted surface of phantom is back at coherence zero

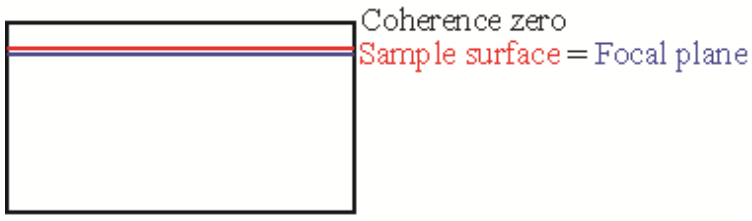

3) Adjust coherence gate– intentionally move ref stage (L3 + ref. mirror together) ~200 microns closer to the BS to shift coherence zero up relative to the focus/surface (sample surface and focal plane should be in middle on image).

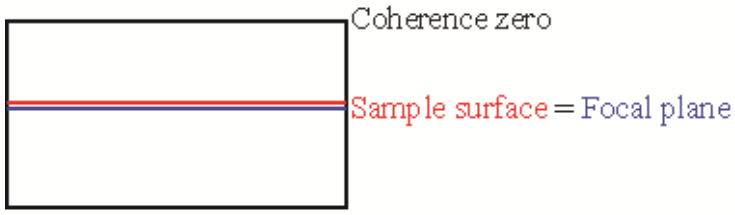

4) Sample position adjustment. At the same time, you want to move the sample ~100 microns closer to the BS so that it is still slightly below coherence zero, but slightly above the focal position.

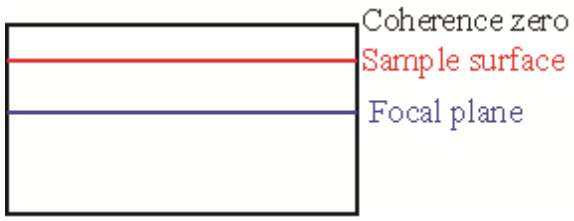

5) Imaging other samples. In general, only the sample position would need to be translated to bring the surface to the correct position, once the correct relative positions of the coherence and confocal gates are set by step 1 above.

Troubleshooting tests suggested by Dan

1. Horizontal line shape. Looking at a sample bead, move it around (up and down) and note whether the horizontal line on the camera becomes curved at certain positions; make a drawing. If it "smiles" at the edges of the field, we might want to use a different lens and/or consider digital correction methods to compensate.
2. Vertical line shape. Same as above except using He-Ne with ref mirror. Since the curvature might depend on moving that last mirror for the He-Ne, might have to wait for the more centered 780nm laser.
3. Field curvature – horizontal. Looking at the sample bead, pay attention to the horizontal line thickness at the edges versus the center (position it to bets focus). It is fuzzier on the edges than the center or vice versa? Now hold a coverslip in front of the CMOS and see if that flips where things look fuzzy (the coverslip will slightly shorten the focal length). If we see this effect, consider purchasing a field curvature correction element.
4. Field curvature – vertical. Same test as above except on the spectrum.

REFERENCES

1. D. Huang, E. A. Swanson, C. P. Lin, J. S. Schuman, W. G. Stinson, W. Chang, M. R. Hee, T. Flotte, K. Gregory, C. A. Puliafito, and J. G. Fujimoto, "Optical Coherence Tomography," Science (80-.). **254**, 1178–1181 (1991).

2. J. G. Fujimoto, M. E. Brezinski, G. J. Tearney, S. A. Boppart, B. Bouma, M. R. Hee, J. F. Southern, and E. A. Swanson, "Optical biopsy and imaging using optical coherence tomography," Nat. Med. **1**, 970–972 (1995).

3. A. L. Oldenburg, B. E. Applegate, J. M. Tucker-Schwartz, M. C. Skala, J. Kim, and S. A. Boppart, "Molecular Optical Coherence Tomography Contrast Enhancement and Imaging," in *Optical Coherence Tomography: Technology and Applications, Second Edition*, W. Drexler and J. G. Fujimoto, eds., 2nd ed. (2015), pp. 1442–1468.

4. A. L. Oldenburg, J. R. Gunther, and S. a Boppart, "Imaging magnetically labeled cells with magnetomotive optical coherence tomography," Opt. Lett. **30**, 747–9 (2005).

5. A. Oldenburg, F. Toublan, K. Suslick, A. Wei, and S. Boppart, "Magnetomotive contrast for in vivo optical coherence tomography.," Opt. Express **13**, 6597–6614 (2005).

6. V. Crecea, A. L. Oldenburg, T. S. Ralston, and S. a. Boppart, "Phase-resolved spectral-domain magnetomotive optical coherence tomography," Proc. SPIE **6429**, 64291X-64291X–10 (2007).

7. A. L. Oldenburg, V. Crecea, S. A. Rinne, and S. A. Boppart, "Phase-resolved magnetomotive OCT for imaging nanomolar concentrations of magnetic nanoparticles in tissues," Opt. Express **16**, 11525–39 (2008).

8. J. Oh, M. D. Feldman, J. Kim, H. W. Kang, P. Sanghi, and T. E. Milner, "Magneto-motive detection of tissue-based macrophages by differential phase optical coherence tomography," Lasers Surg. Med. **39**, 266–272 (2007).

9. J. Wang, M. R. Wang, H. Jiang, M. Shen, L. Cui, and S. K. Bhattacharya, "Detection of magnetic particles in live DBA/2J mouse eyes using magnetomotive optical coherence tomography.," Eye Contact Lens **36**, 346–51 (2010).

10. J. Wang, A. Aljohani, T. Carreon, G. Gregori, and S. K. Bhattacharya, "In vivo quantification of cochlin in glaucomatous DBA/2J mice using optical coherence tomography," Sci. Rep. **5**, 1–8 (2015).

11. A. L. Oldenburg, C. M. Gallippi, F. Tsui, T. C. Nichols, K. N. Beicker, R. K. Chhetri, D. Spivak, A. Richardson, and T. H. Fischer, "Magnetic and contrast properties of labeled platelets for magnetomotive optical coherence tomography," Biophys. J. **99**, 2374–2383 (2010).

12. A. L. Oldenburg, D. Spivak, G. Wu, F. Tsui, and T. H. Fischer, "Optimizing magnetomotive contrast of SPIO-labeled platelets for thrombosis imaging in optical

coherence tomography.," Proc. SPIE **8213**, 82131N (2012).

13. J. Kim, A. Ahmad, M. Marjanovic, E. J. Chaney, J. Li, J. Rasio, Z. Hubler, D. Spillman, K. S. Suslick, and S. A. Boppart, "Magnetomotive optical coherence tomography for the assessment of atherosclerotic lesions using alphavbeta3 integrin-targeted microspheres," Mol. Imaging Biol. **16**, 36–43 (2014).

14. J. Kim, A. Ahmad, J. Li, M. Marjanovic, E. J. Chaney, K. S. Suslick, and S. A. Boppart, "Intravascular magnetomotive optical coherence tomography of targeted early-stage atherosclerotic changes in ex vivo hyperlipidemic rabbit aortas," J. Biophotonics **9**, 109–116 (2016).

15. R. John, R. Rezaeipoor, S. G. Adie, E. J. Chaney, A. L. Oldenburg, M. Marjanovic, J. P. Haldar, B. P. Sutton, and S. A. Boppart, "In vivo magnetomotive optical molecular imaging using targeted magnetic nanoprobes," Proc. Natl. Acad. Sci. U. S. A. **107**, 8085–8090 (2010).

16. J. Koo, C. Lee, H. W. Kang, Y. W. Lee, J. Kim, and J. Oh, "Pulsed magneto-motive optical coherence tomography for remote cellular imaging.," Opt. Lett. **37**, 3714–6 (2012).

17. P. Cimalla, J. Walther, C. Mueller, S. Almedawar, B. Rellinghaus, D. Wittig, M. Ader, M. Karl, R. Funk, M. Brand, and E. Koch, "Improved Imaging of Magnetically Labeled Cells Using Rotational Magnetomotive Optical Coherence Tomography," Appl. Sci. **7**, 444 (2017).

18. P. Cimalla, T. Werner, K. Winkler, C. Mueller, S. Wicht, M. Gaertner, M. Mehner, J. Walther, B. Rellinghaus, D. Wittig, M. O. Karl, M. Ader, R. H. W. Funk, and E. Koch, "Imaging of nanoparticle-labeled stem cells using magnetomotive optical coherence tomography, laser speckle reflectometry, and light microscopy," J. Biomed. Opt. **20**, 036018 (2015).

19. J. Kim, A. Ahmad, and S. a Boppart, "Dual-coil magnetomotive optical coherence tomography for contrast enhancement in liquids.," Opt. Express **21**, 7139–47 (2013).

20. A. Ahmad, J. Kim, N. D. Shemonski, M. Marjanovic, and S. a Boppart, "Volumetric full-range magnetomotive optical coherence tomography.," J. Biomed. Opt. **19**, 126001 (2014).

21. K. J. Lohmann, S. D. Cain, S. A. Dodge, M. F. Catherine, E. Ed, K. J. Lohmann, S. D. Cain, S. A. Dodge, and C. M. F. Lohmann, "Regional Magnetic Fields as Navigational Markers for Sea Turtles," Science (80-.). **294**, 364–366 (2017).

22. K. J. Lohmann, C. M. F. Lohmann, and N. F. Putman, "Magnetic maps in animals: Nature's GPS," J. Exp. Biol. **210**, 3697–3705 (2007).

23. K. J. Lohmann, N. F. Putman, and C. M. F. Lohmann, "The magnetic map of hatchling loggerhead sea turtles," Curr. Opin. Neurobiol. **22**, 336–342 (2012).

24. W. Wiltschko and R. Wiltschko, "Magnetic orientation and magnetoreception in birds and other animals," J. Comp. Physiol. A Neuroethol. Sensory, Neural, Behav. Physiol. **191**, 675–693 (2005).

25. S. Johnsen and K. J. Lohmann, "The physics and neurobiology of magnetoreception," Nat. Rev. Neurosci. **6**, 703–712 (2005).

26. A. J. Kalmijn, "Experimental Evidence of Geomagnetic Orientation in Elasmobranch Fishes," in *Animal Migration, Navigation, and Homing*, K. Schmidt-Koenig and W. T. Keeton, eds. (Springer Berlin Heidelberg, 1978), pp. 347–353.

27. C. T. Rodgers and P. J. Hore, "Chemical magnetoreception in birds: The radical pair mechanism," Proc. Natl. Acad. Sci. U. S. A. **106**, 353–360 (2009).

28. R. J. Gegear, A. Casselman, S. Waddell, and S. M. Reppert, "Cryptochrome mediates light-dependent magnetosensitivity in Drosophila," Nature **454**, 1014 (2008).

29. S. Johnsen and K. J. Lohmann, "Magnetoreception in animals," Phys. Today **61**, 29–35 (2008).

30. A. F. Zuluaga and R. Richards-Kortum, "Spatially resolved spectral interferometry for determination of subsurface structure," Opt. Lett. **24**, 519–521 (1999).

31. W. J. Brown, S. Kim, and A. Wax, "Noise characterization of supercontinuum sources for low-coherence interferometry applications.," J. Opt. Soc. Am. A. Opt. Image Sci. Vis. **31**, 2703–10 (2014).

32. J. A. Izatt and M. A. Choma, "Theory of Optical Coherence Tomography," in *Optical Coherence Tomography: Technology and Applications, Second Edition* (2015).

33. W. Drexler, M. Liu, A. Kumar, T. Kamali, A. Unterhuber, and R. A. Leitgeb, "Optical coherence tomography today: speed, contrast, and multimodality," J. Biomed. Opt. **19**, 071412–071412 (2014).

34. J. A. Izatt, M. A. Choma, and A. Dhalla, "Theory of Optical Coherence Tomography," Opt. Coherence Tomogr. 47–72 (2008).

35. W. Drexler and J. G. Fujimoto, "Introduction to OCT," in *Optical Coherence Tomography: Technology and Applications, Second Edition* (2015), pp. 1–2571.

36. B. E. A. Saleh and M. C. Teich, "Beam Optics," in *Fundamentals of Photonics*, B. E. A. Saleh, ed., Third (Wiley, 2007).

37. Z. Hu and A. M. Rollins, "Optical design for OCT," in *Optical Coherence Tomography: Technology and Applications, Second Edition* (2015), pp. 1–2571.

38. Z. Hu, Y. Pan, and A. M. Rollins, "Analytical model of spectrometer-based two-beam spectral interferometry," Appl. Opt. **46**, 8499–8505 (2007).

39. M. J. C. van Gemert, S. L. Jacques, H. J. C. M. Sternborg, and W. M. Star, "Skin Optics," IEEE Trans. Biomed. Eng. **36**, 1146–1154 (1989).

40. B. Karamata, P. Lambelet, M. Leutenegger, M. Laubscher, S. Bourquin, and T. Lasser, "Multiple scattering in optical coherence tomography. Investigation and modeling," J. Opt. Soc. Am. A **22**, 1380 (2005).

41. J. F. de Boer, B. Cense, B. H. Park, M. C. Pierce, G. J. Tearney, and B. E. Bouma, "Improved signal-to-noise ratio in spectral-domain compared with time-domain optical coherence tomography.," Opt. Lett. **28**, 2067–2069 (2003).

42. B. Liu and M. E. Brezinski, "Theoretical and practical considerations on detection performance of time domain, Fourier domain, and swept source optical coherence tomography.," J. Biomed. Opt. **12**, 044007 (2007).

43. D. V Perepelitsa, "Johnson Noise and Shot Noise," Analysis 2–5 (2006).

44. A. M. Rollins and J. A. Izatt, "SNR analysis of conventional and optimal fiber optic low-coherence interferometer topologies," in *Coherence Domain Optical Methods in Biomedical Science and Clinical Applications IV* (2000), Vol. 3915, p. 60.

45. H. Xu, "Shot Noise," Online 1–6 (2004).

46. F. Rice, "A frequency-domain derivation of shot-noise," Am. J. Phys. **84**, 44–51 (2016).

47. S. Shin, "Characterization and comparison of optical source relative intensity noise and effects in optical coherence tomography," University of Illinois at Urbana-Champaign (2010).

48. "ANSI z136.1-2007 Standard for Safe Use of Lasers," (2007).

49. A. Dubois, L. Vabre, A. C. Boccara, and E. Beaurepaire, "High-resolution full-field optical coherence tomography with a Linnik microscope," Appl. Opt. **41**, 805–812 (2002).

50. J. Barrick, A. Doblas, M. R. Gardner, P. R. Sears, L. E. Ostrowski, A. L. Oldenburg, S. P. R., L. E. Ostrowski, and A. L. Oldenburg, "High-speed and high-sensitivity parallel spectral-domain optical coherence tomography using a supercontinuum light source," Opt. Lett. **41**, 5620–5623 (2016).

51. H. C. Hendargo, A. K. Ellerbee, and J. A. Izatt, "Spectral Domain Phase Microscopy," in *Coherent Light Microscopy*, M. H. Jericho and H. J. Kreuzer, eds. (2011), pp. 199–228.

52. M. A. Choma, A. K. Ellerbee, C. Yang, T. L. Creazzo, and J. A. Izatt, "Spectral-domain phase microscopy," Opt. Lett. **30**, 1162 (2005).

53. L. Froehly and J. Meteau, "Supercontinuum sources in optical coherence tomography: A state of the art and the application to scan-free time domain correlation techniques and depth dependant dispersion compensation," Opt. Fiber Technol. **18**, 411–419 (2012).

54. M. Szkulmowski, M. Wojtkowski, T. Bajraszewski, I. Gorczyńska, P. Targowski, W. Wasilewski, A. Kowalczyk, and C. Radzewicz, "Quality improvement for high resolution in vivo images by spectral domain optical coherence tomography with supercontinuum source," Opt. Commun. **246**, 569–578 (2005).

55. B. Grajciar, M. Pircher, A. Fercher, and R. Leitgeb, "Parallel Fourier domain optical coherence tomography for in vivo measurement of the human eye," Opt Express **13**, 1131–1137 (2005).

56. X. Shu, L. Beckmann, and H. F. Zhang, "Visible-light optical coherence tomography: a review," J. Biomed. Opt. **22**, 1 (2017).

57. P. Mouroulis and J. Macdonald, "Putting it all together," in *Geometrical Optics and Optical Design* (1997), pp. 94–136.

58. A. Small, "Spherical aberration, coma, and the Abbe sine condition for physicists who don't design lenses," Am. J. Phys. **86**, 487–494 (2018).

59. E. P. Goodwin and J. C. Wyant, *Field Guide to Interferometric Optical Testing* (2006).

60. D. L. Marks, A. L. Oldenburg, J. J. Reynolds, and S. A. Boppart, "Autofocus Algorithm for Dispersion Correction in Optical Coherence Tomography," Appl. Opt. **42**, 3038 (2003).

61. Y. Nakamura, S. Makita, M. Yamanari, and Y. Yasuno, "Optimization of line-field spectral domain optical coherence tomography for in vivo high-speed 3D retinal imaging - art. no. 64291P," Coherence Domain Opt. Methods Opt. Coherence Tomogr. Biomed. XI **6429**, P4291–P4291 (2007).

62. Y. Zhang, J. Rha, R. S. Jonnal, and D. T. Miller, "Adaptive optics parallel spectral domain optical coherence tomography for imaging the living retina," Opt. Express **13**, 4792 (2005).

63. A. Dubois, O. Levecq, H. Azimani, A. Davis, J. Ogien, D. Siret, and A. Barut, "Line-field confocal time-domain optical coherence tomography with dynamic focusing," Opt. Express **26**, 33534–33542 (2018).

64. M. a Mall, "Role of cilia, mucus, and airway surface liquid in mucociliary dysfunction: lessons from mouse models," J. Aerosol Med. Pulm. Drug Deliv. **21**, 13–24 (2008).

65. A. Wanner, M. Salathe, and T. G. O'riordan, "Mucociliary clearance in the airways," Am. J. Respir. Crit. Care Med. **154**, 1868–1902 (1996).

66. J. A. Regnis, M. Robinson, D. L. Bailey, P. Cook, P. Hooper, H. K. Chan, I. Gonda, G. Bautovich, and P. T. P. Bye, "Mucociliary clearance in patients with cystic fibrosis and in normal subjects," Am. J. Respir. Crit. Care Med. **150**, 66–71 (1994).

67. G. C. Smaldone, W. M. Foster, T. O'Riordan, M. S. Messina, R. Perry, and E. G.

Langenback, "Regional Impairment of Mucociliary Clearance in Chronic Obstructive Pulmonary Disease," Chest **103**, 1390–1396 (1993).

68. L. Liu, K. K. Chu, G. H. Houser, B. J. Diephuis, Y. Li, E. J. Wilsterman, S. Shastry, G. Dierksen, S. E. Birket, M. Mazur, S. Byan-Parker, W. E. Grizzle, E. J. Sorscher, S. M. Rowe, and G. J. Tearney, "Method for Quantitative Study of Airway Functional Microanatomy Using Micro-Optical Coherence Tomography," PLoS One **8**, 1–8 (2013).

69. A. L. Oldenburg, R. K. Chhetri, D. B. Hill, and B. Button, "Monitoring airway mucus flow and ciliary activity with optical coherence tomography," Biomed. Opt. Express **3**, 1978–92 (2012).

70. M. L. Fulcher and S. H. Randell, "Human nasal and tracheo-bronchial respiratory epithelial cell culture," Methods Mol. Biol. **945**, 109–121 (2013).

71. M. L. Fulcher, S. Gabriel, K. a Burns, J. R. Yankaskas, and S. H. Randell, "Well-differentiated human airway epithelial cell cultures," Methods Mol. Med. **107**, 183–206 (2005).

72. P. R. Sears, W.-N. Yin, and L. E. Ostrowski, "Continuous mucociliary transport by primary human airway epithelial cells in vitro," Am. J. Physiol. Lung Cell. Mol. Physiol. **309**, L99–L108 (2015).

73. Z. Sutto, G. E. Conner, and M. Salathe, "Regulation of human airway ciliary beat frequency by intracellular pH," J. Physiol. **560**, 519–532 (2004).

74. S. Klumpp and D. Faivre, "Magnetotactic bacteria: Magnetic navigation on the microscale," Eur. Phys. J. Spec. Top. **225**, 2173–2188 (2016).

75. J. F. Schenck, "Physical interactions of static magnetic fields with living tissues," Prog. Biophys. Mol. Biol. **87**, 185–204 (2005).

76. P. C. Fannin and S. W. Charles, "On the calculation of the Neel relaxation time in uniaxial single-domain ferromagnetic particles," J. Phys. D. Appl. Phys. **27**, 185–188 (1994).

77. A. L. Oldenburg, W. Luo, and S. A. Boppart, "High-resolution in vivo nanoparticle imaging using magnetomotive optical coherence tomography," Proc. SPIE **6097**, 609702-609702–11 (2006).

78. A. L. Oldenburg, V. Crecea, S. A. Rinne, R. Rezaeipoor, E. J. Chaney, and S. A. Boppart, "Spectral-domain magnetomotive OCT imaging of magnetic nanoparticle biodistribution," Coherence Domain Opt. Methods Opt. Coherence Tomogr. Biomed. Xii **6847**, 84719 (2008).

79. R. G. Lyons, "The Discrete Fourier Transform," in *Understanding Digital Signal Processing*, 3rd ed. (2011).

80. S. R. Aglyamov, A. B. Karpiouk, Y. A. Ilinskii, E. A. Zabolotskaya, and S. Y. Emelianov, "Motion of a solid sphere in a viscoelastic medium in response to applied acoustic radiation force: Theoretical analysis and experimental verification," J. Acoust. Soc. Am. **122**, 1927–1936 (2007).

81. P. Chadwick and E. A. Trowbridge, "Oscillations of a rigid sphere embedded in an infinite elastic solid," Proc. Camb. Philol. Soc. **63**, 1207- (1967).

82. T. Jansson, M. Evertsson, E. Atile, R. Andersson, S. Fredriksson, H. W. Persson, I. Svensson, and M. Cinthio, "Induced tissue displacement in magnetomotive ultrasound imaging - Simulations and experiments," IEEE Int. Ultrason. Symp. IUS 639–642 (2014).

83. Y. A. Ilinskii, G. D. Meegan, E. A. Zabolotskaya, and S. Y. Emelianov, "Gas bubble and solid sphere motion in elastic media in response to acoustic radiation force," J. Acoust. Soc. Am. **117**, 2338–2346 (2005).

84. A. B. Karpiouk, S. R. Aglyamov, Y. A. Ilinskii, E. A. Zabolotskaya, and S. Y. Emelianov, "Motion of a solid sphere in a viscoelastic medium in response to applied acoustic radiation force: Theoretical analysis and experimental verification," J Acoust Soc Am **122**, 1927–1936 (2007).

85. I. G. Lim, S. Park, and J. Oh, "Theoretical development of a magnetic force and an induced motion in elastic media for a magneto-motive technique," J. Korean Phys. Soc. **69**, (2016).

86. M. W. Urban, I. Z. Nenadic, S. A. Mitchell, S. Chen, and J. F. Greenleaf, "Generalized response of a sphere embedded in a viscoelastic medium excited by an ultrasonic radiation force," J. Acoust. Soc. Am. **130**, 1133–1141 (2011).

87. S. Timoshenko and J. N. Goodier, *Theory of Elasticity* (The Maple Press Company, 1934).

88. D. Thapa, B. Levy, D. Marks, and A. L. Oldenburg, "Inversion of displacement fields to quantify the magnetic particle distribution in homogeneous elastic media from magnetomotive ultrasound," **2**, 1–2 (2019).

89. D. Schüler, "Formation of magnetosomes in magnetotactic bacteria," J. Mol. Microbiol. Biotechnol. **1**, 79–86 (1999).

90. Z. Liu, J. Xu, X. Wang, K. Nie, and W. Jin, "A fixed-pattern noise correction method based on gray value compensation for TDI CMOS image sensor," Sensors (Switzerland) **15**, 23496–23513 (2015).

91. T. H. Boyer, "The force on a magnetic dipole," Am. J. Phys. **56**, 688–692 (1988).

92. A. Caciagli, R. J. Baars, A. P. Philipse, and B. W. M. Kuipers, "Exact expression for the magnetic field of a finite cylinder with arbitrary uniform magnetization," J. Magn. Magn. Mater. **456**, 423–432 (2018).

93. D. J. Griffiths, "Magnetic Fields in Matter," in *Introduction to Electrodynamics*, Fourth (Pearson, 1989).

94. J. Simpson, J. Lane, C. Immer, and R. Youngquist, "Simple Analytic Expressions for the Magnetic Field of a Circular Current Loop," Recon 1–3 (2001).

95. T. Nakamura, T. Tsutaoka, and K. Hatakeyama, "Frequency dispersion of permeability in ferrite composite materials," J. Magn. Magn. Mater. **138**, 319–328 (1994).

96. J. Mispelter and A. Briguet, *NMR Probeheads for Biophysical and Biomedical Experiments*, Second (Imperial College Press, 2015).

97. S. Kazemirad, H. K. Heris, and L. Mongeau, "Experimental methods for the characterization of the frequency-dependent viscoelastic properties of soft materials," J. Acoust. Soc. Am. **133**, 3186–3197 (2013).

98. N. Sasaki, "Viscoelastic Properties of Biological Materials," in *Viscoelasticity- From Theory to Biological Applications*, J. de Vicente, ed. (IntechOpen, 2012), pp. 99–122.

99. G. Lamouche, B. F. Kennedy, K. M. Kennedy, C. Bisaillon, A. Curatolo, G. Campbell, and D. D. Sampson, "Review of tissue simulating phantoms with controllable optical, mechanical and structural properties for use in optical coherence tomography," Biomed. Opt. Express **3**, 1381–1398 (2012).

100. T. L. Troy and S. N. Thennadil, "Optical properties of human skin in the near infrared wavelength range of 1000 to 2200 nm," J. Biomed. Opt. **6**, 167 (2001).

101. V. Normand, D. L. Lootens, E. Amici, K. P. Plucknett, and P. Aymard, "New insight into agarose gel mechanical properties," Biomacromolecules **1**, 730–738 (2000).

102. E. J. Chen, J. Novakofski, W. K. Jenkins, and W. D. O. Brien, "Young's Modulus Measurements of Soft Tissues with Application to Elasticity Imaging," IEEE Trans. Ultrason. Ferroelectr. Freq. Control **43**, 191–194 (1996).

103. L. Yang, X. Yu, A. M. Fuller, M. A. Troester, and A. L. Oldenburg, "Characterizing optical coherence tomography speckle fluctuation spectra of mammary organoids during suppression of intracellular motility," Quant. Imaging Med. Surg. **10**, 76–85 (2020).

104. C. Apelian, F. Harms, O. Thouvenin, and A. C. Boccara, "Dynamic full field optical coherence tomography: subcellular metabolic contrast revealed in tissues by interferometric signals temporal analysis," Biomed. Opt. Express **7**, 1511 (2016).

105. R. L. Blackmon, S. M. Kreda, P. R. Sears, B. S. Chapman, D. B. Hill, J. B. Tracy, L. E. Ostrowski, and A. L. Oldenburg, "Direct monitoring of pulmonary disease treatment biomarkers using plasmonic gold nanorods with diffusion-sensitive OCT," Nanoscale **9**, 4907–4917 (2017).

106. R. K. Chhetri, R. L. Blackmon, W. C. Wu, D. B. Hill, B. Button, P. Casbas-Hernandez, M. A. Troester, J. B. Tracy, A. L. Oldenburg, and C. Yang, "Probing biological nanotopology via diffusion of weakly constrained plasmonic nanorods with optical coherence tomography," Proc. Natl. Acad. Sci. U. S. A. **111**, E4289–E4297 (2014).